Dynamic and static conformations at the water-solid interface

Rosa Maria Helena Poetes

Supervisor
Prof. Dr. Ullrich Steiner

A dissertation submitted for the degree of Doctor of Philosophy
September 2009

UNIVERSITY OF CAMBRIDGE

Department of Physics
Biological and Soft Systems Sector
Thin Films and Interfaces Group

Clare Hall

Declaration

This dissertation is the result of my own work and includes nothing which is the outcome of work done in collaboration except where specifically indicated in the text.
I declare that no part of this work has been submitted for a degree or other qualification at this or any other university.
This dissertation does not exceed the word limit of 60,000 words set by the Physics and Chemistry Degree Committee.

Rosa Poetes, September 2009

Acknowledgements

First, I want to thank Prof. Ullrich Steiner who gave me the opportunity to pursue my PhD in Cambridge. Working with him has been a great experience. I particularly appreciated his always open door, and his eagerness to help and discuss any scientific ideas or difficulty whenever they came up.

Thanks go to all former and current members of the Thin Films and Interfaces Group for their help, friendship, and support. Kathrin Holtzman helped significantly with the second project described in this thesis. For her diploma project, she worked with me for one year on the wetting of surfaces. Maik Scherer and Mathias Kolle helped with the colloidal patterning of surfaces and some SEM images. Katherine Thomas has been an amazing proof reader and always offered useful feedback on my thoughts and writing. Thanks also go to Pieter van der Waal, Nicoleta Voicu, Edward Crossland, Mihaela Nedelcu, David Barbero, Pola Goldberg-Oppenheimer, Alex Finnemore, Stefan Guldin, Pedro Cunha, Li Li, Nataliya Yufa, Ellie Kim, and Julian Wechs, who worked on the Teflon surface project as a summer student.

I worked in collaboration on two topics covered in this thesis: Wetting of flowers with Dr. Heather Whitney and on electroactuation of brushes with Dr. Feng Zhou.

Thanks go to all my collaborators and contacts in other departments during my PhD. In particular, I want to thank Prof. Wilhelm Huck and Dr. Oren Scherman and the students in the Melville lab (Andrew Brown, Ron Oren, Tim Kelby, Nan Cheng, Nicolas Nouvel, Feng Tian and Evan Spruijt).

Thanks also go to: Sue Gymer, Suresh Mistry, Pete Bone and Owen Dunn, who have been wonderful technical support; Nadia Stelmashenko, who helped with the sample preparation for polymer brush experiments; Adam Corrigan, who taught me how to analyse particle movements using Matlab; Kristian Franze, who helped with the confocal microscopy measurements; Stephanie Lacour, who always had useful advice for microfabrication problems; David Hasko, who discussed different etching methods with me; Sumeet Mahajan and Robin Cole, who helped me with electroplating, and supplied samples for early experiments.

I want to also thank Prof. Giacinto Scoles for his teaching, mentorship and encouragement during my time in Princeton.

Last, but not least, I thank my husband Nicolas, and my parents Herbert and Ulla, who have supported me to pursue my dreams, wherever they led me.

Abstract

Dynamic and static conformations at the water-solid interface

Rosa Poetes

In this work, we have explored dynamic and static phenomena occurring at the water-solid interface. Controlling the interaction of solids with water is technologically very interesting. Applications include the inside coating of pipes, containers and medical equipment and coating of boats, windows and underwater equipment.

In Part I, we explore the possibility of using low cost and practical triggering mechanisms for fast and reliably switching of the surface wettability in the liquid environment. Electric fields are used as triggers to change the surface properties of charged polymer brushes and hydrogels in water. The response of surface-attached polymers to the external triggers was studied in detail.

We showed that neither charged polymer brushes nor hydrogels are easily exploitable for surface property tuning using electric potentials as switching mechanisms. The two limiting factors for the use of polymer brushes and hydrogels in such systems are the material instability and the low switching speed between swollen and collapsed conformations. While the stability issues could be resolved through further work on the synthetic side, we believe that the long switching times necessary for complete conformational changes are an inherent problem of these densely grafted systems and due to entanglements.

Part II focuses on the influence of structure on surface wettability. Metastable self-cleaning wetting behaviour of water droplets on hydrophilic surfaces was studied. We confirmed and expanded the design parameters for very robust metastable Cassie-Baxter wetting states with high contact angles on hydrophilic surfaces, which were introduced by Tuteja *et al.* [1]. The fundamental difference in the wetting behaviour of disconnected and connected structures was also shown.

The behaviour of superhydrophobic surfaces under water in an open system was also studied. The decay of the air bubble covering the superhydrophobic material (plastron) was quantified for different materials. A strongly non-linear depth dependence of the plastron stability was shown. The limited plastron life-time makes the use of superhydrophobic surfaces for underwater applications (buoyancy increase or drag reduction) technologically challenging.

Contents

1 Introduction

Surface properties are scientifically very interesting, as surfaces often display very different behaviour to that observed in most bulk materials. Understanding and modifying surface properties is also of immense technological importance. The study of the properties of surfaces still offers the chance for surprising scientific discoveries and the development of new technological applications.

Here, we focus on surfaces with complex surface-liquid interactions, in order to advance our understanding of how the solid-liquid interface can be influenced and controlled for technologically relevant materials. The first half (Part I) of this work discusses the tuning of water-surface interactions through conformational changes of polymer layers on the surfaces. This involves the triggering of responsive surface properties by various stimuli. The second half (Part II) discusses surfaces which exhibit underwater hydrophobicity and metastable superhydrophobic wetting states separated by energetic barriers. The unexpected wetting behaviour sheds new light on the possible applications and limitations of very rough and highly structured superhydrophobic materials.

Polymer brushes and hydrogels have been a focus of attention as systems for nano- and micro-actuation for the last number of years [2]. They fulfill multiple important criteria making them particularly interesting as responsive systems: relative ease of production, material flexibility, chemical and physical triggers and relatively high stability. The work presented here explores the feasibility of influencing surface properties using conformational changes of surface-attached polymers in aqueous solutions.

In particular, we explore the potentials and limits of electric stimuli as surface property triggers for polymer brushes and surface-attached hydrogels. In order to establish

the technological relevance of these systems, particular attention was paid to the repeatability, reliability, stability and time-scale of surface property changes associated with triggering of surface-attached polymers with electric stimuli. The project was designed to develop 'open' microfluidic systems: patterned surfaces with individually adressable surface properties could be used to induce directional transport in small scale particles at the solid-liquid interface.

Equilibrium wetting on very rough surfaces has been of great technological and high fundamental interest since the discovery of the 'Lotus effect' [3]. Superhydrophobic surfaces have long been at the centre of our attention, both in order to understand their properties and to develop highly robust and technologically applicable self-cleaning surfaces. Over the last two years, an increasing interest in the non-equilibrium wetting phenomena on surfaces has developed. This was sparked by work on metastable self-cleaning properties observed in a new class of highly structured hydrophilic surfaces [1, 4, 5]. Here, we present experimental work conducted to enhance the understanding of metastable superhydrophobic states. In particular, this work shows the applicability and the limitations of the design parameters by Tuteja *et al.* [1] for surfaces exhibiting multiple energy minima.

Further, underwater non-wetting of superhydrophobic surfaces has been explored in detail in this thesis. Over the last years, due to theoretical studies [6] and technologically motivated work on buoyancy [7, 8] and drag reduction [9] of superhydrophobic surfaces, the need for a better understanding of the behaviour of these systems has increased. Here, we present the first experimental study of the underwater wetting behaviour of superhydrophobic surfaces, in particular a study on the plastron stability.

This thesis is divided into two distinct parts (Part I and Part II). This division is a result of difficulties encountered during my work with the project presented in Part I. The original intention of the polymer brush project was to build a system exploiting polymer brush conformational changes in order to induce directional movements in particles at the solid-liquid interface. The work described in Part I, in particular the slowness of the conformational changes and the poor polymer stabilty, showed

that surface-attached polymers are probably not a good system to reliably achieve directional movement. Therefore, the last year of my PhD was focused on the project described in Part II. As Part I and Part II present distinct projects, the background, sample preparation and methodology sections have been divided accordingly.

Part I

Polymer brushes and hydrogels

2 Polymer theory

This part of the thesis will focus on work done on conformational changes of polymer brushes and surface-attached hydrogels. In the aqueous environment, these systems exhibit both a swollen state and a collapsed state, which have very different surface properties. In particular, the swollen state is very hydrophilic, while the collapsed state is less hydrophilic or mildly hydrophobic. The exact wetting properties depend strongly on the nature of the polymeric material and can be tuned through small changes in the polymerisation chemistry.

In the following, we discuss different triggering mechanisms used to achieve switchable wetting properties using surface-attached polymers.

Understanding the conformational changes of polymer brushes and surface-attached hydrogels in response to external triggering mechanisms is an important step toward temporal and local tuning of wetting properties at the solid-liquid interface.

2.1 Background

2.1.1 Polymers in solution

This section briefly presents some relevant concepts of polymer physics related to conformational changes of polymer brushes and surface-tethered hydrogels [2, 10].

Conformation describes the spatial structure of a polymer. For a free polymer in solution with N bonds and a bond length a, all conformations can be described in

terms of the volume V or radius R of the sphere occupied by a single polymer chain.

The smallest conformation for a non-branched homopolymer is a collapsed globule resulting from strong monomer-monomer attraction, occupying a volume

$$V \propto Na^3 \tag{2.1}$$

This corresponds to a radius of

$$R_{\text{globule}} = V^{1/3} \propto N^{1/3}a \tag{2.2}$$

For a random walk of a polymer chain (theta conditions), the radius of gyration is given by

$$R_{\text{gyration}} \propto \sqrt{N}a \tag{2.3}$$

Long-range repulsion of the monomers result in an extended conformation. An example for this is the strong electrostatic repulsion in the case of charged monomers, which causes the polymer to adopt a highly stretched conformation. In the most extreme case, this gives an extended length L of

$$L_{\text{stretched}} \propto Na \tag{2.4}$$

The size of a polymer chain thus depends strongly on the particular polymer properties, as well as the surrounding environmental parameters. In very few cases does the conformational length extend to the total length of the polymer chain.

In general, attractive interaction of the individual monomers combined with low solubility in the solution leads to coiled conformations. Strong monomer repulsion and good solubility of the polymer in the solution leads to stretched conformations [10].

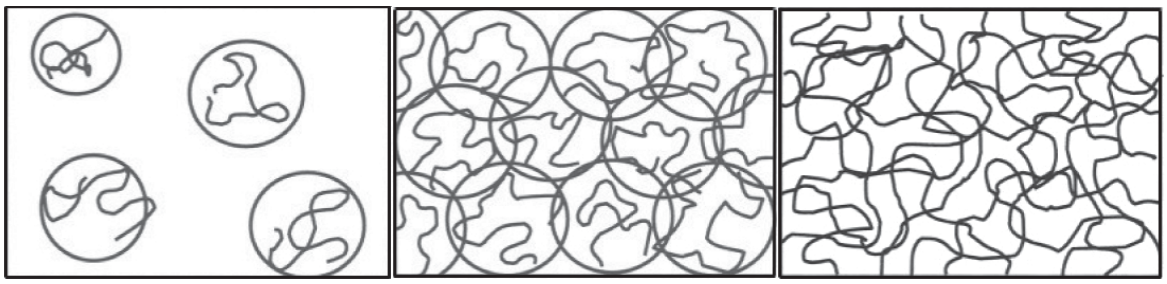

(a) Dilute polymer solution (b) Semi-dilute polymer solution (c) Polymer melt

Figure 2.1: *Overlapping polymer chains in a) dilute polymer solution; b) semi-dilute polymer solution; c) polymer melt*

The conformation of polymers in solution is strongly influenced by the concentration of polymeric material. Therefore, polymer solutions are generally discussed in terms of dilute and semi-dilute solutions, or polymer melts. Figure 2.1 shows qualitative representations of the three different situations.

Polymer conformational states in the dilute regime are not influenced significantly by other polymer chains present in the solution but are strongly dependent on polymer-solvent interactions. In the semi-dilute regime, both solvent conditions and other surrounding polymer chains influence the polymer chain conformation. In the polymer melt, the solvent input can be neglected; only very small quantities of solvent are present. The behaviour is therefore dominated by intra-chain and inter-chain monomer interactions. A detailed mathematical treatment of these three regimes can be found in Rubinstein [10].

2.1.2 Surface-tethered polymers

Surface-tethered polymer layers are made from molecules with an anchor, a molecular body, and a molecular tail. Depending on the grafting density, these layers show very different behaviours. The grafting density can be defined twofold (which causes a large amount of confusion in the literature), so in the following, we shall make the distinction between the molecular weight based grafting density $\sigma_{\mathrm{Mn}} = (H\rho N_{\mathrm{A}})/M_{\mathrm{n}}$ (where H describes the layer thickness, and ρ the layer density) and the reduced grafting density

(a) Mushroom (b) Pancake (c) Polymer brush

Figure 2.2: *Surface-tethered polymers chains are classified as a function of the grafting density and surface-chain interaction as a) mushroom; b) pancake; c) polymer brush [10]*

$\sigma_t = 1/D$ (which is purely a function of molecular separation on the surface D).

Grafted polymer layers are usually described as mushroom, pancake and polymer brush layers [Fig. 2.2]. Mushroom and pancake behaviour correspond to low grafting density σ, but differ in the tail-surface interaction. The thickness of a mushroom layer H scales with the number of monomers and is independent of the grafting density σ in a good solvent.

Polymer brushes have such a high grafting density σ that the chains overlap. This gives a state similar to a semi-dilute polymer solution [10]. As a result of the segment-segment interactions of the chains, polymer brushes, as compared to mushroom and pancake layers, stretch away from the surface [11].

Brittain *et al.* emphasised the usefulness of the reduced tethered density Σ as a quantifying measure of polymer brushes. Σ gives the number of chains that occupy an area equal the area filled by a non-overlapping polymer chain under the same experimental conditions [11].

$$\Sigma = \sigma_{\mathrm{Mn}} \pi R_g^2 \tag{2.5}$$

where R_g is the radius of gyration of a tethered chain under specific experimental

conditions of solvent and temperature [11].

Therefore, according to this definition, the mushroom or pancake regime corresponds to $\Sigma < 1$, while the highly stretched regime (polymer brush regime) corresponds to $\Sigma > 1$ [11].

2.1.3 Polymer brush regimes

Thirty years ago, Alexander [12] and de Gennes [13] showed that in a good solvent, the polymer brush layer thickness H scales as

$$H \approx N\sigma_{\mathrm{t}}^{1/3} \tag{2.6}$$

In a poor solvent, this becomes

$$H \approx N\sigma_{\mathrm{t}}^{1/2} \tag{2.7}$$

In the highly stretched regime ($\Sigma \gg 1$), the polymer brush thickness is given by.

$$H \approx L \approx Na\sigma \tag{2.8}$$

Milner *et al.* [14] allowed the free ends of the chains to be distributed throughout the whole of the grafted layer. This approach yields a more physical parabolic profile of the brush, as there is no singularity at the brush-water interface, and is generally used for the theoretical description of polymer brush density profiles [14]. Since then, the polymer brush conformational phase diagram and conformational descriptions have become more complex and more detailed. In Section 2.1.5, we shall focus in more detail on the behaviour of polyelectrolyte brushes and neutral brushes in salted and unsalted solutions. For the preliminary work done on temperature responsive brushes in Section 4.1, a general understanding of polymer brush collapse as described here is sufficient.

2.1.4 Electrolyte solutions

In order to understand polymer brush conformation in salted solutions, we need to establish how electric fields penetrate electrolyte solutions. Here, we introduce the concept of the Debye screening length λ_{D}

$$\lambda_{\mathrm{D}} = \left(\frac{\kappa \epsilon_0 k_{\mathrm{B}} T}{q^2 N_0} \right)^{1/2} \tag{2.9}$$

where q is the elementary charge of an electron, κ is the relative static electric permittivity, k_{B} is the Boltzmann constant, and N_0 is the total number of charges present in the system. The Debye screening length λ_{D} describes the distance over which charges are screened in an electrolyte solution.

In an electrolyte solution, the Debye length is often denoted by κ^{-1} and becomes

$$\lambda_{\mathrm{D}} = \kappa^{-1} = \left(\frac{\epsilon_0 \epsilon_{\mathrm{r}} k_{\mathrm{B}} T}{2 N_{\mathrm{A}} q^2 I_{\mathrm{c}}} \right)^{1/2} = \frac{1}{\sqrt{8 \pi \lambda_{\mathrm{B}} N_{\mathrm{A}} I}} \tag{2.10}$$

where ϵ_{r} is the dielectric constant of the solution, and I_{c} is the ionic strength of the electrolyte in units of mole/m^3. Alternatively, λ_{B} denotes the Bjerrum length of the medium, which is the separation at which the electrostatic interaction between two elementary charges corresponds to the thermal energy $k_{\mathrm{B}}T$. This gives

$$\lambda_{\mathrm{B}} = \frac{q^2}{4 \pi \epsilon_0 \epsilon_{\mathrm{r}} k_{\mathrm{B}} T} \tag{2.11}$$

In pure water, the Bjerrum length is $\lambda_{\mathrm{B}} \approx 0.7\,\mathrm{nm}$ and the Debye screening length is 960 nm [15]

The decay of the electric potential $\Psi(x)$ of a plate in an electrolyte solution is given by the Debye-Hueckel approximation [16]

$$\Psi(x) = \Psi_0 e^{-\kappa x} \tag{2.12}$$

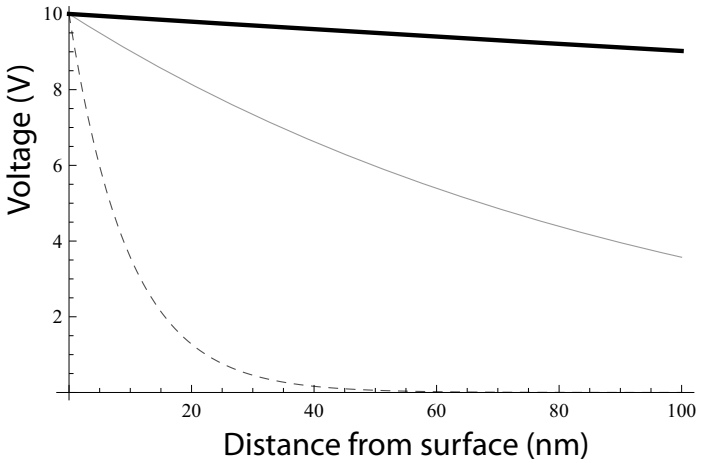

Figure 2.3: *Decay of an electric potential in an electrolyte solution (NaCl or other single charge ions) as a function of distance from the electrode: Thick black - 100 µMol; Thin Gray - 10 mMol; Dashed Grey - 1 Mol*

Figure 2.3 shows that the Debye screening length has a very strong influence on the decay of a potential in an electrolyte solution close to the electrode. We have chosen to show the decay of the electric potential of a plate over the first 100 nm distance from the surface, as this corresponds approximately to the thickness of our polymer brush layers. While the potential decays quickly in strong electrolyte solutions, in weak electrolyte solutions, the decay is nearly linear: for a solution with an ionic concentration of $c_{\text{ion}} < 100$ µMol, the field strength $\Psi_{100\,\text{nm}}$ at 100 nm distance from the electrode is still 90 % of the field strength at the surface Ψ_0. Therefore, the whole polymer brush is subject to the applied potential.

2.1.5 Polyelectrolyte polymer brush regimes

Pincus *et al.* [17,18], Zhulina *et al.* [19] and others established theoretical models in the early 1990s for conformation changes of polyelectrolyte polymer brushes on flat surfaces. In 1994, Borisov *et al.* presented the first phase diagrams of grafted polyelectrolyte polymers in pure water and salted solutions [20].

The following discussion of polyelectrolyte brushes and their different conformational states is based on the scaling theory and simulation argument presented by Csajka *et al.* [21]. While the exact cross-over points between the individual phases are of no

relevance to the work presented here (and are still under theoretical and experimental debate), a general understanding of the four most important states encountered in strongly-charged salt-free polyelectrolyte polymer brush systems is very useful.

It is useful to introduce the Guoy-Chapman length, which describes the thickness of an electric double layer nearby a charged surface, for strongly charged surface-grafted polymer brushes as

$$\lambda_{\mathrm{GC}} = \frac{1}{2\pi\lambda_{\mathrm{B}} N f_{\mathrm{c}} \rho_{\mathrm{A}}} = \frac{1}{2\pi\lambda_{\mathrm{B}} N f_{\mathrm{c}} a\sigma} \tag{2.13}$$

where $Nf_{\mathrm{c}}\rho_{\mathrm{A}}$ denotes the surface charge density, f_{c} denotes the monomer charge fraction [21].

Strongly charged systems (fixed number and position of charges) are given for

$$\lambda_{\mathrm{GC}} \ll H \tag{2.14}$$

Weakly charged systems (pH dependent quantity and position of charges) correspond to

$$\lambda_{\mathrm{GC}} \gg H \tag{2.15}$$

The osmotic regime (OsB) is well understood. In this phase, the brush conformation results from a balance between the chain elasticity (which acts decrease the brush height) and the repulsive osmotic counterion pressure (which acts increase the brush height).

$$H_{\mathrm{OsB}} = N b f_{\mathrm{c}}^{1/2} \tag{2.16}$$

where f is the fraction of charged monomers in the brush.

In the limit where steric effects dominate over electrostatic effects (called the quasi-neutral regime NB), the brush height is given by

$$H_{\mathrm{NB}} = Nb\left(\frac{(1+f_{\mathrm{c}})^2\rho_{\mathrm{A}}\nu_2}{b}\right)^{1/3} \propto Nb\sigma^{1/3} \tag{2.17}$$

where ν_2 is the effective second viral coefficient.

The collapsed brush (CB) corresponds to

$$H_{\mathrm{CB}} = N\rho_{\mathrm{A}}\frac{\nu_2^2\lambda_{\mathrm{B}}^3(1+f_{\mathrm{c}})^4}{f_{\mathrm{c}}^3} \propto Nb\sigma \tag{2.18}$$

For further information about the different approaches used to obtain these results, as well as equations governing the behaviour in weakly charged systems, please refer to Csajka *et al.* [21].

It would be desirable to include direct comparison of the expected cross-over regions, as well as the exact brush conformation for our polymer brushes in these experiments. However, this is not possible, since the values of ν_2, f_{c}, ρ_{A} and indeed N are unknown for grafting-from polymer brushes.

2.1.6 Hydrogels

Hydrogels are three-dimensional polymer networks able to absorb large amounts of water. They swell to many times their dry volume. The networks do not dissolve in water due to the presence of chemical or physical crosslinks, which provide structure and physical integrity. Hydrogels are often classified as neutral or ionic, depending on their side-group chemistry [22]. We shall focus in this section mostly on ionic hydrogels. Environmentally sensitive hydrogels respond to changes in their external environment. This is discussed in Section 2.2.1.

Hydrogel swelling and collapse is often described as a function of the chemical potential of the solution. A complete derivation of the following formula can be found in Yui *et al.* [22]. Swelling of ionic hydrogels is strongly dependent on the degree of ionisation of the network, the ionisation equilibrium, as well as the nature and quantity of counterions present. For highly ionisable materials, the chemical potential equilibrium

becomes

$$\mu_1 - \mu_{1,0} = \Delta\mu_{\text{elastic}} + \Delta\mu_{\text{mix}} + \Delta\mu_{\text{ionic}} \tag{2.19}$$

where μ_1 is the chemical potential of the swelling agent within the gel, $\mu_{1,0}$ is the chemical potential of the pure fluid and μ_{mix} describes the chemical potential change upon mixing dependent on the heat of mixing and the entropy of mixing

$$\Delta\mu_{\text{mix}} = RT(\ln(1 - \upsilon_{2,\text{s}}) + \upsilon_{2,\text{s}} + X_1\upsilon_{2,\text{s}}) \tag{2.20}$$

where $\upsilon_{2,\text{s}}$ is the volume fraction of the polymer in the gel and X_1 is the polymer water interaction parameter [22].

The elastic component $\Delta\mu_{\text{elastic}}$ for gels crosslinked in the presence of water can be expressed as a function of the molecular weight of the polymer between junction points $\bar{M}_{\text{c}}$, the molecular weight of the polymer chains with no crosslinks $\bar{M}_{\text{n}}$, the specific volume of the polymer υ_1, the molecular volume of the swelling agent (water) V_1 and the volume fraction of the polymer in the relaxed state $\upsilon_{2,\text{r}}$

$$\Delta\mu_{\text{elastic}} = RT\left(\frac{V_1}{\upsilon_1 \bar{M}_{\text{c}}}\right)\left(1 - \frac{2\bar{M}_{\text{c}}}{\bar{M}_{\text{n}}}\right)\upsilon_{2,\text{r}}\left(\left(\frac{\upsilon_{2,\text{s}}}{\upsilon_{2,\text{r}}}\right)^{1/3} - \frac{\upsilon_{2,\text{s}}}{2\upsilon_{2,\text{r}}}\right) \tag{2.21}$$

The ionic term is a function of the total concentration of mobile ions within the gel c_{tot}

$$\Delta\mu_{\text{ionic}} = RTV_1\Delta c_{\text{tot}} \tag{2.22}$$

This implies that the collapse of an ionic hydrogel can be triggered by changes to the total number of mobile ions in the gel, which in turn can be influenced by application of electric fields, as explained in Section 2.2.1.

2.2 Switching of surface-tethered polymers

2.2.1 Switching mechanisms

As for polymers in solution, surface-tethered polymers show preferred conformations as a function of internal and external environmental parameters. Both polymer brushes and surface-tethered hydrogels can exhibit very different conformation (and therefore different physical properties) as a function of these parameters. Internal parameters which affect conformation include

- monomer size and charge
- polymer length and entanglement length
- crosslinking density

Environmental parameters include both chemical and physical stimuli

- solution pH (chemical)
- solvent quality (chemical)
- ionic strength and salt concentration of the solution (chemical)
- temperature (physical)
- mechanical force (physical)
- sound (physical)
- light (physical)
- electric and magnetic fields (physical)

Internal parameters cannot be changed once the polymer system has been synthesized. This excludes them from being used as triggers for conformational changes in most technological applications. External parameters however, can be used to study different conformational states.

Chemical triggers involve global changes to the solution environment and therefore require long equilibration times. Further, they are difficult to control precisely for small

systems. Diffusion within the solution also makes local control of these parameters very complex. Chemical triggers are therefore not well suited for locally controllable, repeatable switching mechanism of polymer brushes.

Physical triggers have an inherent advantage in their facility of application over chemical triggers; they can be controlled without global changes to the solution environment. This makes them much more suitable for any technological application. However, even within the group of physical triggers, some methods are more appealing than others due to ease of application.

The use of temperature, sound or mechanical force for the local control of of wetting properties requires significant investment in small actuation systems, e.g. miniature Peltier elements or miniature piezo-crystals, making them technologically unattractive methods. Sound has the additional difficulty of its relatively large wavelength, which makes it hard to control sound diffraction patterns over the small areas required to switch a surface on the µm length scale.

Physical methods such as light, electric and magnetic fields are better adapted for their exploitation as physical triggers. As well as those discussed above, they have the following advantages

- rely on relatively inexpensive and widely available technology
- switching can be achieved between on and off states
- local application of the trigger over well defined areas is feasible

In the work discussed here, we focus our attention mostly on the switching of neutral polymer brushes in solution via temperature control, the switching of polyelectrolyte polymer brushes and surface-tethered charged hydrogels in solution using electric fields, and surface patterning of polymer brush melts using electric fields.

2.2.2 Literature review

It has been shown that different external stimuli can be used to manipulate the conformation of polymer brushes or hydrogels as explained in Section 2.2.1. Here, we present some approaches in chemical and physical switching of surface-attached polymers in the liquid environment.

Examples of chemical switching in polymer brushes which have been reported include pH changes [23], ionic concentration changes [24–27] and solvent/non-solvent changes [28, 29]. Prokhorova *et al.* used solvent / non-solvent changes to induce enhanced movement of particles at the solvent / brush interface on mixed polymer brush surfaces. For a good review of this work, please refer to Advincula [30] and Minko [31].

Changes to the polymer brush conformation achieved using physical triggers has been reported less frequently. One example is the switching of polymer brush wetting behavior using temperature as a trigger [30–32]. Light has also been explored and used as a trigger.

As early as 1978, hydrogel collapse using temperature changes and later electric fields was shown by Tanaka *et al.* [33, 34]. In the experiment, macroscopic polyacrylamide hydrogels were observed in an acetone / water solution under an applied potential. Here, the complete collapse was observed over a very narrow electric potential change. The gels were not tethered to the surface. Yeghiazarian *et al.* showed in 2007, how this change in conformation and associated macroscopic gel size could be used to make macroscopic gels move directionally along a channel by symmetry breaking in the voltage circuitry [35]. Conformational changes in patterned thermo-responsive surface-attached hydrogels have been investigated using imaging ellipsometry [36].

Matyjaszewski and co-workers reported in 2008 a new method to produce surface-tethered ionic copolymer hydrogels via modified ATRP as explained in Chapter 3.1.2 through photolithographic patterning [37]. They showed that these thermoresponsive gels exhibit a lower critical solubility temperature (LCST) and observed the switching between swollen and collapsed states of these gels.

To our knowledge, no groups have previously reported the successful switching of polyelectrolyte polymer brushes or polyelectrolyte surface-tethered ionic hydrogels using electric potentials, except for the work by Zhou *et al.* [38] discussed in Section 4.2.

3 Materials and measurement techniques

3.1 Polymer sample preparation

3.1.1 Substrate preparation

Polymer brushes and surface-attached hydrogels were grown onto silicon or gold substrates. The silicon substrates were cleaned thoroughly, and then used for growth of the initiator layer. The gold substrates were produced by two different methods: Evaporation of a thin chromium (5 nm) and then a thick gold layer (>100 nm)(Section 8.1.2) or by sputtering of first a thin layer of titanium (10 nm) and then a thick layer of gold (>100 nm). The change in procedure was due to buckling of the surface and detachment of the gold layer under electric fields in the experiments carried out in Section 4.3, that had been observed for the standard chromium/gold samples. An example of a buckled gold surface can be seen in Figure 3.1.

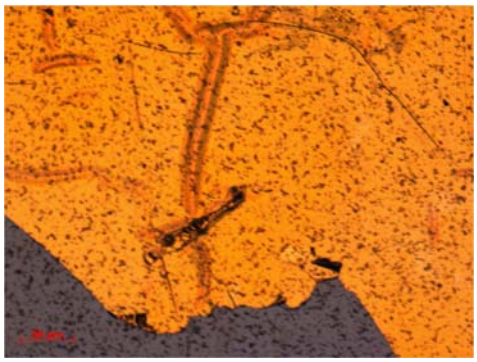

Figure 3.1: *Example of a buckled surface seen in experiments prior to the adhesive chromium layer being replaced by an adhesive titanium layer. The gold buckles and peels off.*

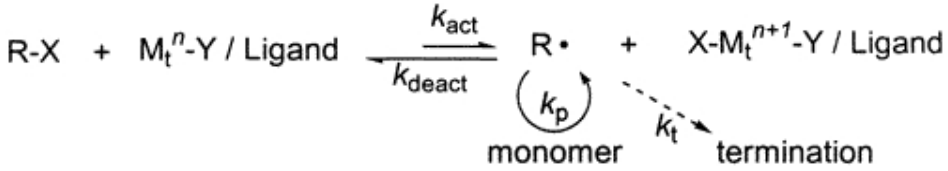

Figure 3.2: *Scheme depicting the transition metal catalysed Atom Transfer Radical Polymerisation (ATRP) as described by Matyjaszewski [39]*

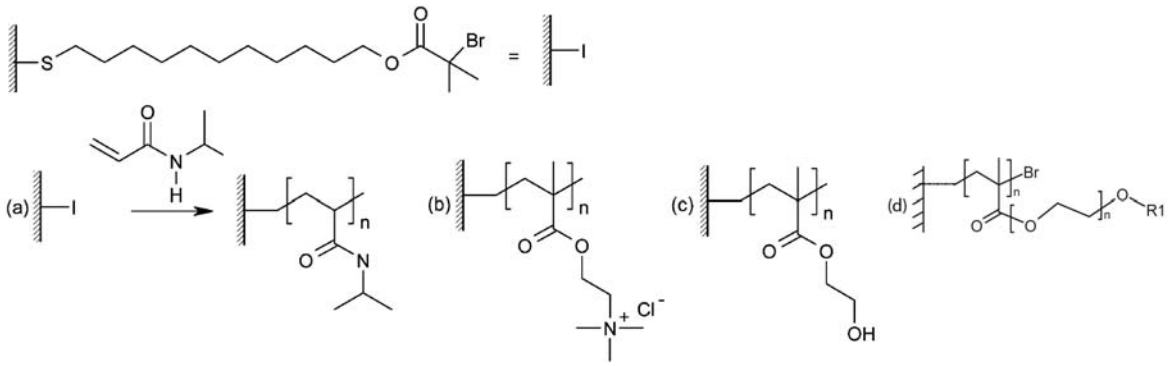

Figure 3.3: *The chemical structure of the four polymer brushes used in our experiments adapted from Edmondson et al. [40]. The top structure shows the initiator used to modify the silicon surface. a) PNIPAM, b) PMETAC, c) PHEMA, and d) POEGMA.*

3.1.2 Polymer brush sample preparation

Nearly all the polymer brushes used in the following experiments were produced via the 'grafting from' method, based on polymerisation of monomers from solution to surface attached initiator groups. The protocol is based on Atom Transfer Radical Polymerisation (ATRP), as first reported by Wang and Matyjaszewski in 1995 [41]. A schematic description of the ATRP protocol is shown in Figure 3.2. The brushes were grown from an initiator layer using the ATRP protocol. For uniform polymer brushes, the initiator was self-assembled on the substrate surface. For patterned brushes the initiator was contact printed onto the substrate, then the first polymer brush was grown using ATRP. After completion of the first brush, the area in between the brushes was functionalised using self-assembly of an initiator, after which a second polymer brush was grown. For further information on polymer brush polymerisation procedures refer to Advincula [2, 30]. Details about this particular polymerisation procedure can be found in the following recent publications [23, 32, 38, 40, 42, 43].

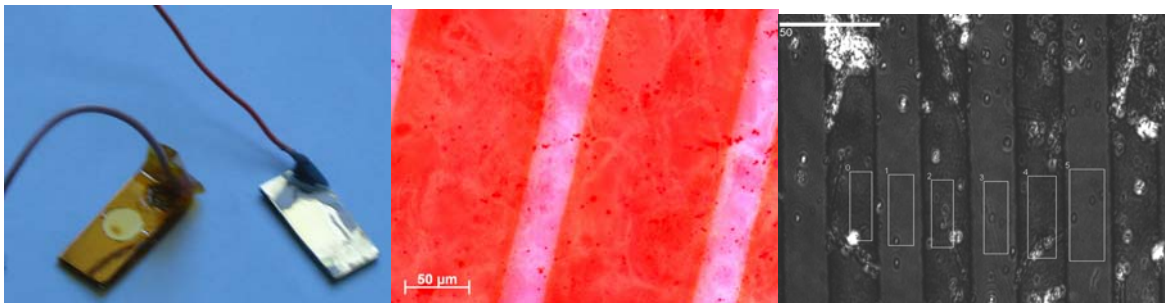

(a) Polymer brush sample mounting (b) Polymer brush stripe pattern (c) Polymer brush in ellipsometer

Figure 3.4: *(a) A polymer brush sample after preparation covered with Kapton tape (left) or nail polish (right) for electric isolation (b) Microscopy image of typical polymer brush stripes (c) Ellipsometric image of the polymer brush as observed with NanoFilm EP3.*

The following polymer brushes were formed via ATRP for use in our experiments[1]: poly[N-isopropylacrylamide] (PNIPAM), poly[2-(methacryloyloxy) ethyltrimethylammoniumchloride] (PMETAC), poly[oligo(ethyleneglycol)methacrylate] (POEGMA), poly[hydroxyethymethacrylate] (PHEMA), and poly(methyl 2-methylpropenoate) (PMMA).

The use of PNIPAM for experiments exploring temperature-induced conformational changes is discussed in Section 4.1. The use of PMETAC for electric field induced conformational changes is discussed in Section 4.2 and 4.3. The polymers POEGMA and PHEMA are used interchangeably as neutral reference polymer brushes. PMMA was used for part of the polymer melt experiments in Chapter 5. The structure of the brushes is shown in Figure 3.4.

All polystyrene (PS) polymer brushes used for some of the experiments discussed in Chapter 5 were produced using the 'grafting to' method [2]. PS chains with a SiCl end-group ($M_n = 135,000\,\mathrm{g/mol}$), NH_2 end-group ($M_n = 300,000\,\mathrm{g/mol}$) and COOH end-group ($M_n = 670,000\,\mathrm{g/mol}$) were spin-coated onto wafers from toluene solutions (25 mg/ml for all solutions) to form films of 250 - 300 nm thickness. M_n denotes the molecular mass. The films were annealed for 148 h at 150°C in a N_2-filled glove box. After annealing the films were rinsed with $CHCl_3$ and ethanol and dried in a stream

[1]The samples were provided by Nan Cheng, Feng Zhou, Tim Kelby, Andy Brown, Evan Spruijt, and Ron Oren in the Melville Laboratory under the supervision of Prof. W. Huck.

[2]Some of these samples were made by Ron Oren, some I prepared myself

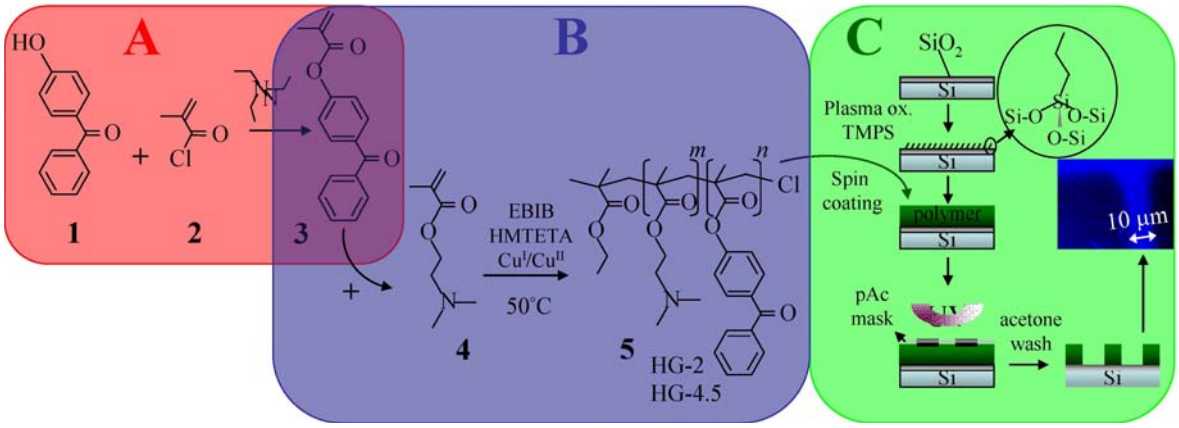

Figure 3.5: *This scheme describes the preparation steps involved in making poly-(DMAEMA-stat-BPMA) hydrogels on surfaces [44]*

of nitrogen. The film thicknesses reduced after rinsing and annealing to approximately 30 nm.

All polymer brush samples were washed in pure H_2O for at least 3 h before use in our experiments. This was done to insure the removal of adsorbed non-tethered polymer on the brush. The samples were first measured dry. They were discarded, if their thickness was too low ($d_{\mathrm{dry}} < 10\,\mathrm{nm}$) or their refractive index was outside the expected range for polymer brush samples ($1.45 < n_{\mathrm{dry}} < 1.70$), or if other fitting problems occurred for the original dry measurement. If found suitable, the samples were attached to a wire using silver dag (Acheson electrodag, Silmid Ltd.). The bare substrate areas and the exposed wire were covered with Kapton tape (Tesa 51408 Kapton high grade masking tape) or isolated with transparent nail polish.

This prevented contact between the solution and the covered areas and therefore focused the experimental triggers on the exposed areas. An example of the samples as prepared can be seen in Figure 3.4.

3.1.3 Hydrogel polymerisation and preparation

Surface- attached polyelectrolyte hydrogels with permanent crosslinks (poly(DMAEMA-*stat*BPMA)) were used to make covalently attached hydrogel patterns on silicon sur-

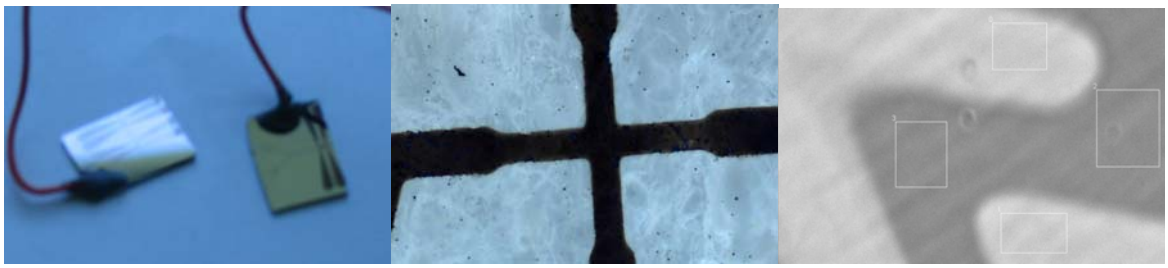

(a) Hydrogel sample mounting (b) Hydrogel pattern (c) Hydrogel in ellipsometer

Figure 3.6: *Hydrogel samples a) Mounting of hydrogel sample for electric field experiments; b) Hydrogel pattern under microscope: The black cross is the dry printed hydrogel, the surrounding area is the silicon reference surface; c) Hydrogel as seen in the ellipsometer (with ROIs): Measurements were performed on the hydrogel (bright regions) and the reference silicon surface (dark regions)*

faces [3] [44]. The protocol was adapted from Matyjaszewski *et. al.* [37].

The polymer was synthesized by ATRP in solution and was then spin coated on patterned silane-activated silicon wafers. Covalently attached, crosslinked hydrogel patterns were obtained with approximately 4.5% crosslinker content after short UV light exposure. More detail on the protocol can be found in Figure 3.5. Thickness of the hydrogels was adjusted using higher or lower concentrations of the spin coating solution. The hydrogel patterns are found to be stable in water for several days and swell by a factor of 2 to 3 when immersed into water [44].

Before use in the ellipsometric experiments, the samples were washed for at least 3h in 18MΩ water. They where then measured and connected to the external circuit as described for the polymer brush samples in Section 3.1.2.

3.2 Ellipsometry

Ellipsometry uses the polarisation of light in order to obtain information about surfaces and films on surfaces. Analysis of the reflected light can be used to acquire information about sample properties, such as layer thicknesses and refractive indices.

[3]The polymer hydrogels were made by Evan Spruijt, who describes this process in detail in his Master's thesis.

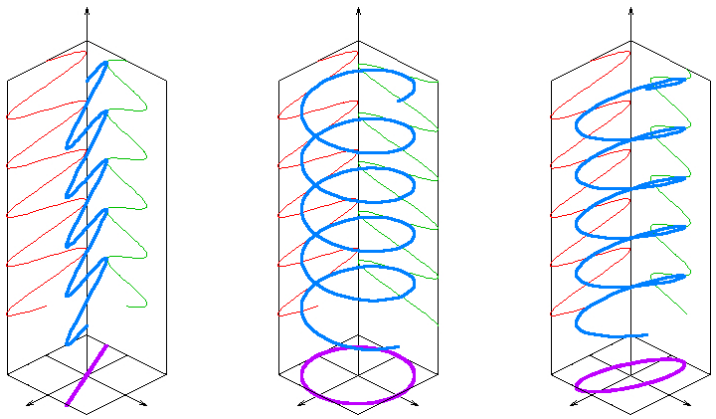

Figure 3.7: *This figure shows linearly, circularly, and elliptically polarised light and their projection onto a 2D scheme. [46]*

The propagation of light in any medium is influenced by the motion of electrons and atomic nuclei, which form macroscopic electric currents. The electric field $\vec{E}(t)$ propagates in a uniform, isotropic medium with complex permittivity ϵ in the following way [45].

$$\left[\Delta^2 - \frac{\epsilon(\omega)}{c^2}\frac{\partial^2}{\partial t^2}\right]\vec{E}(\vec{r},t) = 0 \tag{3.1}$$

where ω denotes the angular frequency and c the speed of light.

The propagation of a general elliptic monochromatic light wave [Fig. 3.7] can be described by the corresponding electric field vectors. The magnetic part of the wave can be ignored for non-magnetic materials.

$$\vec{E}(t) = \begin{bmatrix} E_{\mathrm{x}}(t) \\ E_{\mathrm{y}}(t) \end{bmatrix} = Re\left\{\begin{bmatrix} Xe^{i\Delta} \\ Y \end{bmatrix}\right\} e^{i\omega(t-t_0)} \tag{3.2}$$

From this equation, the ellipsometric quantities Δ and Ψ can be defined as follows: Δ denotes the relative phase difference between the ellipsometric amplitudes X and Y, and $\tan\Psi = X/Y$ is defined as the ratio between the relative amplitudes.

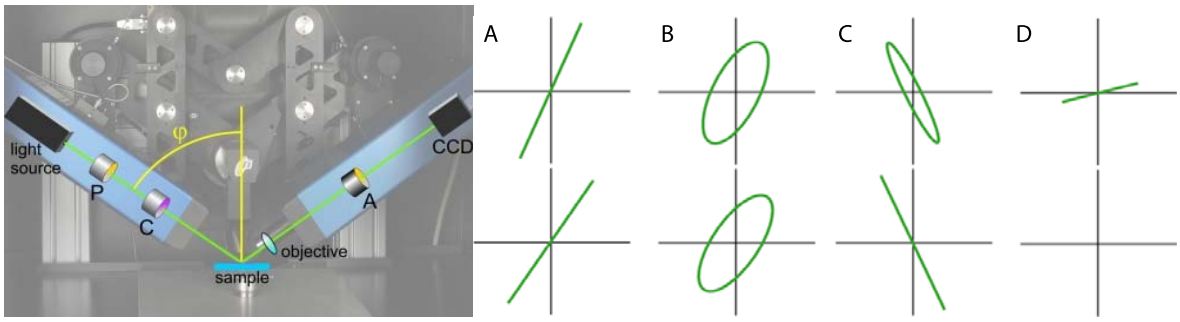

(a) Nanofilm component setup (b) Polarisation of light in ellipsometer

Figure 3.8: *(a) Standard setup of a PCSA nulling ellipsometer implemented in the Nanofilm EP3 [47] (b) Change to the polarisation of the light during its path through the ellipsometer: Top line for non-nulling condition, bottom line for perfect nulling condition. Light polarisation is shown after polariser (A), compensator (B), sample (C) and analyser (D).*

3.2.1 The Nanofilm imaging ellipsometer

All nulling ellipsometers are based on a light source, a rotating **P**olariser, a **C**ompensator plate, a **S**ample, a rotating **A**nalyser, and a detector (PCSA setup), as shown in Figure 3.8. The polarisation of the light reflected from the sample, and thus the values for Ψ and Δ, are connected to the rotation angles of the polariser and analyser, at which the complete extinction of the transmitted light is achieved, as schematically depicted in Figure 3.8.

The imaging ellipsometer (Nanofilm EP3 spectroscopic imaging ellipsometer) was used for these experiments (Fig. 3.8). It has a variable angle of incidence (AOI) of $42° < \varphi < 80°$. Measurements can be performed with a continuous wave diode-pumped solid state laser (JDSU CDPS532M) at $\lambda = 532\,\text{nm}$ with a maximum output power of 50 mW or with a Xenon arc lamp (Osram xenon short arc xbo, 75w/2 ofr) and a filter wheel to address 46 distinct wavelengths between 365 nm and 1000 nm. Ellipsometric measurements of Δ and Ψ have inherent errors dependent on the measurements setup. These are denoted as Err(Δ) and Err(Ψ) in the following. Measurements were taken in 1-zone mode for increased speed Err(Δ) = 1° and Err(Ψ) 0.5° ($t_{1z} \approx$ 20s) or 4-zone mode for increased accuracy Err(Δ) = 0.1° and Err(Ψ) = 0.05° ($t_{4z} \approx$ 90s). A spectroscopic measurement with 4-zone accuracy over 20 distinct wavelengths takes

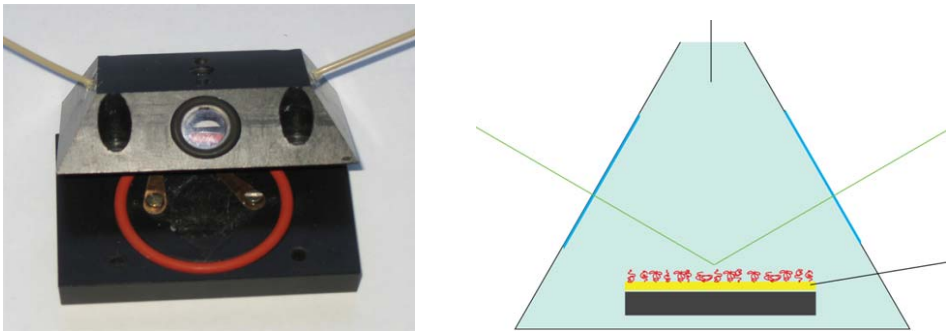

(a) Photo of liquid cell (b) Scheme of liquid cell

Figure 3.9: *(a) Photograph of the liquid cell open (b) Schematic image of the cell setup with wiring for application of electric stimulus*

between 30 min and 1 h due to the time required for the rotation of the optical elements. Objectives between 5× and 50× were used for the ellipsometric measurement and imaging of the surface.

In the following, specific regions of interest (ROI) were chosen to exclude dust particles and enable the measurement of different areas of patterned surfaces. Δ and Ψ values were averaged over these regions. Measurements were taken on minimum pattern sizes of 10×10 µm.

A closed cell with an in- and outlet and temperature control allowed for the measurement of surfaces in the liquid environment. The temperature could be controlled between 20°C and 50°C with 0.1°C accuracy and 0.2°C stability. The cell windows are perpendicular to the optical axis for AOI= 60°. At this angle, the windows of the cell have no effect on the measured data. Measurements were therefore performed using spectroscopic measurements or small angle variation $58° < \varphi < 62°$. The software allows for small corrections due to the cell windows for angles in this range.

For observation of polyelectrolyte brushes in electric fields (Section 4.3) a two electrode system was setup in the liquid cell. An external voltage was applied using the sample as the working electrode and a wire placed in the liquid at the top of the cell as the counter electrode. In early experiments, the voltage was applied using an external voltage generator (Farnell LT30/2 30 V 2 A Dual Output Power Supply), where the current flow was monitored with an external current meter. Later experiments were

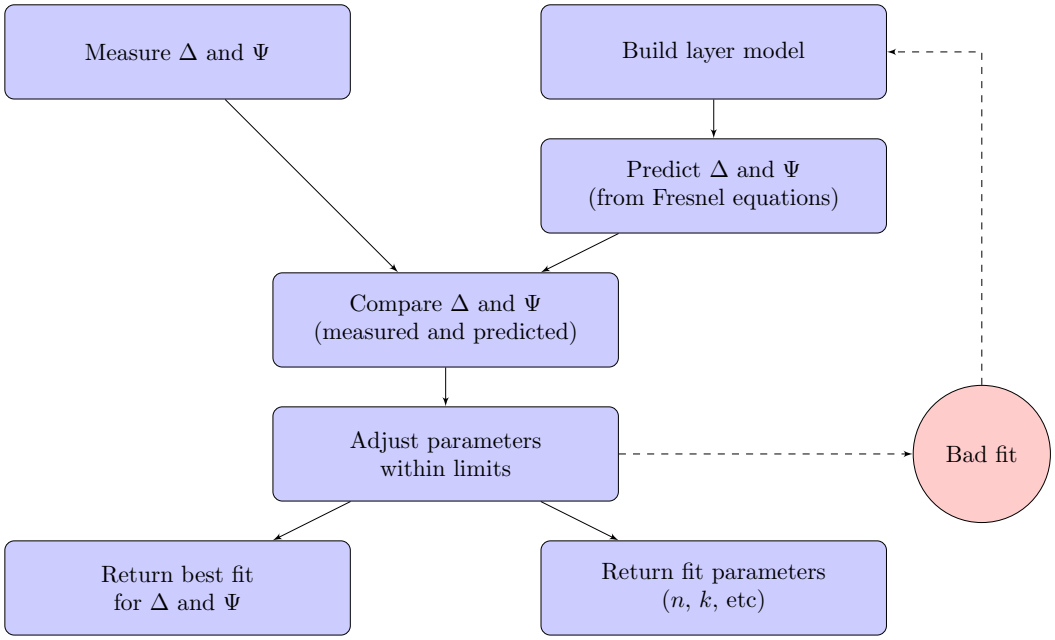

Figure 3.10: *Ellipsometric modeling procedure used to insure correctness of automated procedure during ellipsometric measurements.*

performed using an electrochemical driver (CH Instruments, electrochemical analyzer) and an electrochemistry program (CH Instruments) using cyclic voltametry settings with a fixed applied voltage. For these experiments, the current curves were recorded as a function of time.

3.2.2 Ellipsometric data analysis

Many ellipsometric models exist for different materials. For a complete discussion of ellipsometric modeling please refer to ellipsometry textbooks [45, 48, 49]. In the following, only the most elementary aspects will be discussed, as advanced modeling was not necessary for our experiments.

Spectroscopic ellipsometry in the visible range is well adapted to probe wet systems due to its high accuracy for thin films and its non-invasive nature. Work on polymer brushes in liquids using spectroscopic ellipsometry has been carried out by a few groups [50–55].

The complex refractive index $\tilde{n}$ is generally defined as

$$\tilde{n} = n - ik \tag{3.3}$$

The two components of this complex number are the refractive index $n(\lambda)$ and extinction coefficient $k(\lambda)$, both of which are wavelength dependent. The refractive index n is given by $n = \sqrt{\epsilon_r \mu_r}$, where ϵ_r is the material's relative permittivity, and μ_r is its relative permeability. The absorption loss is indicated by k when the electromagnetic wave propagates through the material. For most polymeric materials, in particular for the polymer brushes and hydrogels used here, $n(\lambda)$ can be treated as a constant and $k(\lambda) = 0$ for visible light. However, most semiconducting materials and metals (including gold and silicon, the substrate materials) display strongly wavelength dependent optical properties.

Ellipsometric data is taken as a function of wavelength λ and the angle of incidence AOI (φ). While Δ and Ψ can be measured relatively easily, the measurement does not provide instantaneous unique solutions for the desired surface properties, such as layer thickness d, or optical properties of the materials. Interpretation of ellipsometric data (except for the measurement of a substrate only) is always dependent on assumptions made in the model. In order to avoid misinterpretation of the ellipsometric data, it is thus necessary to be very careful with any assumptions used in the model calculations. A good procedure for analysing ellipsometric data is depicted in Figure 3.10.

In general, all ellipsometric measurements reported here were done using a bottom-up approach. First, the substrate was fully characterised and $n_0(\lambda)$ and $k_0(\lambda)$ were saved to a dispersion file. The sample was then measured with its first layer and analysed using the substrate dispersion file. The new variable parameters were $n_1(\lambda)$, $k_1(\lambda)$, and d_1 of the first layer. This process was repeated for further layers.

All brushes were grown on silicon or gold substrates. Due to the large variation in optical properties of gold, every evaporated or sputtered gold substrate was measured independently and a new dispersion file for $n_{Au}(\lambda)$ and $k_{Au}(\lambda)$ was created. The optical properties of silicon were observed to be highly reproducible and were therefore kept fixed. The thin native oxide layer on silicon samples was measured for each new batch

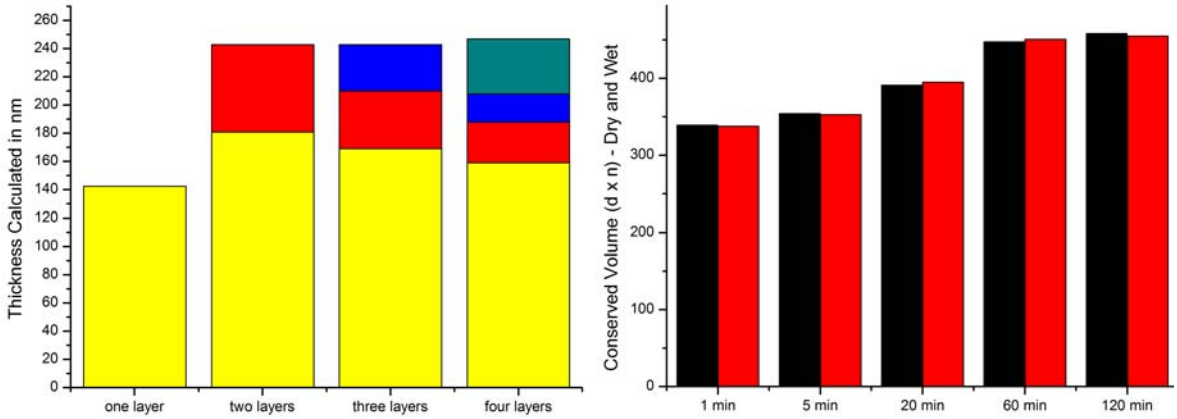

Figure 3.11: *This figure shows on the left the different thicknesses achieved for a polydisperse brush using multiple layer models; on the right, we see the volume conservation for a wet and a dry PNIPAM polymer brush*

of silicon wafers. The refractive index for the oxide layer was fixed $n_{SiO_2}(\lambda) = 1.5$ and $k_{SiO_2}(\lambda) = 0$ [56]. The thickness of the oxide layer was measured at $\lambda > 600\,\text{nm}$, where $k_{Si} < 0.01$ [56]. A spectroscopic measurement of the sample was then used to create a dispersion file for $n_{Si}(\lambda)$ and $k_{Si}(\lambda)$, using the information obtained for silicon oxide.

All polymer layers used in this research had $k_{pol}(\lambda) = 0$, such that the only variable parameters in the polymer layers were n_{pol} and d_{pol}. All polymer brushes and hydrogels were initially measured in air. The thickness and refractive index in air was used as a reference for later comparison of the values obtained in liquid. In liquids, it was postulated that the refractive index of the surface-tethered polymer fulfilled the following criterion: $n_{water} < n_{polymer\text{-}wet} < n_{polymer\text{-}dry}$.

Depending on the polydispersity of the polymer brush, the data analysis could be achieved with a simple dilution model as explained above or would require a complex multiple layer model. In the first case, the brush was modeled as described above for a dry homogeneous layer, taking into account the liquid environment. Values for the liquids were taken from the ellipsometer database [47].

For highly polydisperse brushes, modeling using a single homogeneous layer did not yield good correspondence between modeled and measured data as can be seen in Figure 3.11. In these cases, it was concluded that the water did not evenly swell the brush.

A more complex model of the swollen brush was needed. In these cases, the polymer brush was modeled as a 2-layer, a 3-layer, and a 4-layer system as shown for a PNIPAM brush in Figure 3.11. As can be seen in this example, the total thickness of the brush converged for multiple layers. In this particular case, the data from the 3-layer fit was chosen, as the mean squared error (MSE) from the analysis was lowest. The 1-layer model, however, can be observed to be entirely unfit, as its thickness is significantly smaller than given for all other models. This showed the high polydispersity of the sample. Samples with such high polydispersity were discarded.

Volume conservation arguments were performed for most polymer brush or hydrogel swelling experiments. While the height and refractive index change for different brush conformations in the liquid environment, the total volume per area V/A of brush is conserved. The calculation is based on the fractional mixing of polymer and water, where the refractive index is assumed to be linearly related to the volume fraction of material in the brush.

$$V/A \approx n_{\mathrm{water}} d_{\mathrm{water}} + n_{\mathrm{dry}} d_{\mathrm{dry}} = n_1 d_1 + n_2 d_2 + n_3 d_3 \tag{3.4}$$

Volume conservation arguments provide a consistency check for ellipsometric analysis in liquids (Figure 3.11). In Section 4.3, we will see that this argument can be used to detect reduction of polymeric material due to rupture in highly stressed surface-tethered polymer films.

4 Triggering conformational changes in aqueous solutions

This chapter covers the results of four different experiments designed to explore triggered conformational changes in polymer brushes or hydrogels in aqueous solutions. Section 4.1 discusses experiments based on temperature as a conformational trigger for polymer brushes. Section 4.2, Section 4.3 describe experiments involving electric signals as triggering mechanisms for polyelectrolyte polymer brushes. Section 4.4 covers experiments with electric triggers for surface-attached charged hydrogels.

The use of electric stimuli in order to achieve conformational changes and therefore influence surface properties is technologically very favourable. Electric stimuli have many important advantages for fluidic or circuitry device design. Advantages over other physical triggers as treated in Section 2.2.1 include

1. Electric stimuli can be applied with very high frequencies
2. Changes in applied potentials are easily programmable.
3. Applications based on electric systems can easily be integrated into other primary electric circuitry
4. Electric stimuli can be applied in a localised manner, as exemplified by display technology.

In the Section 4.2, Section 4.3 and Section 4.4, changes observed in polyelectrolyte polymer brushes and charged hydrogels in response to applied electric stimuli are described. Three different experiments are reported here: inducing conformational

changes in polymer brushes coated onto cantilevers observed using a modified AFM setup (Section 4.2), inducing conformational changes using electric stimuli in polymer brushes on flat surfaces (Section 4.3) and in polyelectrolyte hydrogels on surfaces (Section 4.4) observed using imaging ellipsometry.

In experiments involving polyelectrolytes, we used PMETAC. Its structure is shown in Figure 3.3 (Section 2.1.5). PMETAC is a strong polyelectrolyte. PMETAC becomes positively charged in water, when the N^+ and Cl^- charge pair dissociates, which occurs for all non-extreme pH values. Therefore, for all practical purposes it shall be assumed here that the charges dissociate, and that the positive charges are attached to the polymer brush, while the negative charges are dissolved close to the brush in a counter ion cloud.

4.1 Temperature induced conformational changes

PNIPAM is a thermo-responsive polymer that exhibits a LCST (lower critical solution temperature) in water of $T_{\mathrm{LCST}} \sim 32°\mathrm{C}$ [42]. The chemical structure is shown in Figure 3.3. Below the critical temperature ($T < T_{\mathrm{LCST}} = 32°\mathrm{C}$), the polymer is soluble in water and the surface-tethered polymer becomes hydrophilic; above the critical temperature ($T > T_{\mathrm{LCST}} = 32°\mathrm{C}$), the polymer becomes hydrophobic and the brush collapses. PNIPAM has been studied extensively over recent years due to its relatively easy production and its interesting properties as a model system for microactuation [57]. Therefore, PNIPAM was chosen as the ideal model system to test the setup and confirm the measureability of conformational changes in thin polymer layers in solution using ellipsometry.

Changes in the raw data of temperature dependent brushes

In the following, samples with low polydispersity and high homogeneity of the polymer brush were chosen. These samples had the characteristics that d_{dry} and n_{dry} of the dry and the swollen polymer could be fitted well with a 1-layer model. The samples

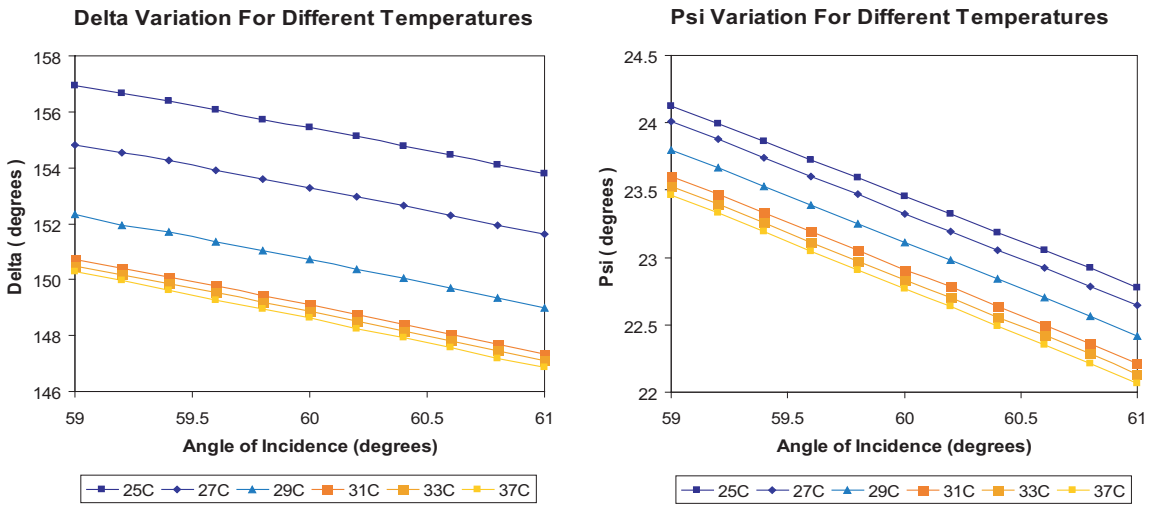

Figure 4.1: Δ *and* Ψ *as a function of AOI for several temperatures below and above the LCST. As can be seen, significant differences exist between the 25° C, 27° C, and 29° C data. The data for 31° C, 33° C, and 35° C are very similar.*

were measured in water and slowly heated to observe the transition from a swollen polymer brush conformation to a collapsed brush conformation. Data was taken in temperature steps ($\Delta T = 2°\mathrm{C}$). These data were taken by varying the angle of incidence ($59° < \mathrm{AOI} < 61°$) for different temperatures, with a stabilisation time of 15 min for each data point, which was when the Δ and Ψ values had stabilised. Figure 4.1 shows the results of these measurements. Faster measurements were found to result in hysteresis behaviour for heating versus cooling measurements. It can be seen that the Δ and Ψ values converge for $T \gg T_{\mathrm{LCST}}$, indicating no significant changes in the polymer brush conformation above the T_{LCST}, as to be expected for a fully collapsed polymer brush.

Conformational changes in temperature-responsive brushes

A patterned PNIPAM and POEGMA sample was measured to observe the changes in responsive versus non-responsive polymer brushes. The temperature-dependent data were analysed with respect to thickness and refractive index. The values for layer thickness and refractive index were calculated from the Δ and Ψ curves. The results for n_{pol} and d_{pol} are shown in Figure 4.2. They confirm the expected change in polymer brush thickness and polymer brush refractive index with temperature, including the

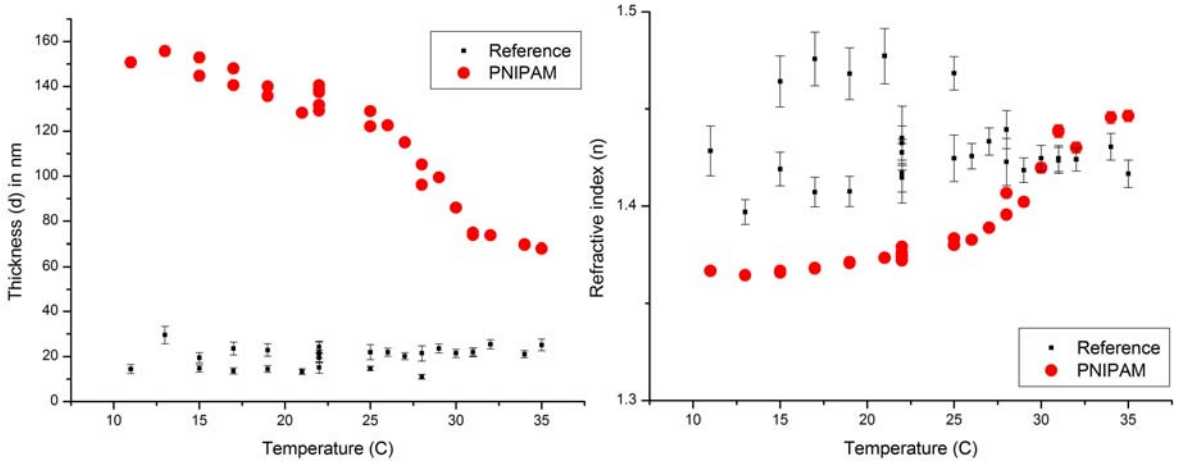

(a) Thickness (d) in nm (b) Refractive index (n)

Figure 4.2: *Thickness (a) and refractive index (b) changes in swollen PNIPAM brushes as a function of temperature are denoted by large round data points. The data was combined from consequtive heating and cooling measurements on the same sample. The reference data (small squares) were taken from the POEGMA reference area and show no significant changes with temperature.*

stabilisation of values for $T \gg T_{\mathrm{LCST}}$.

It should further be noted that the thickness of the PNIPAM thermoresponsive brush brush has decreased significantly in thickness from 160 nm swollen thickness at 12°C to 80 nm thickness for $T > T_{\mathrm{LCST}}$. This is nearly the thickness of the dry brush. Further, the refractive index increased from $n_{\mathrm{swollen}} = 1.37$ to $n_{\mathrm{collapsed}} = 1.45$. The POEGMA brush, however does not show any significant changes with temperature in thickness or refractive index. Due to the lower thickness of the POEGMA reference layer, the variation and errors in the refractive index are significantly higher. The behaviour shown in Figure 4.2 was reproduced for all homogeneous PNIPAM polymer brushes that were measured.

Discussion

The results for temperature-dependent brushes in a liquid were consistent with our expectation. The T_{LCST} temperature of PNIPAM was confirmed and the corresponding collapse was observed repeatedly. The measurements of PNIPAM samples thus proved

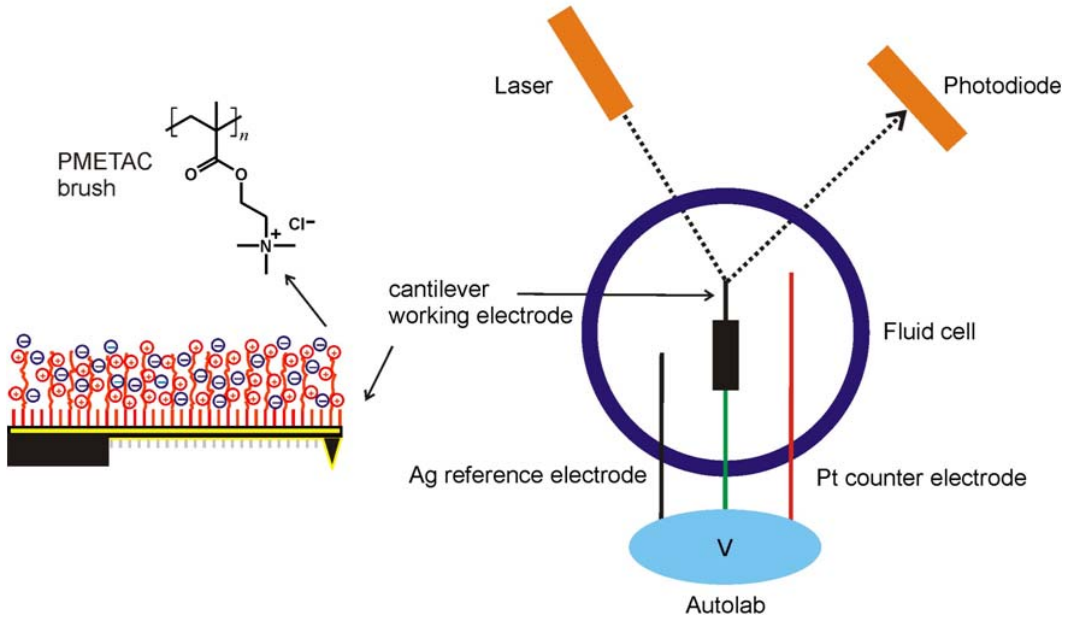

Figure 4.3: *The experimental setup used for triggering polyelectrolyte covered cantilevers in an AFM setup: AFM Cantilever covered with PMETAC polymer brush in swollen state, electrochemical cell setup with working electrode, counter electrode, reference electrode, as well as the laser based detection system. [38]*

that imaging ellipsometry can be used as a method to characterise polymer brush layers in the liquid environment and detect conformational changes. It further showed the possibility to independently resolve changes in thickness and refractive index for polymer brushes in liquid and distinguish between responsive and non-responsive polymers in binary patterned samples.

4.2 Triggering a coated AFM cantilever

In 2008, Zhou *et al.* showed that changes in polyelectrolyte polymer brush conformation in water, with low salt content, can be achieved using electric fields [2,38]. The experiment was based on an AFM cantilever coated with PMETAC which was observed in an electrochemical cell with an AFM photo-diode deflection detection system. The backsides of the cantilevers were passivated with a neutral thin self-assembled monolayer for protection purposes. A schematic of the coated cantilever and the electrochemical setup is show in Figure 4.3. Experiments were performed in 1 mM NaCl, 10 mM NaCl,

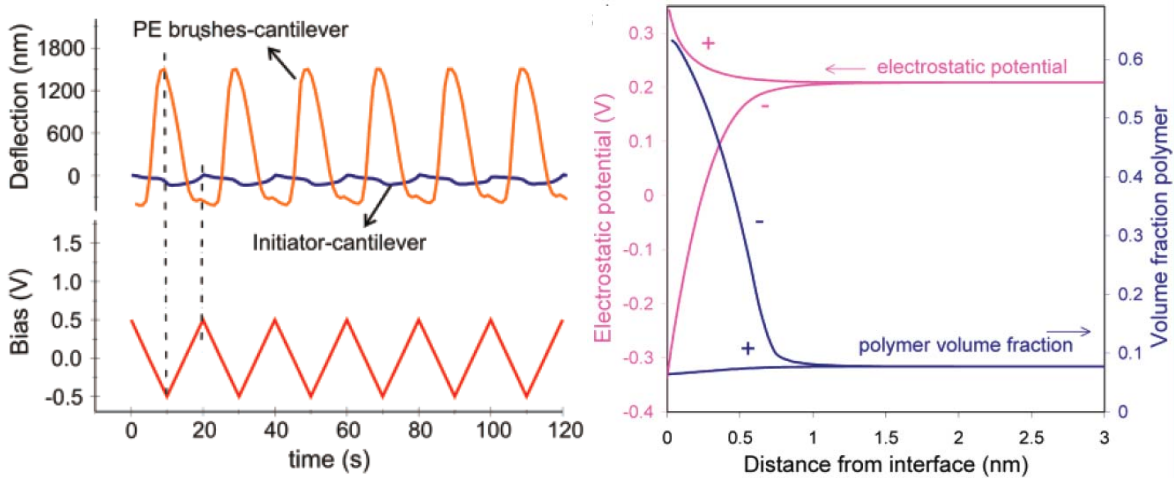

(a) Deflection of cantilever (b) Field calculation

Figure 4.4: *(a) The deflection of a polyelectrolyte coated cantilever and an initiator coated cantilever in response to applied potentials. The deflection of the polyelectrolyte cantilever is about one order of magnitude larger than for a cantilever with a uncharged self-assembled monolayer. (b) Calculated changes in the electostatic potential and the volume fraction of the polymer as a function of distance from the interface. [38]*

and 100 mM NaCl solutions.

Conformational changes in salted solutions

A triangular potential was applied between +0.5 V and -0.5 V with a frequency of up to 0.05 Hz. The frequency of actuation was limited by the data acquisition time of the AFM. Changes in the deflection of the polymer brush coated cantilevers were too fast to be resolved by the second-based detection system. The deflection observed for cantilevers with grafted polyelectrolyte polymer brush coatings was significantly stronger than that for cantilevers coated only with self-assembled monolayers of the same type as used as initiator layers for the polymer brush growth (Figure 4.4).

Two interesting observations can be made. Firstly, the deflection of the cantilever occurs in the same direction for both negative and positive applied potentials. Secondly, the deflection is significantly greater for negative potentials. Results of the observed deflection in response to an electric potential can be seen in Figure 4.4.

For negative and positive applied voltages, the total ion concentration increases

strongly with proximity to the surface. Calculations have shown that the deflection of the cantilever is due to a conformational change in the first nanometers of the brush only (Figure 4.4). Both positive and negative applied potentials lead to expansive stresses at the brush covered interface, and therefore did not reverse the direction of deflection [38].

Discussion

The changes in the polyelectrolyte conformation in the first nanometres of the polymer brush are caused by a local change in the electrical double layer. Due to the low screening length, conformational changes can occur only in a very thin layer of the brush close to the electrode. At larger distances from the cantilever, the electric potential of the cantilever is screened and has no effect on the polymer brush conformation. This localised change in the first nanometres is sufficient to cause a change in surface stress, which in turn results in a change in the deflection of the AFM cantilever. The results suggest that this system is a promising route for nano-actuation based on surface stress changes [38].

This experiment shows the possibility of achieving conformational changes in polyelectrolyte polymer brushes using applied potentials. The use of such a system in a deflection based setup as a future micro- or nano-actuator may be possible.

Due to the low screening length in salted solutions, even very strong fields cannot penetrate the brush completely, which renders improbable a conformational change at the polymer brush liquid interface triggered by an electric potential. These experiments have shown how to achieve a partial conformational change in a polymer brush. However, this system is not adapted for changes in the properties of the entire brush. When working toward surface property changes at the polymer brush - liquid interface, the conformational changes must occur over the complete brush height. Therefore, solutions with high screening length and very low salt concentrations must be found.

4.3 Triggering complete polyelectrolyte conformational changes

This section reports the results obtained for conformational changes in polyelectrolyte polymer brushes in 18 MΩ water. The PMETAC polyelectrolyte brushes were measured with spectroscopic imaging ellipsometry in order to investigate changes in response to externally applied electric potentials. For more information on the setup, please refer to Section 3.2.1.

Two types of polymer brush samples were used:

- Neutral and charged patterned polymer brushes were produced by contact printing 10-50 µm wide stripes of polyelectrolyte PMETAC polymer brushes spaced 10-50 µm apart [58]. Spaces between the stripes were filled with neutral POEGMA polymer brushes (Figure 3.3). On these samples, measurements were conducted in both areas simultaneously.
- Polyelectrolyte PMETAC brushes were also grown without neutral reference area to confirm the behaviour of PMETAC without lateral confinement.

The polymer brush samples were first measured and characterised in their dry state, as described in Section 3.2.2. The dry brush thickness d_{dry} and the dry refractive index n_{dry} were recorded. The brushes were then introduced into the liquid cell filled with 18 MΩ water and left to equilibrate in water, which took between 10 min and 1 h. Equilibrium was defined as the state, where no more significant changes could be observed in the intensity detection of the individual regions of interest. The swollen brush thickness d_{swollen} and refractive index n_{swollen} were then measured. After equilibration, the brushes were subjected to repeated electric stimuli, with applied DC potentials varying between $-10\,\mathrm{V} < U < 10\,\mathrm{V}$.

Two types of measurements were conducted for better understanding of the impact of electric stimuli on conformational states of polyelectrolyte polymer brushes.

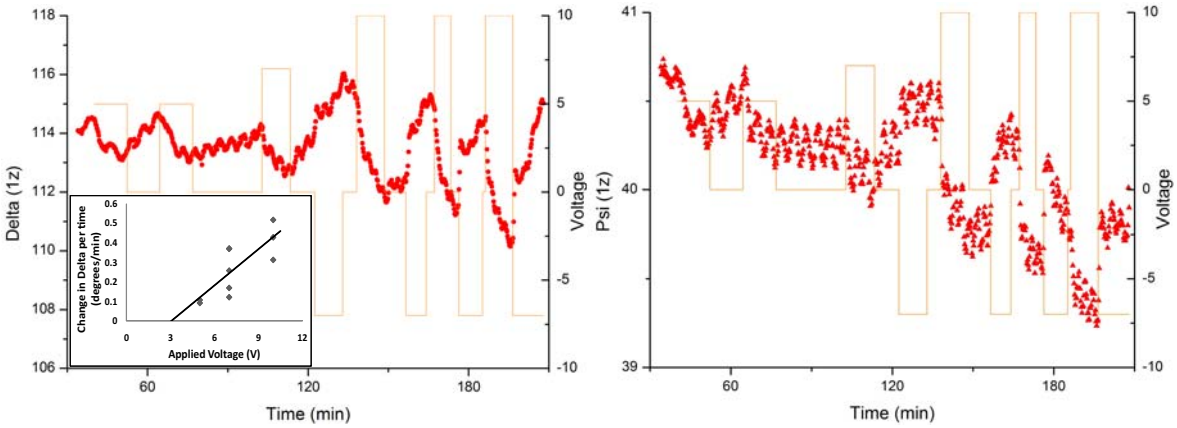

(a) Changes in raw data Δ

(b) Changes in raw data Ψ

Figure 4.5: *Data set NC081007, S1a: Changes in the raw data in response to an externally applied potential: (a) Changes in* Δ*. The inset shows the absolte changes in* Δ/min *as a function of absolute applied voltage. The solid line is a best fit with two free fitting parameters. Here, we can see the onset threshold* $V_{min} \approx 3\ V$ *(b) Changes in* Ψ *(left Y-axis). The thin orange line shows the onset, duration and strength of the applied potential (right Y-axis).*

- Quick 1-zone measurements were used to establish changes in the raw ellipsometric data, while long spectroscopic measurements were used to specify changes in the brush thickness and refractive index. The results from these measurements are discussed in Section 4.3.1.
- Spectroscopic measurements of the brush were done to establish how the observed changes in the raw data translated to changes in the polymer brush thickness and refractive index, to see whether these could be correlated with conformational changes. The results of these measurements are discussed in Section 4.3.2.

4.3.1 Raw data changes upon application of an electric stimulus

In order to establish, whether the electric stimulus had any measurable effect on the polyelectrolyte polymer brushes, we observed changes in the raw Δ and Ψ measurements over time in response to the application of repeated electric stimuli. All 1-zone measurements were done at $\lambda = 532\,\text{nm}$ and AOI $= 60°$. The measurements were done using a self-written script, which allowed for the automatic repeat of the 1-zone measurement algorithm. Each 1-zone measurement takes approximately 10 - 20 s (de-

pending on the exact parameters chosen). It is the fastest measurements that can be done with the Nanofilm Imaging Ellipsometer.

From 1-zone measurements, we obtained information about the stimulus threshold, the speed of changes in the raw Δ and Ψ data, and the repeatability of switching.

It is useful to remember that the inherent measurement errors associated with 1-zone measurements in Δ and Ψ are $\mathrm{Err}(\Delta) = \pm 1$ and $\mathrm{Err}(\Psi) = \pm 0.5$ (Section 3.2.1). The lack of precision in the 1-zone measurement means that the data cannot be used for accurate interpretation of height and refractive index information. For this reason, spectroscopic measurements were performed on all samples before and after exposure to the electric stimulus to check whether the brush thickness had reduced or whether the observed changes were completely reversibly.

In Figure 4.5, we can see a typical measurement of the raw Δ and Ψ signals for a polyelectrolyte polymer brush over time. Prior to exposure to the electric stimulus, the sample was measured in the dry and swollen state: $d_{\mathrm{dry}} = 55 \pm 4\,\mathrm{nm}$, $n_{\mathrm{dry}} = 1.45 \pm 0.03$, $d_{\mathrm{swollen}} = 146 \pm 16\,\mathrm{nm}$, $n_{\mathrm{swollen}} = 1.37 \pm 0.01$. In the repeated 1-zone measurement, the measured raw data values returned to their 'unperturbed' measurement values when the stimulus was reversed. This means that the changes occurring within the polymer brush are reversible and are not associated with bond breakage or destruction of the layer itself. No significant stabilisation of the recorded raw data occurred over the time frame of the applied pulses. However, the raw data corresponding to the 'unperturbed' polymer brush state stabilised after removal of the stimulus.

A significant amount of long term drift and short term fluctuation can clearly be seen in the data. During reference measurements without the application of an electric stimulus, the drift values were significantly lower, even though the heating due to the laser was the same. Therefore, the applied electric field must be the reason for the much stronger drift observed during measurements under the electric stimulus. This makes drift in electric stimulus experiments difficult to avoid.

The changes observed in the raw Δ and Ψ signals were seen to vary as a function of applied voltage: Stronger applied fields caused faster and greater changes to the raw

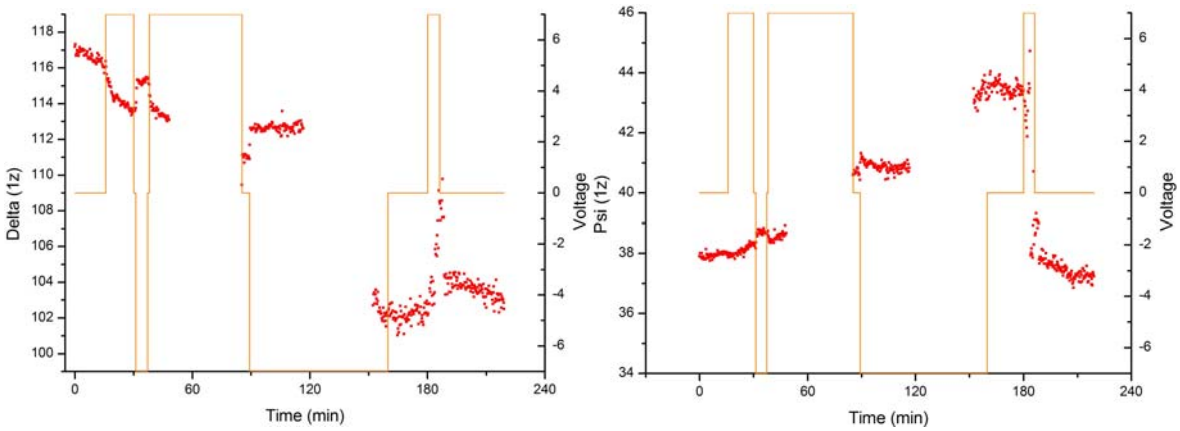

(a) Changes in raw data Δ (b) Changes in raw data Ψ

Figure 4.6: *Data set NC081007, S1b: A decaying polymer brush. Changes in the raw data in response to an externally applied potential: (a) Changes in* Δ *(b) Changes in* Ψ *(left Y-axis). The thin black line shows the onset, duration and strength of the applied potential (right Y-axis).*

signals. In Figure 4.5, the first applied signal was already large enough to cause changes in the raw data, which means that $U_{\text{threshold}} < 5\,\text{V}$. Most data sets showed threshold values between $3\,\text{V} < U_{\text{threshold}} < 5\,\text{V}$. The time scale observed for the stabilisation of the raw data signals was on the order of minutes.

In Figure 4.6, we can see an example of a polymer brush which was destroyed during measurements. Distinction between thermal drift and degradation was very difficult, without the subsequent dry measurements of the brush. The brush was measured in the dry and swollen state before exposure to the electric stimulus: $d_{\text{dry}} = 39 \pm 5\,\text{nm}$, $n_{\text{dry}} = 1.45 \pm 0.03$, $d_{\text{swollen}} = 111 \pm 2\,\text{nm}$, $n_{\text{swollen}} = 1.37 \pm 0.01$.

After exposure to the electric stimulus, the brush had reduced significantly: $d_{\text{reduced}} = 16 \pm 5\,\text{nm}$, $n_{\text{reduced}} = 1.57 \pm 0.3$. The large error in the reduced polymer brush refractive index is another strong indication that the polymer has been partially degraded. It can be seen that a significant amount of the polymer brush material has been washed away during exposure to the electric field.

It is difficult to determine the timing of the polymer brush degradation from the 1-zone measurement in Figure 4.6. However, when comparing the changes observed in the raw Δ and Ψ signals for the non-degraded sample in Figure 4.5, we can note that

the changes Δ and Ψ in Figure 4.6 are about one order of magnitude stronger. Upon removal of the electric stimulus, the Δ and Ψ signals do not return to their unperturbed value. In particular the very large jump in the signals after 120 min could correspond to brush degradation.

Discussion

From the 1-zone measurements of polyelectrolyte polymer brushes in pure 18 MΩ water in response to electric stimuli, we can conclude

- A threshold voltage of approximately $U_{\text{threshold}} \sim 3\,\text{V}$ is required for detectable changes in the raw Δ and Ψ signals
- The time frame for brush actuation was on the order of minutes: $t_{1z} \approx 10\,\text{min}$ corresponding to raw data signal changes in Δ and Ψ.

In the following Section 4.3.2, we will show a more detailed analysis of the polymer brush conformation, via spectroscopic measurements, upon application of the actuation potential.

4.3.2 Spectroscopic characterisation of changes in the polymer brush

While localised 1-zone measurements have been used to identify the threshold voltage and the timescale involved in measureable changes of the raw data, spectroscopic measurements are necessary to identify the changes that are taking place within the brush layer. 4-zone spectroscopic measurements allow for high precision observation of the delicate changes involved in the swelling and the collapse of the polyelectrolyte polymer brush in pure 18 MΩ water. For the spectroscopic measurements, the wavelength was varied over the visible range using optical filters to address distinct wavelengths between $430\,\text{nm} < \lambda < 690\,\text{nm}$ in $\Delta\lambda = 10\,\text{nm}$ steps (at AOI = 60°). Each spectroscopic measurement took 45 min and yielded one thickness d and one refractive index n value.

As in Section 4.3.1, the samples were first measured dry, then introduced into 18 MΩ water and left to equilibrate, and then measured in their swollen state. Afterwards, electric potentials above the threshold potential $U > U_{\text{threshold}} = 3\,\text{V}$ were applied and spectroscopic measurements commenced.

Conformational changes in polyelectrolyte brushes

The polyelectrolyte polymer brushes exhibited three types of behaviour in response to the electric stimulus. The first group of samples showed little or no change in the polyelectrolyte polymer brush upon application of the external electric potential (Case 1). The polymer brush samples were seen to swell or collapse slightly, but the changes were not correlated to the externally applied potential. The changes were not reproduced in all regions of interest. Some possible explanations for this behaviour could be

- Contamination of the solution with ionic species resulting in a strongly reduced Debye screening length. Very low levels of contamination from tubing or cell windows can be sufficient to decrease the Debye screening length of 18 MΩ water such that the electric fields is almost completely shielded. Contamination is particularly problematic for measurements lasting multiple days.
- Leakage of the applied field. Reasons could include poor isolation of the uncoated sample areas.
- Detachment of electrical contacts due to heating.
- Measurements occurring below the threshold voltage required for conformational changes. This source was minimised by using $U > U_{\text{threshold}} = 3\,\text{V}$ as established in Section 4.3.1.

The second type of behaviour shows the polyelectrolyte polymer brushes initially swelling, then collapsing upon application of an external field, but not reswelling after removal of the field (Case 2). This behaviour corresponds to that seen in Section 4.3.1 in Figure 4.6. The observed initial changes are attributed to degradation rather than

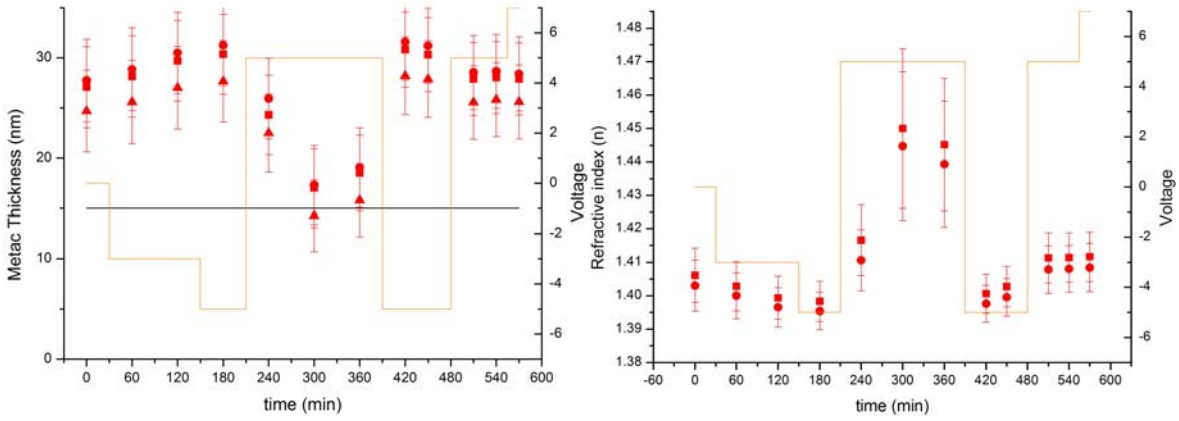

(a) Thickness changes (d) in nm (b) Refractive index changes (n)

Figure 4.7: *Data set NC081219: Thickness (a) and refractive index (b) changes in a polyelectrolyte polymer brush in response to an applied electric potential (left Y-axis). The horizontal line shows the dry thickness of the polymer brush, the data points show the polymer brush thickness and refractive index as measured in solution with spectroscopic ellipsometry. The thin black line shows the onset, duration and strength of the applied potential (right Y-axis).*

conformational changes.

The third, and perhaps most interesting behaviour, corresponds to reversible conformational changes of the polyelectrolyte polymer brush (Case 3). The polymer brush swells upon immersion into the liquid cell to its equilibrium thickness, collapses upon application of the external stimulus, and swells again completely once the trigger is removed. This behaviour is the only behaviour that could be used to influence the brush - liquid interface properties.

In Figure 4.7 and Figure 4.8, we can see examples of complete polyelectrolyte brush collapse on application of the electric field (Case 3). In both cases, the polyelectrolyte brush collapses to its dry thickness and nearly regains its dry refractive index. Both the brushes are seen to regain their earlier swollen thicknesses and lower diluted refractive indeces once the trigger is removed.

Figure 4.7 shows an example of a pure PMETAC brush. The applied voltage was very high ($U = 7\,\mathrm{V}$). The brush collapsed in response to the field down to its dry thickness d_{dry} and swelled again to its swollen thickness d_{swollen} when the stimulus was removed (Case 3). It is difficult to establish a collapse time from the data, as the measurement

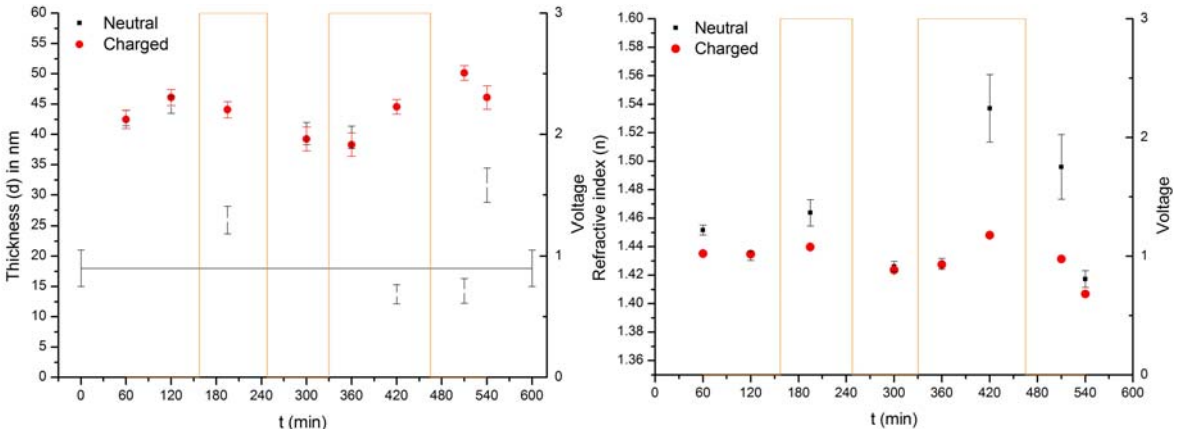

(a) Thickness changes (d) in nm (b) Refractive index changes (n)

Figure 4.8: *Data set FZ070317: Thickness (a) and refractive index (b) changes in a polyelectrolyte polymer brush (charged) and a reference brush (neutral) in response to an applied electric potential (left Y-axis). The horizontal line shows the dry thickness of the two polymer brushes, the data points show the polymer brush thickness and refractive index as measured in solution with spectroscopic ellipsometry. The thin black line shows the onset, duration and strength of the applied potential (right Y-axis).*

time is dominant over the switching time $t_{\text{spec}} > t_{\text{switch}}$, so therefore $t_{\text{switch}} < 45\,\text{min}$ for this particular sample and applied voltage.

Figure 4.8 shows an example of the changes seen on a patterned polyelectrolyte and neutral polymer brush surface (Case 3): We can see that the neutral POEGMA polymer brush did not experience the same changes in d and n as the charged PMETAC polymer brush. The changes in the neutral brush could be mostly attributed to fluctuations or thermal drift, while the changes in the polyelectrolyte brush were correlated to the applied trigger. The polyelectrolyte brush collapsed to nearly its dry thickness and the refractive index increased strongly. In contrast to the pure PMETAC brush sample, however, the collapse took much longer, with $45\,\text{min} < t_{\text{switch}} < 90\,\text{min}$. The applied voltage was $U = 3\,\text{V}$.

From the spectroscopic 4-zone measurements of polyelectrolyte polymer brushes in $18\,\text{M}\Omega$ water, we can conclude that the changes observed using spectroscopic measurements are even slower than those seen in the raw ellipsometric data signals using 1-zone measurements in Section 4.3.1.

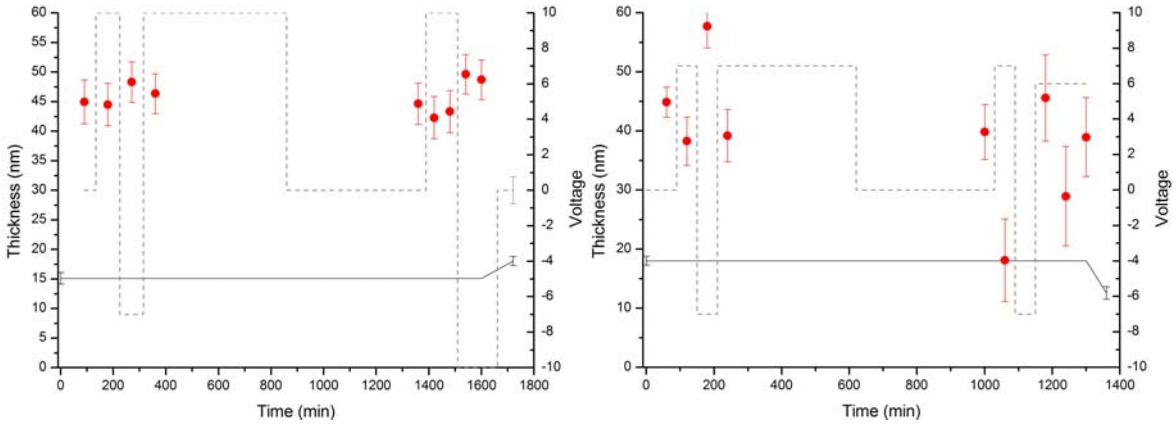

(a) First 24 h experiment (b) Second 24 h experiment

Figure 4.9: *Data set NC081203: Thickness (left Y-axis) changes in a polyelectrolyte polymer brush in response to an applied electric potential (a) First 24 h experiment: Thickness does not change (b) Second 24 h experiment: Thickness changes. The horizontal line shows the dry thickness of the two polymer brushes, the data points show the polymer brush thickness as measured in solution with spectroscopic ellipsometry. The thin black line shows the onset, duration and strength of the applied potential (right Y-axis).*

Figure 4.9 shows results from a brush exhibiting mixed behaviour (Case 1 and Case 3). The sample was immersed into water, then subjected to electric stimuli, but no change to the brush could observed (Figure 4.9a). The sample was removed from the solution and remeasured dry. No significant decay had occurred over the 24 h immersion time or due to the applied electric fields. The sample was reimmersed into water and the experiment repeated. For this second experiment, changes in the sample thickness d and refractive index n were observed (Figure 4.9b). The two experiments conducted on the same sample showed the strong dependence of the experimental outcome on the external conditions.

The need to achieve relatively high potentials over the complete brush layer, inherently places a very large strain on the polymer brush anchoring layer, as the potential is strongest in this region. This could be a reason for the degradation observed in so many experiments.

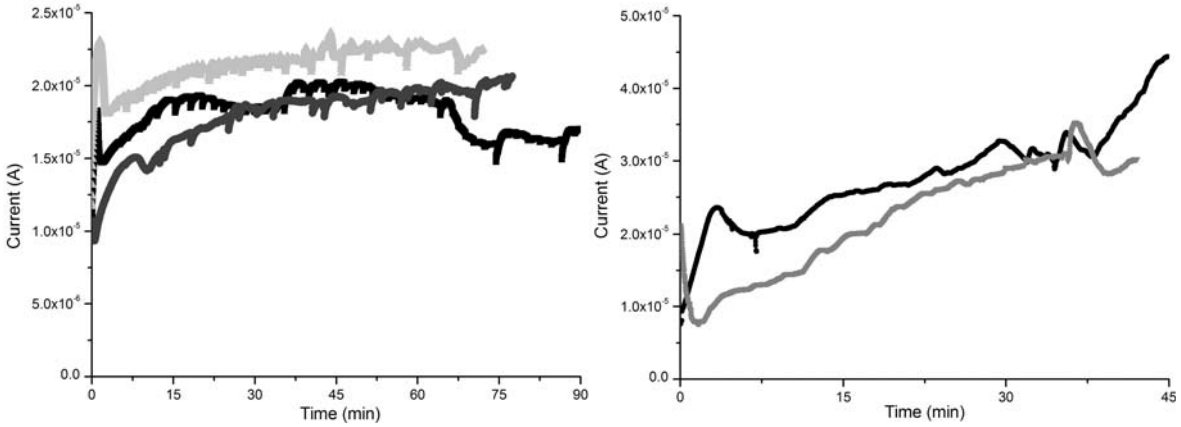

(a) Applied voltage $U = 3\,\mathrm{V}$ (b) Applied voltage $U = 7\,\mathrm{V}$

Figure 4.10: *Detected current across the polymer brush in the ellipsometric liquid cell upon application of an external field (a) $U = 3$ V. Data from NC081203. No changes were seen for any of the curves in the conformation of the brush. (b) $U = 7$ V. Data from NC090106. Changes in the brush were observed for the application corresponding to the black current curve. No changes were seen for the grey curve.*

Electric current changes in polyelectrolyte polymer brushes

The current signal across the liquid chamber upon application of the electric stimulus to the polyelectrolyte polymer brush was observed and recorded. We can see two typical current data plots in Figure 4.10a and Figure 4.10b. For all experiments, the applied voltage is kept constant. As can be seen, the current fluctuated greatly during the experiment. It was difficult to infer conformational changes from the current data.

Figure 4.10a shows current traces for three consecutive applications of an electric stimulus to a samples ($U = 3\,\mathrm{V}$). None of these stimuli resulted in conformational changes in the sample. Strong fluctuations in the current traces can be seen that could not be explained.

Figure 4.10b shows current traces for an applied potential of $U = 7\,\mathrm{V}$ for the two consecutive sample runs shown in Figure 4.9. The grey current curve shows one of the early applied potentials that did not result in changes in the polymer brush conformation (Figure 4.9a). The black current curve shows the application of the same potential later, which did result in collapse of the polymer brush (Figure 4.9b). The observed current is on the same order of magnitude as observed for the $U = 3\,\mathrm{V}$ traces. The grey

and black curves in Figure 4.10b show no recognisable qualitative or quantitative features, so no clear distinction between the traces could be made. Therefore, the current signals could not be used as an additional indicator whether conformational changes occured in the polyelectrolyte polymer brushes.

While monitoring and controlling the current flow in order to prevent burning of the samples was achieved through limitation of the current ($A < 50$ µA), the observed current flow could not be used to determine whether significant conformational changes in the polymer brush occurred during the measurement.

Discussion

The spectroscopic measurements of changes in the conformation of polyelectrolyte polymer brushes in pure 18 MΩ water in response to electric stimuli showed three different types of behaviour: No changes, reversible conformational changes, and changes due to degradation. In all cases, the information about the polymer brush conformation was drawn from the changes in thickness d and refractive index n.

The observed behaviour can be explained by two factors: The electric potentials required to see changes in the spectroscopic measurements of thickness and refractive index are large. Further, the lower threshold $U_{\min}$ for changes varies between samples. This could be the reason why some samples showed no response to the applied stimuli. The required electric potentials are very close to the maximum applied potential that can be supported by the polymer brush layer without degradation. This is $U_{\max}$. In order to achieve conformational changes, it is necessary to find $U_{\min} < U < U_{\max}$. It is possible that this parameters space is very small.

For the samples that showed conformational changes in response to applied electric stimuli, we can conclude that

1. It is possible to achieve a complete collapse of a polyelectrolyte polymer brush using electric stimuli as triggers.
2. The conformational changes are reversible.

3. Switching is relatively slow with $45\,\text{min} < t_{\text{switch}} < 90\,\text{min}$. Therefore, the time needed to change the conformation inside the polymer brush is approximately 1 h.

4.4 Switching charged hydrogel conformation

Experiments involving hydrogels were carried out on surface-grafted charged hydrogels based on METAC monomers in pure 18 MΩ H_2O. The trigger was based on an electric potential as described in Sections 4.3.1 and 4.3.2. Information on the polymerisation, patterning, and crosslinking procedures for the production of hydrogel samples can be found in Section 3.1.3 [44].

As described in Section 3.2.1, ellipsometric techniques were used to investigate the behaviour of charged surface-attached hydrogels in response to an external electric stimulus in 18 MΩ H_2O. As for polyelectrolyte brushes, both one-wavelength 1-zone measurements and 4-zone spectroscopic measurements were performed.

All hydrogels were washed in 18 MΩ H_2O prior to any measurements. They were precharacterised dry and d_{dry} and n_{dry} were noted and used for reference. The hydrogels were introduced into the liquid cell, left to swell and equilibrate. Once stabilisation of the Δ and Ψ signals occurred, the hydrogels were exposed to repeated electric potential pulses. The electric potential setup is described in Section 3.1.2

Hydrogel raw data measurements

The effect of an external electric stimulus on the hydrogels was initially investigated using 1-zone measurements. The influence of the electric stimuli on the raw Δ and Ψ values, and therefore on the brush, was recorded as a function of time. The data showed similar behaviour to that seen in the polyelectrolyte polymer brushes (see Figure 4.11 and 4.12).

Figure 4.11 and Figure 4.12 show that the Δ and Ψ raw data of the charged hydrogel

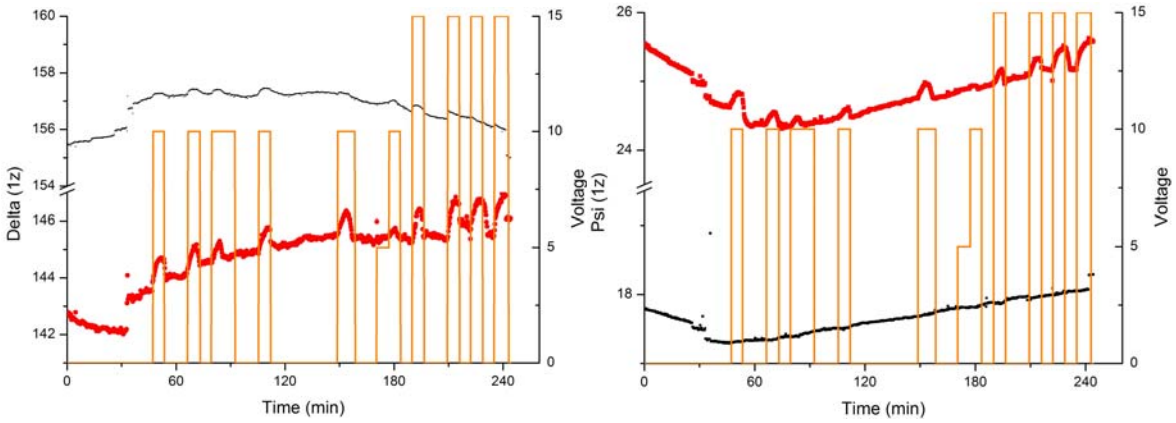

(a) Changes in raw data Δ (b) Changes in raw data Ψ

Figure 4.11: *1-zone measurement on hydrogel ES080626-S5. The thick red data line shows Delta (a) and Psi (b) measurements of the hydrogel response, the thin black line shows the reference signal measurement just outside the hydrogel covered pattern area on the sample. The vertical lines denote the applied voltage (right Y-Axis). Voltage timing was noted manually, causing small discrepancies in timing between actuation and response data. Changes in the raw data upon application of an external field can be clearly seen.*

responded to the electric stimulus. Changes in the applied stimulus could be directly correlated in time to changes observed in the ellipsometric raw data. The measured raw data values returned to their 'unperturbed' measurement values when the stimulus was removed.

The Δ and Ψ raw data changes for the hydrogel patterned area were significantly stronger than those in the reference region (Figure 4.11 and 4.12). However, some small changes could be seen in the reference data. These changes were not observed for pure silicon wafers. We must therefore conclude that small amounts of reactive polymer must have absorbed to the reference regions, creating a very thin film of adsorbed polymer $d_{\text{rest}} < 5\,\text{nm}$. The response to an applied potential of $U = 10\,\text{V}$ was significantly greater than that to $U = 5\,\text{V}$. In some cases, changes could only be observed for Δ or Ψ, as seen in Figure 4.12

The time scale for the changes in charged hydrogels in the raw data was on the order of minutes. The electric pulses were applied for 10 to 15 min. In only very few cases did stabilisation of the measured raw data values occur before the stimulus was

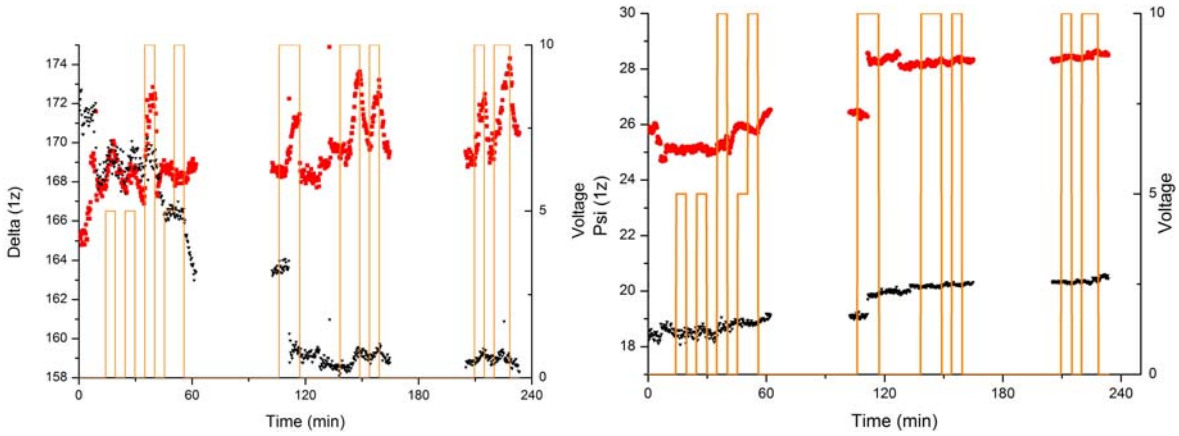

(a) Changes in raw data Δ (b) Changes in raw data Ψ

Figure 4.12: *1-zone measurement on hydrogel ES0617-S4b. The large square data points shows Delta (a) and Psi (b) of the hydrogel response, the small triangular data points shows the reference signal just outside the hydrogel covered pattern area on the sample. The vertical lines denote the applied voltage (right Y-Axis). Changes in the raw data upon application of an external field can be clearly seen.*

removed. Additional experiments showed that even for very long pulses (over 1 h), no stabilisation of the raw data could be achieved. After 1 h of exposure to an electric field, however, the gels had disintegrated and decreased in volume. No distinction between disintegration and reversible changes could be made from observation of the raw data.

The hydrogels exhibited some stability problems. These were less frequently observed for hydrogels than for the polyelectrolyte polymer brushes in Section 4.3. The polymer brush 1-zone measurements regularly showed signs of very strong drift (Section 4.3.1), while the hydrogels proved to be relatively stable. Further, some hydrogel samples were exposed to repetitive cycles of external potentials of up to $U = 10\,\mathrm{V}$ over multiple days. At the end of the experiment, the hydrogel layers had not significantly reduced in thickness. This differences between the hydrogels and the brushes can possibly be attributed to the fact that the hydrogels were crosslinked internally. Even when one chain-surface bond broke, the chain most likely was still attached to the surface via its bonds to neighboring chains. An example of a decaying hydrogel sample is shown in Figure 4.13.

An example of a hydrogel showing mixed behaviour can be seen in Figure 4.13.

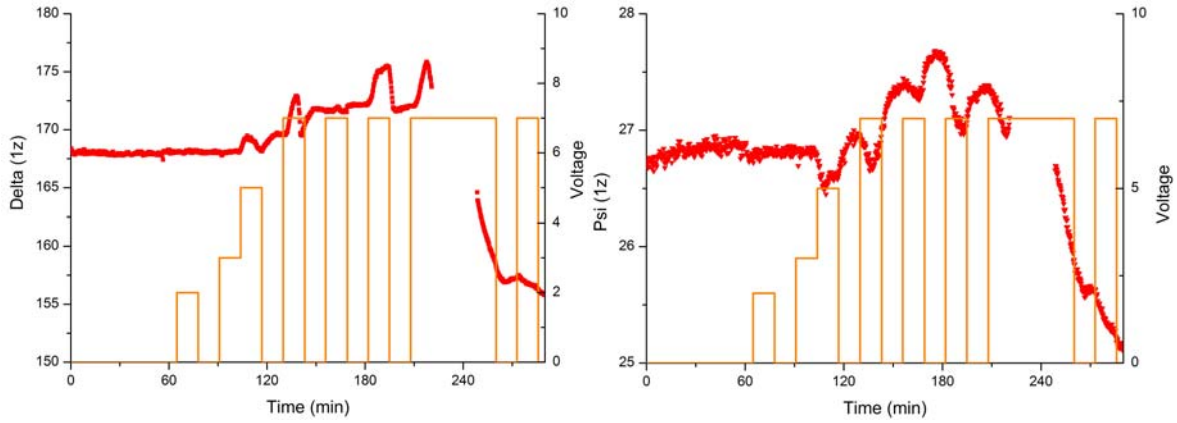

(a) Changes in raw data Δ (b) Changes in raw data Ψ

Figure 4.13: *Degradation observed for a hydrogel sample as a function of applied voltage. While the changes in the raw data are reversible for the short application of low voltages, the changes in response to the longer $U = 7$ V stimulus at 210 min are irreversible.*

The Δ and Ψ raw data returned to their unperturbed values after an applied voltage of $U = 5\,\mathrm{V}$. The later applications of $U = 7\,\mathrm{V}$ did not seem to allow for complete relaxation. The long term exposure to $U = 7\,\mathrm{V}$ at 210 min seems to have caused destruction of the hydrogel. In the dry measurements after the experiment, the hydrogel was found to have reduced in thickness.

In Figure 4.13, we can also clearly identify a threshold voltage of $U_{\mathrm{threshold}} \geq 5\,\mathrm{V}$; no changes were observed in the raw Δ and Ψ signals for applied voltages of $U = 3\,\mathrm{V}$ and $U = 4\,\mathrm{V}$ for this sample. The threshold varied between samples, $U_{\mathrm{threshold}} \approx 5 \pm 2\,\mathrm{V}$. A similar threshold had also been observed for the polyelectrolyte polymer brushes as explained in Section 4.3.1.

By comparing the behaviour of surface-attached charged hydrogel samples in response to electric stimuli with the behaviour seen in charged polymer brushes, we can conclude that the behaviour seen for the two systems is very similar. The changes seen in the 1-zone hydrogel measurements are mostly similar to the changes observed in Section 4.3.1 for polyelectrolyte PMETAC brush layers. A significant difference between the two systems was seen in the different stability behaviour in response to the applied electric stimuli: Hydrogels were found to be generally more stable than polymer brushes.

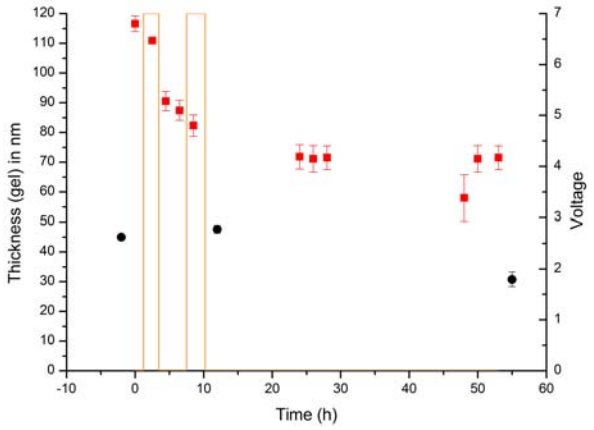

Figure 4.14: *Degradation of a hydrogel sample over several days of repeated field application. The voltage was often applied between the measurements shown here, and is therefore not included in the graph. Repeated $U = 7$ V pulses were applied.*

Spectroscopic measurements on hydrogels

Spectroscopic measurements, as discussed in Section 4.3.2, were also performed on PMETAC surface-grafted charged hydrogel patterns. While the 1-zone measurements for charged surface-attached hydrogels and polyelectrolyte brushes yielded very similar results for both systems, the spectroscopic measurements showed some significant differences.

For the polyelectrolyte hydrogels, two types of behaviour were observed.

Firstly, during some experiments, the hydrogels were observed to swell initially and collapse upon application of an external stimulus. However, no significant reswelling occurred on removal of the stimulus. Remeasurement of the gel in the dry state showed a significant reduction in the volume of the gel. Figure 4.14 shows an example of a sample which exhibited this degeneration behaviour over several days. The hydrogel initially survived repeated application of electric stimuli up to $U = 7\,\mathrm{V}$, followed by degradation on day three from about $d_{\mathrm{swollen}} = 45\,\mathrm{nm}$ to $d_{\mathrm{degraded}} = 30\,\mathrm{nm}$, a loss of about 30% of its total volume. Measurements were mostly performed between applications of the electric potential when $U = 0\,\mathrm{V}$.

Secondly, relatively small changes in the hydrogel thickness were observed upon application of the electric stimulus for many samples. The hydrogel was seen to swell

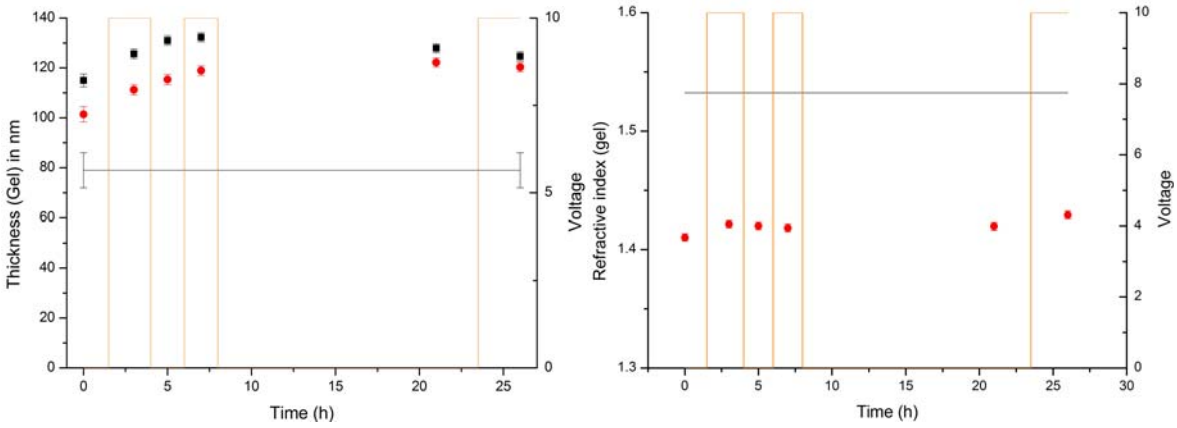

(a) Changes in hydrogel thickness Δ (b) Changes in hydrogel refractive index Ψ

Figure 4.15: *Spectroscopic measurement on hydrogel ES0617-S4b. The large square data points shows the thickness and refractive index of the hydrogel response. The vertical lines denote the applied external voltage (right Y-Axis). The horizontal line shows the dry reference values.*

or collapse by 10% to 20%. The changes appeared to correlate to the applied field, but were smaller than expected for the complete collapse of the gel. The changes in conformation were within or just outside the margin of error associated with thickness and refractive index measurement of swollen polymers as measured in the absence of an applied stimulus.

The data shown in Figure 4.15 was taken on the same sample as the 1-zone measurement data in Figure 4.12. While no macroscopic changes in the polymer brush thickness or refractive index were observed, some small changes must have occurred in the gel, as changes in the raw Δ and Ψ data could be seen when the field was applied. These may have arisen from very localised changes similar to those reported in Section 4.2, where collapse occurred in the first few nanometres of the brush. Ellipsometric measurements do not allow for modeling and measurement of such fine changes within the layer, as they do not cause significant changes to the optical behaviour of the sample.

Complete collapse was not observed for the charged surface-grafted hydrogel samples. This behaviour could be due to the chemical difference between the PMETAC hydrogel and the PMETAC polymer brush. In particular, the copolymer nature of the hydrogel might have caused a reduction in the charges to volume ratio when compared to the

PMETAC polymer brush. This could have caused a less strongly charged hydrogel, and therefore a weaker response of the hydrogel to the electric stimulus.

Secondly, the crosslinking of the hydrogel layer has a strong influence on the dynamics of the collapse. This could have resulted in a significant increase to the timescale necessary for the complete collapse, as the crosslinks could have acted like entanglements slowing down the movement of the chains. The crosslinks could also have introduced an energy barrier that is high enough to prevent the complete collapse of the charged surface-grafted hydrogel.

Discussion

We have shown that charged surface-grafted hydrogels containing METAC monomer react to externally applied potentials in pure water. The changes are reversible and take place on a time-frame of minutes. The changes are clearly correlated to the applied potentials and have threshold values dependent on the sample of $U_{\text{threshold}} \approx 5\,\text{V}$.

In comparison to the polyelectrolyte polymer brushes analysed in Section 4.3.2, the nature of the changes induced by the electric field in the hydrogels could not be identified. Changes in thickness and refractive index of the swollen hydrogel were very small and did not correspond to a complete collapse of the layer. The crosslinked nature of the hydrogels could be the reason for the higher stability of the charged hydrogels in field, but also for the reduced response to the applied electric stimuli.

4.5 Conclusions

In this chapter, we have showed how external triggers can be used to change conformational changes in polymer brushes and hydrogels. Section 4.1 showed the feasibility of triggering thermo-responsive polymer brushes and observing the changes in the brushes using ellipsometry. Section 4.2, 4.3.1 and 4.3.2 showed the possibilities and difficulties of triggering polyelectrolyte polymer brush conformational changes using electric stim-

uli. Section 4.4 described the difficulties of inducing strong changes in surface-tethered hydrogels.

From the experimental results in Section 4.2, Section 4.3.1 and 4.3.2, we can make some general conclusions about triggering conformational changes in polyelectrolyte polymer brushes.

In Section 4.2, we have seen that partial conformational changes can be triggered in polyelectrolyte brushes in salted solutions. These changes are fast (seconds to tens of seconds), on a small scale (only part of the brush conformation is changed) and are highly reversible. The changes can be achieved with small applied voltages ($U_{\text{cantilever}} = 0.5\,\text{V}$). As only small voltages are necessary to introduce the conformational changes in the first few nanometres of the brush, there is no danger to the polymer brush stability.

Technologically, these experiments showed the possibility of micro-actuation via changes in the surface energy at the polymer brush - solid interface. Any actuation principles relying on a change at this interface could be achieved using this method. Actuation and deflection of the AFM cantilever was shown. However, due to the low screening length in salted solutions, this approach is not applicable for surface energy changes at the polymer liquid interface, as the upper part of the brush does not experience a conformational change.

In Section 4.3.1 and 4.3.2, we showed that conformational changes in polyelectrolyte polymer brushes in pure water can be achieved. These changes necessitate the application of large potentials ($U_{\text{threshold}} > 3\,\text{V}$) and are comparatively slow (minutes to hours). The complete collapse of a brush (full conformational change of the polyelectrolyte polymer brush layer) was achieved. Due to the high necessary potentials, and the risk of degradation for such high potentials, the parameter space for which the conformational changes could be achieved seems to be small. This corresponds to the varied responses to stimuli that were observed in Section 4.3.2: no change, reversible conformational changes, irreversible degradation.

For the correct parameters, the conformational changes seen in the polyelectrolyte polymer brushes in response to applied electric stimuli in the film are strong (complete

collapse) and reversible. As the brushes collapse completely (and expulse the H_2O) from within), a strong polymer - liquid surface energy change should occur simultaneously. This change should also cause a less hydrophilic polymer brush surface.

From a technological perspective these systems are of limited use, due to their slow responsiveness combined with the small parameters space for fully reversible changes. With further work, the parameter space for strong reversible conformational changes could probably be established; however, it is well possible that the slow response times are an inherent difficulty due to the upper limit on the electric stimulus necessary to avoid degradation.

The conformational changes of an unhindered polymer chain in solution occurs very quickly. The slow response times here are indicative of the formation of of entangled states in the collapsed polymer brush, from which the brush can recover only very slowly. Future brush relaxation experiments might therefore be useful to probe non-equilibrium chain morphologies in end-grafted polymer layers.

In Section 4.4, we have shown that charged surface-grafted hydrogels react to externally applied potentials in pure water. The changes seen in the ellipsometric raw data are reversible above the threshold voltage and below the degradation voltage ($U_{\min} < U < U_{\max}$). The changes occur within minutes of the stimulus application.

The exact nature of the changes induced in the hydrogels with electric stimuli could not be identified. The changes seen in the ellipsometric raw data for hydrogels could not be correlated to thickness or refractive index changes in the swollen hydrogels. The complete collapse of the charged hydrogel was therefore not achieved. The higher stability of the hydrogels in electric fields could be due to their crosslinked nature. This could also be the reason for their lower response to the external stimulus.

Hydrogel actuation using electric stimuli is therefore of a limited use from a technological perspective. Further work identifying the nature of the changes seen in the ellipsometric raw data in response to the applied gels would be necessary. Similarly, an investigation of the influence of crosslinking density on the reactivity of the hydrogels could yield more interesting charged surface-grafted systems combining the robustness

of hydrogels and the higher reactivity of polymer brushes. Nonetheless, the time-frame associated with changes in the system seems to be an inherent problem of these systems. The possibility of future technological applications of switching surface-attached polymers with electric stimuli must therefore be questioned.

5 Instabilities in molten polymer brushes

Here, we discuss theoretical predictions and initial experimental approaches toward patterning of molten polymer brushes using electric field induced instabilities. In contrast to solution-based systems described in the earlier chapters, this work was carried out in the melt.

Patterning of molten polymer brushes through electric field induced instabilities could be used for contactless electro-hydrodynamic lithography (EHD): When using this technique in normal melts, the polymer sooner or later touches the master. While this can be avoided by carefully choosing the relevant parameter set [59], the required parameter balance is not very robust. It is therefore useful to explore instabilities in end-grafted polymer melts, where the material displacement is strongly restricted by the end-grafted nature of the chains in the film.

The calculation in Section 5.3 is based on prior work by Fredrickson, Ajdari, Leibler and Carton [60] and Shenoy and Sharma [61]. In Sections 5.1 and 5.2, we will provide the background for the theoretical calculation from these two publications. In Section 5.3, we will present a combination of these two theories, and in Section 5.4 the results of some initial experiments on polymer brushes in electric fields. Experiments in Section 5.4 were carried out using the methods from Schäffer *et al.* [62].

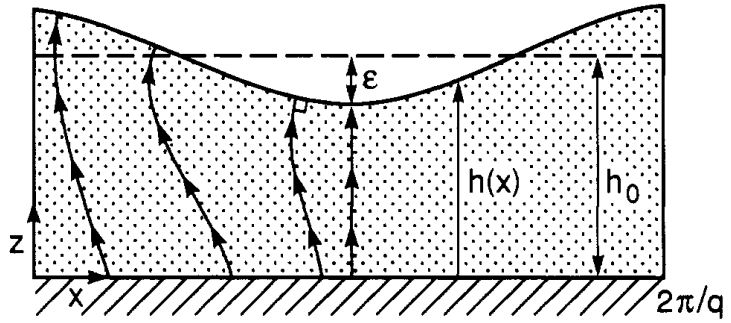

Figure 5.1: *Molten thin film developing instabilities by Fredrickson [60]*

5.1 Fredrickson's polymer brush

Fredrickson *et al.* presented a theoretical argument exploring how a molten polymer brush responds to a non-uniform volume-conserving deformation using a perturbative calculation of the brush free energy. They model the molten polymer brushes as elastic films with a free energy per area of grafting surface. They explain in particular that while instabilities with short wavelength can develop, long wavelength are suppressed due to the end-grafting of the polymer chain to the surface. They show in their study that the elastic restoring force at long wavelength and the interfacial tension penalty for short wavelength should lead to an energetically preferred wavelength for the instability development. Further, they show that for a non-uniform deformation a molten polymer brush can be treated in similarly to an incompressible, isotropic, elastic film. The full derivation of this argument is given in Fredrickson [60].

Fredrickson *et al.* describe the development of instabilities with a wavelength $\lambda_{\mathrm{F}} = 2\pi/q$ for a polymer brush of thickness h_0 as shown in Figure 5.1. In Section 5.3, we will make use of the expressions derived by Fredrickson *et al.* [60] for the free energy of the molten polymer brushes in an elastic film model and for the shear modulus. These equations are therefore repeated explicitly.

$$f_{\mathrm{t}} = f^{(0)} + \gamma + \frac{1}{4}\left(\frac{\epsilon}{h_0}\right)^2 \left\{\gamma(qh_0)^2 + \mu_0 h_0 \left[3(qh_0)^{-2} + 2qh_0\right]\right\} \tag{5.1}$$

This means that the elastic energy is dependent on the shear modulus of the brush

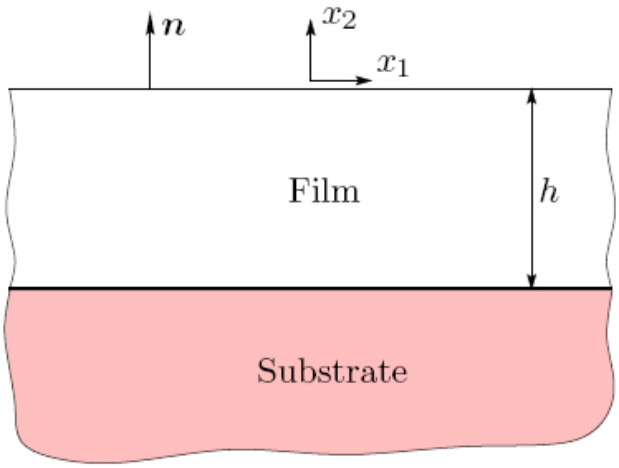

Figure 5.2: *Molten polymer film of height h on a substrate as used in the calculation by Shenoy and Sharma [61]*

in the melt. The shear modulus is given by

$$\mu_0 = 3k_\mathrm{B}T\frac{v\sigma^2}{b^2} \approx 3k_\mathrm{B}Tb\sigma^2 \tag{5.2}$$

with $v = b^3$ [60].

5.2 Shenoy's thin film stability calculation

Shenoy and Sharma developed a theory for the formation of instabilities in thin solid films [61]. This work focuses on the question of stability of a thin solid film bonded to a rigid substrate whose free surface experiences an effective force. They show that it is possible, for sufficiently large interaction forces, to reduce the net potential energy of the system by a periodic non homogeneous deformation in the film.

Shenoy *et al.* [61] showed that the stability of a thin solid film, whose surface is exposed to a destabilising force, can be determined from a threshold value which depends on three parameters. These parameters are Poisson's ratio, the normalised second derivative of the interaction potential hY/μ, and the normalised surface energy $\gamma/\mu h$. In the following, we will refer to the threshold parameter I_S and the critical threshold

value index as I_c.

The critical threshold value I_c is given as

$$I_c = \frac{hY_c}{\mu} \tag{5.3}$$

Shenoy *et al.* give an example calculation for the exact value of the threshold parameter for a film interacting with an electric field. The equation describing the interaction of the film and the field is given by

$$U(\vec{u} \cdot \vec{n}) = \frac{\epsilon_0 \epsilon_p p V^2}{2(\epsilon_p d - (\epsilon_p - 1)(h + \vec{u} \cdot \vec{n}))} \tag{5.4}$$

For the case of an elastic film in an electric field, the threshold value $I_c = 6.63$. This value allows distinction between a stable film ($I_S < 6.63$) and an unstable film ($I_S > 6.63$). The value I can then be calculated for different experimental conditions in order to establish whether a film will develop instabilities or stay stable as a function of the experimental parameters.

5.3 Theoretical prediction of instability formation

As it has been shown in Fredrickson's work [60] that a molten polymer brush behaves similar to an elastic film, we have used this work in combination with the calculations by Shenoy and Sharma [61]. Here, we combine these two theories in order to explain the development of instabilities in molten polymer brush films. By assuming that the molten polymer brush behaves like an elastic solid film, we can use equation 5.2 from Fredrickson to describe the long wavelength instability formation.

Using the approach described by Shenoy *et al.* and the instability values for an electric field induced instability given by Equation 5.6, Poisson's ratio for polymer $\nu = 0.5$ and the shear modulus from Fredrickson *et al.*, we can obtain an stability condition for polymer brushes in the melt under the influence of an electric field.

Figure 5.3: *The expected deformation of a molten polymer brush under an applied electric field. The surface grafting limits the lateral mass transport in the film during instability formation.*

The second derivative of equation 5.4 for a planar film where the field is applied perpendicularly to the surface is then given by

$$Y = U''(0) = \frac{\epsilon_0 \epsilon_\mathrm{p}^3 V^2}{(\epsilon_\mathrm{p} d - h(\epsilon_\mathrm{p} - 1))^3} \tag{5.5}$$

For a molten polymer brush, Shenoy *et al.* 's threshold parameter is then given by

$$I_\mathrm{S} = \frac{hY}{\mu} = \frac{1}{3k_\mathrm{B}Tb\sigma^2} \frac{\epsilon_0 \epsilon_\mathrm{p}^3 V^2 h}{(\epsilon_\mathrm{p} d - h(\epsilon_\mathrm{p} - 1))^3} \tag{5.6}$$

where b is the monomer size, σ denotes the grafting density, T the temperature, ϵ_p the relative permeability of the polymer, ν the Poisson ratio, and $\gamma = 29.7\,\mathrm{mN/m}$ the surface energy.

The results of the stability calculation are shown in Figure 5.4 for polystyrene. Polystyrene fulfills two important criteria: Firstly, it is relatively easy to polymerise on surfaces and brushes with over 100 nm thickness can be easily obtained. Secondly, it has a high permittivity, which means it is more strongly affected by electric fields than most other polymers. Therefore, the stability calculation was performed for polystyrene.

For the calculation, the following constant values were used: $b = 6.8\,\text{Å}$, $0.01 < \sigma < 0.3\,\mathrm{nm}^{-2}$, $T = 170°\mathrm{T} = 443°\mathrm{K}$, $\epsilon_\mathrm{p} = 3.6$, $\nu = 0.5$, $\gamma = 29.7\,\mathrm{mN/m}$. The values for h, d where set to experimentally reasonable values of $d = 2h = 200\,\mathrm{nm}$. The voltage was raised to a maximum value of $U = 150\,\mathrm{V}$.

We calculated the applied electric field as a function of the distance, such that

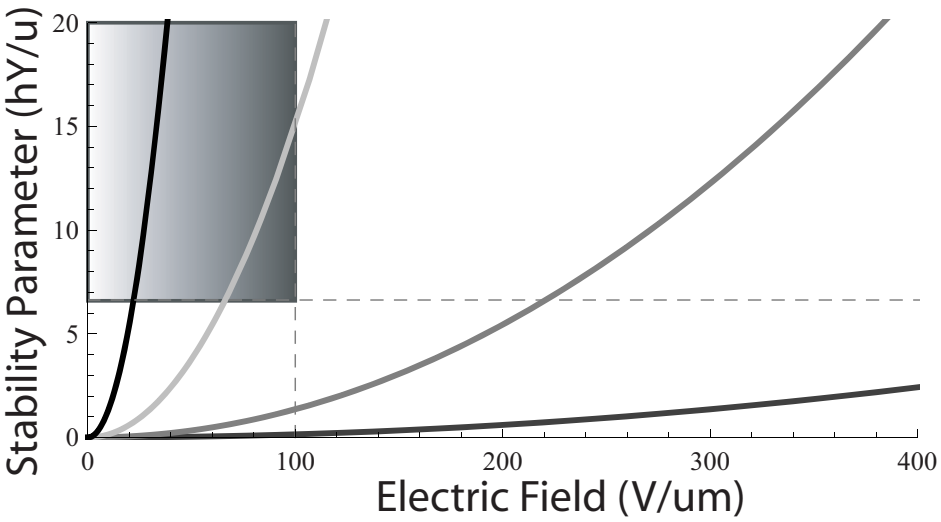

Figure 5.4: *Stability curves as a function of voltage for PS polymer brush layers of 100 nm thickness with a 200 nm electrode spacing. The different curves correspond to the following grafting densities (chains per nm^2): Black - 0.01, Light grey - 0.03, Grey - 0.1, Dark grey - 0.3. The important region in the graph is the upper left where the two requirements for the destabilisation of polymer brushes are fulfilled: $hY/\mu > 6.63$ and $E = U/d < 100\ V/\mu m$*

$$E = \frac{V}{d} \tag{5.7}$$

Experimentally, it has been seen that electric fields above a threshold field of $E_0 = 100\,\mathrm{V/\mu m}$ cause dielectric breakdown. Therefore, we have introduced an upper limit of $E_0 = 100\,\mathrm{V/\mu m}$ for the stability calculation in Equation 5.6.

Two important parameter dependences in equation 5.6 are noted: First, the thinner the gap between the film and the upper electrode, the more likely instabilities are to develop. Second, the instability development also depends on σ^2, such that polymer brushes with a lower grafting density are better suited for these experiments.

While thinner films and thinner air gaps are generally better for the development of instabilities, the difficulty of detection of very small wavelength patterns with small changes in height, means that films must have a minimum thickness of $h > 50\,\mathrm{nm}$, in order for the instabilities to be easily distinguishable by atomic force microscopy.

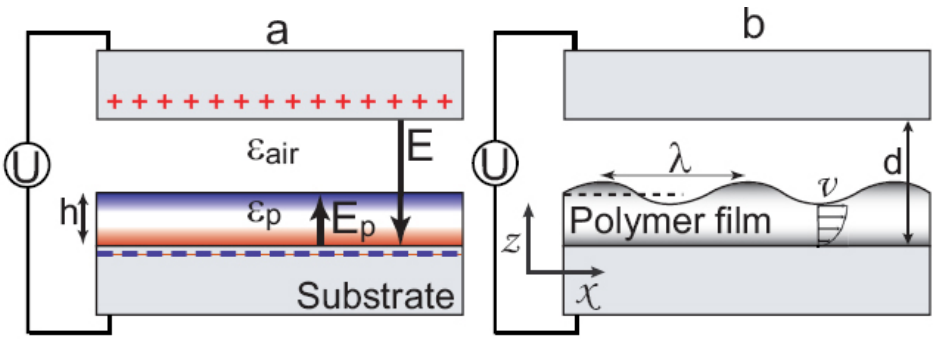

Figure 5.5: *Schematic representation of the experimental set-up from [63]. It assumes the free flow of the polymer in the film. For polymer brushes, instabilities will develop slightly differently, as lateral flow is restricted. a) The externally applied potential U causes polarisation in the parallel plate capacitor, which causes an electric field E in the polymer layer b) Coupling of the electrostatic forces at the polymer/air interface amplify instabilities with a well-defined wavelength λ.*

Figure 5.4 shows the conclusion from our calculation for polystyrene brush films with thicknesses between $50\,\text{nm} < h < 100\,\text{nm}$, low original surface roughness and high permeability. The figure shows that brushes of relatively low grafting densities ($\sigma < 0.03$) are needed to observe the instability.

For polymer brushes, the grafting density σ, the molecular weight M_N and the film thickness h are related as follows:

$$h \propto N\sigma \propto M_\text{N}\sigma \tag{5.8}$$

In order to obtain thick films $h > 50\,\text{nm}$ with low grafting densities $\sigma < 0.03$, the molecule needs to be extremely long and have a very heigh molecular weight. This means, that the desired parameter space for instability development is extremely small.

5.4 Instability experiments

For the experiments, PS and PMMA polymer brushes were used. The PMMA brushes were prepared by ATRP as described in Section 3.1.2. The grafting density was adjusted using a mixed monolayer approach [43].

The PMMA brush samples had chain grafting densities of $\sigma = 0.01$, $\sigma = 0.07$, $\sigma = 0.15$, $\sigma = 0.34$. The films were, unfortunately, quite thin and they were rather rough.

Low grafting density, high molecular weight brushes are more easily prepared by a grafting-to approach. Grafting-to PS brushes had film thicknesses of $27.6 \pm 0.8\,\mathrm{nm}$ for SiCl-PS, $20.9 \pm 0.9\,\mathrm{nm}$ for NH_2-PS and $35.2 \pm 3.5\,\mathrm{nm}$ for COOH-PS. Calculated grafting densities were 0.13 chains/nm^2, 0.04 chains/^{2} and 0.03 chains/^{2} respectively.

The polymer brushes were prepared on silicon substrates with a gold coating on the backside for enhanced contact with the electrodes. Contact was further improved by application of a thin layer of silver dag between the copper electrodes and the sample backside. The samples were annealed in an oven under vacuum for several days at temperatures $T \ll 170°\mathrm{C}$. The temperature was chosen to avoid degradation of the polymer. The voltage was current-limited to $I < 0.2\,\mathrm{A}$. Experiments were carried out at $T = 170°\mathrm{C}$. The experimental setup in Figure 5.5 was adapted from Harkema *et al.* [63].

Both, PMMA grafting-from brushes and PS grafting-to brushes showed no changes in the surface topography after exposure to the electric field E. The samples were observed by AFM[1], as shown in Figure 5.6.

No significant surface topography changes were observed. This was attributed to the following issues encountered during the experiments:

1. The number of impurities in the polymer brush was very high. As can be seen from the stability calculation in Figure 5.4, the air gap between the film and the upper electrode needs to be as small as possible and not larger than the thickness of the film. As can be seen from Figure 5.6, the average roughness is relatively low ($R_{\mathrm{average}} \approx 5\,\mathrm{nm}$). However, the maximum roughness ($R_{\mathrm{max}} \approx 100\mathrm{nm}$), even on a relatively small patch of 50 nm x 50 nm is too high to achieve the necessary small gap width of 50 nm.

[1] AFM measurements performed by Ron Oren.

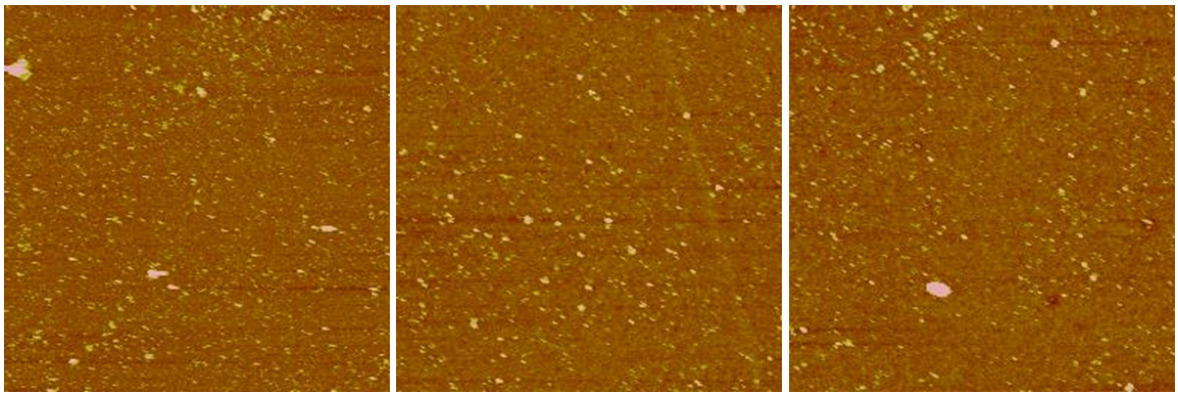

Figure 5.6: *AFM micrographs (20 µm × 20 µm of PMMA polymer brushes with low grafting densities but high amounts of impurities. From left to right: a) 30% initiator, $d \approx 23\,nm$, $R_{average} = 4.25\,nm$, $R_{max} = 127$ nm; b) 30% initiator, $d \approx 40$ nm, $R_{average} = 3.0\,nm$, $R_{max}74 =$ nm; c) 30% initiator, $d \approx 40$ nm, $R_{average} = 5.4\,nm$, $R_{max} = 179\,nm$.*

2. The very low grafting densities resulted in very thin films. All films had thicknesses $d < 50\,\text{nm}$. This, in combination with the difficulty of achieving very flat surfaces due to the impurities in the brushes caused experimental parameters to be shifted into the stable regime. Therefore, no surface buckling could be observed.

The theoretical calculation showed the feasibility of inducing topographic changes in polymer brush melts using electric fields. There are still many challenges to be solved before these changes can be induced experimentally; the major issues are on the synthetic and chemical side of the experiments. Only once cleaner and thicker samples can be produced, successful topographical changed due to instability creation can be achieved. As stated in equation 5.8, the molecular weight of the polymer must therefore be extremely high. The detailed choice of parameters for patterning of end-grafted films is equally difficult as described for non-grafted melts [59].

6 Polymer brushes and hydrogels: Conclusions

In this part, we discussed the results of experiments involving polymer brushes and hydrogels (surface-attached polymers) in solutions, as well as polymer brushes in the melt. The purpose of this work was to gain a better understanding of the possibilities and limitations when using polymer brushes in nanosystems. The feasibility of two particular applications where explored here: the use of polymer brushes or surface-attached hydrogels as nano-actuators or switchable surface energy modifiers at the liquid-surface interface and the use of polymer brushes in the melt to achieve sub 100 nm patterns on surfaces. The focus of this work was the interaction of surface-attached polymers with electric potentials in aqueous solutions or in the melt. The use of electric stimuli was chosen, as the implementation of switching or patterning based on electric signals is of high technological interest: Triggering of conformational changes or surface topography changes using electric stimuli, allows for easy integration of the mechanisms into existing systems, as well as easy maintenance and production.

The initial experiments had the purpose of establishing, whether surface-attached polymers can be switched using electric stimuli. These experiments were covered in Chapter 4.

We explored important characteristics of these systems with respect to their applicability for surface property changes. Surface property changes can be achieved through complete conformational changes of surface-attached polymer layers (complete collapse). The most important features studied in this work were:

1. Feasibility of switching of conformational changes with electric stimuli
2. Reversibility of conformational changes
3. Time-scales associated with the conformational changes

For polymer brushes, the feasibility of switching of conformation using electric stimuli was shown. The time scale associated with such changes was very long ($t \approx 1\,\mathrm{h}$) and the reversibility of such changes was rather poor. Therefore, the use of polymer brushes in systems requiring surface property changes (and thus complete conformational changes) is limited to systems, which do not require fast switching speed. Further work on the reversibility, tunability, and stability of such systems would be necessary before they could be used, as degradation of the polymer during experiments was shown to be a significant problem.

It was also shown that partial conformational changes at the solid-polymer interface could be achieved faster and with a higher rate of reversibility. These partial changes are not associated with surface property changes, but can be exploited for actuation at the solid-polymer interface through the induction of surface stresses.

In the experiments on hydrogels, we found that no complete conformational changes in the system could be achieved. This was attributed to the crosslinking between the individual chains. Small changes in response to the externally applied stimulus could be identified in the raw data. Partial conformational changes at the solid-polymer interface could be a possible explanation for this behaviour, but could not be explored further using ellipsometric techniques. The use of hydrogels for nano-actuation or surface property changes could not be demonstrated.

In Chapter 5, the use of electric fields for small scale patterning of polymer brush melts was studied. The possibility of using electric potentials to induce instabilities in polymer melts was explored both theoretically and experimentally. While the theoretical calculation showed the possibility of using electric stimuli to destabilise a polymer brush melt and induce surface patterns, the preliminary experiments did not yield the desired results. This could be attributed to the relatively small parameter space for which the destabilisation threshold can be reached. We found that the main limitations

were the polymer brush composition (long polymer chains with very low grafting density are required) and film cleanliness (high initial surface roughness was observed). By improving these two parameters, we believe that the destabilisation of polymer brush melts could be used to create sub 100 nm features on surfaces.

While these systems are clearly not very useful from a practical point of view (in terms of surface actuation), the results of our experiments raise interesting scientific questions. As the molecular relaxation of individual chains are quick, the slow dynamics of brush swelling and relaxation reveal the transition between frustrated non-equilibrium states, which are currently not well understood [64]. More detailed time resolved swelling and collapse experiments (possibly comparing end-grafted brushes and unattached melt layers in solvent vapour atmospheres) in the presence of external stimuli are therefore useful to understand the details of chain conformation in thin polymer films.

Part II

Wetting of surfaces

7 Wetting theory

In this chapter, we explain the theory of wetting of solid surfaces with liquids. This chapter introduces necessary concepts for the experimental work on wetting explored in Chapter 8, 9, 10 and 12 and 13. In the context of the theories presented on metastable wetting and underwater wetting, some relevant recent experimental and theoretical work in the area will also be presented.

The classical theories by Laplace [65] and Young [66] are explained in Section 7.1. The wetting of rough surfaces and the theories by Wenzel [67] and Cassie and Baxter [68] are discussed in Section 7.2. In Section 7.3, metastable wetting states on surfaces will be explored. Section 7.4 will discuss wetting on natural surfaces. In Section 7.5, the concepts and theories of underwater wetting of surfaces and air bubble dissolution in water are explained.

The phenomenon of wetting is pertinent to many industrial and technological areas of interest [69], including

- chemical industry: e.g. wetting of paints, inks, insecticides
- soil science: e.g. penetration of liquids into porous rocks
- automobile industry: e.g. wetting of water on wind screens
- life sciences: motion of insects on water, wetting of the eye

In this work, we will focus on two topics of recent interest in wetting theory: Metastable Cassie-Baxter wetting states on hydrophilic materials and the stability of superhydrophobic Cassie-Baxter wetting states underwater. Both topics are of interest

to advance our understanding about wetting on surfaces, but are also of considerable technological importance.

Research on superhydrophobic and self-cleaning surfaces has so far been limited to a relatively small range of materials, as hydrophobicity of the material itself was necessary to achieve superhydrophobic surface wetting. With the possibility of creating metastable superhydrophobic wetting states, on hydrophilic materials, with long life-times, the class of materials available for these self-cleaning surfaces could be significantly expanded. Super-structured hydrophilic materials with Cassie-Baxter wetting properties have been a focus of research since 2007, when Tuteja *et al.* published a first experimental study of such materials [4], followed by Marmur's theoretical work a year later [5]. Here, we hope to expand on the understanding of metastable Cassie-Baxter wetting states on hydrophilic materials.

The second topic covers the behaviour of superhydrophobic wetting states underwater. Little prior work in this area has been published, even though the topic is of immense technological interest. Superhydrophobic surfaces have received considerable attention for their ability to stay dry underwater, as well as their ability to reduce the friction between a liquid and a solid and increase buoyancy of materials [7, 8]. In this work, we investigate the stability and limitations of Cassie-Baxter air-films on superhydrophobic surfaces underwater.

7.1 Young's equation and classical wetting theory

The term wetting describes the most energetically favourable contact between a solid surface and a liquid, resulting from the interactions between the three coexisting phases that are present at the contact point: the solid, liquid and vapour phase. The energy balance results from the interaction energy of the phases: The surface energy of the solid (in contact with the vapour phase) γ_{sv}, the surface tension of the liquid (in contact with the vapour phase) γ_{lv}, the solid-liquid interaction energy γ_{sl}.

Wetting describes the interfacial behaviour of three coexisting phases (any combi-

Figure 7.1: *(A) Wetting of a solid surface by a liquid drop in a vapour environment. (B) Wetting of a solid surface with a vapour bubble in a liquid environment.*

nation is possible). Examples are a small drop of a liquid in a vapour environment wetting a surface or a bubble of gas wetting a solid surface in a liquid environment. Both situations are shown in Figure 7.1.

In the following sections, I will focus on wetting of solid materials by liquid droplets in a vapour atmosphere. Section 7.5 treats the inverted situation; a solid material in contact with gas bubbles surrounded by a liquid.

Attractive forces between the liquid and the solid cause a liquid drop to spread across the surface. Repulsive forces between the solid and the liquid or cohesive forces within the liquid cause a reduced surface-liquid contact area. The equilibrium between these opposite forces results in a uniquely defined contact behaviour between two materials: The inherent contact angle θ_Y, which was defined for the first time by Young [66] in 1805.

Young formulated the first equation describing the contact angle θ_Y of a liquid on an ideal flat surface.

$$\cos\theta_Y = \frac{\gamma_{sl} - \gamma_{sv}}{\gamma_{lv}} \tag{7.1}$$

A hydrophobic material has an inherent water contact angle $\theta_Y > 90$ (Figure 7.2 A), a hydrophilic material has an inherent water contact angle $\theta_Y < 90$ (Figure 7.2 C). Equivalent definitions exist for contact angles of oils on surfaces: An oleophobic material has an inherent oil contact angle $\theta_{(Y,\,oil)} > 90$, an oleophilic material has an inherent oil contact angle $\theta_{(Y,\,oil)} < 90$. In the following, the terms hydrophobic and hydrophilic will be used to describe surfaces wetted by water, as nearly all experiments

Figure 7.2: *Contact angle θ_Y of water on (A) a hydrophobic surface ($\theta_Y > 90°$) (B) a neutral surface ($\theta_Y = 90°$) (C) a hydrophilic surface ($\theta_Y < 90°$)*

reported here are concerned with water-solid wetting behaviour. For non-water liquids, the term 'lyophilic' is used for low contact angle conditions and 'lyophobic' is used when higher contact angles occur. Where another liquid is used in this work, this is explicitly mentioned.

7.2 Wetting on rough surfaces

7.2.1 Wenzel and Cassie-Baxter wetting

Wetting on non-ideal rough surfaces is more complex than described by Young's theory. Wenzel [67] and Cassie and Baxter [68] established two different theories for wetting on rough surfaces. They both found that the surface roughness enhances the inherent wetting behaviour of the material; hydrophilic surfaces become more hydrophilic and hydrophobic surfaces more hydrophobic.

Wenzel's wetting model describes the most common wetting behaviour. It is characterised by complete contact between the liquid and the surface. For hydrophobic materials (Figure 7.3 A), there is no gap between the droplet and the surface, and the contact angle $\theta_Y > 90°$. In Figure 7.3 C, there is no gap between the droplet and the surface and the contact angle $\theta_Y < 90°$. This corresponds to hydrophilic Wenzel wetting. Wenzel wetting is the only energetically stable wetting behaviour on hydrophilic rough surfaces and the most common wetting behaviour on hydrophobic surfaces.

Wenzel wetting is characterised by the following equation and is strongly dependent

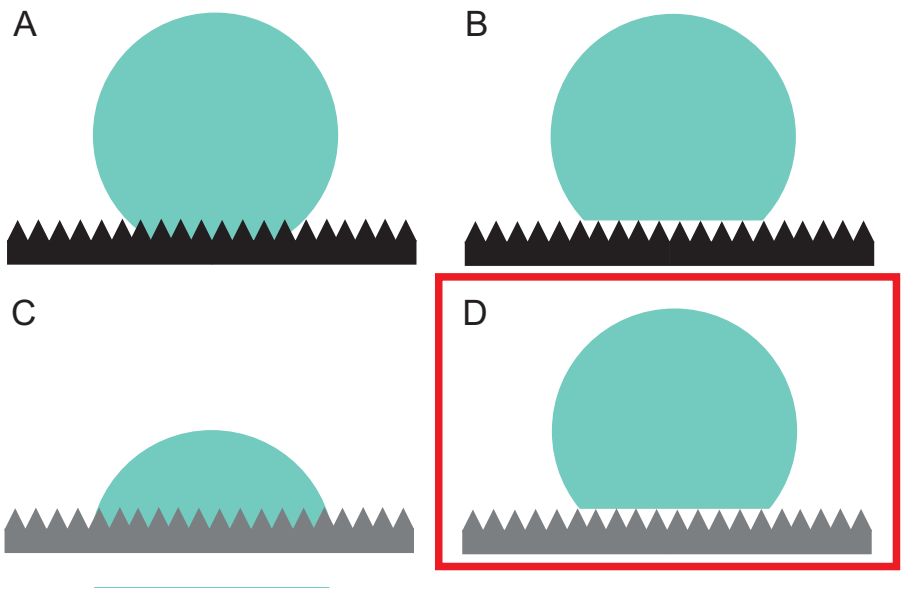

Figure 7.3: *Wetting on rough surfaces: Hydrophobic surfaces are shown black, hydrophilic surfaces are grey (A) Hydrophobic surface with a Wenzel drop (B) Hydrophobic surface with a Cassie-Baxter drop (C) Hydrophilic surface with a Wenzel drop (D) Hydrophilic surface with a metastable Cassie-Baxter drop (Section 7.3)*

on the surface roughness $r_\mathrm{f} = A_\mathrm{true}/A_\mathrm{apparent}$, which is a measure of the true (A_true) versus the apparent (or projected) surface area (A_apparent).

$$\cos\theta_\mathrm{W} = r_\mathrm{f}\cos\theta_\mathrm{Y} \tag{7.2}$$

In Figure 7.3 B, there is a thin air-filled gap between the droplet and the surface and the contact angle $\theta_\mathrm{Y} > 90°$. This corresponds to hydrophobic Cassie-Baxter wetting. Energetically stable Cassie-Baxter wetting, only exists on hydrophobic surfaces with high roughness factors. For Cassie-Baxter wetting, the drop sits on the highest surface features and does not penetrate into the deeper holes. This air-pocket state corresponds to partial non-wetting of the surface, which is the most favourable solution for the energy equation for very rough hydrophobic materials.

Therefore, the effective water contact angle θ_eff is given by

$$\cos\theta_\mathrm{eff} = \langle\cos\theta_\mathrm{x}\rangle_\mathrm{x} = f\cos\theta_\mathrm{Y} + (1-f)\cos(\pi) \tag{7.3}$$

This gives the effective macroscopic water contact angle for Cassie-Baxter wetting [68]

$$\cos\theta_{\mathrm{CB}} = f\cos\theta_{\mathrm{Y}} + f - 1 \tag{7.4}$$

where, f corresponds to the fraction of the surface in contact with the liquid phase (or the fraction of the surface at a significantly 'higher' level) than the rest of the surface. Marmur [70] explains, that the roughness of the fraction of the surface in contact with the liquid, r_{f} also has an influence on the surface wetting properties, such that a more precise definition of the air-pocket state is given by

$$\cos\theta_{\mathrm{CB}} = r_{\mathrm{f}} f\cos\theta_{\mathrm{Y}} + f - 1 \tag{7.5}$$

For this version of the Cassie-Baxter equation, when $f = 1$ and $r_{\mathrm{f}} = r$, the Cassie-Baxter equations becomes the Wenzel equation.

Figure 7.3 D shows Cassie-Baxter wetting on a hydrophilic surface. This case is energetically unstable and was not originally discussed by Cassie and Baxter. It will be explored in detail in Section 7.3.

As a distinction between Wenzel and Cassie-Baxter wetting cannot always be made easily in experiments, the measured static contact angles are denoted by θ_{S}. The distinction in wetting behaviour observed in the experiments is made upon the analysis of the wetting data, taking into account the contact angle hysteresis, $\Delta\theta$.

The hysteresis $\Delta\theta$ is measure of the difference between the advancing θ_{A} and the receding contact angles θ_{R}.

$$\Delta\theta = \theta_{\mathrm{A}} - \theta_{\mathrm{R}} \tag{7.6}$$

The hysteresis for ideal Cassie-Baxter wetting is very small $\Delta\theta_{\mathrm{CB}} \approx 0$, as $\theta_{\mathrm{A}} \approx \theta_{\mathrm{R}} \approx \theta_{\mathrm{S}}$ [71]. The drop detaches easily and does not spread on the surface.

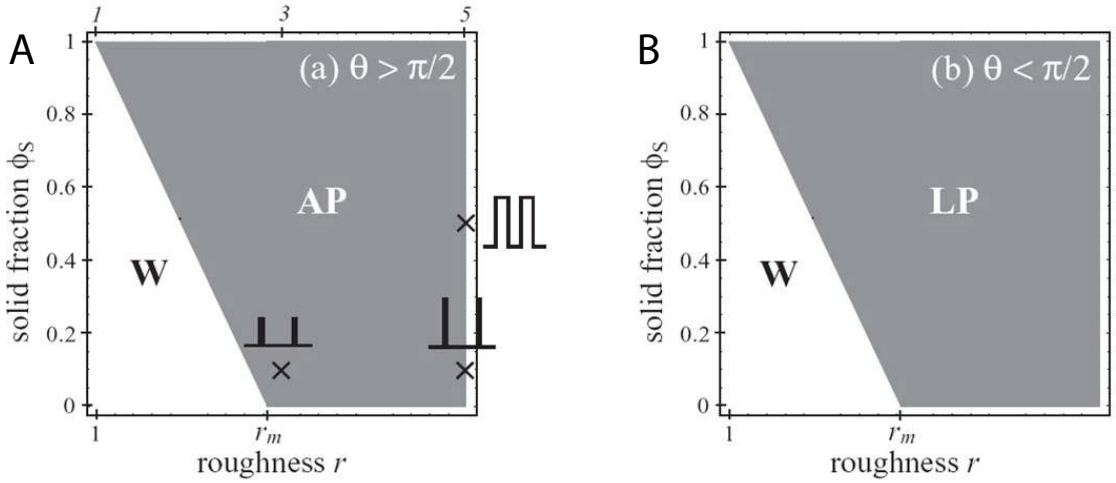

Figure 7.4: *(A) Roughness and solid fraction coverage cross-over regimes for Wenzel (W) versus air-pocket Cassie-Baxter (AP) wetting for hydrophobic surfaces.*
(B) cross-over for Wenzel (W) to perfect liquid penetration (LP) wetting for hydrophilic surfaces - Examples of textures are included schematically [72]

The hysteresis behaviour is very different for Wenzel wetting drops. As the liquid phase conforms completely to the surface features, Wenzel drops 'stick' to the surface, even if the surface is hydrophobic. For Wenzel drops on hydrophilic surfaces, $\Delta\theta_{\mathrm{W}} \approx \theta_{\mathrm{A}} \approx \theta_{\mathrm{S}} < 90°$, and $\theta_{\mathrm{R}} \approx 0$. For Wenzel drops on hydrophobic surfaces, the receding contact angle $\theta_{\mathrm{R}} \ll 90°$. Therefore, for all Wenzel drops, the hysteresis $\Delta\theta_{\mathrm{W}}$ is large .

The cross-over between Wenzel and Cassie-Baxter wetting has been studied theoretically by Ishino *et al.* [72] for surfaces covered with pillar arrays. It has been found that the penetration versus air-pocket state wetting depends strongly on the roughness r_{f} and the solid fraction f of the structure. In their work, Ishino *et al.* showed that for every roughness value, there is a characteristic cross-over contact angle from the hydrophobic Wenzel to the hydrophobic Cassie-Baxter wetting regime. This is shown in Figure 7.4.

Imbibtion is the diffusion of the liquid into the structured surface in order to maximise the contact area between the surface and the liquid. This has been described in detail by Bico *et al.* for highly structured hydrophilic surfaces [73]. This behaviour corresponds to strongly enhanced wetting on very rough hydrophilic surfaces. It is described in Figure 7.4 B by the liquid penetration regime (LP). The behaviour is also shown in

Figure 7.6, which shows a mixed Wenzel and liquid penetration wetting state.

For all classical cases, the cross-over between Wenzel and Cassie-Baxter wetting can therefore be uniquely determined and has been studied in detail. It is of great importance to note that for both Wenzel and Cassie-Baxter wetting, Young's equation still holds locally [74]. The global contact angle is influenced by the structure of the surface, but the local contact angle at the three-phase contact point is still is given by Young's equation. It is determined by the energy balance of the three phases and is therefore the only minimum solution to the energy balance.

Ishino *et al.* [72] calculated that for surfaces with a higher solid fraction f, the roughness required for Cassie-Baxter wetting decreases (Figure 7.6). For a solid fraction of $f = \phi_S = 0.6$, the minimal roughness for Cassie-Baxter wetting is about $r_{min} > 1.5$, whereas for a solid fraction of $f = \phi_S > 0.2$, the minimal roughness for Cassie-Baxter wetting is about $r_{min} = 2.5$.

It was noted by Ishino *et al.* [72], that pushing drops on surfaces that just fulfill the Cassie-Baxter wetting requirements, can result in Wenzel wetting of the drop. This suggests that the air-pocket state for these parameters is only a metastable configuration. It also implies difficulty in comparison of experimental and theoretical results, as metastable states can be mistaken for stable states and vice versa. Therefore corrections to the graphs in Figure 7.4 might be necessary.

Nosonovsky *et al.* have presented an alternative map of global contact angles as a function of roughness r_f shown in Figure 7.5 [75]. This map shows a non-linear change to the contact angle as a function of roughness and does not reproduce the results by Ishino *et al.*

Ishino *et al.* have also shown that mixed wetting states can exist on surfaces. In the case where the liquid locally penetrates into the grooves, a 'mushroom state' can develop via nucleation and growth from surface defects or due to local perturbation (Figure 7.6 A). Similarly, the drop can spread on a hydrophilic surface beyond the contact angle by capillary forces causing a partial Wenzel, partial liquid penetration mixed wetting state termed 'Sunny-side up' (Figure 7.6 B). Depending on the equilibrium

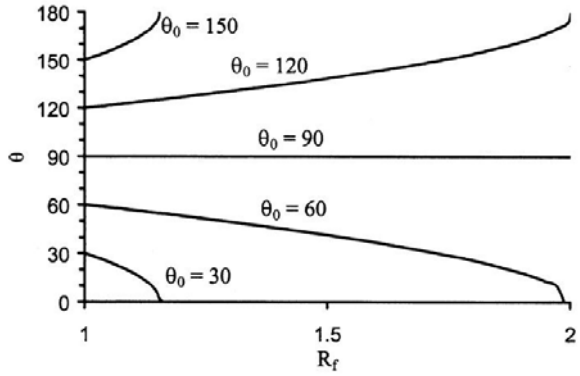

Figure 7.5: *Effect of roughnesss on the contact angle of a drop on a surface [75]*

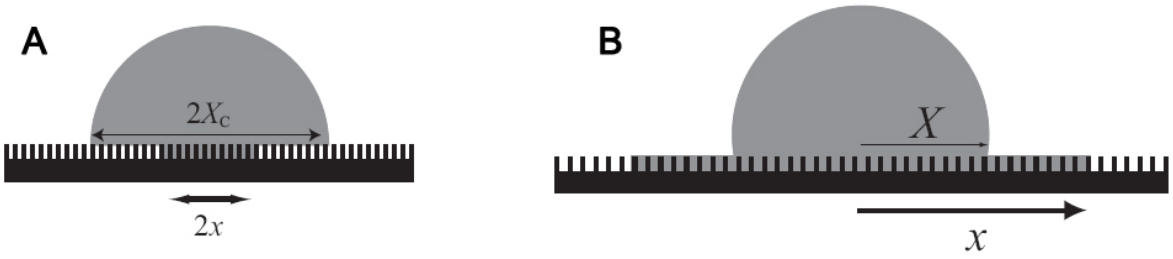

Figure 7.6: *(A) Partial Cassie-Baxter and partial Wenzel wetting state termed 'mush-room state' on a hydrophobic surface (B) partial Wenzel wetting and partial imbibtion 'Sunny-side up' wetting on a hydrophilic surfaces. [76]*

conditions, states with no penetration, partial penetration and complete penetration can exist. States with partial Cassie-Baxter partial Wenzel wetting are given by

$$\cos\theta_{\mathrm{C}} = \frac{1-f}{r_{\mathrm{f}}-f} \tag{7.7}$$

where θ_{C} is the critical contact angle and f is the fraction of solid/liquid interface where the drop penetrates the grooves [76].

While the division between Wenzel and Cassie-Baxter behaviour is theoretically very distinct, in real life situations, mixtures of these two behaviours can exist. Small amounts of structural damage or small surface defects can cause a Cassie-Baxter drop to have a small area with Wenzel wetting. In this case, the drop exhibits mixed behaviour. Further, very strong changes in structures can cause local pinning (local sticking of the receding drop) to the surface, due to edge effects or other local changes. This also can then strongly influence the perceived wetting of the surface. This behaviour is

due to the necessity to fulfill Young's equation at any moment in time, which causes rupture-like jumps of the contact line.

7.2.2 Superhydrophobicity

Due to the presence of air-pockets under the droplet, the small contact area between the liquid and the solid phase and the resulting small contact angle hysteresis, Cassie-Baxter drops easily 'roll' off a surface. This is why Cassie-Baxter surface wetting is often called superhydrophobic wetting. This behaviour has been observed by Barthlott *et al.* [3] on the surface of *Nelumbo nucifera* leaves (commonly called Lotus leaves) and is also termed the 'Lotus effect'.

Superhydrophobicity has been differently defined by many authors. In the following work a surface is termed superhydrophobic if

- water drops exhibit Cassie-Baxter wetting
- the static contact angle is very high $\theta_S > 150°$
- the contact angle hysteresis is low $\Delta\theta \ll 90°$ and the receding contact angle is large $\theta_R > 90$.

Superhydrophobicity has been observed on many different surfaces [77], including highly structured surfaces with micropillars [78], natural surfaces, biomimetic superhydrophobic structures [79, 80], carbon-nanotubes on surfaces [81], alumina nanowires [82], silicon 'nanograss' [83] and fibrous textile surface structures [79].

From a technological perspective, a surface needs to fulfill two characteristics to become superhydrophobic:

1. The surface needs to be made of or coated with a hydrophobic material.
2. The surface needs to be very rough, with roughness values of $r \geq 2$ and have high aspect ratio structures.

Three very good review articles on the many different superhydrophobic surfaces

studied over the last decade have been written by Callies *et al.* [77], Roach [81] and Blossey [84].

7.3 Metastable wetting of surfaces

In 1964, Johnson *et al.* described the possibility of metastable wetting for surfaces with multiple energy landscape minima [85, 86]. Metastable wetting states allow for solutions of the wetting equation on rough surfaces beyond those given in Section 7.2. A metastable Cassie-Baxter wetting state on a hydrophilic substrate is shown schematically in Figure 7.3. In terms of energy landscapes, the different wetting states observed on a surface can be described as global (stable wetting states) or local minima (metastable wetting states) and are separated by an energy barrier. These metastable states only exist on very heterogeneous surfaces. The inherent temporal stability of a metastable wetting state under external forces, strongly influences the likelihood of experimentally observing this state. Further, it means that metastable states with a sufficiently large energy barrier and thus longer life-time could be of technological interest.

The concept of metastable wetting on surfaces has attracted more attention in the recent years. Marmur further explored the concept of local and global energy minima in a theoretical study [70], while Tuteja *et al.* made the first experimental study using two types of surfaces exhibiting metastable wetting [1, 4]. In this study, Tuteja *et al.* also showed the existence of superoleophobic surfaces, which according to classic wetting theory cannot be achieved due to the low surface tension of oils.

Switching from metastable Cassie-Baxter to stable Wenzel wetting has been repeatedly shown [1, 4, 77]. Switching from Wenzel to Cassie-Baxter wetting is significantly more difficult, as this would require the water to be removed from the holes or grooves in the surface. This can only be done by adding energy to the system to overcome the energy barrier between the two wetting states, as shown by Krupenkin *et al.*, who passed electric currents through the substrate to induce a Wenzel to Cassie-Baxter

wetting transition [87].

Metastable wetting states, as all other wetting states, need to locally fulfill Young's equation (Equation 7.1). This means that metastable wetting can only exist on surfaces with two local solutions for Young's equation. Johnson *et al.* showed that for a very high surface roughness r_f this can be achieved for a sinusoidal surface [85, 86]. Tuteja *et al.* worked on surfaces with overhangs, which provided a second contact line solution [1, 4].

In his theoretical work, Marmur explores the possibility of metastable wetting on hydrophilic and hydrophobic surfaces by exploring the Gibbs energy derivative, in order to establish the existence of local minima [70]. This approach has later been used by Tuteja *et al.* to calculate energy landscapes for their surfaces (Section 7.3.3).

7.3.1 Gibbs energy stability criteria on hydrophobic surfaces

This derivation is based on work by Marmur [70]. Marmur derived the Gibbs energy stability criteria for hydrophobic and hydrophilic surface wetting, which allows us to distinguish between stable and metastable wetting states. These stability criteria were used by Tuteja *et al.* in their work calculating energy landscapes (Section 7.3.3).

The Gibbs energy describing wetting of a surface is given by

$$G = \gamma_\mathrm{sv} A_\mathrm{sv} + \gamma_\mathrm{lv} A_\mathrm{lv} + \gamma_\mathrm{sl} A_\mathrm{sl} \tag{7.8}$$

where A_sv, A_lv, and A_sl describe the contact areas between the three phases.

Marmur then expressed the Gibbs free energy in a dimensionless form as a function of the drop radius R, the surface roughness ratio of the wet surface area r_f, the surface contact fraction f (the fraction of the projected area of the solid surface that is wetted by the liquid), the apparent contact angle θ and Young's contact angle θ_Y [70].

$$G^* = F^{2/3}(\theta)\,[2 - 2\cos\theta - \Phi(f)\sin^2\theta] \tag{7.9}$$

where

$$F(\theta) = 2 - 3\cos\theta + \cos^3\theta \tag{7.10}$$

and

$$\Phi(f) = r_f f \cos\theta_Y + f - 1 \tag{7.11}$$

The condition for a local extremum of the Gibbs energy is that the first partial derivatives are zero. This gives

$$\frac{\partial G^*}{\partial f} = -F^{-2/3}(\theta)\sin^2(\theta)\left[\cos(\theta_{\mathrm{Y}}\frac{\mathrm{d}(r_{\mathrm{f}}f)}{\mathrm{d}f}\right] = 0 \tag{7.12}$$

and

$$\frac{\partial G^*}{\partial \theta} = 2F^{-5/3}(\theta)\sin(\theta)(\Phi - \cos(\theta))(1 - \cos(\theta)) = 0 \tag{7.13}$$

In order to have a local minimum, it is further necessary that

$$AC - B^2 > 0 \tag{7.14}$$

where

$$A = \frac{\partial^2 G^*}{\partial f^2} \qquad \wedge \qquad B = \frac{\partial^2 G^*}{\partial f \partial \theta} \qquad \wedge \qquad C = \frac{\partial^2 G^*}{\partial \theta^2} \tag{7.15}$$

Equation 7.13 is fulfilled when

$$\cos(\theta) = \Phi \qquad \text{or} \qquad \theta = \pi \tag{7.16}$$

Equation 7.12 is fulfilled for

$$\frac{\mathrm{d}(r_\mathrm{f} f)}{\mathrm{d}f} = -(\cos(\theta_\mathrm{Y}))^{-1} \qquad \text{or} \qquad \theta = \pi \tag{7.17}$$

Marmur explores the four combinations of these solutions excluding trivial solutions, as well as solutions that can be reduced to the established equations by Cassie-Baxter and Wenzel. He shows that the two solutions containing new information are (a) the first solution in equation 7.17 and (b) $\theta = \pi$ and $f = 0$.

Marmur solves the equations 7.14, 7.16 and 7.17 for $90° < \theta < 180°$ and derives solutions for a hydrophobic surface.

The possible solutions for the Gibbs energy equation show a transition from heterogeneous (Cassie-Baxter) to homogeneous (Wenzel) wetting on hydrophobic surfaces. Marmur showed in this case that the lower contact angle θ_CB or θ_W is always associated with the lowest energetic minimum.

The findings can be reduced to the following statements [70]

- In addition to the equations given in Section 7.2, the sign of the second derivative $\mathrm{d}^2(r_\mathrm{f} f)/\mathrm{d}f^2$ determines whether a local minimum in G^* exists. If the derivative is negative, a local minimum does not exist even if the Cassie-Baxter equation is satisfied. If the derivative is positive and a local minimum exists, a heterogeneous wetting regime exists and it is described by the Cassie-Baxter equation.
- The homogeneous wetting regime exists as a border minimum in G^* and is expressed by the Wenzel equation.

7.3.2 Gibbs energy stability criteria on hydrophilic surfaces

In later work, Marmur solved the Gibbs equation for high contact angle states on low contact angle materials ($0° < \theta_\mathrm{Y} < 90°$) [5]. In order to do this, Marmur adjusts the surface equations to allow for complex rough structures with concave and convex side-wall geometries. This then changes equations 7.9 and 7.11 to the following

$$G^* = F^{-2/3}(\theta)\,[2 - 2\cos\theta - \Omega\sin^2\theta] \tag{7.18}$$

where

$$\Omega = r_f f \cos\theta_Y + f - 1 \tag{7.19}$$

For these equations, Marmur finds solutions that allow for low contact angle materials to exhibit high contact angle Cassie-Baxter wetting states. He follows the same derivation as for hydrophobic materials (Section 7.3.1). He shows the feasibility of Cassie-Baxter wetting states on hydrophilic materials through the analysis of two example surfaces, for which he follows the same analysis as for the hydrophobic materials. Due to the discontinuity in the derivative of the surface topography necessary for metastable Cassie-Baxter wetting states on hydrophilic surfaces, no general solution as given for hydrophobic materials can be found [5].

7.3.3 Gibbs free energy landscapes

Tuteja *et al.* calculated the energy landscape of two differently structured surfaces based on the Gibbs energy stability criteria established by Marmur [70] (Section 7.3.1 and Section 7.3.2). The wetting of a surface is discussed in terms of the filling depth of the structures, such that $0 < h < 1$, where $h = 1$ corresponds to a drop sitting on top of the highest surfaces structures and $h = 0$ corresponds to a completely wetted Wenzel drop.

Tuteja shows that

$$G^* = \frac{\gamma_{lv}\pi R^2}{4\pi R_0^2}[-2 - 2\cos\theta_t^* - \sin^2\theta_t^*(R_\phi\phi_s\cos\theta_t^* + \phi_s - 1)] \tag{7.20}$$

where γ_{lv} is the liquid vapour surface tension, R is the radius of the drop in contact with the surface, R_0 is the original radius of the drop (at $h = 1$), R_ϕ is the ratio of the

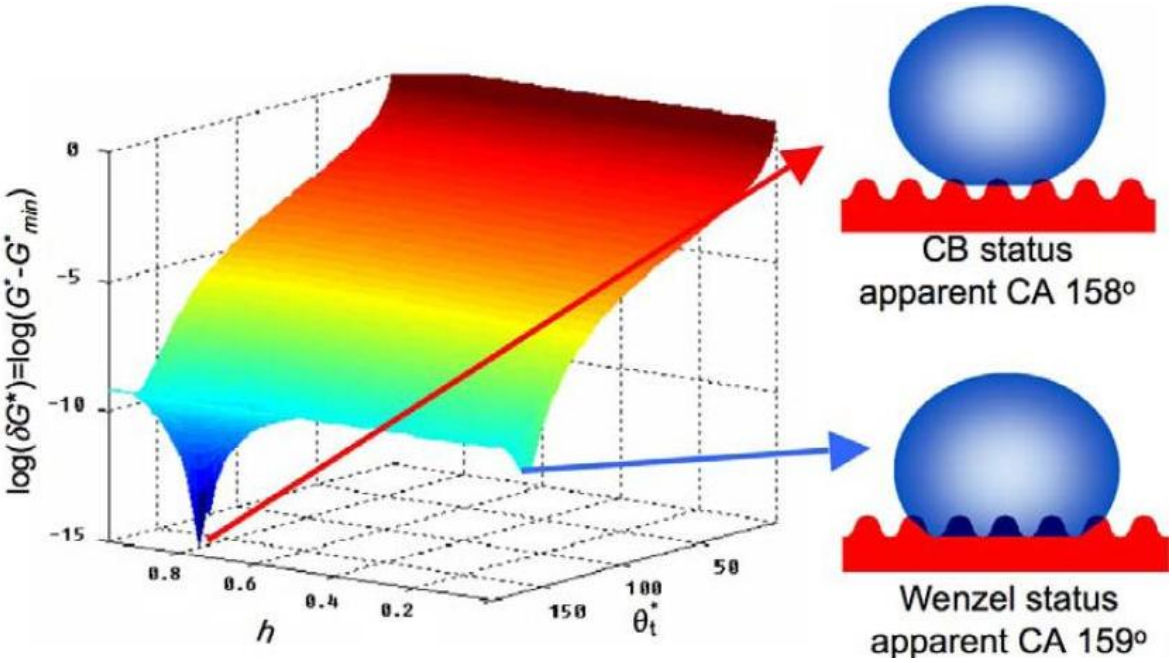

Figure 7.7: *Energy landscape of a highly structured hydrophobic surface designed by Tuteja et al. [4].*

total wet area to the projected wet area and ϕ_s is the ratio of the projected wet area to the total projected area. θ_t^* is the temporary contact angle and θ^* will be the final apparent contact angle once the Gibbs free energy density is minimised.

The first surface is a hydrophobic surface with roughness features. According to the distinction between Cassie-Baxter and Wenzel wetting surfaces established by Ishido *et al.*, the surface should exhibit Cassie-Baxter wetting. As can be seen in Figure 7.7, the energy landscape of this surface has two minima: A global Cassie-Baxter minimum, and a local Wenzel minimum. Therefore, while it will generally adapt a Cassie-Baxter wetting state, metastable Wenzel wetting states can also be observed on this surface.

The energy landscape of a highly structured hydrophilic surface is shown in Figure 7.8. As can be seen, it has two distinct minima corresponding to a Wenzel and a Cassie-Baxter wetting state. They are achieved for different 'filling heights' of the water in the structure. Both fulfill Young's contact angle equation locally.

The surface of the theoretical structure in the energy landscape (Figure 7.8) is made purely of hydrophilic materials (inherent $\theta_{\mathrm{Y}} = 60°$), so according to classical wetting

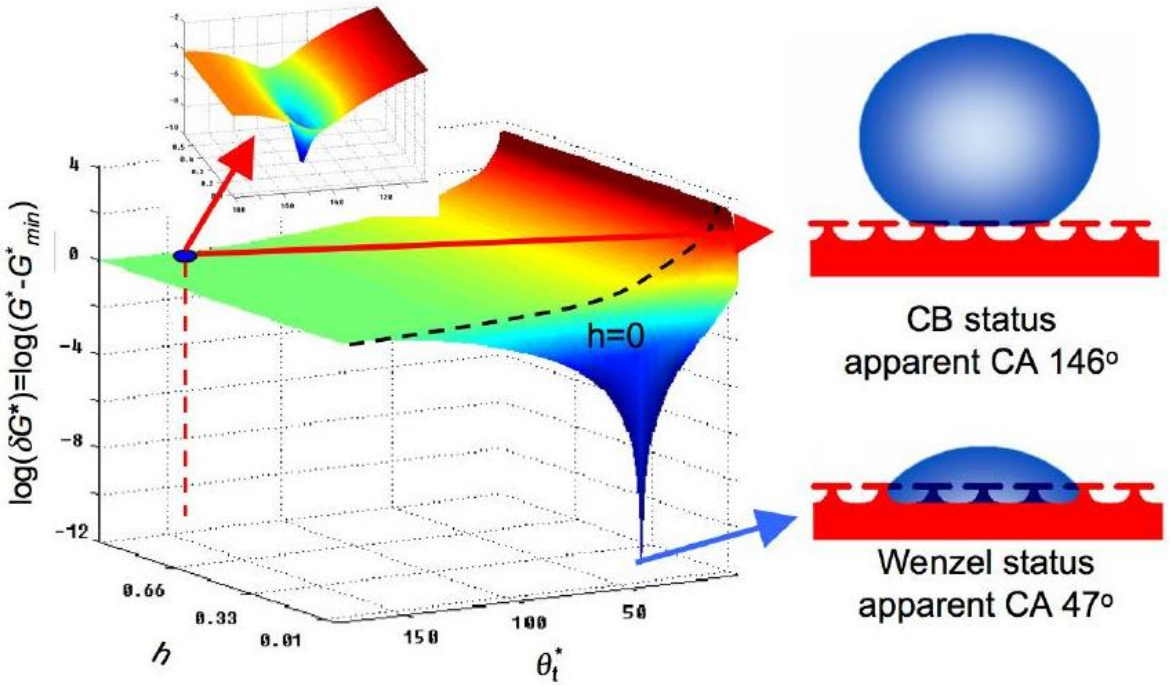

Figure 7.8: *Energy landscape of a highly structured hydrophilic surface designed by Tuteja et al. [4].*

theory as described in Sections 7.1 and 7.2, no Cassie-Baxter wetting state should exist. However, due to pinning overhang structures, a local minimum corresponding to the Cassie-Baxter wetting state is observed. While the Wenzel minimum is clearly the global minimum, the local minimum indicates that a Cassie-Baxter state can be achieved.

Due to the relatively low energy barrier between the Cassie-Baxter and Wenzel minimum in the energy landscape, it is obvious that the Cassie-Baxter wetting state will only be metastable on this surface. Switching to a Wenzel wetting state will occur as soon as enough energy is introduced to overcome the energy barrier. For many metastable wetting states, the thermal energy $E_\mathrm{T} = k_\mathrm{B}T$ is enough to reach the stable wetting state.

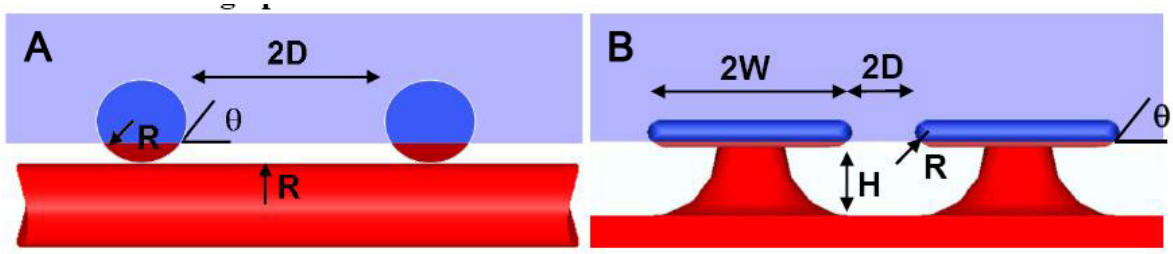

Figure 7.9: *Reentrant structures as discussed by Tuteja et al. [4]: (A) hydrophilic fibres and (B) hydrophilic micro hoodoo structures. Both schematics show a possible metastable Cassie-Baxter wetting contact line fulfilling* $\theta_Y = 60°$.

7.3.4 Design criteria for structured surfaces

As shown by Marmur [70] and others [4], highly structured surfaces can exhibit stable and metastable wetting states. Hydrophilic surfaces cannot have an energetically stable hydrophobic wetting state, but a metastable hydrophobic Cassie-Baxter wetting state can exist. Similarly, surfaces with stable superoleophobic wetting states do not exist due to the low surface tension of oils, but surfaces with metastable superoleophobic wetting states can be designed through careful structuring of the surface topography, following specific surface design criteria.

High aspect ratio and roughness have been found to be of great importance in the design of superhydrophobic surfaces from hydrophobic materials [88]. However, these are not sufficient to allow for a secondary local minimum in the Gibb's energy landscape necessary for superoleophobic surfaces or hydrophilic surfaces with Cassie-Baxter states (Section 7.3.3). Young's contact angle equation must be fulfilled locally, so the structures need to have overhangs (termed by Tuteja *et al.* 'reentrant structures'). Reentrant structures allow for multiple possibilities for a liquid/solid/gas interface to fulfill Young's equation. Examples of two reentrant structures as discussed by Tuteja *et al.* are shown in Figure 7.9.

Both the structures shown in Figure 7.9 have an intrinsic contact angle of $\theta_Y = 60°$. It can be seen, that the local contact angle is the same for both structures. The solution shown is the metastable solution for both structures. The stable, Wenzel wetting state corresponds to complete filling of the structures and is not shown.

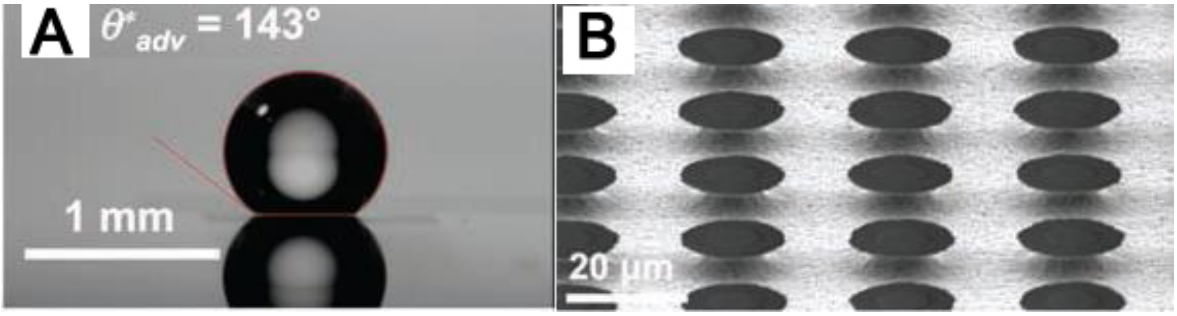

Figure 7.10: *(A) Droplet of octane on micro hoodoo structure; (B) Micro hoodoos with reentrant curvature. [4]*

For these structures, significant stretching or bending of the meniscus is necessary to change from the metastable state to the complete wetting state. This corresponds to the energy barrier shown in Figure 7.7 and 7.8. Therefore, external energy must be input to surpass this energy barrier.

For some metastable wetting states, thermal energy $E_{\mathrm{T}} = k_{\mathrm{B}}T$ is enough to reach the stable wetting state. For these states, their life-time is very short and they cannot be experimentally observed. For higher energy barriers, the life-time of the state increases. The energy barrier can be surmounted with time by thermal fluctuations or through externally applied energy (pressure or other stimuli).

Some structures designed by Tuteja *et al.* had superoleophobic properties resulting from the overhanging geometry. An example of these structures and the contact angle with octane can be seen in Figure 7.10.

Tuteja *et al.* also investigated the design criteria for overhanging surface structures [1]. They introduced 'robustness parameters' for the microhoodoo metastable wetting state stability analysis as a function of the microhoodoo geometry: the spacing (D), height (H), radius (R), and width (W).

The robustness height H^* is given by

$$H^* = \frac{2Rl_{\mathrm{cap}}}{D^2(1+\sqrt{D*})}\left[(1-\cos(\theta)) + \frac{H}{R}\right] \tag{7.21}$$

The robustness angle T^* is given by

$$T^* = \frac{l_{\text{cap}}}{D}\left[\frac{\sin(\theta - \Psi_{\min})}{1+\sqrt{D*}}\right] \tag{7.22}$$

The feature spacing ration D^* is given by

$$D^* = \left[\frac{W+D}{D}\right]^2 \tag{7.23}$$

The robustness factor A^* combines the robustness height H^* and the robustness angle T^*

$$\frac{1}{A^*} \approx \frac{1}{H^*} + \frac{1}{T^*} \tag{7.24}$$

The general design criteria introduced by Tuteja *et al.* [1] can be summarised as follows:

- High values of A^* indicate a high robustness of the metastable Cassie-Baxter wetting state
- High values of D^* result in high apparent contact angles θ.

7.4 Natural surface wetting

Wetting of natural surfaces has been at the center of scientific interest since 1997, when Barthlott *et al.* described superhydrophobicity on plant leaves and termed the phenomenon 'the Lotus effect' [3](Figure 7.11). The effect exists for many natural surfaces besides the sacred lotus leaf (*Nelumbo nucifera*) including [89, 90]:

- Red Clover (*Trifolium pratense*)
- Lady's Mantle (*Alchemilla*)
- Nasturtium (*Tropaeolum*)
- Wild Mustard (*Brassica oleracea*)

(a) Drop on a lotus leaf (b) Close up of a drop on a lotus leaf

Figure 7.11: *Wetting on a lotus leaf: The silvery film under the water droplet indicating the Cassie-Baxter air-film can easily be identified.*

- European smoketree (*Cotinus coggygria*)

The question of whether the Lotus leaf is truly hydrophobic has recently been under debate. Cheng *et al.* showed that the leaf is not superhydrophobic if water vapour instead of water droplets are used to create the liquid film on the leaf [91]. Large drops on the leaf normally roll off and exhibit perfect superhydrophobic behaviour, whereas small drops (as those created by vapour) show Wenzel wetting and stick to the surface.

The epicuticular waxes on the Lotus leaf (as on other plants) have contact angles very close to 90°, as reported by Holloway *et al.* [92]. Some work has even shown that the wax has a hydrophilic contact angle of $\theta_{\text{wax}} = 74 \pm 8°$ [91]. It is unclear whether the Lotus leaf is truly an example of classic Cassie-Baxter superhydrophobicity or an example of a long-lived metastable superhydrophobic state using hydrophilic materials, as those explained in Section 7.3.3.

No reports of superhydrophobic aquatic plants could be found and some superhydrophobic plant surfaces can be wetted by full immersion of the surface into water. In 2000, Herminghaus noted that the superhydrophobic Cassie-Baxter air-film observed at

the surface of *Cotinus coggygria* disappears upon immersion of the leaf to 20 cm below the water line [90]. Further the superhydrophobicity of the plant surface in contact with water droplets stayed intact even when the plant was dried, showing that the change in underwater wetting was not due to the death of the leaf. This was one of the earliest reports in the literature of history-dependent underwater wetting of superhydrophobic surface. This phenomenon will be explored further in Chapter 12.

7.5 Underwater wetting

Interest in superhydrophobic coatings for underwater applications has increased over recent years. Potential applications include buoyancy effects (like water spiders [93] or boats [7]), drag reduction of materials in water [9], anti-fouling coatings [8] and coating the inside of pipes (superoleophobic) [94].

Stability issues of the air-film plastron on superhydrophobic surfaces have been mentioned by Herminghaus [90], but also by Koch *et al.* [93]. Herminghaus notes that *Cotinus coggygria* leaves wet at 20 cm depth in water. Koch discusses a study by Cerman (submitted) [95], which shows air-film stability for a biomimetic sample submersed underwater for up to 4 days, and for the *Salvinia* leaf submersed underwater for up to 17 days.

In order to judge whether and how any of these effects can be exploited technologically, it is vital to understand more about Cassie-Baxter air-pocket films on submerged superhydrophobic surfaces. The following questions are important

- Does the air-film survive movement of the water, as expected for a moving ship?
- For how long is the air-film stable? Does it repair itself?
- Does depth matter? Is the decay of the air-film pressure dependent?

In order to be of technological interest, an air-film would need to be stable for sufficiently long times. According to Marmur [6] this is theoretically possible (Section

7.5.1). Further, it needs to resist movement of the water, as well as the hydrostatic pressure due to submersion.

A systematic study of the stability of the air-film plastron of superhydrophobc surfaces underwater has, to our knowledge, not yet been done. Our experiments and results on this are presented in Section 12.5.2. We have found that our work can be explained by combining different established theories of meniscus stability arguments and air bubble dissolution underwater. The necessary framework theories will be presented in Section 7.5.2 and 7.5.3. Here, we will focus on some basic wetting concepts.

The Laplace pressure p_{L} describes the pressure difference between the inside and the outside of a droplet or a bubble [69] and is given by

$$p_{\mathrm{L}} \equiv p_{\mathrm{in}} - p_{\mathrm{out}} = \frac{2\gamma}{a} \tag{7.25}$$

where a is the radius of the bubble or droplet and γ refers to the surface tension. This implies that the Laplace pressure is greater for smaller drops or bubbles than for larger ones and is considered one of the driving forces behind the thermodynamic instability of small bubbles or droplets in a surrounding phase.

For a general surface, the Laplace pressure is given by the Young-Laplace equation

$$p_{\mathrm{L}} = \gamma \left(\frac{1}{A} + \frac{1}{A'} \right) = \gamma C \tag{7.26}$$

where A and A' are the radii of curvature of the surface and C is the curvature of the surface [69]. For 'ideal' drops, drops that do not experience gravitational effects, the Laplace pressure drives the liquid to adopt a spherical shape, even when in contact with a surface (Figure 7.1).

The solubility of air in water is given by Henry's law:

$$c = k_{\mathrm{H}} p_{\mathrm{g}} \tag{7.27}$$

where c is the solubility of the gas in the liquid, k_{H} is the proportionality constant for a given gas liquid system and p_{g} is the partial gas pressure.

7.5.1 Stability of underwater superhydrophobicity

In 2006, Marmur explored the possibility of stable underwater Cassie-Baxter air-films on superhydrophobic surfaces [6]. Marmur uses the same approach as for the stability of Cassie-Baxter wetting of water drops on superhydrophobic surfaces (Section 7.3.1). The analysis is valid for air-bubbles significantly larger than the roughness length-scale. Marmur further assumes that the curvature of the air-bubbles is given by the Laplace pressure and hydrostatic pressure as

$$R = \frac{2\gamma}{hg\rho} \tag{7.28}$$

Using the Gibbs energy (Equation. 7.8), Marmur finds the same criteria for stable or metastable Cassie-Baxter wetting states as found for water drops on superhydrophobic surfaces:

$$\frac{\mathrm{d}\phi}{\mathrm{d}f} = -(\cos\theta_{\mathrm{Y}})^{-1} \tag{7.29}$$

where $\phi = r_{\mathrm{f}} f$ and

$$\frac{\mathrm{d}^2 G^*}{\mathrm{d}f^2} = -\frac{\mathrm{d}^2\phi}{\mathrm{d}f^2}\cos\theta_{\mathrm{Y}} > 0 \tag{7.30}$$

In general, the state with the lower energy should be the stable wetting state. The stability of the wetting states on the surface is determined by the Gibbs energy difference between the Wenzel and Cassie-Baxter wetting states

$$\Delta G^* = 1 - f_0(1 + \cos\theta_{\mathrm{Y}}) + r\cos\theta_{\mathrm{Y}} \tag{7.31}$$

where f_0 is the roughness at the top of the asperities.

Marmur further points out that this condition is more difficult to fulfill underwater due to the additional conditions imposed by the Laplace curvature equation (eqn. 7.28) and the length scale. However, Marmur explains that for some surfaces thermodynamically stable Cassie-Baxter wetting states should exist. If the roughness is greater than the minimum roughness defined by the stability criterium for the Gibbs energy difference (Equation 7.31):

$$r > -\frac{1}{\cos_Y} + f_0 \left(1 + \frac{1}{\cos_Y}\right) = r_{\min} \tag{7.32}$$

Therefore, according to Marmur thermodynamically stable Cassie-Baxter wetting states should exist underwater for extremely rough surfaces [6].

7.5.2 Air-bubble life-time underwater

Theoretical work by Epstein *et al.* [96] and Ljunggren *et al.* [97] predicts values for the life-time of spherical air bubbles underwater, that are not in contact with a surface. Work by Eriksson *et al.* [98] showed that air bubbles on superhydrophobic surfaces underwater are only metastable. No life-time calculation for air bubbles on superhydrophobic surfaces has been done, however.

The following derivation for the behaviour of air bubbles underwater is based on Epstein-Plesset [96] and Ljunggren *et al.* [97]. Many steps are missed out in particular when solving the partial differential equation. For a full derivation, please refer to the original works.

Ljunggren *et al.* looked at a gas bubble underwater, that was not in contact with any surface (Figure 7.12). The total pressure on the bubble p, the surface tension of the bubble γ, the radius as a function of time $a(t)$, the atmospheric pressure p_0 and the spherical coordinate r are shown. The following can be used to describe the bubble behaviour in this case:

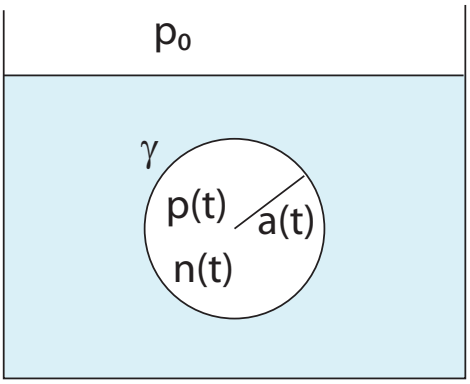

Figure 7.12: *Scheme illustrating the approach used by Ljunggren et al. to derive the life-time of a bubble in water. Adapted from [97]*

$$p(t) = p_0 + p_\mathrm{L} = p_0 + \frac{2\gamma}{a(t)} \tag{7.33}$$

The ideal gas law for a spherical bubble states

$$\frac{4\pi}{3} a^3(t) p(t) = n(t) RT \tag{7.34}$$

Therefore, we get

$$a(t) = \frac{2\gamma}{p(t) - p_0} \tag{7.35}$$

For small bubbles with $a(t) \ll 2\gamma/p_0$, Ljunggren *et al.* derive

$$a^2(t) = 3n(t)RT/(8\pi\gamma) \tag{7.36}$$

Therefore, $a(t) \propto \sqrt{n(t)}$ which leads to a differential equation with diffusive flow and convective flow terms. As the convective flow term is negligible in comparison with the diffusive term, because the gas concentration in the liquid is much lower than the gas concentration in the gas bubble, we get an equation of the form

$$\frac{\partial y}{\partial t} = D\frac{\partial^2 y}{\partial x^2} \tag{7.37}$$

where $x = r - a(t)$, $y(x,t) = rc(r,t)$, where $c(r,t)$ denotes the change of the concentration of the dissolved gas.

Solving these equations with appropriate boundary conditions, Ljunggren *et al.* find that $c(r,t)$ changes over time. If Henry's law (equation 7.27) is assumed to hold at the gas-liquid interface, it can be used to find an expression for $c(x,t)$.

Ljunggren *et al.* use this to derive an expression for the life-time of a small bubble

$$t_1 = \frac{Ka^2(0)}{3RTD} \tag{7.38}$$

This equation holds for bubbles up to $a(0) = 100\,\text{nm}$.

For larger bubbles, Ljunggren *et al.* refer back to the Epstein and Plesset equation and show its equivalence to their methodology. They rewrite the original equation as:

$$t_1 = \frac{Ka^3(0)p_0}{6RTD\gamma} \tag{7.39}$$

Therefore, for small bubbles (equation 7.38) the life-time is independent of the surface tension γ and the external pressure p_0, while for large bubbles (equation 7.39), both of these factors influence the bubble life-time.

In their example calculation, Ljunggren *et al.* used the following constants: $K(N_2) = 1.56\times10^5\,\text{J/mole}$, $D_{\text{H2O}} = 2\times19^{-9}\ \text{m}^1/\text{s}$, $\gamma = 72\times10^{-3}\,\text{N/m}$ and $p_0 = 1.013\times10^5\,\text{N/m}^2$.

For small bubbles, the associated life-time is $t_1 < 1$ µs, while for large bubbles, the life-time varies as a function of the original bubble size $a(0)$, the pressure p_0. A life-time of $t_1 = 85$ days for a bubble with an original size of 1 mm of air in water at ambient pressures is calculated [97].

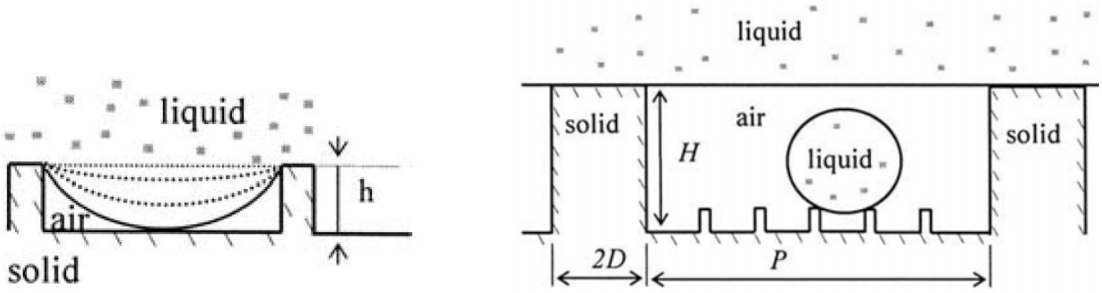

(a) *Capillary wave in a meniscus* (b) *Condensation under the meniscus*

Figure 7.13: *Instability development in the meniscus of a Cassie-Baxter water drop on a superhydrophobic surface [99].*

7.5.3 Meniscus stability underwater

The meniscus is the interface between two materials (fluid-fluid or fluid-gas) of different density. The behaviour of the meniscus is important for the stability of an air-film underwater. Instability and breakdown of the meniscus underwater can be due to two factors:

- Dissolution of the air-film in water by diffusion
- External forces acting on the meniscus

Diffusion of the gas in the air-film into the surrounding liquid, as described by Ljunggren *et al.* [97] for an air-bubble in water, can cause a reduction of the meniscus height. This reduction in height reduces the meniscus stability.

Nosonovsky *et al.* discuss the influence of external forces on the meniscus stability of Cassie-Baxter water drops on superhydrophobic surfaces [99], including an increasing amplitude of a liquid-air interface capillary wave, the influence of the weight of the droplet, as well as condensation of small droplets within the Cassie-Baxter air-film. All of these factors can decrease the stability of a Cassie-Baxter wetting state of a drop on a surface. In particular if secondary roughness exists on a smaller scale, below the meniscus interface, Nosonovsky *et al.* predict a reduction of the meniscus stability under external forces, as shown for a liquid-air interface capillary wave in Figure 7.13.

The meniscus of a Cassie-Baxter air-film on a submerged superhydrophobic surface should be influenced by the same perturbation forces. In particular, an increase in the amplitude of the liquid-air interface capillary wave should lead to a reduction of meniscus stability. Also, an increase in the interfacial pressure (in this case due to the hydrostatic pressure not weight) should reduce the stability of the Cassie-Baxter air-film meniscus underwater.

The total pressure acting on a surface-attached air-bubble underwater is depth dependent, due to the hydrostatic pressure component p_{hydro} [100].

$$p(h) = p_0 + p_{\text{L}} + p_{\text{hydro}} = p_0 + \frac{2\gamma}{a(t)} + \rho_{\text{hydro}} g h \tag{7.40}$$

where ρ_{hydro} is the density of water, g the gravitational constant and h is the immersion depth.

The meniscus needs to fulfill both the Laplace curvature (Equation 7.25) and the Young contact angle (Equation 7.1). Therefore, an undesired shift in the meniscus due to the external forces described by Nosonovsky *et al.* [99] or an reduction of the meniscus height due to diffusion could be sufficient to destabilise the Cassie-Baxter air-film and cause pinning to underlying structures.

8 Exploring wetting - sample preparation

This chapter describes the sample preparation for all surface wetting experiments.

Samples for surface wetting experiments were prepared using a number of different surface structuring procedures. Two approaches were taken to create surfaces with complex surface structures and high roughness:

1. Surfaces with regular ordered structures
2. Surfaces with non-ordered high surface roughness

The first type of surface was used to investigate metastable wetting states of droplets on the surfaces, so that the wetting states could be analysed as a function of the surface features. The second type was used for underwater experiments, since the roughness and hydrophobicity of these surfaces, was significantly greater than seen for the surfaces with ordered structures.

For regularly ordered structured surfaces, samples were produced using classic microfabrication techniques, either on their own or combined with colloidal self-assembly to obtain smaller structures. The technical information on the individual microfabrication techniques available was taken from Madou [101] and used to design a protocol. The steps involved in the fabrication of structured surfaces are described in the fabrication protocol (Section 8.1).

For the underwater wetting experiments, the samples were produced differently. The priority for these experiments is high roughness and strong superhydrophobicity of the materials (Section 8.2). The majority of surfaces produced for underwater wetting

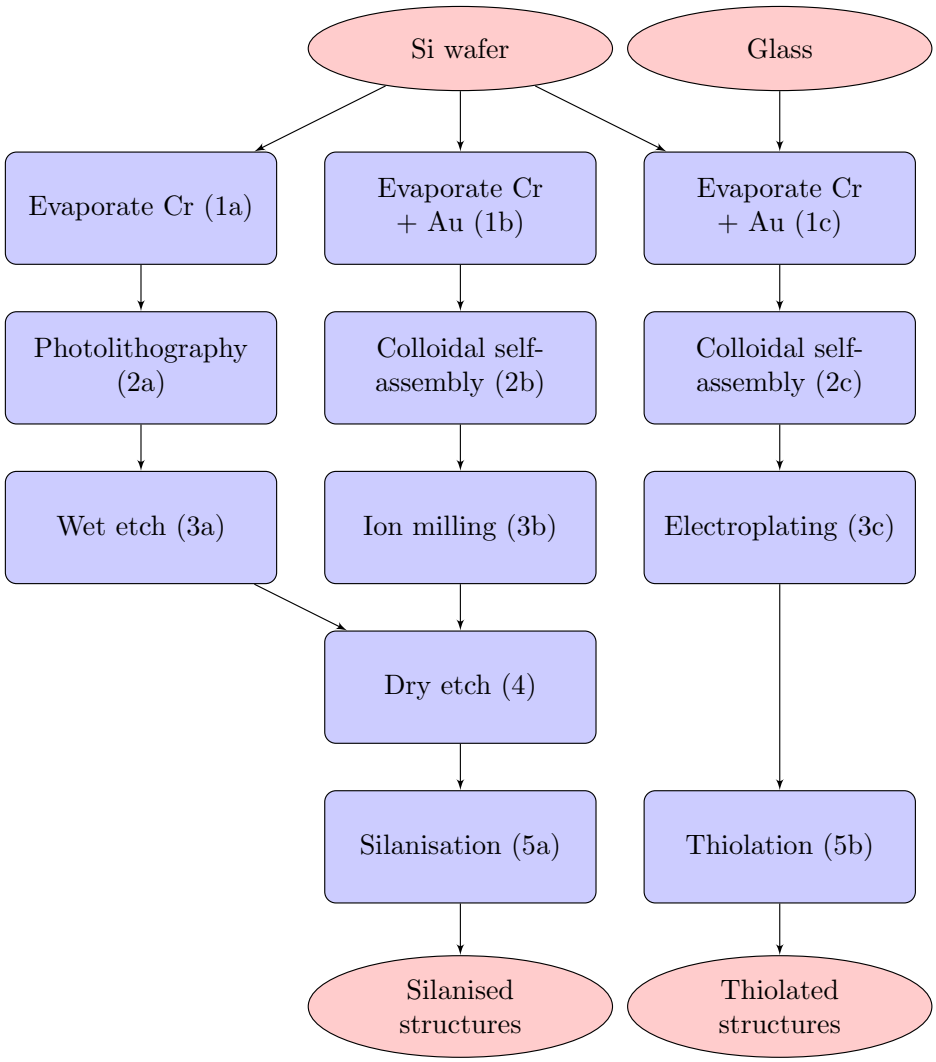

Figure 8.1: *Sample preparation procedure for all regularly ordered feature arrays involving microfabrication techniques.*

experiments were made from super rough-Teflon [102] (Section 8.2.1). For comparison, additional underwater experiments were conducted on alternative superhydrophobic materials.

Experiments were also carried out to look at the underwater and surface wetting of natural samples. *Antirrhinum* flower petals were used for surface wetting experiments and *Nelumbo nucifera* leaves for the underwater wetting (Section 8.3).

8.1 Regularly structured surfaces

Figure 8.1 shows the steps involved in the sample preparation of highly regular structured silicon and metal features on surfaces. The roughness required to observe interesting wetting effects has been achieved for these samples through structured surface features. All three types of samples (shown in Figure 8.1 by the three different paths in the flow chart) were made using a similar approach: First, the surfaces were structured for high roughness and/or overhanging features and second, the surface chemistry was modified. Figure 8.1 shows first the structure creation process: These are discussed in the following sections: Evaporation of metal (Step 1a, 1b, 1c) - Section 8.1, photolithography (2a) - Section 8.1.3, colloidal self-assembly (2b, 2c) - Section 8.1.4, wet etching (3a) - Section 8.1.5, ion milling (3b) - Section 8.1.6, electroplating (3c) - Section 8.1.7, dry etching (4) - Section 8.1.8 and the chemical surface modification (5a, 5b) - Section 8.1.9.

All samples were produced to study metastable wetting: The surface structures were arranged in a regular pattern microarray (cubic or hexagonal). A large area of was covered with the structure to allow for contact angle measurements ($A_{\mathrm{min}} > 0.3\,\mathrm{mm} \times 0.3\,\mathrm{mm}$). The structures on the surface ranged from 0.6-100 µm in separation and from 0.6-20 µm in height.

The different fabrication procedures in Figure 8.1 were chosen to complement each other by covering different structure sizes. The trial of different methods were carried out in parallel reducing the possibility of encountering a dead-end in the production process. This was necessary for timely sample fabrication.

For the samples prepared by classic photolithography, a photolithographic mask was designed, such that the effect of changing specific parameters on the wetting behaviour could be explored. The parameters for microfabricated structures (similar to those discussed in Section 7.3.4) are discussed in Section 8.1.1. For structures based on colloidal self-assembly, the design criteria are discussed in more detail in Section 8.1.4.

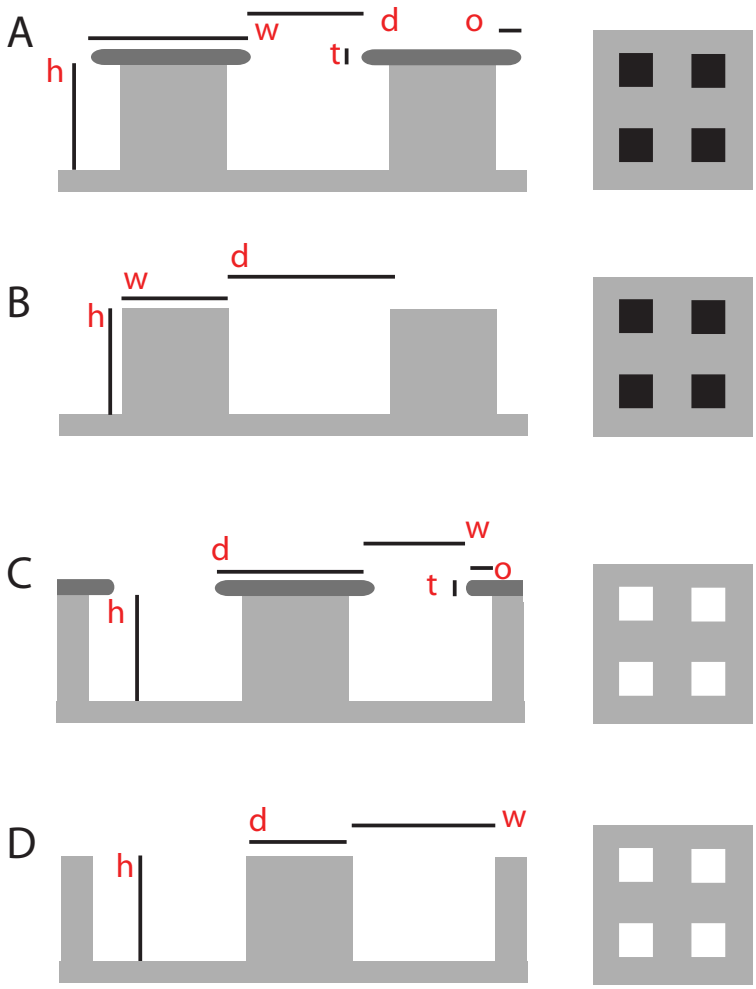

Figure 8.2: *Four structures prepared by photolithography for the wetting experiments: (A) Hoodoos, (B) Pillars, (C) Traps and (D) Holes, shown schematically from the side and above. Black features are chromium, light grey features are silicon. In the top view, black areas are elevated features (pillars and hoodoos), white areas are negative features (holes and traps).*

8.1.1 Microfabrication mask design

Four types of features were created as arrays in order to establish the dependence of structural parameters on wetting behaviour. These structures will be referred to as hoodoos (A), pillars (B), traps (C), or holes (D). Pillars and holes correspond to structures with no overhangs. Microhoodoos and microtraps exhibit overhanging features. The four types of structures are schematically depicted in Figure 8.2.

These four structures are characterised using the following parameters: *Type* (squares, circles), the height of the feature h, the width of the structure w, the next neighbourgh

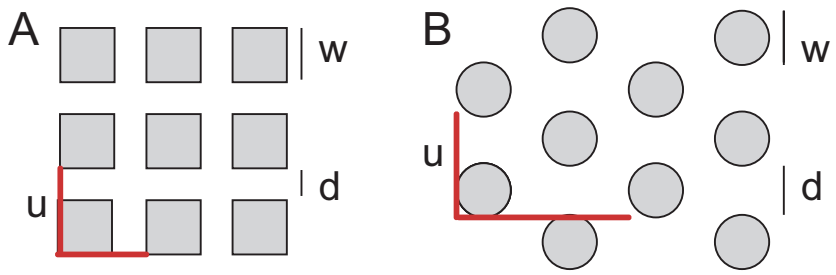

Figure 8.3: *(A) Cubic and (B) hexagonal unit cells (u) for mask design showing the feature width (w) and separation (d).*

distance d, the aspect ratio A, where $A = h/w$, the packing arrangement (hexagonal or cubic) P, the top surface fraction f, as well as the chromium layer thickness t and overhang width o.

The mask was designed in AutoCAD. All features were designed to fill 1 cm^2 area. In order to exploit inexpensive mask design technology (JD Photo Tools), the mask features and feature separation distances were all greater than 8 µm. Due to printing difficulties, from interference of the repeating structures, some mask areas were nonetheless unusable. The original mask patterns were hexagonally arranged circles or cubically arranged squares. The unit cell was varied between 30 µm $< u <$ 100 µm for the major axis. The feature width of the masking patterns were 8 µm $< w <$ 50 µm.

8.1.2 Metal film deposition

For all silicon-metal based samples, silicon wafers with a 6 inch (Si-Mat Silicon Materials) or 4 inch diameter (Compart Technology Ltd) were cut in half. As their electrical properties were of no relevance to this work, low quality wafers were used. For electroplating, both silicon and glass substrates were used. Chromium was used as a masking material for dry etching (Section 8.1.8) or as a thin adhesive layer for gold. Gold was used to help the self-assembly of colloids and thiols, and to create a conducting surface for electroplating (Section 8.1.7).

All metal films were deposited by evaporation (BOC Edwards 306 evaporator) (Figure 8.1 1a, 1b, 1c). The materials and metal film thicknesses used for the different

patterning techniques are given in table 8.1

Step	Metal	Thickness (nm)
Step 1a	Chromium	150-350
Step 1b	Chromium	50-350
Step 1b	Gold	0-50
Step 1c	Chromium	5-10
Step 1c	Gold	50-150

Table 8.1: *Metal film thicknesses produced by evaporation (Microfabrication steps 1a,b,c)*

The rate of evaporation for the first 10 nm of any layer was kept below 0.05 nm/sec in order to achieve good binding and smooth layers. For the rest of the deposition, the evaporation speed was increased up to a maximum of 0.3 nm/sec. The evaporation of thick layers of chromium causes significant heating of the evaporator; film thicknesses above 150 nm of chromium were therefore evaporated in two steps. Further, in order to avoid strong thermal stresses in the samples and the equipment, the system was left to cool for at least 30 min after the evaporation of thick layers of chromium.

8.1.3 Photolithography

The transfer of the mask patterns (Section 8.1.1) was achieved via photolithography (Figure 8.1 2a). The wafers were cut into approximately 2 cm^2 squares using a diamond scribe. They were cleaned with a N_2 gun in order to remove small splitters and immersed in an ultrasonic solvent bath (5 min in acetone and 5 min in isopropanol). The samples were dried using N_2.

AZ 5124 (MicroChemicals) was used as a convenient photoresist for this procedure. AZ 5124 can be used for positive and negative replication of the mask pattern. This was desired so that both traps and microhoodoos could be created from the same mask features.

The protocol for negative and positive replication differed in its details, but involved the same general steps: spin coating of the photoresist (AZ 5214), baking at different temperatures, exposure of the photoresist using a Mask aligner (Karl Suss Mask

Step	Pillars and hoodoos	Holes and Traps
Spinning Speed	6000 rpm	8000 rpm
Spinning Time	30 s	30 s
Spinning Film Thickness	1.4 µm	1 µm
Pre-Baking Temperature	95°C	95°C
Pre-Baking Time	60 s	60 s
Exposure Time	11 s	8 s
Baking Temperature	-	125-135°C
Baking Time	-	60 s
Flood Exposure Time	-	60 s
Developing Time	15-20 s	20-45 s
Hard Baking Temperature	95°C	95°C
Hard Baking Time	180 s	180 s

Table 8.2: *Processing steps for negative and positive replication of the mask pattern via photolithography*

Aligner, MJB3) and development of the pattern using a 1:4 mixture of AZ developer (AZ Electronic Materials) and deionised water. The exact parameters used for each of these individual steps for positive and negative pattern replicas are given in Table 8.2.

While the protocol for negative replication of the masking pattern was easily perfected and adjusted, the protocol for the positive replication of the masking pattern showed significant difficulties. This is due to the double development procedure and is a known problem for reversible photoresists. Very good edge definition for negative features (pillars and hoodoos) was achieved; edge definition for positive features (holes and traps) remained poor in comparison.

8.1.4 Colloidal self-assembly

Other patterning techniques were used to obtain large patterned surface areas with reproducible pattern size and separation. One of these methods was self-assembly of colloidal layers (Figure 8.1 2b, 2c). Patterning of surfaces using colloidal layers was inspired by work done Scherer *et al.* [103] and Abdelsalam *et al.* [104].

The colloids were assembled into hexagonal 2D crystals, such that hexagonal symmetry was obtained. The features produced via colloidal self-assembly were significantly

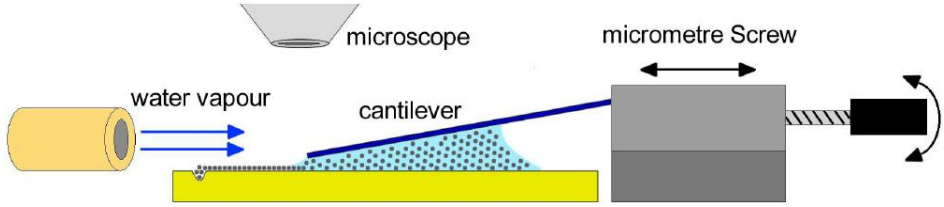

Figure 8.4: *Setup used for monolayer assembly via colloidal suspension pulling [103].*

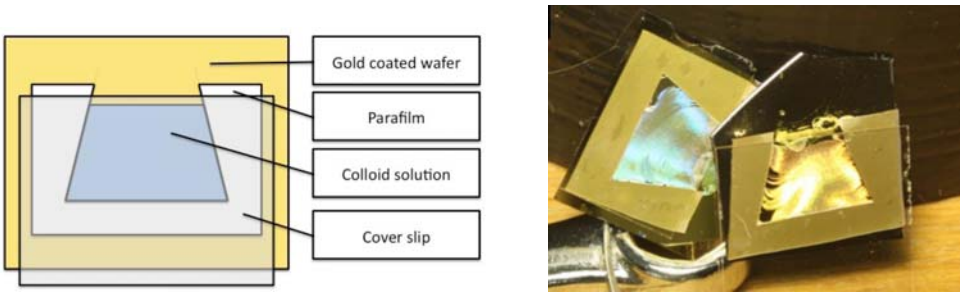

(a) (b)

Figure 8.5: *(a)Schematic of colloidal self-assembly cell viewed from above. The parafilm acts as a spacer between the gold coated wafer and the cover slip (b) Photograph of dry colloidal self-assembled film before removal of the cover glass. The two cells are tilted at different angles to show the angular dependence of the colloidal crystal colour appearance [105]*

smaller than those achieved by photolithography. Scherer *et al.* found that colloids around 2-5 µm allow for the easiest assembly of the colloidal monolayer. For ion milling the monolayers were used as a masking material ($d_{\text{ion}} = 3$ µm in diameter). Therefore, the features obtained always fulfilled $d + w = 2 - 5$ µm.

For ion-milling patterning the following procedure was used (Figure 8.1 2b): Silicon substrates were coated with chromium and gold. Aqueous colloidal solutions containing 3 µm PS microspheres (Duke Scientific) were centrifuged to obtain higher concentrations of microspheres. Colloidal films were produced by a self-assembly mechanism based on capillary forces in liquid solutions (Figure 8.4). The monolayers were grown by pulling a suspension containing the colloids over the Cr and Au coated Si substrate. The growth of the monolayer was controlled by a micrometre screw and humidity control. Observing the growing monolayer under the microscope allowed for low defect density and very regular colloidal monolayers to be produced. For further details, please refer to Scherer [103].

For inverse colloidal patterning via electroplating, colloidal monolayers were prepared using the method from Abdelsalam *et al.* [104](Figure 8.1 2c). Silicon wafers or glass substrates coated with chromium and gold layers were immersed into thiol solutions for 7 days immediately after evaporation of the metals (Section 8.1.9). A thin cover-slip (Agar Scientific, N. 2) was then glued onto the substrate using parafilm with a trapezoid shaped hole, by heating the sandwich to 100°C for 30 s. The colloidal solution (Duke Scientific) was injected into the trapezoid shaped cavity and the samples were left to evaporate at $T_{\text{evap}} = 15.0 \pm 0.1$°C at an angle of 10° from the horizontal. After evaporation of the liquid, the glass slide and parafilm was removed by heating to 100° for 30 s. For further detail, please refer to Holtzmann [105]. The samples were then used for electroplating (Section 8.1.7).

8.1.5 Wet etching

After the photolithographic process described in Section 8.1.3, the pattern was transferred from the photoresist to the chromium layer (Figure 8.1 3a). This was necessary, as the dry etching process described in Section 8.1.8 required a very selective masking material. Alternative masking materials including photoresist and aluminium were tried but were not selective enough to compete with the protocol developed for chromium.

The samples were completely submerged into the chromium etchant CR-7S (Lodyne chrome etch, Rockwood electronic). CR-7S is a highly selective chromium etchant. CR-7S contains $HClO_4$ + $Ce(NH_4)_2(NO_3)_6$ + H_2 and was used as supplied. It etches approximately 50 nm/min, which leads to etching times in the range of 3-6 min for our samples. Etching speed was also influenced by the feature size. Undercutting of the features has not been observed to be a significant problem; side etching of the structures would not have a significant effect on the micrometre scale.

Samples were submerged into CR-7S under regular agitation. During etching, the etched areas appeared darker caused by the roughening of the chromium during etching. The colour of the protected areas was unchanged. Once the chromium was removed

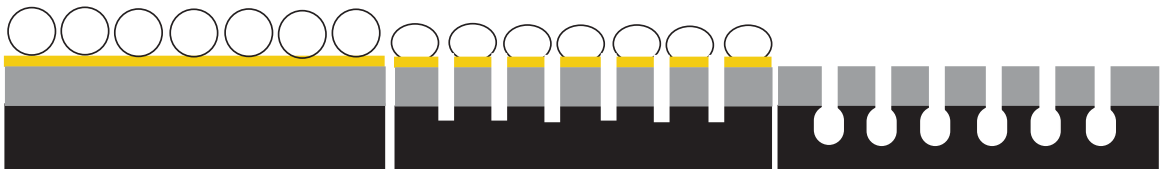

(a) Colloidal film (b) Colloidal milled film (c) Dry etched colloidal film

Figure 8.6: *Schematic of colloidal structuring (a) Colloidally assembled film on gold and chromium (b) Ion milled colloidal film (c) Ion milled and dry etched microhoodoo structures after removal of the colloidal monolayer.*

from the desired areas, the samples recovered their shiny appearance, due to the very flat Si layer underneath. While a small colour difference between Cr and Si was observed, the darkening and subsequent brightening of the etched areas was found to be the best way to establish the correct etching time.

After observation of the features under an optical microscope, the photoresist was removed in an ultrasonic bath, immersing the samples first in acetone and then in isopropanol. The samples were dried and checked prior to dry etching.

8.1.6 Ion milling

Ion-milling (Figure 8.1 3b) is a microfabrication technique that allows ballistic etching through a contact mask using highly collimated, high-energy Argon ions [106]. In contrast to ICP etching (Section 8.1.8), ion milling is a purely physical etching process and therefore has a very low selectivity for different materials. For our application, this is a large advantage, as it allows for etching of the colloidal mask at the same rate as the underlying chromium and gold layer.

Prior to ion milling, the colloidal films were heated on a hot plate at 110°C to increase their adhesion to the surface. The beam voltage and current were set to 500 V and 20 mA respectively, the milling time was approximately 40 min. The pattern achieved by colloidal self-assembly was transferred into the metallic layer by ion milling (purpose-built Whizzy Miller).

Following ion milling, the chromium and gold patterns at the surface were used as

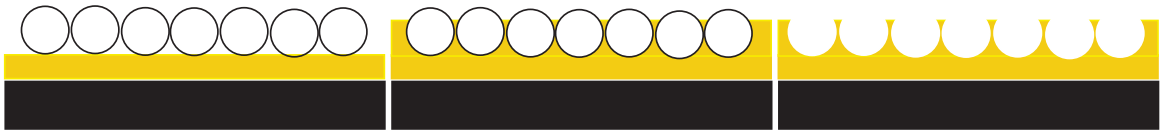

(a) Self-assembled colloidal monolayer on gold (b) Electroplated gold in colloidal monolayer gaps (c) Inverse colloidal structure

Figure 8.7: *Inverse colloidal structure preparation procedure. (a) Self-assembled colloidal monolayer on gold. (b) Colloidal monolayer with gold electroplated into the gaps between the colloids. (c) Inverse colloidal structure resulting from the removal of colloids in solvent.*

etching masks, as described in 8.1.8.

8.1.7 Electroplating

This work was inspired by work done by Abdelsalam *et al.* [104], who showed that inverse colloidal structures exhibit surprising wetting behaviour. As previous work was done without knowledge of the metastable wetting state, a repetition of the wetting experiments with more attention to the possible influence of overhanging structures was desired. The design was based on the previous work and is shown in Figure 8.7.

Electroplating allows for the slow filling of a porous structure from bottom to top (Figure 8.1 3c). For colloidal monolayers as produced in Section 8.1.4, electroplating allows for the formation of an inverse colloidal layer with variable filling heights. This means that structured layers can be produced with different characteristics dependent on the filling height.

Initial electroplating experiments were conducted with an electroplating gold solution (TG-25RTU, Technic Inc.) and EP3 brightener (EC4073, Metalor) using the setup described by Abdelsalam *et al.* [104]. As these experiments were not very reproducible, alternative structures were made using platinum instead of gold for the electroplating. The solution was 9 mM chloroplatinic acid in 60:40 H_2O/MeOH. For further information on electroplating and the procedure, refer to Abdelsalam *et al.* [104] and Holtzmann [105].

8.1.8 Dry etching

Inductive coupled plasma (ICP) etching is a well established dry etching technique (Figure 8.1 4). It has strong selectivity as well as relatively high etch rates due to the combination of highly selective reactive ionic gases (as in reactive ion etching) with the inductive coupled plasma surface bias (which allows for an increased directionality and higher etch rates). The instrument used was the 180 Plasmalab System 100 (Oxford Instruments). The recipe was established by repeated variation of the Si etching recipe provided by Oxford Instruments [107].

Table 8.3 shows the etching conditions used for microfabricated structures. The parameter variation stems from the fact that larger features required relatively deep etching, while smaller features can only have relatively short overhangs if stability is to be preserved. Removal of the overhanging features after etching (when desired) was achieved by a second wet etch used to remove the chromium (Section 8.1.5).

Parameter	Units	Value
RF power	W	25-35
ICP power	W	500-1500
Chamber pressure	mtorr	7-15
He backing	torr	10
SF_6	sccm	25
C_4F_8	sccm	50
Temperature	°C	0 or 20
Etch rate Si	nm/min	50-150
Etch rate Cr	nm/min	2
Selectivity	-	1:25 - 1:50

Table 8.3: *Etching Conditions for ICP etching.*

Using the parameters in Table 8.3 gives relatively well defined and reproducible surface structures. The edges are not straight but slightly undercut (overhang between a few hundred nm and 5 µm). The structures can be etched to a maximum depth of 15-20 µm, inducing an upper limitation on the feature aspect ratio of $A = 1$ for features with a width of 20 µm.

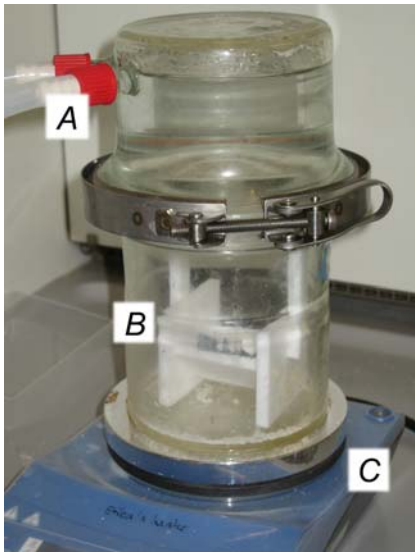

Figure 8.8: *Setup used for silanisation (A) Cooling system (B) Sample holder made of Teflon to hold samples in silane vapour atmosphere (C) Heater.*

8.1.9 Surface chemistry modification

Silanes

Silane chemistry was chosen as a self-assembling surface modifier, since silanes can be used to tune surface energy very precisely and as silanes self-assemble into a dense monolayer on both silicon and chromium surfaces (Figure 8.1 5a) [108, 109].

Samples were exposed to pure O_2 plasma for at least 1 h prior to silanisation. The setup was based on vapour phase silanisation at $T_{\mathrm{sil}} \approx 135°\mathrm{C}$. The silanes were kept under vacuum in a decicator to avoid contact with air humidity during storage. The silanisation setup was flushed with N_2 prior to closing to remove humid air. The samples were left in the silane vapour phase for 2 to 5 days.

Silanisation was performed in parallel on structured and unstructured surfaces, as small amounts of humidity can strongly influence the silane contact angles. All silanised structured samples were therefore always compared to the contact angle measured on the unstructured silanised chromium or silicon wafers.

The silanes used were Hexamethyldisilazane (HDMS) and (3-mercaptopropyl)trimethoxysilane (MERC). Water drops on flat silicon and flat chromium coated with

HDMS had a contact angle of $\theta_{\mathrm{HDMS}} = 90-110°$ (Literature value $110-120°$). Surfaces coated with MERC had a lower contact angle of $\theta_{\mathrm{Merc}} = 80-85°$ (Literature value $70-104°$ [110]). Surfaces coated with MERC had a higher contact angle reproducibility than surfaces coated with HDMS.

Thiols

Thiols assemble onto silver, gold or platinum (Figure 8.1 5b). Thiol chemistry, like silane chemistry, is relatively easy to control and produces characteristic dense self-assembled monolayers with repeatable surface energies. Surfaces were immersed into a pure thiol solution after 1 h of O_2 plasma cleaning. They were left in the solution for 3 to 7 days. Flat gold substrates were used as reference materials as described in Section 8.1.9 for silane surface chemistry.

Thiolisation was used twice during the inverse colloidal structuring and electroplating protocol: Once before the colloidal self-assembly and once to tune the suface energy of the final platinum or gold structures obtained by electroplating. It was found that thiols on the gold substrate helped the colloidal assembly. A mixture (6:4) of 1-Dodecanethiol (Alfa Aesar) and 12-Mercaptododecanoid acid (Sigma Alrich) was used.

The inverse-colloidal structures were thiolated after removal of the colloids (Figure 8.1 5B) to allow for controlled measure of the contact angle.

8.2 Rough surfaces for underwater experiments

8.2.1 Rough Teflon surfaces

Teflon® sample preparation was based on work done by Harms [111] and van der Wal [102, 112]

Polytetrafluoiroethylene (PTFE), also called Teflon® (DuPont) was obtained as a white colloidal water-based dispersion. Its melting point is 335°C for the bulk material

(a) Waterdrop rolling off Teflon surface (b) Waterdrop still on Teflon surface

Figure 8.9: *Superhydrophobic Teflon surfaces repel water. (a) Water drops rolling off the surface. (b) Water drops still on the surface: Here we can see the silvery Cassie-Baxter air-film underneath the water droplet.*

and 385°C for the porous material [111]. Teflon® was chosen for the production of superhydrophobic surfaces due to its very low surface energy ($\gamma_{\mathrm{PTFE}} = 20\,\mathrm{mN/m}$ [113]). DuPont proposes a two-step coating process to obtain PTFE surfaces. The substrate is coated with a primer (primer 459-804) and then with a water-based colloidal PTFE solution (top-coat 852 - 200).

Samples were sprayed (Sealey Air Brush Kit AB 931) with primer and then with the Teflon® solution. The optimum spraying distance was found to be roughly 15 cm and the angle for the substrate 10°. The exact processing steps are [105, 111]:

- Bead blast surface until rough.
- Apply a thin layer of primer with spray gun covering the substrate evenly.
- Bake sample on hot plate at 250°C for 15 min.
- Apply a thin layer of top coat with spray gun until surface is covered.
- Bake sample on hot plate at 320°C for 10 min.
- Place sample on hot plate at 170°C and wait 2 min to allow it to heat up.
- Apply thin secondary layer of top coat with spray gun while heating until the surface is partially covered.
- Bake sample on hot plate at 410°C for 6 min.

The samples were measured after production to characterise their superhydrophobicity. Samples that did not display even superhydrophobic behaviour were discarded. Samples had static contact angles between $155° < \theta_{\text{static}} < 168°$, depending on the exact processing conditions.

8.2.2 Copper grid boats

Boats were produced according to the procedure described by Pan *et al.* [7] and Larmour *et al.* [114]. The boats were produced from copper mesh (Anping Jiangtai Wire Mesh Producing Co., Ltd) by cutting a boat shape from the mesh. The corners were closed together carefully to avoid openings on the side, through which water could penetrate the structure. Simple coated copper mesh sheets were also produced for underwater wetting measurements. The procedure was the following:

- Cut boat layout or plane sheet from copper grid.
- Fold into boat or use as cut.
- Clean in acetone and isopropanol using an ultrasonic bath.
- Insert for 20 s into an $AgNO_3$ solution (20 mMol $AgNO_3$ in H_2O).
- Wash in water to remove reaction side products.
- Insert into the thiol solution (5 mMol Dodecanol in ethanol).
- Wash with ethanol.
- Dry with N_2.

The boats were then placed onto a water bath and weighed down until the water-line nearly reached the upper edge of the boat. The boats were observed daily to establish whether the air-film stayed or whether the boat had sank due to loss in buoyancy.

In order to compare the stability of the air-film on these copper structures, their behaviour under water was tested as for the Teflon samples. The coated copper sheet was immersed in an immersion water tank (Section 9.2.2) and observed over days to establish its air-film stability.

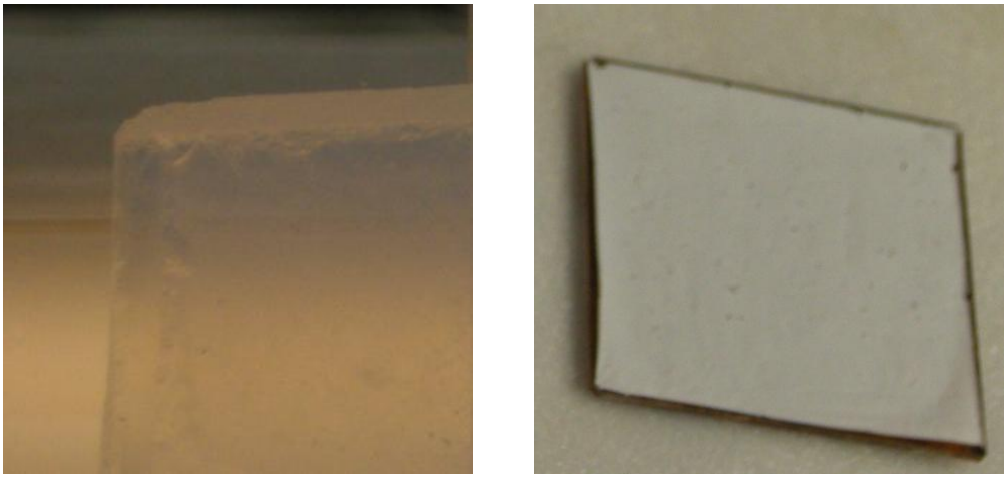

(a) Aerogel (transparent) (b) Cellulose gel

Figure 8.10: *Gels after preparation (a) transparent ambiphobic aerogel (b) White hydrophobic cellulose gel*

8.2.3 Superhydrophobic gels

Two types of gels were imported from Finland[1]: Superambiphobic aerogels and superhydrophobic cellulose gels (Figure 8.10).

The cellulose based hydrogels were prepared according to modified recipes by Paakko *et al.* [115]. The gels are freeze-dried and mechanically strong. A typical cellulose gel sample (still in its mold) is shown in Figure 8.10b.

The fluorosilanized nanocellulose aerogels were prepared by Jin *et al.* [116] using a recipe modified from Hüsing [117]. A typical aerogel sample is shown in Figure 8.10a.

Before surface modification the gels were mounted on steel plates to allow for easy mounting in the water column. As for the Teflon sample under water experiments, the gels were mounted in the immersion tank setup. The air-film decay was observed using the same method as described for the Teflon surfaces in Section 8.2.1.

[1]The gels were prepared by Robin Ras and Hua Jin

8.3 Natural surfaces

8.3.1 *Antirrhinum* flower petals

Fresh *Antirrhinum* flower buds were cut one to two hours before the measurements were conducted.[2] Measurements on the flowers were done using glass slides for support; a piece of the flower (cut carefully from the flower bud) was glued onto the glass slide with double sided tape (inner flower petal side facing up). The flower was pressed down at the edges but care was taken not to touch the inside area used for the measurements. The flower was always mounted as flat as possible.

All water contact angle measurements were done on the outward facing strongly coloured lips of the top and bottom surface of the flower. Care was taken only to measure the untouched central area of the mounted flower petal. Few measurements could be repeated on the same areas, as the flowers often retained small droplets after the measurement, which influenced the wetting behaviour.

8.3.2 *Nelumbo nucifera* leaves

The *Nelumbo nucifera* leaves were cut freshly in the morning approximately one to two hours before starting the experiments [3]. Care was taken not to bend or scratch the leaves, as this was found to cause local defects in the surface hydrophobicity. The leaves were attached to a sample holder for immersion into the water tank using strong adhesive tape and were observed as described in Section 9.2.2 for the Teflon samples.

During the experiments, the *Nelumbo* leaves were found to deteriorate. This was due to the unexpectedly long survival of the air bubble film on the leaves. Due to the immersion depth of about 50 cm, it was impossible to keep the leaves alive during the experiments.

[2]The flowers were obtained from the Cambridge University Plant Sciences. Special thanks go to Matthew Dorling for flowers and advice on transport and manipulation of the flowers.

[3]Special thanks go to Heather Whitney for transporting the *Nelumbo* plant, to Alan Langley for taking care of the plant and to Cambridge Botanical Gardens and Bristol Botanical Gardens

9 Exploring wetting - observation methods

9.1 Sample characterisation

In order to understand the wetting of different surface structures, the samples need to be extensively characterised for comparability of their wetting behaviour. In particular, this requires the measurement of feature size and density, as well as depth, height, overhang thickness and overhang width (Section 8.1). The methods described here provide both qualitative and quantitative sample information.

9.1.1 SEM

Scanning electron microscopy (SEM) uses electrons instead of light as an illumination and measurement system. It accelerates electrons toward the specimen and collects and analyses the electrons that are reflected into the half space of the incident beam. In order to create an image of the sample, an electron beam is raster scanned over the surface and the recorded signals are combined to give an image of the surface. Scanning electron microscopy shows a convoluted image of electrical conductivity and topography. In order to avoid difficulties with artifacts and charging, all non-conducting materials must be coated with a conducting layer. For further information on SEM, please refer to Goldstein [118].

All microfabricated silicon-metal samples (Section 8.1) were imaged using a scanning tunnelling microscope (Leo Variable pressure SEM). As all components of the samples were conducting, no coating layer was necessary. The images obtained from the electron

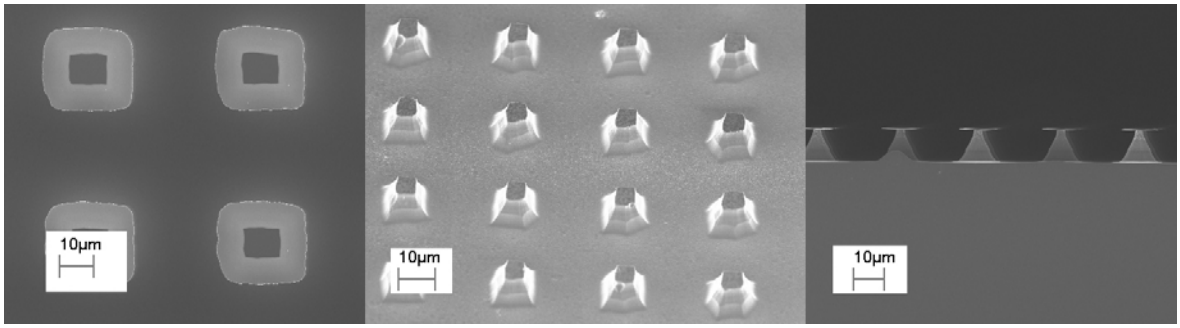

Figure 9.1: *SEM images (A) Top view (B) 45° angle (C) Cross-section*

microscope were later analysed with ImageJ in order to obtain correct measurements of the essential features of the samples. Samples were imaged from the top (normal SEM setup), at a 45° angle, and cross-sectionally (90° angle). Examples of the images obtained for these different sample mounting techniques are shown in Figure 9.1.

Measurement conditions for all samples were: InLens setup, 5 keV acceleration voltage of the electron beam, vacuum in the chamber below 5×10^{-5} mbar, working distance (sample - electron gun emitter distance) around 3 mm.

For the microfabricated hoodoo, pillar, hole and trap structures (Section 8.1), all samples were imaged in cross section. This had the advantage that high precision measurements of the feature height, width, the overhang width and the remaining chromium layer thickness could be taken. Images at the 45° angle show distortion of features and make measurements difficult. In Figure 9.2, we can see an annotated SEM image of an overhang structure.

As can be seen in Figure 9.2, the feature distance can be misleading in cross sectional images, especially for hexagonally packed features or samples that have been broken off axis. Therefore, the feature distance was always cross-checked with optical microscopy or AFM.

SEM was used to determine both qualitative and quantitative sample information. The cleanliness and regularity of the sample features was checked. Further, the feature width ($2W$), feature height (H), feature-to-feature distance ($2D$) and the overhanging layer thickness (T) and width (O) were measured (Figure 9.2).

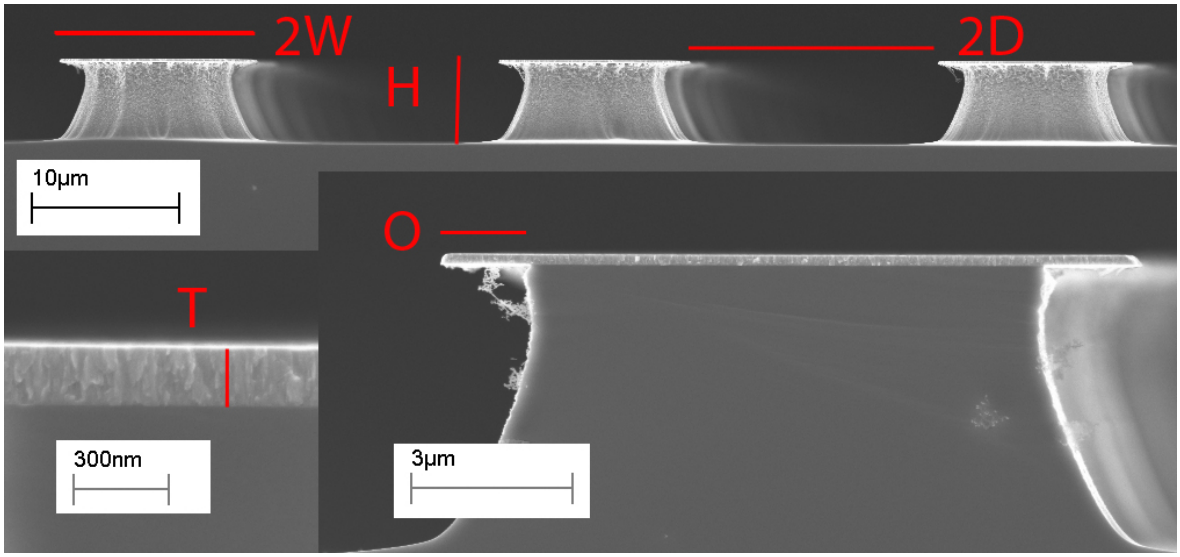

Figure 9.2: *Microhoodoo Feature Measurements (2W) Hoodoo width, (H) Hoodoo height, (2D) Hoodoo-to-hoodoo distance (T) Chromium thickness, (O) Overhang width*

9.1.2 Optical Microscopy

Most structures used for the surface wetting experiments were characterised using optical microscopy. This allowed for verification of the features during the microfabrication process in order to avoid under- or overdevelopment of the lithographic features (Section 8.1.3), as well as under- and overetching of features (Section 8.1.5). Optical microscopy was also used to determine the quality of the features produced by all different structuring mechanisms.

Additionally, the surface coverage and feature width of the microfabricated hoodoos, pillars, traps and holes were measured. An optical microscopy image of a microfabricated surface is shown in Figure 9.3. Optical microscopy images of the microfabricated features were analysed with ImageJ to calculate the surface coverage σ_{features} of the hoodoos, pillars, traps and holes on the surface.

Optical microscopy was also used to verify the structure quality after wetting measurements. For early samples with relatively thin overhangs, the surface tension of the drops used for measurements often destroyed the overhanging structures due to the capillary forces (Section 10.1.4). The air-film on the Teflon samples used for underwater wetting experiments was observed using an optical microscope in a makeshift liquid

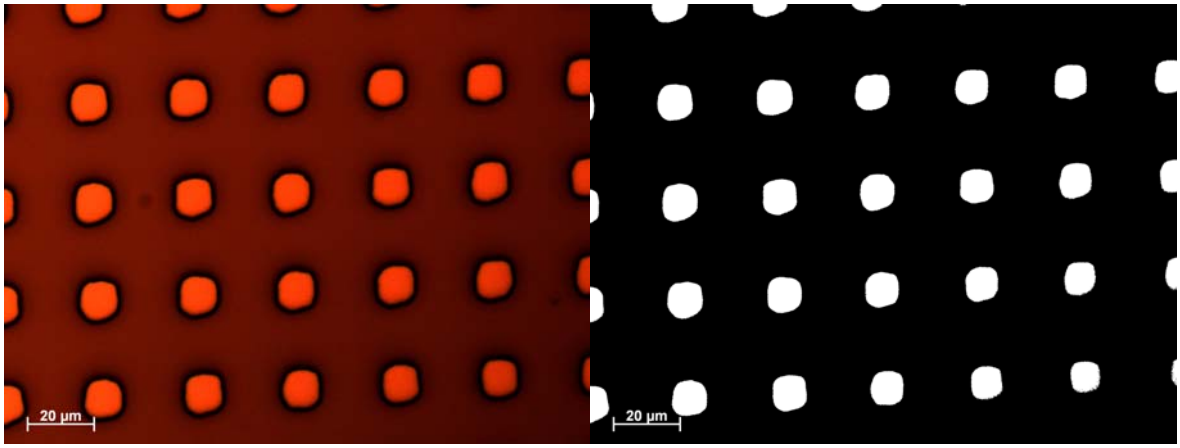

(a) Untreated image (b) Image after thresholding

Figure 9.3: *Optical microscopy image of microfabricated chromium and silicon hoodoos. Images were used to determine the surface coverage of the features. (A) Untreated image, (B) Image after thresholding.*

cell (Section 9.2.3).

9.2 Wetting Characterisation

In order to observe the wetting transitions described in Sections 7.3 and 7.5, the wetting states on the surface must be observed and characterised. For metastable wetting of drops on structured surfaces, this was done through static and dynamic contact angle measurements (Section 9.2.1). For underwater Cassie-Baxter to Wenzel transitions, this was achieved through optical observation of the air film on the surface in a water column (Section 9.2.2) and as a close up measurement of individual air bubbles using classical optical and confocal microscopy (Section 9.2.3).

9.2.1 Contact Angle Measurements

Contact angle measurements were conducted using a KSV CAM 200 goniometer (KSV Instruments). In contact angle goniometry, the drop is imaged from the side and the drop shape is then analysed with image analysis software. Images were taken using a planar CCD camera. The CCD camera and the water dispensing system are controlled

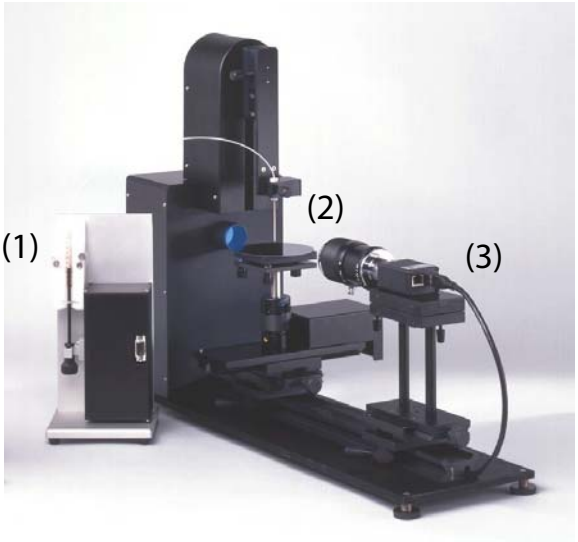

Figure 9.4: *KSV CAM 200 goniometer: (1) liquid dispenser, (2) sample stage and (3) camera.*

from a computer (KSV Instruments). The water dispensing system was filled with millipore water (R = 18 MΩ). The flatness of the sample holder and the camera were checked regularly with a water balance to assure perfectly perpendicular contact angle measurements. The setup is shown in Figure 9.4.

Static contact angles are measured on drops with a volume between 8 µl $< V <$ 20 µl. The drop pictures were fitted using the contact angle goniometer software. For static contact angles, the Young-Laplace fitting algorithm was used and a base-line tilt was allowed.

Dynamic contact angles were measured by continuously increasing or decreasing the size of a drop on a surface. The increasing and decreasing speed was between 0.5 µl/s $<$ $s_{\text{drop}} <$ 2 µl/s. The images of the advancing and receding drops were analysed using ImageJ (Drop_analysis package) [119]. The software provided by KSV Instruments was not very well adapted for fitting advancing or receding drops. An example of advancing and receding drops on a structured substrate and the fit provided by ImageJ Drop_analysis is shown in Figure 9.5.

Contact angle measurements were performed on each surface at least twice, in order to ensure the accuracy of the measured contact angle. For surfaces showing metastable

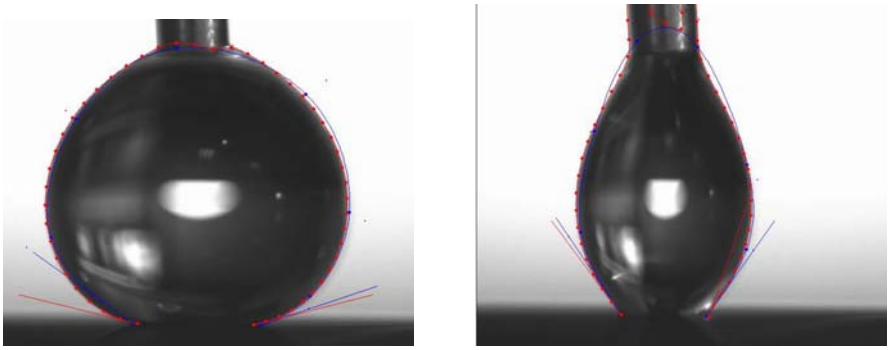

(a) Advancing contact angle (b) Receding contact angle

Figure 9.5: *(a) Advancing and (b) receding contact angles. The two fitting lines show the starting values and final fit for the drop shape found using the ImageJ Drop_ analysis software.*

wetting states, measurements were repeated up to 10 times, in order to obtain a measurement of both the metastable and the stable wetting states where possible.

Comparing contact angle measurements

In order to achieve comparability of contact angle measurements for the microfabricated and patterned surfaces, a reference sample was always treated with the same surface chemistry as the patterned surface. The reference sample was either a pure silicon substrate or a silicon substrate with a chromium layer for the microfabricated experiments. It was found that the difference between contact angles measured on chromium coated or pure silicon substrates was smaller than the variation within each set. The contact angles measured on the flat reference samples that had undergone the same treatment were used as the reference contact angle θ_Y for the patterned samples.

9.2.2 Immersion tank setup

The water tank was custom built to study the behaviour of air bubbles on a superhydrophobic surface underwater. The setup was created to be completely transparent and easy to clean, empty and fill (Cambridge Glassblowing).

Samples were immersed and measured in fresh still, deionised water saturated with

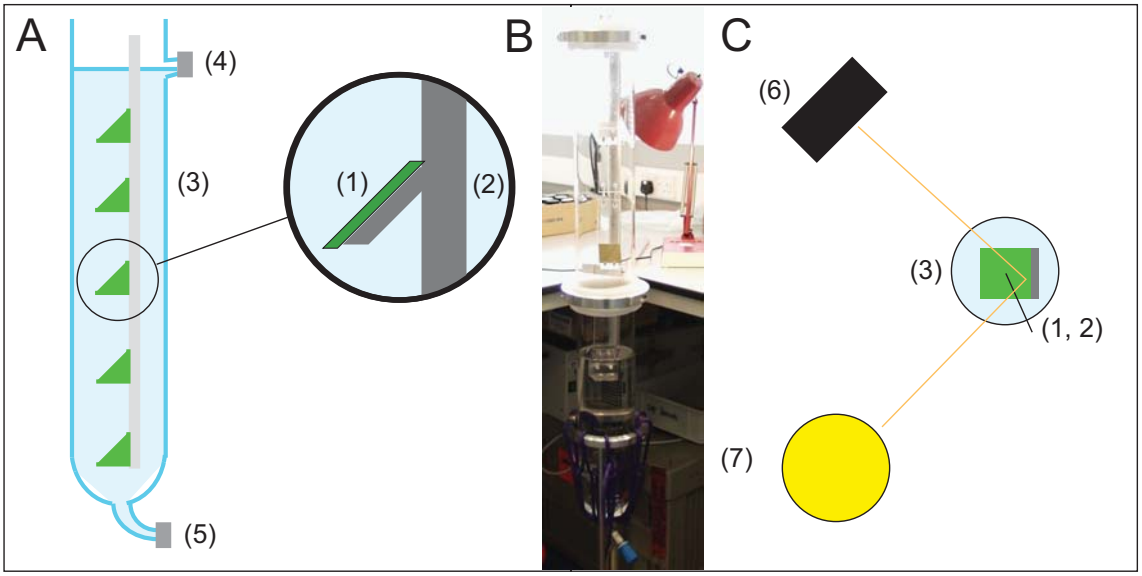

Figure 9.6: *Immersion tank setup: (A) Side view with five immersion depth (from top to bottom): H1 - 29 cm, H2 - 54 cm, H3 - 81 cm, H4 - 106 cm and H5 - 131 cm under the water surface. (B) Photo of immersion tank setup (C) Schematic top view: (1) Teflon sample, (2) Sample holder, (3) Water column, (4) Outflux, (5) Influx, (6) Camera setup and (7) Light source*

air, and in continuously pumped water.

For the static underwater experiments, the tank was filled with water ($R_{\mathrm{H20}} = 15\,M\Omega$). The water was left to sit between 5 and 10 min before the samples were immersed into the water. The water was not changed or stirred until sample removal.

The flowing underwater experiments involved a water pump circulating water from the bottom to the top of the tank. The water was cycled with an aquarium pump (Newa water systems, New Jet 1700) and aerated with an aquarium bubbler (Hydor Ario 4). Water saturated or oversaturated with air was introduced into the tank slowly from the lower influx.

The behaviour of the samples in the different environments were compared with respect to each other, but also with respect to the immersion depth.

Samples were attached to a plastic holder and immersed into the water slowly. The samples were kept at an angle of approximately 45°. The samples were illuminated from the side (approximate 30° of angle) and observed from the angle of reflection (Figure

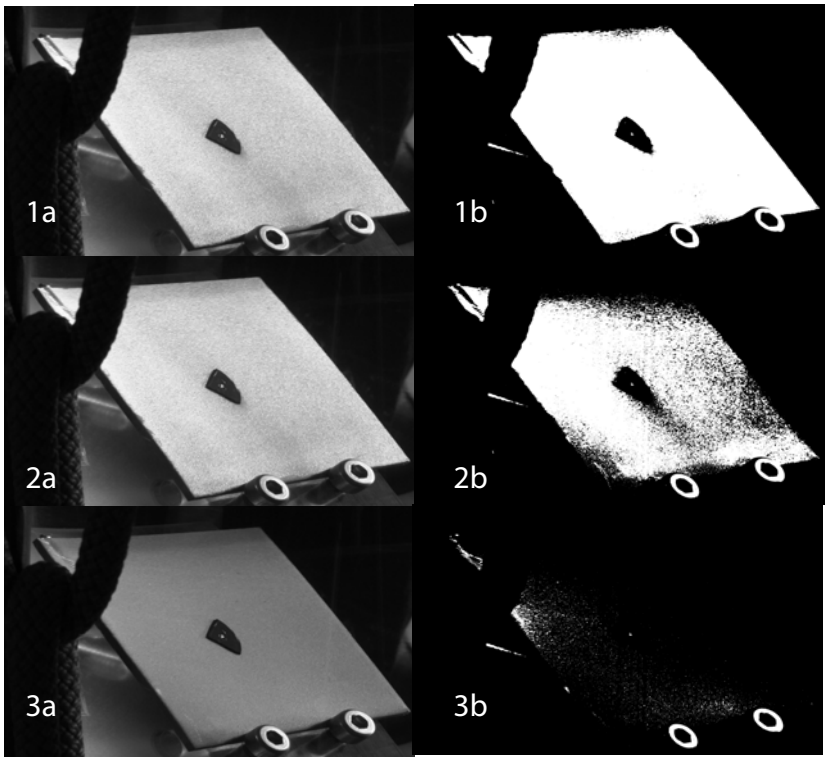

Figure 9.7: *Air-film decay and threshold analysis. Images were taken (1) at the beginning, (2) during decay and (3) at the end. (a) untreated image, (b) image after thresholding in ImageJ.*

9.6). From this position, the air-film on the surface appears as a reflective mirror surface. During the air-film decay over time, the total amount of highly reflective sample area decreased, until the sample was found to be completely green. Data was recorded for two samples mounted at different heights simultaneously with two cameras (Olympus Camedia E10 and a Canon EOS 450D). Images of the surface were taken at fixed intervals $5\,\mathrm{min} < \Delta t < 15\,\mathrm{min}$. The decay of the air-film was measured as a change in intensity of the sample surface reflection.

The air-film coverage for all image sets was presumed to be directly proportional to the amount of white (highly reflective air-film) and green (natural Teflon surface colour) in the picture. For the data analysis, pictures were treated in ImageJ as an image sequence, converted to 8bit gray scale, cropped, the relevant parts selected, the rest whitened and then a threshold was set. The threshold was set for the whole image sequence and checked for the beginning, the end, and a central value. The image sequence was converted to a black and white image sequence (above and below the

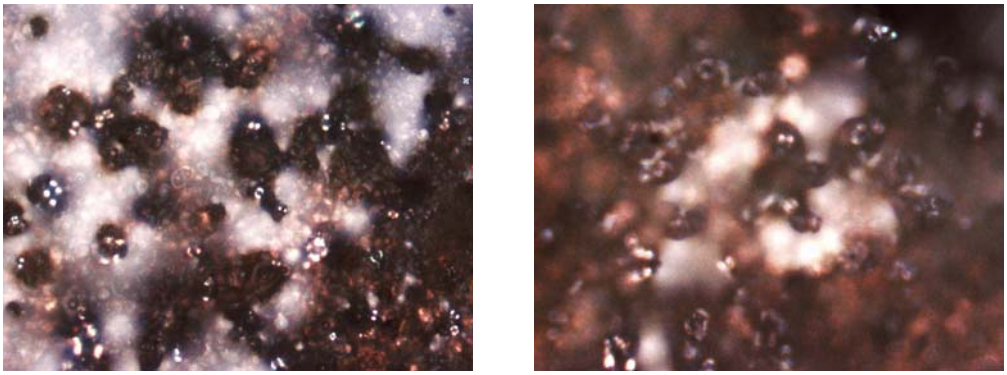

(a) Teflon surface underwater ($t = 0$) (b) Teflon surface underwater ($t = 6\,h$)

Figure 9.8: *Teflon surface underwater observed using an optical microscope. Due to the difficulty and the time required to assemble the liquid cell, and the pressure exerted on the O-ring glass slide cell during assembly, the first picture already shows a partial air-film only. Focusing difficulties also make it difficult to see which features are below and which above the air-film.*

threshold value) and the area containing the air film (brighter than the threshold) was normalised and plotted against time. An example of the air-film decay measurement through image analysis is given in Figure 9.7.

9.2.3 Optical Microscopy & Confocal Microscopy

Surface images of the air-film were taken with a normal optical microscope by O-ring glass slide cell method. The surface under the microscope was difficult to focus. Figure 9.8 shows the surface and the air-film underwater.

Due to the pressure exerted on the water and the air-film on the sample upon mounting of the cell, optical observation of the air-film proved difficult. Further, no quantitative information about the air-bubble shape on the surface could be drawn from images taken with a normal optical microscope.

Confocal microscopy was used to take images of the air-film on the Teflon surfaces. Confocal microscopy is an optical imaging technique based on classic optical microscopy. It is used to increase image contrast and allows for 3D reconstruction of a specimen or surface. This is done by using a spatial pinhole to reduce the focus depth

and scanning a stack of consecutive focus layers, which are recombined into a 3D image. For further information on confocal microscopy, please refer to Pawley [120].

The confocal microscopy images were acquired with a LSM 510 META confocal microscope (Zeiss) using a 25x immersion objective (NA = 0.8). The focus distance of the objective was below 300 µm, which is why care had to be taken not to touch the extremely rough Teflon specimen. The images were taken using a HeNe-layer ($\lambda = 633\,\mathrm{nm}$). The water film on the sample had a thickness of $d_{\mathrm{H2O}} = 1 \pm 0.5\,\mathrm{cm}$.

In the confocal microscopy setup, the high refractive index contrast between air ($n = 1.0$) and water ($n = 1.33$) or Teflon ($n = 1.35$) allowed for high contrast 3D image stacks that could be used to make a surface topography reconstruction (Figure 12.9b) as well as measure the bubble size, height and curvature (Figure 12.11b).

Confocal microscopy also allowed for repeated measurements of the air-film in one area. This was used to observe changes in the air-film. As for samples observed with other techniques including the water tank (Section 9.2.2), a decay of the air-film associated with a Cassie-Baxter to Wenzel wetting transition was observed for many areas. The significantly decreased plastron life-time with respect to measurements done outside the confocal microscopy setup was attributed to localised heating due to the high energy laser light used for measurement.

10 Surface Wetting - Results

This chapter explores the wetting of water droplets on different micro-structured surfaces. In Section 10.1, the wetting behaviour of different photolithographically microfabricated structures with and without overhangs is discussed. Section 10.2 and Section 10.3 describe the wetting behaviour observed on microstructures based on colloidal self-assembly.

10.1 Microfabricated regular structures

In this section, we discuss the influence of overhanging features, feature size and the design parameters derived by Tuteja *et al.* [1] on the metastable Cassie-Baxter wetting state of water droplets on highly structured surfaces: Overhanging positive features, overhanging negative features and features with little or no overhangs are studied separately. Structures were characterised in terms of their surface fraction f, overhang width O, width $2W$, distance $2D$, height H and overhang thickness T (Section 7.3.4).

Microfabricated surface structures were silanised and then measured and characterised. Many samples exhibited a metastable Cassie-Baxter wetting state, a mixed mushroom wetting state and a stable Wenzel wetting state. The definition of these states can be found in Section 7.2. Static contact angles varied greatly, as they are not uniquely defined [88]. In this section, we have therefore reported the advancing θ_{A} and receding θ_{R} contact angles and the contact angle hysteresis $\Delta\theta$. The wetting behaviour of the droplets on the surfaces was seen to depend strongly on the way the droplet was deposited. This history dependent wetting behaviour only exists on samples with

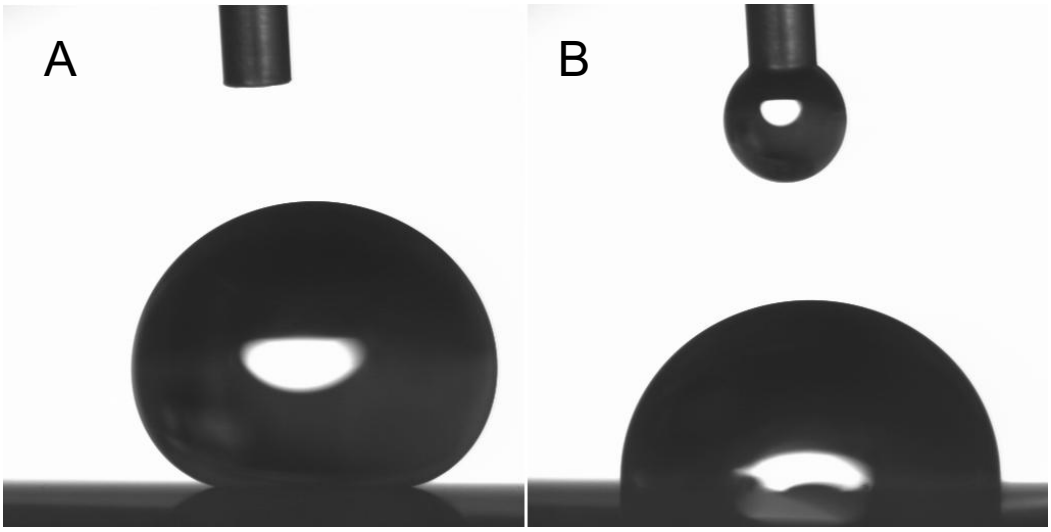

Figure 10.1: *Microhoodoo sample exhibiting Cassie-Baxter (A) and Wenzel (B) wetting. The contact angle for the two states were (A)* $\theta_{CB} = 155°$ *and (B)* $\theta_W = 86°$. The contact angle on the silane layer was $\theta_Y = 80°$.

multiple energy minima.

All surfaces reported in this section were modified with (3-mercaptopropyl)trimethoxysilane as described in Section 8.1.9 ($\theta_Y = 80 - 85°$). Using a slightly hydrophilic surface allowed for relatively easy preparation of surfaces with metastable wetting states.

10.1.1 Positive overhanging structures: Microhoodoos

Wetting on structures with positive overhangs (microhoodoos) was quantified through contact angle measurements (Section 9.2.1). Positive structures with overhangs allow for multiple energy minima in the energy landscape and therefore show both stable Wenzel wetting states and metastable Cassie-Baxter wetting states.

In Section 7.3.4, we described the design criteria mentioned by Tuteja *et al.* [1]. These included high values of the stability parameter A^* and high values of the spacing ratio D^* (Equation 7.21-7.24). The stability parameter A^* is a measure of two other stability parameters (H^* and T^*), which denote the stability of the metastable wetting state due to the feature height ratio H^* and the reduced feature edge angle T^*. D^* denotes the ratio of feature size to feature spacing. High values for A^* and D^* should lead to

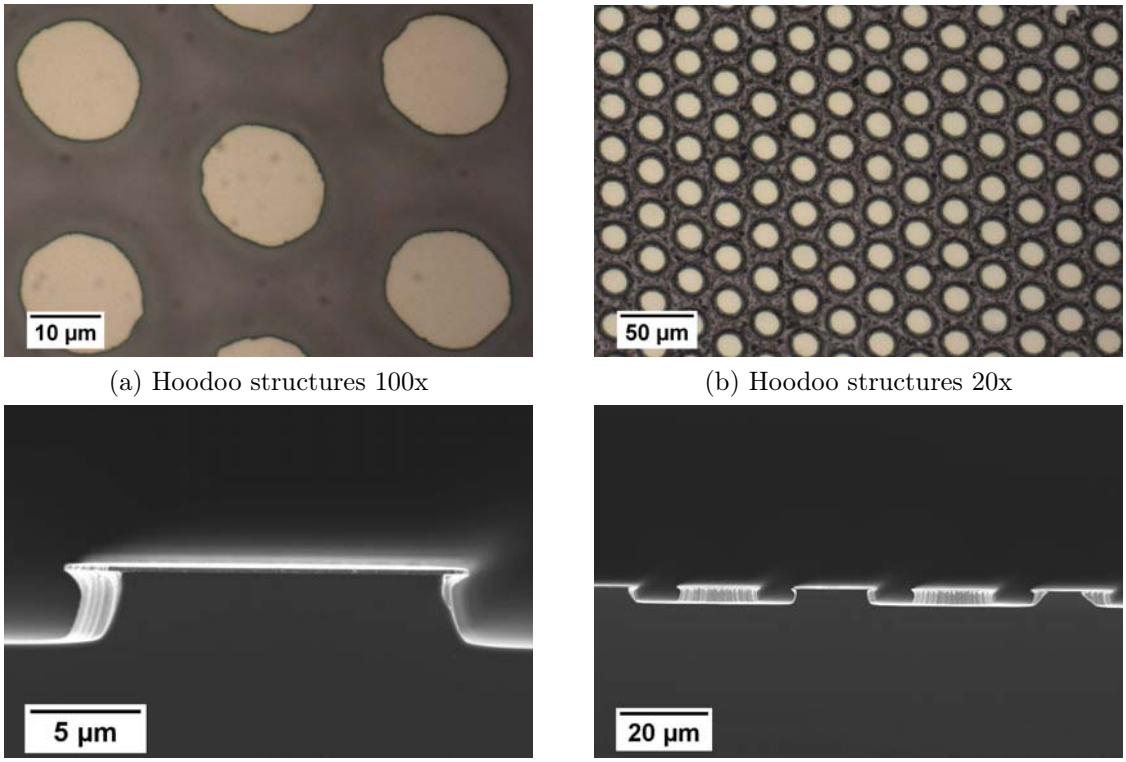

(a) Hoodoo structures 100x (b) Hoodoo structures 20x

(c) (d)

Figure 10.2: *Overhanging positive surface features (microhoodoos) in an optical microscope: Sample S194e (a) 100x objective (b) 20x objective. Crosssectional SEM image of traps: Sample S191a (c) close up of one hoodoo (d) multiple hoodoos*

highly robust metastable wetting states with high contact angles. For all measured hoodoo structures, the values for D^* and A^* were calculated using the formula derived by Tuteja *et al.* [1] (Section 7.3.4). The observed wetting behaviour was quantified with respect to the design parameters and compared to experimental results by Tuteja *et al.* [1].

Metastable and stable contact angle measurements

According to Tuteja *et al.*, A^* describes the robustness of the metastable wetting state (higher A^* results in more robust metastable wetting states) and D^* influences the apparent contact angle θ (higher D^* results in higher θ). They further described an independence of the contact angle θ on the surface fraction f in contact with the liquid. This is in contrast to normal Cassie-Baxter wetting (Equation 7.4). Here, we will explore the effect of these parameters on our microhoodoo structures.

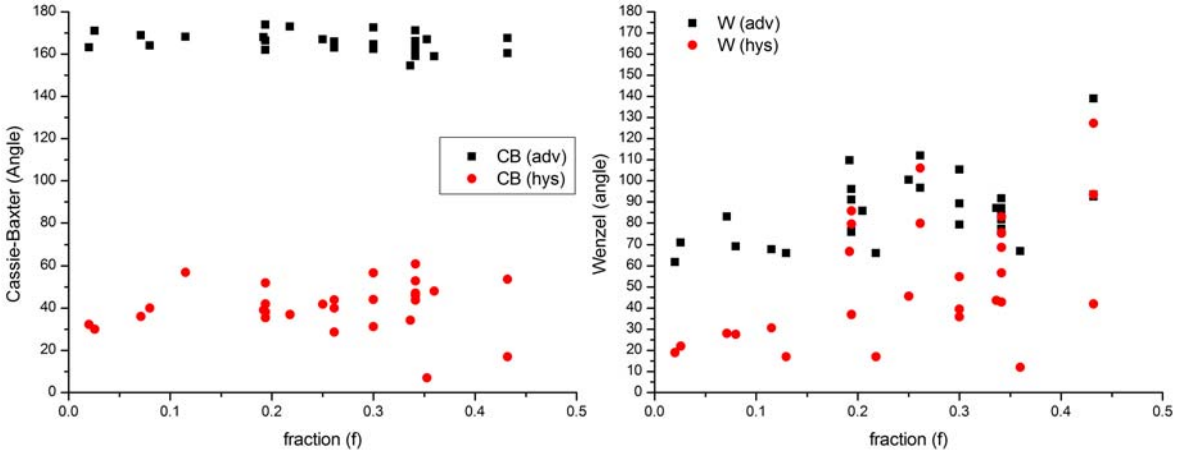

(a) Cassie-Baxter wetting (f)

(b) Wenzel and mixed wetting (f)

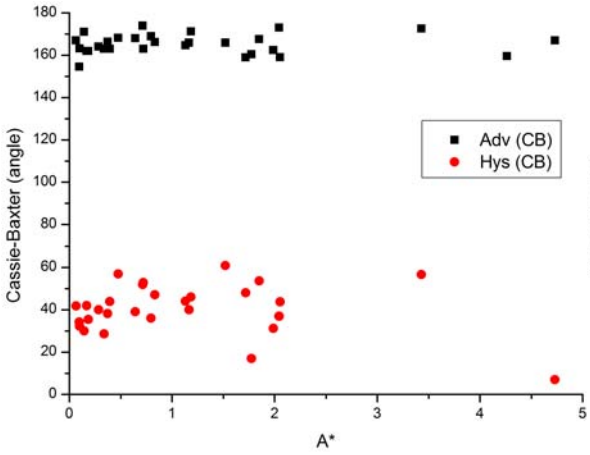

(c) Cassie-Baxter wetting (A^*)

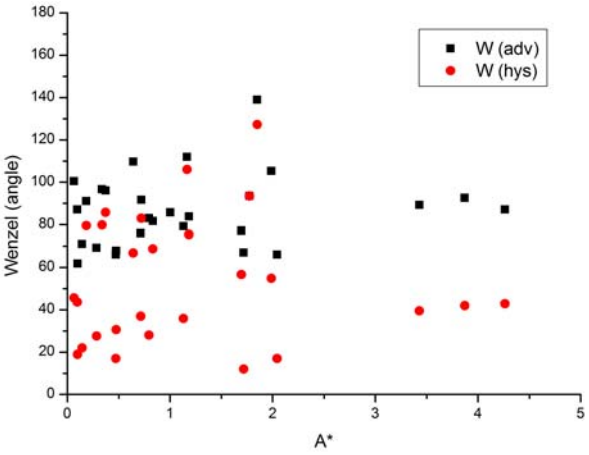

(d) Wenzel and mixed wetting (A^*)

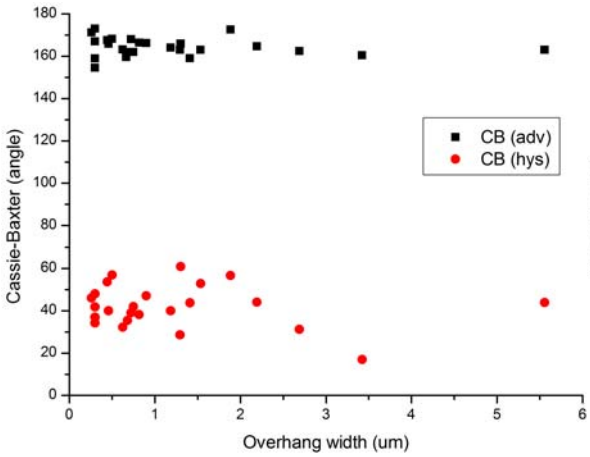

(e) Cassie-Baxter wetting (O)

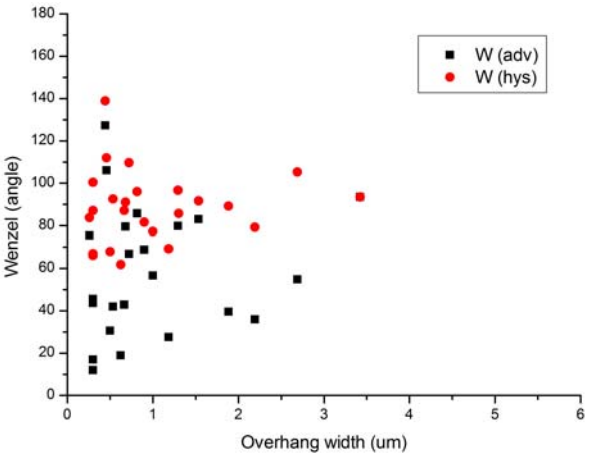

(f) Wenzel and mixed wetting (O)

Figure 10.3: *Dependence of the contact angles (θ_A and $\Delta\theta$) on the parameters f (a, b), the robustness factor A^* (c, d) and the overhang width O (e, f). The changes for the metastable Cassie-Baxter contact angles are plotted in (a, c, e); the changes for the mixed mushroom state and the stable Wenzel contact angles are shown in (b, d, f).*

In Figure 10.3, the contact angle θ is shown for all observed wetting behaviours as a function of f, A^* and O. A distinction was made between measurements corresponding to Cassie-Baxter air-pocket wetting and measurements that showed either a pure Wenzel wetting state or a mixed Cassie-Baxter and Wenzel wetting state. This mixed wetting state was observed frequently on the microhoodoo structures. Its characteristics correspond well to the mushroom state described by Ishino *et al.* (Section 7.2, Figure 7.6 [76]). The mixed state could be due to a higher pressure in the central area of the droplet caused by the drop weight. The energy barrier between the Cassie-Baxter and Wenzel state is overcome.

Figures 10.3a, 10.3c and 10.3e show the contact angles measured for the pure metastable Cassie-Baxter wetting state on the surface. Figures 10.3b, 10.3d and 10.3f show the contact angles measured for the pure Wenzel wetting state and the mixed mushroom wetting state.

Figure 10.3a shows no dependence of the metastable Cassie-Baxter contact angle on the surface fraction of microhoodoos f. This is in contrast to surfaces with a stable hydrophobic Cassie-Baxter state on non-overhanging structures: For these surfaces, a strong dependence of the Cassie-Baxter contact angle on the surface fraction f is given by the Cassie-Baxter equation (Equation 7.4). The contact angle of the metastable Cassie-Baxter wetting state on hydrophilic surfaces does not seem to depend on the surface fraction f.

Figure 10.3b shows that for the mixed mushroom state and the stable Wenzel wetting state, the advancing contact angle θ_A and the contact angle hysteresis $\Delta\theta$ increase slightly with increasing surface fraction f. This corresponds to the expected behaviour for Wenzel wetting. The data shows stable Wenzel states with advancing contact angles in the hydrophilic regime ($\theta_\mathrm{A} < 90°$) and mushroom states with advancing contact angles in the hydrophobic regime ($\theta_\mathrm{A} > 90$). For all of these wetting states, the receding contact angle is very low, as it is dominated by the drop behaviour in the central area. Therefore, all of these states show very low receding contact angles and very high contact angle hysteresis.

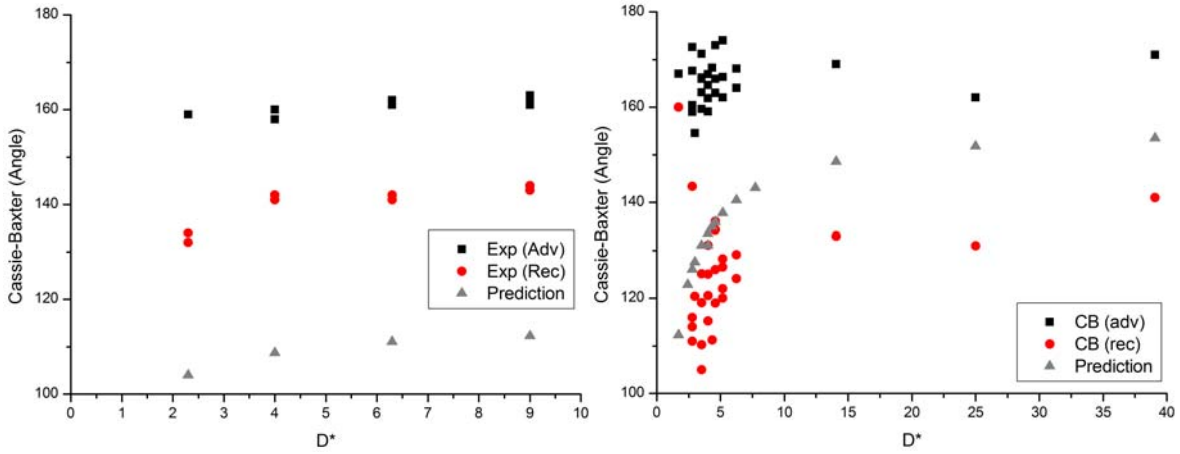

(a) Wetting as a function of D^* [1]

(b) Wetting as a function of D^*

Figure 10.4: *Contact angles as a function of the spacing ratio D^*: (a) Experimental data and prediction for the metastable Cassie-Baxter wetting state as reported by Tuteja et al. [1] (b) Experimental data and prediction for the metastable Cassie-Baxter wetting state reported here.*

As expected from the arguments provided by Tuteja *et al.*, no influence of A^* on the apparent contact angle for the metastable Cassie-Baxter or the mixed mushroom and the stable Wenzel wetting state was observed on surfaces covered with microhoodoo structures (Figure 10.3c and 10.3d). While Tuteja *et al.* observed nearly the same contact angles for all their microhoodoo structures, the contact angles measured in our experiments varied greatly.

In order to investigate possible factors causing the variance seen in the data, we studied the influence of the overhang width O on the contact angles. Figure 10.3e shows the advancing contact angles for metastable Cassie-Baxter states as a function of the overhang width O. Figure 10.3f shows the advancing contact angles for the mixed mushroom and the stable Wenzel wetting states as a function of the overhang width O. As for the robustness parameters A^*, no influence of O on the contact angle was observed. This is not surprising, since the droplet on the surface in the metastable Cassie-Baxter wetting state is not in contact with the lower part of the microhoodoo structure. There should therefore be no influence on the wetting behaviour due to the overhang width O.

Tuteja *et al.* postulated a dependence of the apparent contact angle θ_S on the spacing

ratio D^*, this is found by reformulating the Cassie-Baxter relationship

$$\cos(\theta_{D*}) = -1 + \frac{1}{D*}(\sin\theta_Y + (\pi - \theta_Y)\cos\theta_Y) \tag{10.1}$$

In their work, Tuteja *et al.* did not experimentally show the dependence of θ_S on D^* [1]. Further, their experimental results and the theoretical prediction do not correspond to each other. This can be seen clearly in Figure 10.4a, where we plot their experimental data and the predicted values for the static contact angle θ_S from Equation 10.1 using the values reported by Tuteja *et al.* ($\theta_Y = 55$). The predicted static contact angle θ_S is lower than both the experimental values for the advancing θ_A and for the receding θ_R contact angles. This is surprising as this violates the general relationship $\theta_A > \theta_S > \theta_R$. The experimental data and predicted values by Tuteja *et al.* are not in good agreement.

The dependence of the apparent contact angle on D^* for our measurements is plotted and compared to the theoretical values based on Equation 10.1. The experimental data and the prediction are in good agreement (Figure 10.4b). The advancing contact angle was always larger than the predicted static contact angle, which in turn was larger than the experimentally measured receding contact angle for most cases. The experimental data also showed the expected non-linear dependence for low values of D^*. Our measurements support the predictions of Equation 10.1. The disagreement of the experimental data by Tuteja *et al.* with the predicted values perhaps implies a more complex dependence of the contact angle on the design parameter D^* or experimental difficulties with the measurements.

Throughout the experiments reported here, no dependence of the contact angle on the surface fraction f, the robustness parameter A^* or the overhang width O was observed. The dependence of the contact angle on the spacing ratio D^* as predicted by Tuteja *et al.*was shown experimentally. In contrast to the experiments reported by Tuteja *et al.*, the contact angle values measured for the metastable Cassie-Baxter wetting state and for the mixed mushroom and stable Wenzel wetting states varied significantly.

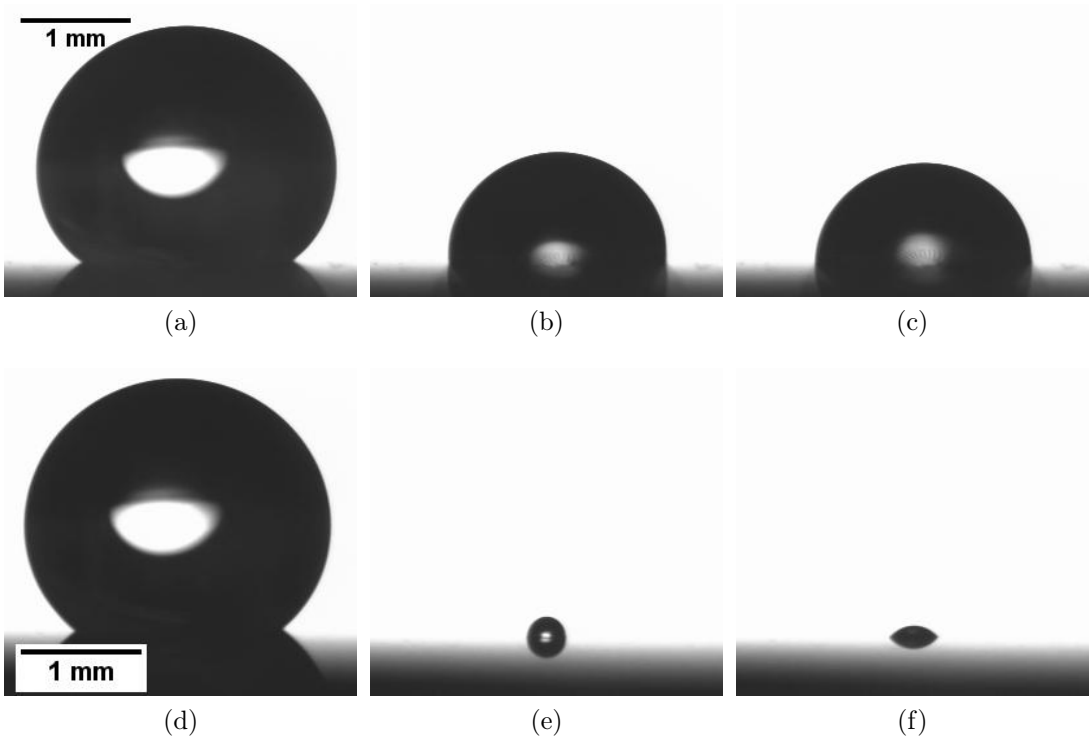

Figure 10.5: *Evaporation of a water drop on the microhoodoo surface: S190e (a-c) and S194f (d-f) (a) Original Cassie-Baxter drop as deposited (b) Last imaged drop before wetting transiton (c) Wenzel drop after transition.* $R_{critical} = 1.92\,mm$ *and* $A^* = 0.64$*; (d) Original Cassie-Baxter drop as deposited (e) Last imaged drop before wetting transiton (f) Wenzel drop after transition.* $R_{critical} = 0.35\,mm$ *and* $A^* = 1.16$

Stability of the metastable state

Tuteja *et al.* observed the evaporation of a droplet on the microhoodoo surface in order to establish the break-through pressure between the metastable Cassie-Baxter and the stable Wenzel wetting state. For water droplets with radii smaller than the capillary length of the liquid ($\lambda_{\mathrm{H2O}}(c) = \sqrt{(\gamma/\rho g)} \approx 2\,\mathrm{mm}$), the local pressure at the composite interface is given by the Young-Laplace equation (Equation 7.25). Tuteja *et al.* used the radius of the droplet before it transitioned to the Wenzel state to compute the breakthrough pressure.

We repeated this experiment. A water droplet was placed on the microhoodoo structure and allowed to evaporate under ambient conditions. A picture of the droplet was taken every $\Delta t = 2-5\,\mathrm{min}$. On most samples, a transition from the metastable Cassie-Baxter to the stable hydrophilic Wenzel wetting state was observed during evaporation.

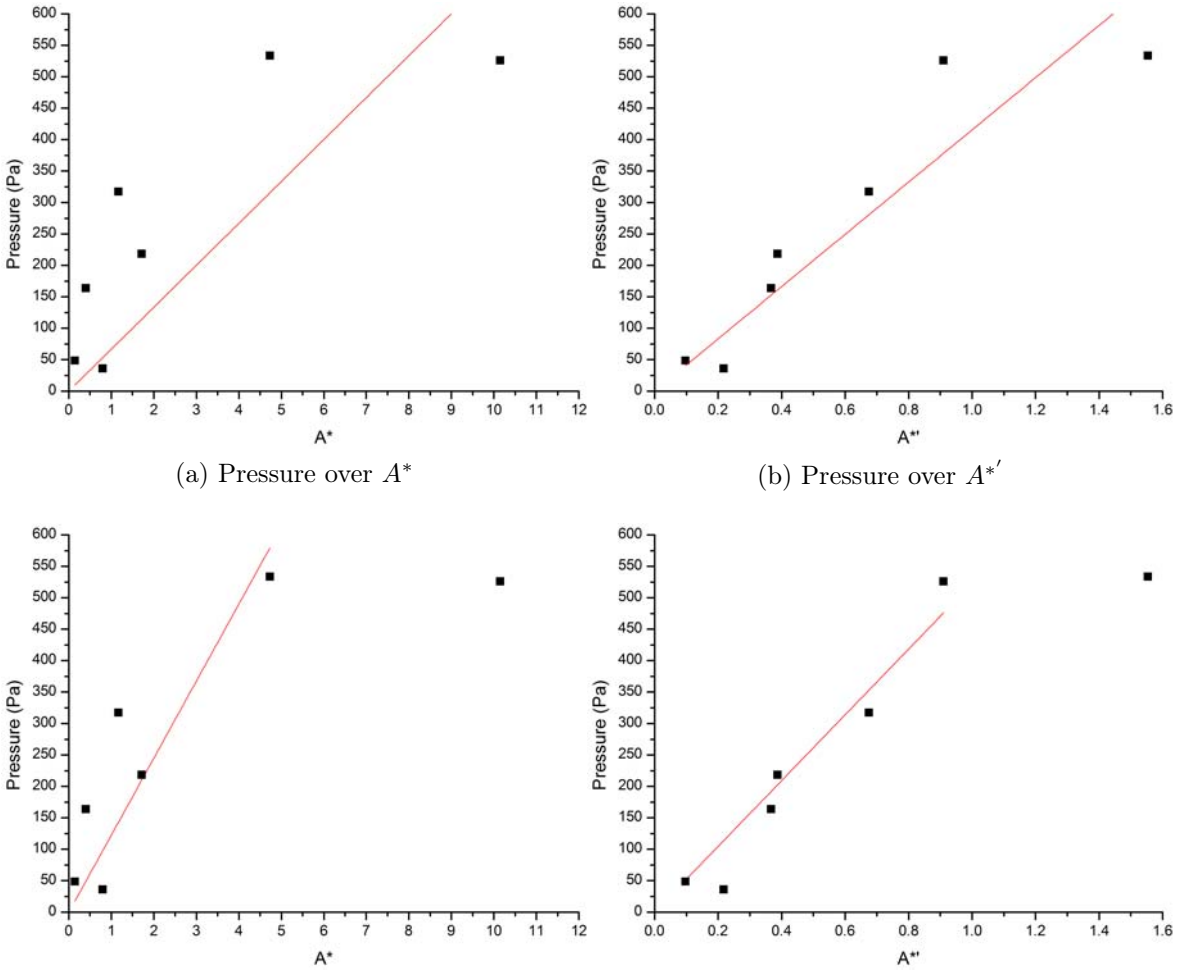

(a) Pressure over A^*

(b) Pressure over $A^{*'}$

(c) Pressure over A^* (excluded data point)

(d) Pressure over $A^{*'}$ (excluded data point)

Figure 10.6: *Pressure dependence on the robustness parameters A^* and $A^{*'}$.*

The radius of the droplet just before the transition from Cassie-Baxter to Wenzel wetting was measured and plotted as a function of the stability parameters (Figure 10.6).

Figure 10.5 shows two examples of the transition from Cassie-Baxter to Wenzel wetting during evaporation of the drop. As can be seen, the water droplets have very different radii before and after the transition occurs.

Tuteja *et al.*predicted and showed a linear relationship between the breakthrough pressure P and the robustness parameter A^*. The break-through pressure data taken for our microhoodoos did show a reasonably linear behaviour as a function of the robustness factor A^* (Figure 10.6a). Excluding the data point for high A^* improved the fit significantly (Figure 10.6c). Data points corresponding to surfaces with very high or

very low values of A^* are difficult to analyse. For low values of A^*, the break-through of the droplet is immediate. Therefore, the break-through radius is not properly defined. For high values of A^*, the drop stays in the Cassie-Baxter state for a long time, increasing the likelihood of premature break-through via a fluctuation induced transition at surface defects.

In their analysis, Tuteja *et al.* did not include the overhang width O in the stability analysis (Figure 9.2). The overhang width should have no significant effect on the apparent contact angle as seen in Section 10.1.1, but should influence the stability of the metastable Cassie-Baxter wetting state. We have therefore included the overhang width as an additional parameter in the stability analysis. For the samples measured here, the overhang width varied greatly ($0.1\ \mu\text{m} < O < 5\ \mu\text{m}$).

We have adjusted the stability equation for A^* (Equation 7.24) to include the dimensionless overhang width O^*, where $O^* = O/C$, and C is a unit length. We called this new stability value $A^{*'}$:

$$\frac{1}{A^{*'}} \approx \frac{1}{H^*} + \frac{1}{T^*} + \frac{1}{O^*} \tag{10.2}$$

Plotting the overhang pressure as a function of the adjusted robustness factor $A^{*'}$ improves the fit significantly (Figure 10.6b). Excluding the data point at high $A^{*'}$, we achieve an even better fit (Figure 10.6d). While the changes to the linear fit are only small in both cases, the associated errors decreased for both fits. The small difference is not surprising, as the dimensionless overhang width O^* is only one of three stability parameters.

The stability of the metastable wetting state was also measured for surfaces with multiple overhanging features (Figure 10.7). These were fabricated by repeated dry etching (Section 8.1.8). On these structures, the break-through pressure was not found to relate to the robustness factors A^* or $A^{*'}$. The possibility of multiple pinning made the analysis of these structures more complex.

Interestingly, many of the surfaces with multiple overhangs exhibited break-through

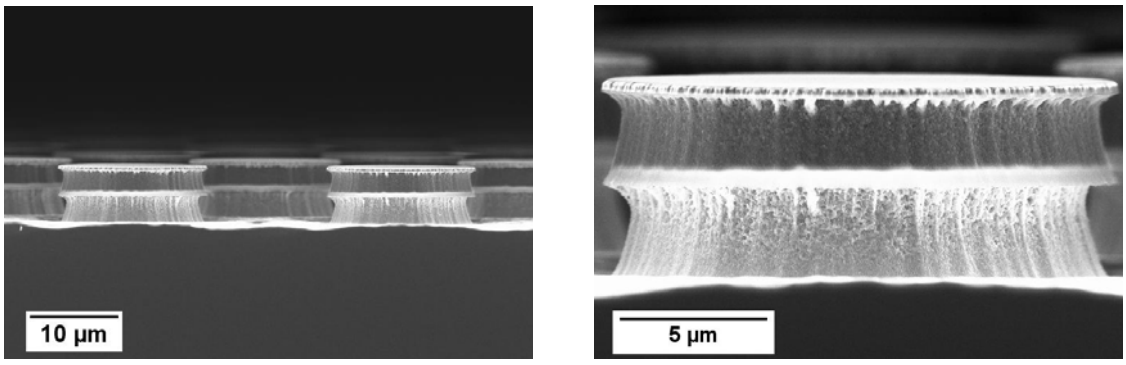

(a) Multiple microhoodoos (b) Close up of one microhoodoo

Figure 10.7: *Microhoodoos with two overhangs at different heights caused by repeated dry etching. The structure allows for repeated pinning of the contact line.*

pressures above the measurable limit of our setup ($R_{\min} \approx 0.25\,\mathrm{mm}$, $P_{\max} \approx 600\,\mathrm{Pa}$). For these samples, no Wenzel wetting state was observed during evaporation. Due to measurement limitations, the existence of a Wenzel state for radii smaller than $R_{\min}$ cannot be excluded. Many of the samples with multiple overhangs had very low stability values for A^* and $A^{*'}$. Therefore, careful design of multiple overhangs could allow for significant improvements to the stability of the metastable Cassie-Baxter wetting state on hydrophilic surfaces.

10.1.2 Negative overhanging structures: Traps

The wetting behaviour of traps (negative structures with overhangs) was investigated. An experimental study of similar structures and their wetting behaviour has not been previously reported. Figure 10.8 shows optical and SEM images of the microfabricated trap structures used for the experiments. The fabrication is described in Section 8.1.

Exploring the wetting of traps with very low or very high surface coverage was difficult. The photolithography and developing of small trap features using the positive developing procedure (Section 8.1.3) only produced low quality samples. Further, surfaces with very large holes were not stable during wetting measurements, due to the high underetching fraction. The effects of structure breakage are described in more detail in Section 10.1.4. The contact angle measurements of water droplets on inverted overhanging structures therefore only covered surface fractions from $0.35 < f < 0.75$

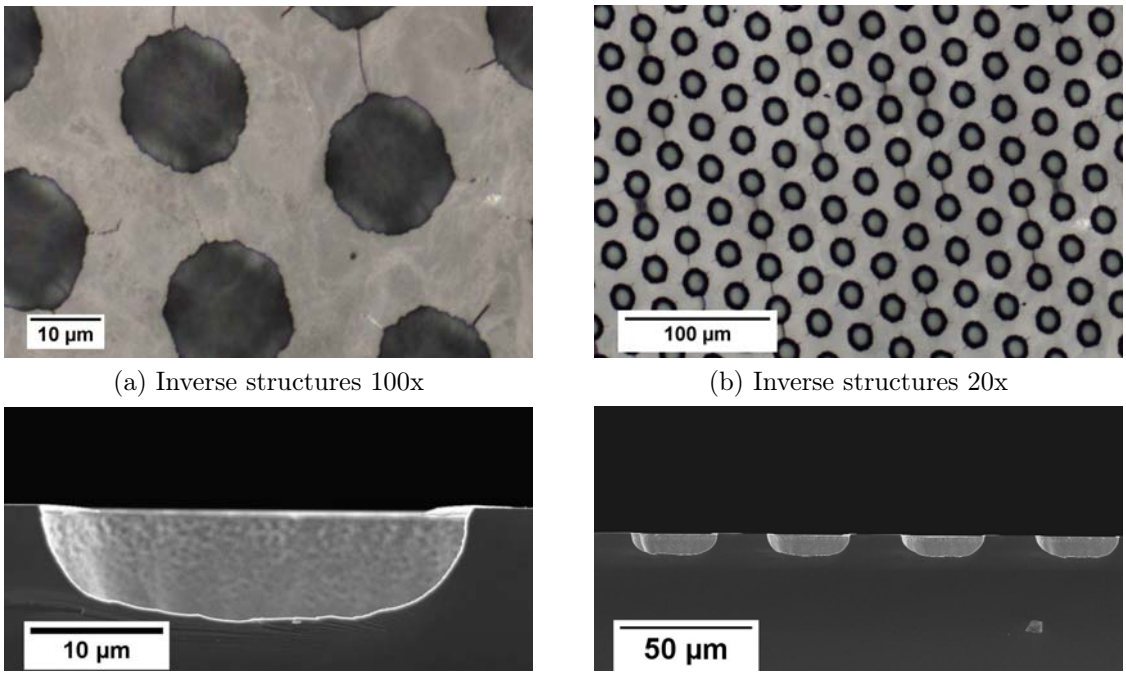

(a) Inverse structures 100x

(b) Inverse structures 20x

(c) Trap with overhangs

(d) Multiple traps

Figure 10.8: *Overhanging negative surface features (traps) in an optical microscope: Sample S173 (a) 100x objective (b) 20x objective. Crosssectional SEM image of traps: Sample 63: (c) close up of one trap (d) multiple traps*

(Figure 10.9).

Surfaces with trap structures, did not show a metastable superhydrophobic Cassie-Baxter wetting state as seen for the microhoodoo structures. Only mixed mushroom states and stable Wenzel-like wetting states were seen. A slight dependence of the advancing contact angle and the contact angle hysteresis on the surface fraction f was found: Contact angles and contact angle hysteresis were higher for smaller surface fraction areas f in contact with the water droplet as indicated by the line in Figure 10.9. Static contact angles varied greatly due to their history dependence. Therefore, advancing contact angles and the contact angle hysteresis were used to quantify the surface wetting.

Due to the large microfabricated overhangs (Figure 10.8), metastable wetting states had been expected. Two particularities of these structures could explain the fact that metastable wetting was not observed: First, the contact line exhibits important differences for inverted structures in comparison to positive structures and second, the overhanging structure of traps has a local saddle point in curvature.

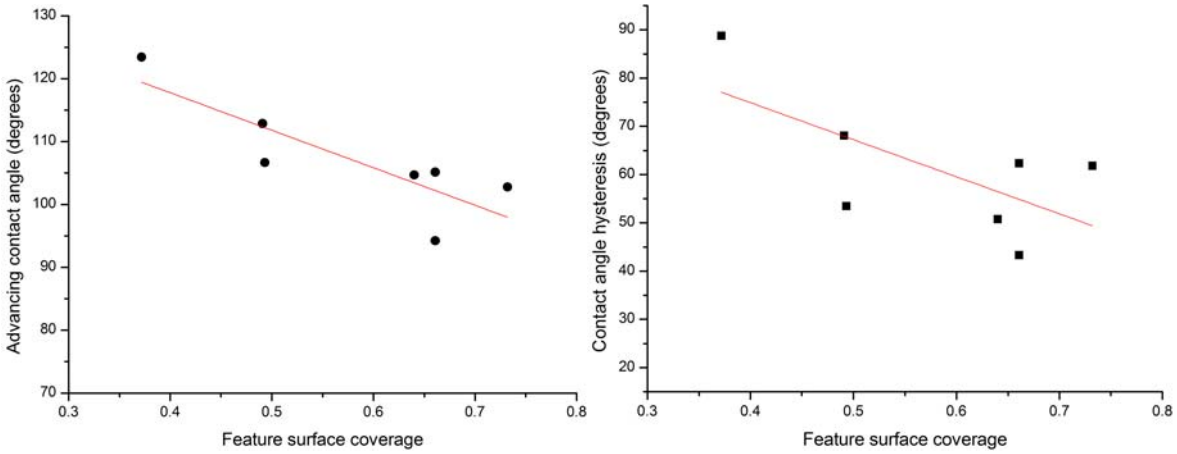

(a) Advancing contact angle (b) Contact angle hysteresis

Figure 10.9: *Wenzel wetting on microfabricated traps as a function of the surface fraction f. The contact angles are significantly below the Cassie-Baxter regime. The hysteresis is large.*

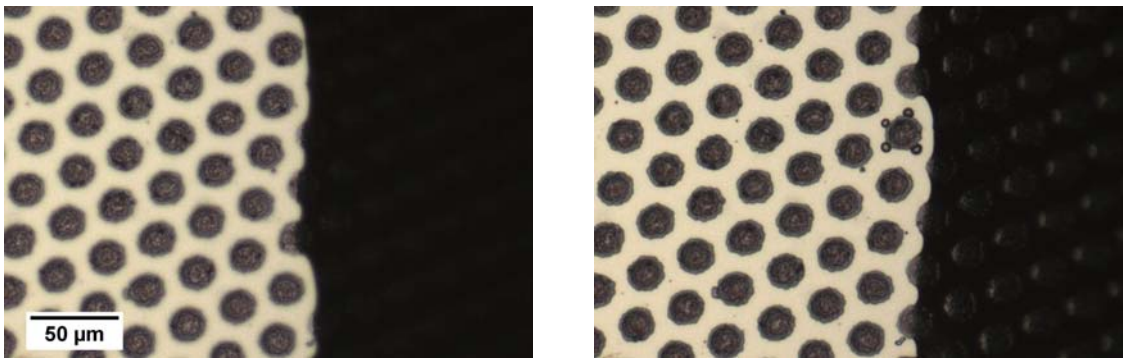

(a) (b)

Figure 10.10: *Retracting contact line on a surface exhibiting inverse features. The traps act as pinning points for the receding contact line.*

In the case of positive microhoodoo structures, the macroscopic contact line of a Cassie-Baxter drop spans between different hoodoos. The droplet is not in contact with the lower surface, but is suspended between the individual hoodoos. The microscopic contact line is therefore pinned to the hoodoo edges. For inverse trap structures, the contact line is not suspended anywhere along the circumference of wetted surface area. Therefore, the local surface condition for most points on the contact line is given by the Young's equation for a flat surface. The hollow structures underneath the drop therefore act purely as pinning points. This behaviour can be seen in Figure 10.10, where a retracting contact line on a surface with inverse structures is shown.

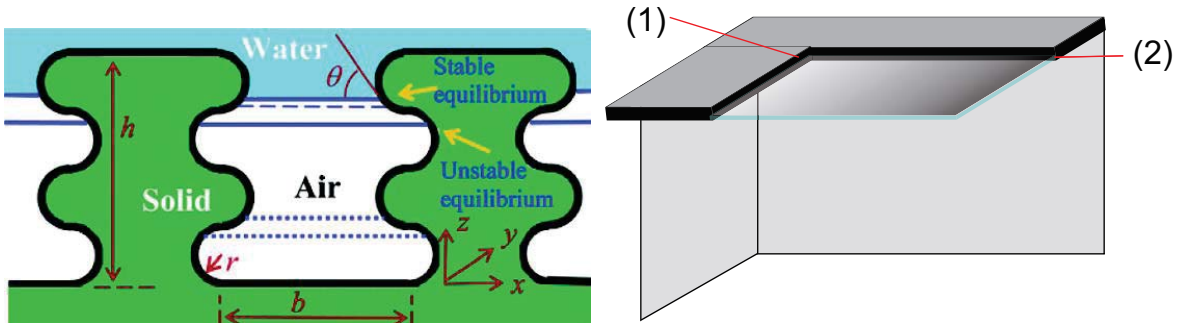

(a) Convex and concave curvature [121]

(b) Corner of trap structure

Figure 10.11: *(a) Stable versus unstable Cassie-Baxter states for a surface structure exhibiting concave and convex curvature [121] (b) Schematic showing the corner of a trap structure: (1) Corner point exhibits a saddle point: Concave and convex curvature could lead to meniscus instability (2) Flat edge exhibits only convex curvature and therefore corresponds to a stable interface*

Another explanation for the lack of metastable Cassie-Baxter wetting states on inverted surfaces was provided in theoretical work by Nosonovsky *et al.* [99]. They predicted differences in the wetting behaviour of concave and convex surface structures: Convex (bumpy) surface structures should cause a robust metastable interface, whereas a concave (groovy) surface structure causes an unstable interface (Figure 10.11a). This would explain the Wenzel wetting of traps. The corners of the trap overhangs are saddle points exhibiting concave and convex curvature, which could lead to a local instability and the instantaneous breakdown of metastable Cassie-Baxter wetting states (Figure 10.11b).

10.1.3 Positive and negative structures with no overhangs

The contact angles were measured on positive and negative structures without overhangs (Pillars and Holes) as described in Section 9.2.1. All structures were produced by removal of the overhang through wet etching (Section 8.1.5). This was carried out after the wetting behaviour of the structures with overhangs had been studied.

It was expected that structures without overhangs should display pure hydrophilic Wenzel wetting as described in Section 9.2.1. This was not the case (Table 10.1).

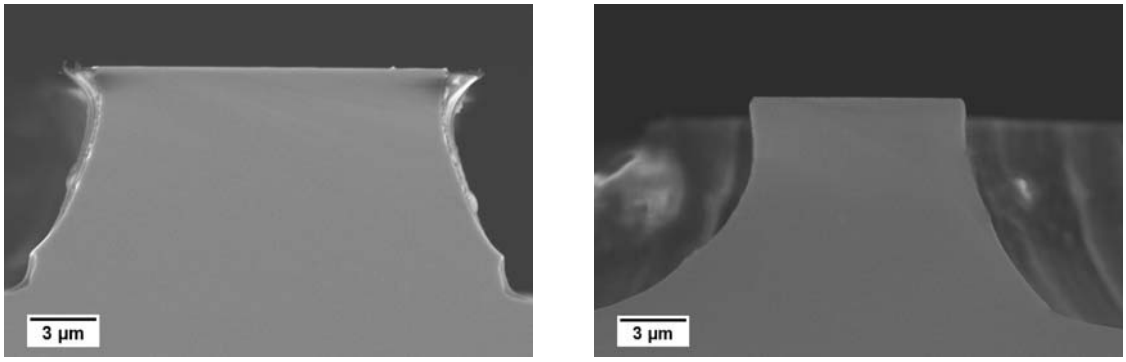

(a) Pillars (S188X) (b) Holes (S170X)

Figure 10.12: *SEM pictures of the microstructures after removal of the chromium overhangs*

Sample	Structure	Static CA	Advancing CA	Receding CA	Hysteresis
S170X	Holes	89	109	19	90
S172X	Holes	86	112	25	88
S173X	Holes	108	120	13	107
S184X	Pillars	63	65	28	36
S186X	Pillars	84	78	30	54
S188X	Pillars	86	99	21	77

Table 10.1: *Contact angles measured on structures without overhangs (holes and pillars).*

Further study of the samples showed that the etching procedure used for the sample preparation introduces a very small Si overhang due to the protection of the features by the chromium layer and slightly curved side-walls introduced by the plasma etching as reported in Section 8.1.8 (Figure 10.12). This small unevenness of the side wall seems to result in the existence of mixed mushroom wetting states. Few samples exhibited no overhanging structures (S184X). These samples showed classical Wenzel wetting (Table 10.1).

One sample (S188X) showed a very unstable Cassie-Baxter wetting state. The state was so unstable that it could not be measured. The existence of the very weak metastable Cassie-Baxter state can be explained by the overhangs in the silicon structure of the sample even after removal of the chromium layer, which were the widest for Sample S188X. This can be seen in Figure 10.12a. It can therefore be concluded that even very small overhangs allow for a metastable Cassie-Baxter wetting state.

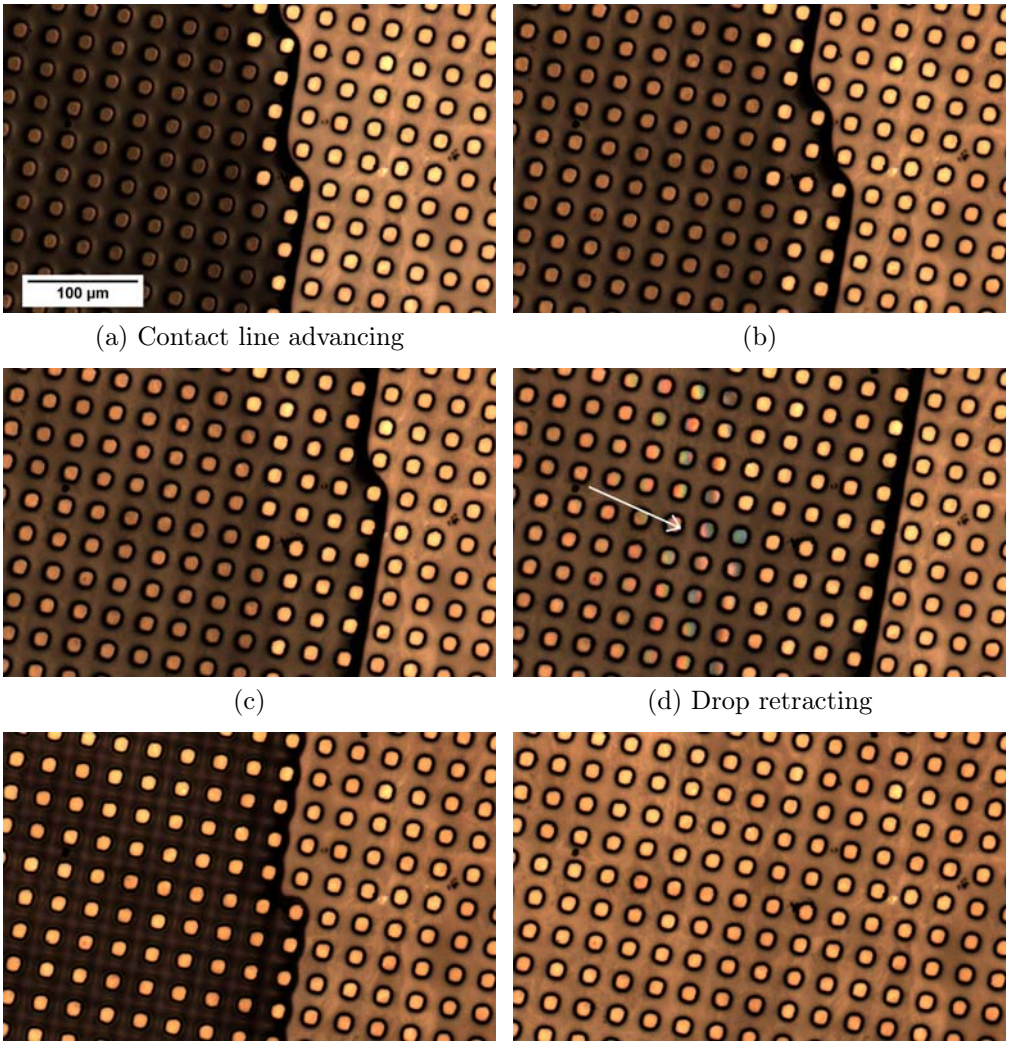

(a) Contact line advancing (b)

(c) (d) Drop retracting

(e) Contact line retracting (f)

Figure 10.13: *Imbibtion and dewetting for microhoodoo structure S144. The arrow in (d) shows the receding contact line on the microhoodoo structure. The contact line under the microhoodoos recedes later independently.*

The Cassie-Baxter wetting state was nonetheless much less stable than reported for the original sample with 1.8 µm overhangs, as it could not be measured before breakthrough. The difference between the stability of the wetting state before and after removal of the chromium overhang is another indication that the stability parameter A^* might have to be modified, as suggested in Section 10.1.1, to $A^{*'}$ in order to include the influence of the overhang width on the wetting state stability.

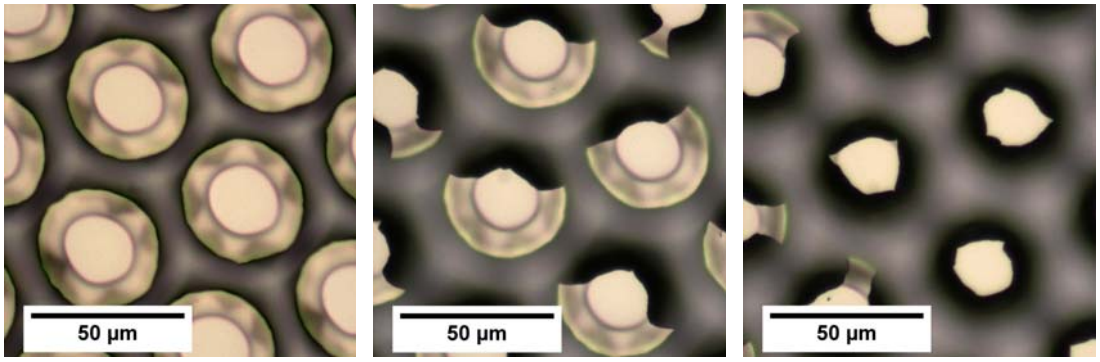

(a) Before exposure to water

(b) Breakage of structures indicates force direction during deposition or evaporation

(c) Breakage of structures in central area due to high impact forces

Figure 10.14: *Microhoodoos before and after exposure to water drop: For thin overhangs, capillary forces are strong enough to break the structure.*

10.1.4 Imbibtion, break-off, and other phenomena

Many samples with hoodoo geometries experienced strong Wenzel wetting behaviour, once the metastable Cassie-Baxter state had broken down. In particular, this led to very high contact angle hysteresis and imbibtion of the structures as described by Quere [88], with the contact lines following the post structure as shown by Dorrer *et al.* [80]. Figure 10.13 shows the changes during spreading and retracting of a drop: The series covers a time span of approximately 10 min. The contact line always follows the microhoodoo structures.

During the spreading phase, the contact line slowly moves forward (Figure 10.13a-10.13c) until it reaches the maximum extension of the drop (Figure 10.13d). Now, the drop starts receding, while the imbibtion layer stays extended, as can be seen by the retracting interference and the change in colour of the hoodoo structures (Figure 10.13d, retracting contact line indicated by arrow). At this point, the drop corresponds to the 'Sunny-side-up drop' mentioned by Ishino *et al.* (Section 7.2) [76]. The drop then recedes quickly due to evaporation (Figure 10.13e-10.13f).

Early samples were produced with relatively thin layers of chromium ($d_{\mathrm{Cr}} < 100\,\mathrm{nm}$). These layers showed significant stability problems due to breaking of the overhanging structures under capillary forces. The changes to the surface after deposition of a drop

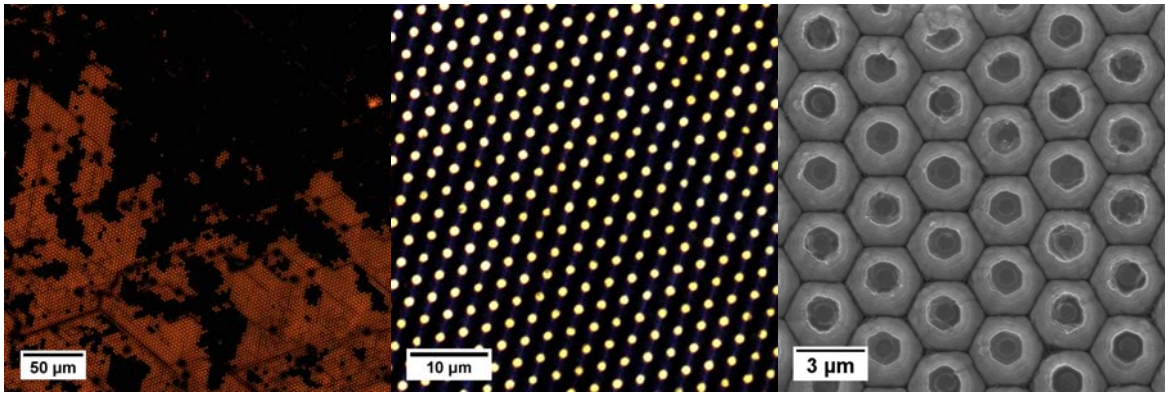

(a) 20x magnifcation (b) 100x magnification (c) SEM image

Figure 10.15: *Colloidally patterned surface after ion-milling and removal of colloids but before dry etching (a) Areas with perfect colloidal patterning, cracks and unpatterned areas (b) Close up of successful colloidal patterning (c) SEM image of the structure*

on the surface can be seen in Figure 10.14. This showed that thicker overhangs are necessary to produce microfabricated structures for the investigation of surface wetting. Further, this problem shows that careful evaluation of the thickness of the overhanging structure is necessary for technologically interesting surfaces, as a compromise between wetting properties and stability will need to be found.

10.2 Colloidal microhoodoos

Colloidal microhoodoos were prepared as described in Section 8.1. Samples prepared by the colloidal patterning technique showed promise over small areas of the pattern (Figure 10.16b), but difficulties for large area measurements (Figure 10.16a). The colloidal films exhibited cracks during formation, which were transfered during ion milling (Figure 10.15a). Additional issues were the removal of colloids stuck to the patterned film, as well as non-patterning due to multi-layers of the colloidal mask prior to ion milling.

Dry etching of these masks yielded structures corresponding to the masking pattern. In Figure 10.16, perfectly formed microhoodoos can be seen next to areas exhibiting large etching problems. The microhoodoo size was dependent on the ion milling time.

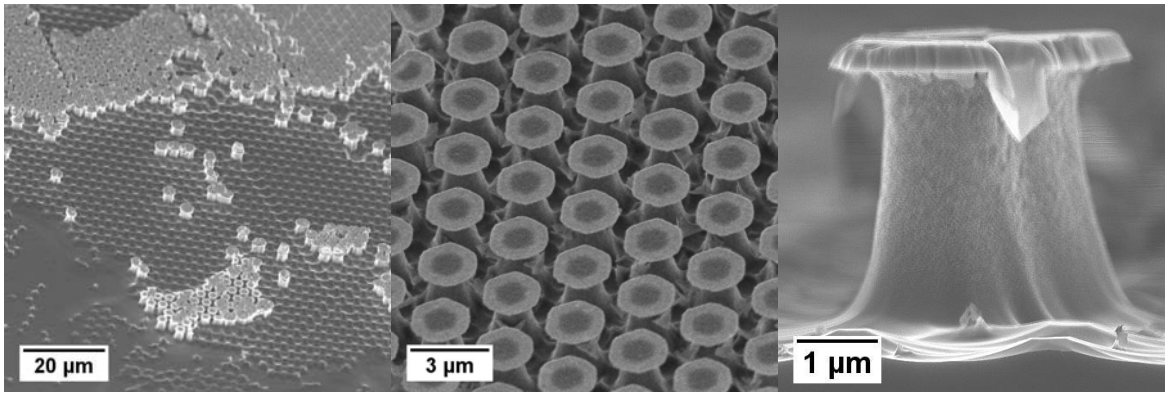

(a) (b) (c)

Figure 10.16: *Finished microhoodoo structures produced from masks made using colloidal monolayers. (a) Large area of microhoodoos showing different patterning difficulties. (b) Close up (45°) of successful microhoodoos produced by colloidal patterning (c) Cross-sectional image of one microhoodoo showing underetching.*

Hoodoos were produced with a top width of $W = 1.5 - 4$ µm. The ion etching of very small features often caused a distortion of the plasma field, which prevented undercutting for many samples. Only a few samples with a perfect hoodoo geometry as given in Figure 10.16c were achieved.

Due to the low surface coverage of perfect hoodoos arrays, resulting defects in the colloidal layers, wetting measurements proved to be difficult. Microhoodoos were silanised as before (Section 8.1.9). Measurements of the surface wetting remained inconclusive. Only one sample was found to exhibit a mixed Cassie-Baxter and Wenzel surface wetting state. This sample was the only surface were a large area of overhanging features was achieved. Due to the high value of H^* and T^*, the calculated robustness factor A^* for this sample was very high ($A^*_{\text{Hoodoo}} \approx 150$). Nonetheless, the wetting state observed on the surface was not a pure metastable Cassie-Baxter wetting state, but a mixed Cassie-Baxter and Wenzel mushroom wetting state (R3). All other samples had advancing and receding contact angles below $\theta < 90°$ (Table 10.2).

In order to obtain a better understanding of wetting on small microhoodoos like these, the difficulties experienced in the production of the samples must be resolved. This requires large areas of defect free colloidal monolayers and a better understanding of the ion milling timing. Further, the etching parameters given in Section 8.1.8 must

Sample	Advancing CA	Static CA	Receding CA
R3 - 3 µm	136	139	30
R4 - 3 µm	95	71	24
R5 - 3 µm	75	66	58
R7 - 5 µm	83	74	51
R8 - 3 µm	73	63	20

Table 10.2: *Contact angles (in degrees) for wetting behaviour on microhoodoos produced by colloidal self-assembly, Measurement error* $\pm 5°$.

be readjusted for very small structures.

A systematic study of this system allows for wetting measurement on very small microhoodoos (which according to Tuteja *et al.* [1] should have very high D^* and very high A^* values) and should therefore be the ideal system for long lived metastable wetting states.

10.3 Inverse colloidal structures

Wetting on inverse colloidal structures was tested as described in Section 9.2.1. The experimental results reported here are covered in detail by Holtzmann [105]. Plating metals (gold or platinum) into the interstitial space in colloidal layers was considered a promising approach to study metastable wetting on a second inverted surface structure. The sample preparation was described in Section 8.1. The metal was plated into the colloidal layer (Figure 10.17a). The colloids were removed, leaving an inverse structure of the original layer (Figure 10.17b). Figure 10.17b shows the large number of defects inherent in this method.

In prior work, Abdelsalam *et al.* [104] studies the wetting of these inverse colloidal films. The contact angle measurements were analysed as a function of the filling height ξ. Electroplating through a complete monolayer corresponded to $\xi = 1$. A sample with $\xi = 0.25$ has therefore a filling height to $1/4$ of the monolayer height. The results by Abdelsalam *et al.* (Figure 10.18a) showed a strong dependence of the contact angle on the ξ. Further, the gold surface showed Cassie-Baxter wetting states, even though

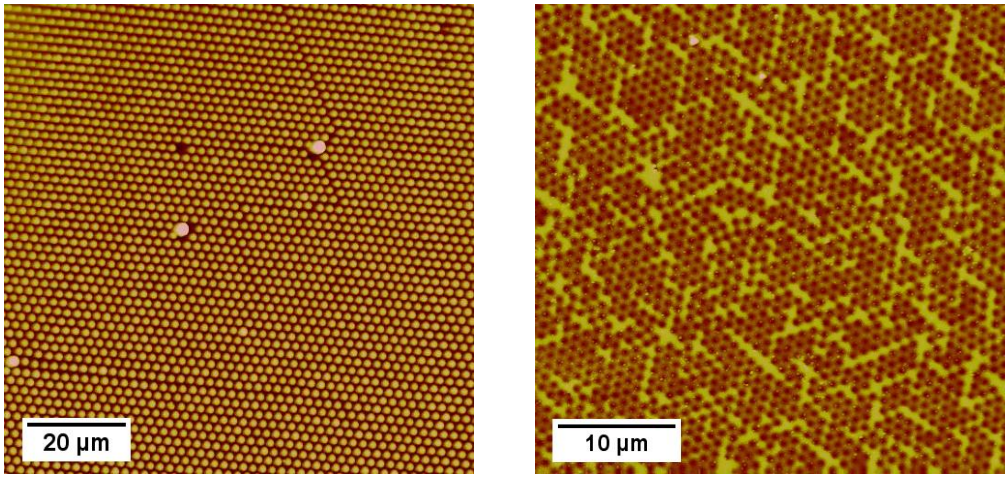

(a) Colloidal film (b) Inverse electroplated film

Figure 10.17: *AFM image of colloidal structuring (a) Colloidal self-assembled film with 3 µm colloids (b) Inverse electroplated structures with 600 nm holes.*

gold is a hydrophilic material. In addition, the highest contact angles were measured for structures near the 50% filling height. These structures have no overhangs and therefore should not exhibit metastable Cassie-Baxter wetting states for hydrophilic surfaces.

A qualitative prediction of the Cassie-Baxter wetting states on hydrophobic and hydrophilic inverse colloidal structures is given in Figure 10.18. If metastable Cassie-Baxter wetting states could exist on inverse colloidal films, these should only be found for structures with overhangs. Overhangs exist for all filling height $\xi > 0.5$, but not for $\xi < 0.5$. Therefore, Figure 10.18c shows a cross-over point from pure Wenzel wetting to metastable Cassie-Baxter wetting. Further, the results in Section 10.1.2 suggest that no metastable Cassie-Baxter wetting should be found on inverse structures, which allow for a fully connected contact line.

Figure 10.18b shows the prediction for Cassie-Baxter wetting on a hydrophobic inverse colloidal surface structure as a function of filling height ξ. As can be seen, the prediction corresponds very well to the experimental results by Abdelsalam *et al.* (Figure 10.18a). It seems likely, therefore, that the gold surface, which had not been passivated in the experiments, was contaminated with hydrophobic materials, for example machine oils.

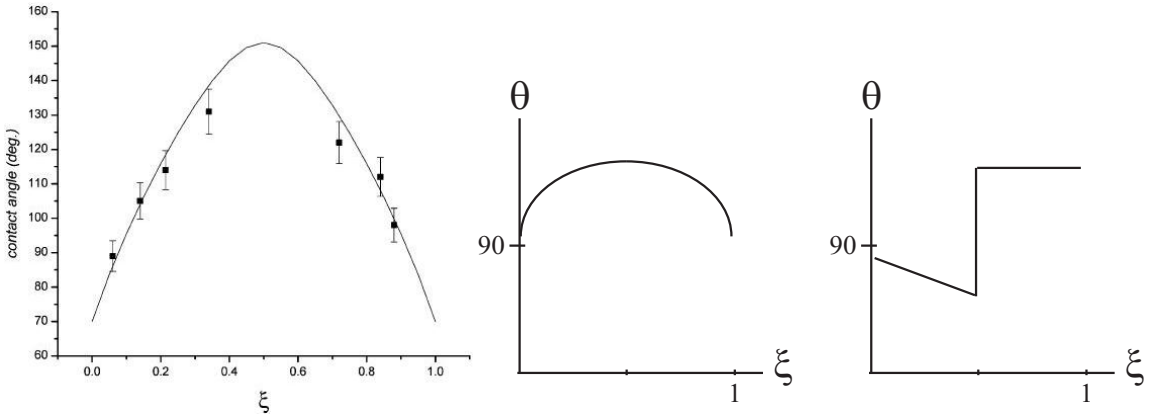

(a) Experimental results [104] (b) Hydrophobic prediction (c) Hydrophilic prediction

Figure 10.18: *Contact angles θ on inverse colloidal structures as a function of monolayer filling height ξ: Comparison of experimental results and theoretical explanation (a) Contact angle measurements by Abdelsalam et al. [104] (c) Qualitative prediction for Cassie-Baxter wetting on a hydrophobic surface (d) Qualitative prediction for stable Wenzel and metastable Cassie-Baxter wetting on a hydrophilic surface.*

In order to resolve the inconsistency, we attempted a repeat experiment. The production of large areas of inverse colloidal structures was problematic, due to difficulties with the electroplating into the colloidal film. Very few structures were produced with large enough areas to test their wetting behaviour. Only very few samples could be used. Thiolation of these samples (Section 8.1.9) yielded contact angles close to $\theta_Y = 91°$.

Due to the high inherent contact angle of the thiolated surface, the resulting data could not be used to determine the wetting of hydrophilic inverse structures. The measured contact angles θ_S for the surfaces were between $105° - 140°$. No contact angles θ_S were measured below 90°. Therefore, the behaviour corresponds to Cassie-Baxter wetting on a hydrophobic surface, as shown in Figure 10.18b.

A repetition of the experiment with better control of the surface chemistry is necessary, to establish the wetting behaviour of hydrophilic inverse colloidal films with overhangs.

10.4 Surface wetting : Discussion

The wetting behaviour of water droplets on different surfaces was explored in this chapter and compared to wetting theory (Chapter 7). Measurements described here were based on contact angle measurements (Section 9.2.1).

Measurements of surface wetting phenomena on lithographically fabricated microhoodoo arrays (Section 10.1.1) were compared to the measurements performed by Tuteja *et al.* [1]. Metastable wetting states were observed for most samples. Contact angles and metastable state stability were analysed with respect to the design parameters D^* and A^*. While some measurements confirmed the experiments conducted by Tuteja *et al.*, others did not.

The independence of the contact angle on the stability parameters A^* was confirmed. The dependence of the contact angle on the spacing ratio D^* had not been convincingly shown by Tuteja *et al.*, but was confirmed in our experiments. Evaporation measurements yielded Cassie-Baxter to Wenzel wetting transitions. The predicted dependence of the break-through pressure on the stability parameter A^* could be improved by inclusion of the dimensionless overhang width O^* into a new stability parameter $A^{*'}$. This improved the fit of the data, and yielded a very good linear dependence of the break-through pressure P on the new stability parameter $A^{*'}$. Measurements on microhoodoos with multiple overhangs exhibited the highest break-through pressures observed. Careful design of microhoodoos with multiple pinning lines could allow for highly robust metastable wetting states.

The dependence of the break-through pressure P on the overhang width O was confirmed, when measurements of samples with very small overhangs were taken. Removal of the chromium layer left small overhanging features for many hoodoo surfaces. However, the surfaces showed significantly smaller break-through pressures after removal of the chromium overhang. Therefore, the overhang width has a direct influence on the stability of the metastable Cassie-Baxter wetting state. Further experiments are necessary to verify the dependence of the break-through pressure on the overhang width

O.

The wetting behaviour of water droplets was also observed on lithographically fabricated trap structures (Section 10.1.2). No metastable Cassie-Baxter wetting states were observed. This was attributed to the continuous contact line and the saddle point of the trap structure in the overhang corner. Both of these factors are predicted to strongly limit the possibility of metastable wetting states.

Very small microhoodoo structures were fabricated using self-assembled colloid films as a surface patterning technique (Section 10.2). The method was promising, as the small feature size and large aspect ratio should allow for very high energy barriers for the Cassie-Baxter to Wenzel transition. The A^* values calculated for these small features were very large. The experimental results, however, showed the difficulty in exploiting surfaces with structural defects, as only one mixed mushroom states and no pure metastable Cassie-Baxter wetting states were observed on the microhoodoo surface. This was attributed to the large quantity of defects, which originated from defects in the colloidal monolayer.

Experiments on the wetting of surfaces based on self-assembled colloidal films were also conducted on inverse colloidal structures prepared by electroplating (Section 10.3). While the experiments were inconclusive, qualitative arguments suggest that the wetting states observed by Abdelsalam *et al.* were due to hydrophobic surface contamination. Further work repeating the wetting experiments on hydrophilic inverse colloidal structures is needed to confirm the theory of inverse surface structure wetting.

11 Wetting on *Antirrhinum* flower petals

This chapter explores the wetting behaviour on two genotypes of *Antirrhinum* flower petals. The work described here was part of a general study looking at the physical properties of *Antirrhinum* flower petals. The influence of structure on the physical properties of the petals, in particular wettability and thermal behaviour, were studied to improve the understanding of the interaction between the flower and potential pollinators. The complete work, including the thermal behaviour, can be found in Whitney *et al.* [122].

Contact angle measurements were performed on two different *Antirrhinum* lines, the wild type (mx^+Nv^+) and the mixta mutant genotype (mx^-Nv^+), in order to establish, whether there is a difference in wetting behaviour of the two flower petals. The two lines differ only in the shape of petal cells. The colour of the two flower lines is nearly the same and both have identical cuticular wax composition. Any difference in wettability can therefore be attributed solely to the difference in petal cell shape. These experiments were performed to establish how the structure of the petal epidermis and the presence or absence of conical cells influences petal wettability.

The petal cell shape directly determines the surface roughness, as can be seen in Figure 11.1. The mixta petals are formed of very flat conical cells [123], whereas the wild cells are conical in shape and protrude from the surface.

The influence of petal structure on surface wetting was studied by comparing wetting measurements of the wild (mx^+Nv^+) and the mixta (mx^-Nv^+) Antirrhinum genotypes.

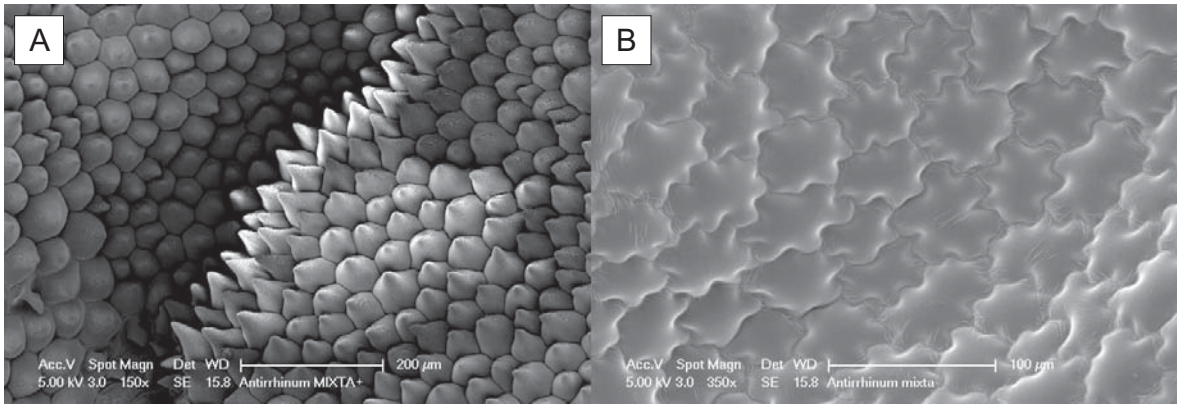

Figure 11.1: *SEM images of Antirrhinum flower petals (A) the wild type (mx^+Nv^+) and (B) the mixta mutant (mx^-Nv^+) [122]*

11.1 *Antirrhinum* wild type (mx+Nv+)

Measuring the wetting behaviour on *Antirrhinum* flower petals, we found three distinct wetting behaviours for fresh wild type petals. These are shown in Figure 11.2.

Thirty-one measurements were taken using ten flower petals. The behaviour of the drops on the petals mostly corresponded to Wenzel wetting (drop behaviour C), however Cassie-Baxter wetting (drop behaviour A) and partial Cassie-Baxter partial Wenzel wetting (drop behaviour B) were also seen. All wetting behaviour observed corresponded well to the standard wetting regimes seen on hydrophobic surfaces. The mixed wetting state probably corresponds to the mushroom wetting state introduced by Ishino *et al.* (Figure 7.6) [76]. Pure Cassie-Baxter wetting was observed on four occasions, the mixed state was observed seven times and pure Wenzel wetting was observed twenty times. The results are given in Table 11.1.

Differences in the wetting observed could be a result of small changes in the surface roughness from petal to petal and area to area.

Wetting behaviour	Advancing CA	Receding CA	Hysteresis
Pure Cassie-Baxter	148 ± 6	109 ± 22	39
Mixed mushroom state	140 ± 18	91 ± 16	50
Pure Wenzel	135 ± 17	73 ± 19	52

Table 11.1: *Contact angle measurements (in degrees) for the three wetting states found on Antirrhinum wild type (mx^+Nv^+).*

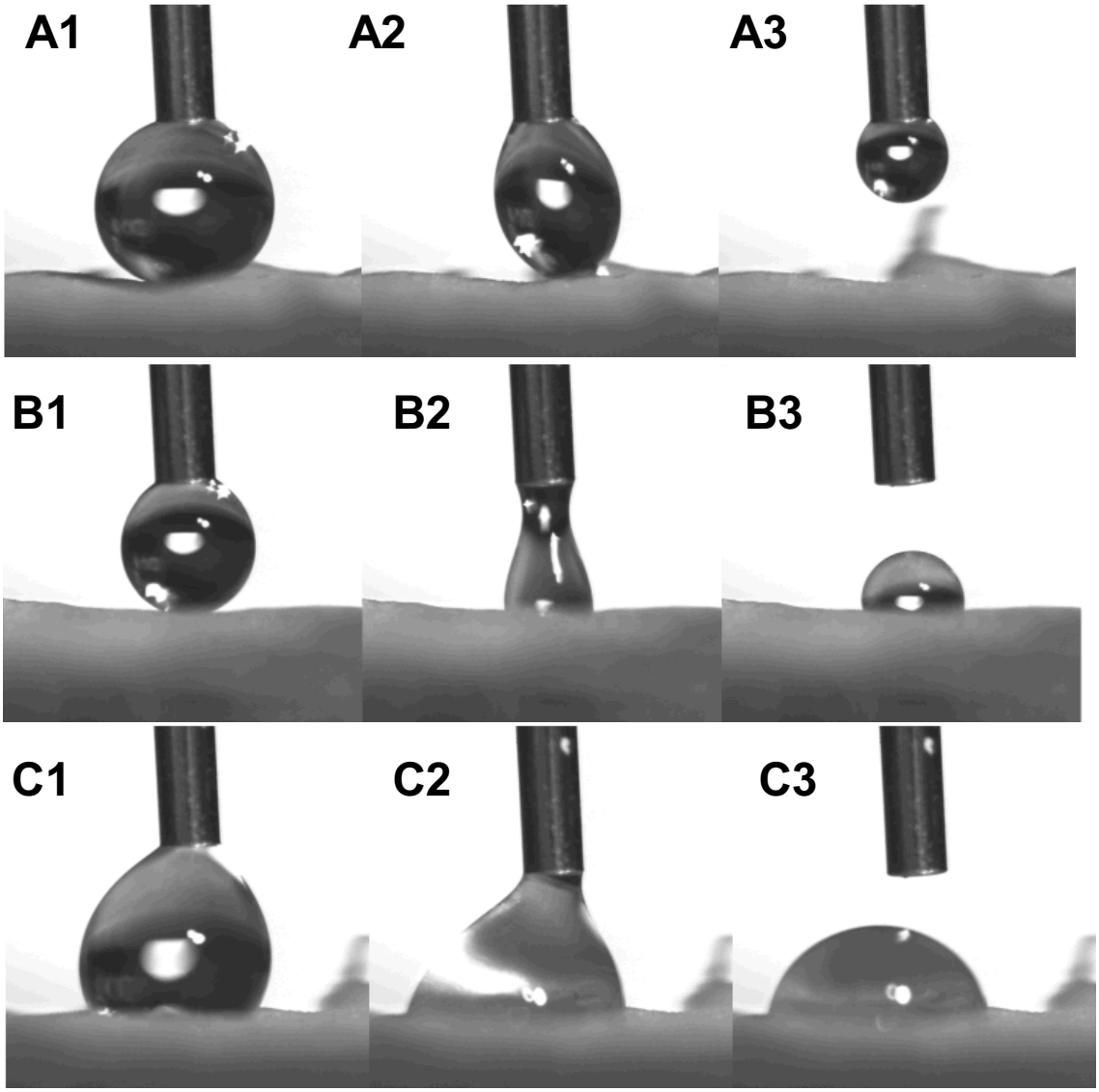

Figure 11.2: *Images are for advancing (1), receding (2, 3) drops.* ***Drop behaviour A*** *(1, 2, 3): The drop shows very high advancing contact angles and receding contact angles greater than 90°. The drop can be completely removed from the surface without rupture. This behaviour corresponds to a Cassie-Baxter wetting state.* ***Drop behaviour B*** *(1, 2, 3): The drop shows very high advancing contact angles and high contact angles greater than 90°. Part of the drop recedes and part sticks to the surface. This behaviour can be explained by pinning or by mixed Cassie-Baxter mixed Wenzel wetting.* ***Drop behaviour C*** *(1, 2, 3): The drop shows high advancing contact angles. The receding contact angle is less than 90°. The hysteresis is very large. This behaviour corresponds to hydrophobic Wenzel wetting. When receding, a small amount of the drop remains on the surface with a static contact angle below 90° and then spreads.*

The existence of three different wetting behaviours on the surface and the small differences between the contact angles measured for the three states, suggests that the surface has two energy landscape minima. While the dominance of Wenzel wetting suggests that the Wenzel minimum is the global minimum, the wetting behaviour is characteristic of the cross-over regime between Wenzel and Cassie-Baxter wetting, where small surface changes or impact changes can cause changes to the wetting behaviour.

11.2 *Antirrhinum* mixta mutant type (mx-Nv+)

The wetting behaviour observed on the mutant genotype *Antirrhinum* mixta ($mx^{-}Nv^{+}$) flower petals was less complex than for the genotype *Antirrhinum* wild type ($mx^{+}Nv^{+}$). Fourteen measurements were taken using ten flower petals. For mixta, all fourteen measurements showed Wenzel wetting on hydrophobic surfaces (drop behaviour C). Two additional measurements were discarded from the analysis due to analysis difficulties.

The static contact angles for mixta ($mx^{-}Nv^{+}$) were relatively reproducible. The results are shown in Table 11.2.

Wetting behaviour	Advancing CA	Receding CA	Hysteresis
Pure Wenzel	120 ± 14	74 ± 14	45

Table 11.2: *Advancing and receding contact angles and contact angle hysteresis (in degrees) measured for the genotype Antirrhinum mixta mutant.*

11.3 *Antirrhinum* wetting explanation

The two *Antirrhinum* lines showed distinctly different wetting behaviour. The measurements conducted on the mixta mutant ($mx^{-}Nv^{+}$) showed pure Wenzel wetting. The wild type ($mx^{+}Nv^{+}$) showed pure Cassie-Baxter, mixed Cassie-Baxter and Wenzel and pure Wenzel wetting. Wenzel wetting was the dominant wetting behaviour on the surface. The contact angles measured on the wild type were significantly larger

than on the mutant mixta.

The differences in wetting behaviour of the two *Antirrhinum* lines correspond well to the wetting theory explained in Chapter 7. The higher roughness of the wild type, as seen in Figure 11.1 increases the inherent surface hydrophobicity. While the wild type petals are not self-cleaning, their high contact angles could allow for easier water removal and less contamination of the surface compared to the mutant type. Further, the difference in surface wettability might be an important factor in the distinction between the two flower petals by pollinators [122].

12 Underwater wetting - Results

This chapter discusses the results from our underwater wetting experiments performed on various superhydrophobic surfaces.

The stability of a plastron (air-film covering a surface under water) was studied quantitatively on superhydrophobic Teflon surfaces in an immersion tank setup (Section 12.1). The results of these experiments were compared to the qualitative study of the stability of plastrons on other superhydrophobic surfaces (Section 12.2). The stability of the plastron on Teflon surfaces was further examined by confocal microscopy (Section 12.3). In Section 12.4, the wetting of water droplets on the superhydrophobic Teflon surfaces before and after long-term immersion in H_2O is explored via contact angle measurements. Section 12.5 offers some theoretical qualitative explanation for the phenomena observed experimentally in the other sections. A summary of the experimental results and a comparison to the qualitative theoretical explanation is offered in Section 12.6.

12.1 Underwater plastron on Teflon surfaces

Superhydrophobic Teflon samples were prepared according to the protocol discussed in Section 8.2.1 and observed in an immersion column as described in Section 9.2.2. The plastron was not stable under the experimental conditions; all samples showed a decay of the plastron with time. The stability of the plastron was analysed through observation of the change in intensity of the plastron reflectivity. The sample surface was imaged and the plastron surface coverage was measured as a function of the initial

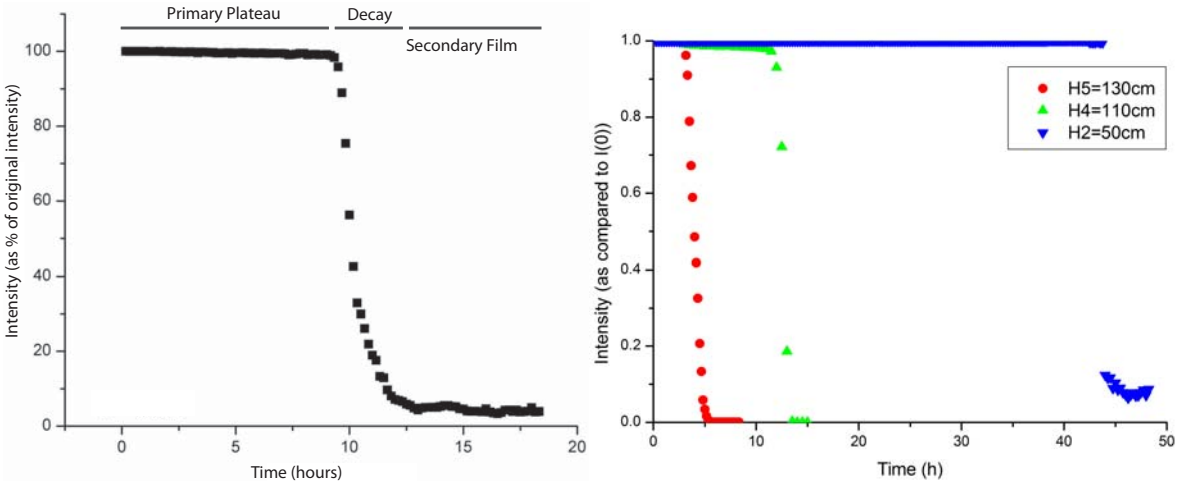

(a) Sample 090318 (b) Sample 090309

Figure 12.1: *(a) Decay of intensity measured on Sample 090318. (b) Intensity decay for three different immersion depth. It can be seen that the decay is very rapid and the plateau long.*

coverage. The plastron reflection intensity was plotted as a function of immersion time.

Most samples exhibited a non-linear loss of the plastron. The intensity of the plastron reflection was found to stay constant (with minor fluctuations) for a very long time (plateau, Figure 12.1a). This was then followed by a relatively rapid change of intensity (decay, Figure 12.1a). In general, the intensity change over time could be described by a stable region (plateau), where no significant changes to the plastron could be seen, and an unstable region (decay), where a fast change was observed. The plateau lasted hours to weeks; the decay occured within hours (Figure 12.1b).

The total plastron life-time t_{Tot} was defined as the sum of the stability plateau time t_{stable} and the decay time t_{decay} ($t_{\mathrm{Tot}} = t_{\mathrm{stable}} + t_{\mathrm{decay}}$). A few samples showed multiple plateau and decay regions, perhaps due to coating quality differences.

A very thin stable secondary air-film was often present on the samples even after the primary plateau and decay (Figure 12.1). This film was characterised by a very low plastron reflectivity (normally less than 10% of the initial plastron reflection intensity). The secondary air-film was attributed to an additional roughness on a smaller lengthscale (Section 12.5, Figure 12.17).

Secondary air-films were more prominent for samples immersed to low depths up to

80 cm. The secondary air-film was excluded from the life-time analysis of the plastron on Teflon surfaces. This was done in order to avoid difficulties with the data comparison at smaller and larger immersion depths, the air-film stability was measured when 50% and when 90% of the original reflection intensity had been lost. These data points should not be influenced by the presence or absence of a secondary air-film. However, for some samples, a secondary air-film may have been unknowingly included in the stability analysis.

Two general statements can be made about the underwater plastron stability:

1. The plastron was less stable in flowing water than in still water.
2. The plastron stability decreased with immersion depth

These observations will be discussed and analysed in depth in later sections. Some qualitative observations are noted here:

Samples removed from the watertank often showed a loss of hydrophobicity. For some samples no change could be seen, while other samples showed a significant change of their wetting behaviour. The effect and possible methods for superhydrophobicity recovery are discussed in Section 12.4.

In general, the primary air-film on the samples was found to be relatively even and flat. For some samples, the air-film showed bubble formation. In many cases, the upper edge of the sample supported the growth of one large bubble. Edge bubbles were found to grow with time and rip off at some point. After lift-off of the edge bubble, the surface area still exhibited a normal plastron. The growth of large surface bubbles could be due to Oswald ripening.

Rarely, bubble growth was seen for other sample areas. Central bubbles were only observed in experiments, where light sources were placed too close to the immersion tank setup, causing localised heating. While the edge bubbles did not influence the air-film stability measurement, the central bubbles disrupted the normal decay process. Experiments exhibiting central bubble formation were excluded from the data analysis.

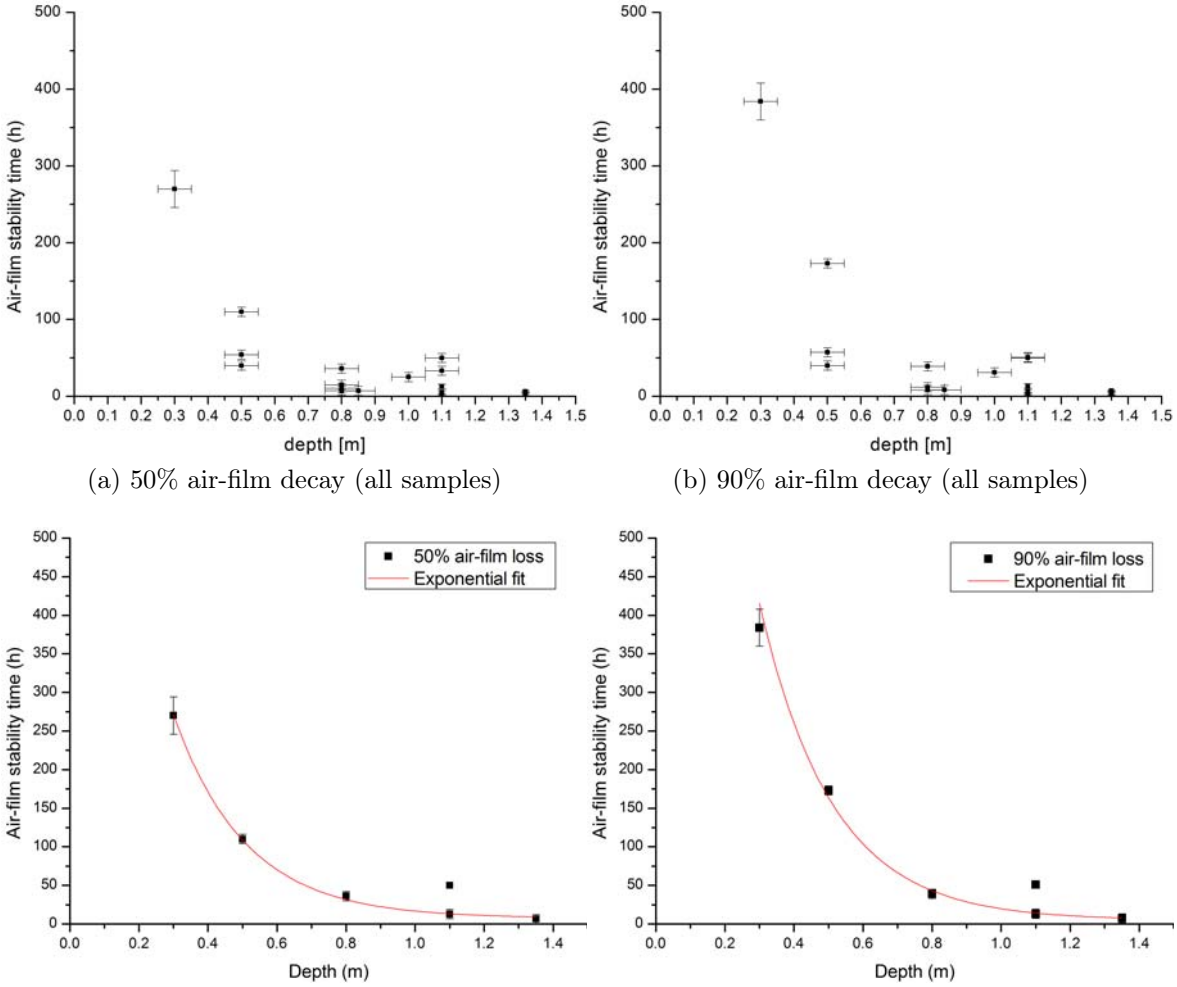

(a) 50% air-film decay (all samples)

(b) 90% air-film decay (all samples)

(c) 50% maximum life-time

(d) 90% maximum life-time

Figure 12.2: *Depth dependence of the plastron stability for still water: (a)+(b) Air-film dissolution data (c)+(d) Maximum time for each immersion depth and fit.*

The quality of the water before and after the experiments was checked. The water stayed clear and no significant changes to the water quality could be measured. The conductivity of the water in the immersion column was measured before and after experiments. It was found that even for experiments lasting two weeks, only a small change to the conductivity could be observed ($\sigma_\mathrm{i} = 1.34 \pm 0.05\,\mathrm{S/m}$, $\sigma_\mathrm{F} = 2.4 \pm 0.1\,\mathrm{S/m}$).

Still water

The observed intensity change was used to measure the depth dependence of the plastron stability time. Figure 12.2 shows the life-time of the plastron as a function of

immersion depth for all samples measured in fresh still water (early measurements were excluded due to comparability issues with respect to water quality). In Figure 12.2a and 12.2b, we can see that the plastron stability depends on immersion depth. The stability time for 90% plastron intensity for a small immersion depth of $H(1) = 30\,\mathrm{cm}$ is significantly larger than for a large immersion depth $H(5) = 135\,\mathrm{cm}$ ($t_{\mathrm{Tot,\,S}}(1) = 384\,\mathrm{h} = 2\,\mathrm{days}$, $t_{\mathrm{Tot,\,S}}(5) = 7\,\mathrm{h}$).

The differences in stability times measured at one immersion depth were attributed to the exact immersion procedure (the angle at which immersion takes place seems to influence the plastron stability) and to sample differences. In order to eliminate these effects, the maximum stability time for each immersion depth was plotted in Figure 12.2c and 12.2d. Plotting the maximum life-times for different immersion depth offered a clearer picture of the depth dependence of the air-film stability.

In Figure 12.2c and 12.2d an exponential function was fitted to the data. This fit is purely empirical and does not reflect a theoretical model. We have plotted two different maximum life-times for an immersion depth of $H(4) = 110\,\mathrm{cm}$, as the maximum life-time for this height was perceived on a sample showing slightly abnormal behaviour. All other four immersion experiments were well described by the exponential fit. The best fitting results were found for the exponential of the form

$$t = T_0 + T_1 e^{-cH} \tag{12.1}$$

where T_0 introduces an offset and T_1 and c are the constants giving the exponential decay of the life-time t as a function of the immersion depth H.

In Section 12.5, we will explore the depth dependence of the plastron stability and compare the plastron stability times to theoretical calculations. We will further attempt to understand the physics underlying the two stability regimes of the primary plastron (plateau and decay) observed during these experiments.

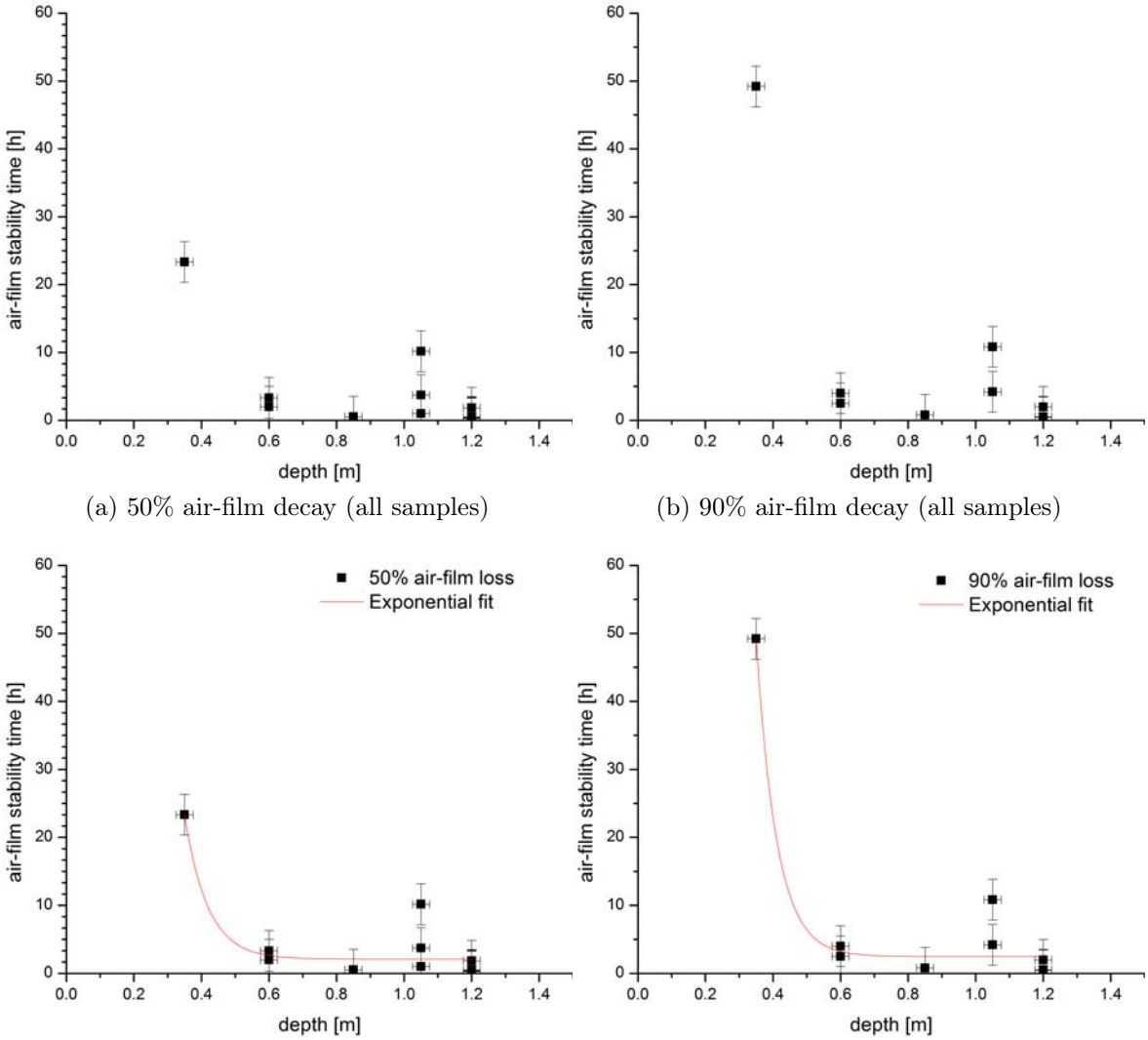

(a) 50% air-film decay (all samples)

(b) 90% air-film decay (all samples)

(c) 50% maximum life-time

(d) 90% maximum life-time

Figure 12.3: *Depth dependence of the plastron stability for flowing water: (a)+(b) Air-film dissolution data (c)+(d) Maximum time for each immersion depth and fit.*

Flowing water

The same kind of immersion measurements were carried out for samples in flowing water. As can be seen in Figure 12.3, the plastron decayed significantly faster ($t_{\mathrm{Tot,\,S}}(1) = 49\,\mathrm{h} = 2\,\mathrm{days}$, $t_{\mathrm{Tot,\,F}}(5) = 2\,\mathrm{h}$). Further, as can be seen in Figure 12.3c and 12.3d, the influence of immersion depth on the plastron stability not easily fitted. We believe that this is due to the two destabilising influences on the plastron stability: the immersion depth and the water flow.

	H(1)	H(2)	H(3)	H(4)	H(5)
Still	384 ± 24	173 ± 6	39 ± 6	52 ± 6	7 ± 1
Flowing	50 ± 6	4 ± 2	4 ± 2	10 ± 3	2 ± 1

Table 12.1: *Comparison of plastron stability times (in hours) derived from 90% plastron decay time for still and for flowing water.* $H(1) \approx 25 - 30\,cm$, $H(2) \approx 50 - 55\,cm$, $H(3) \approx 80 - 85\,cm$, $H(4) \approx 105 - 110\,cm$, $H(5) \approx 130 - 135\,cm$.

(a) Top, $t = 0\,\mathrm{h}$ (b) $t = 1\,\mathrm{h}$ (c) $t = 46\,\mathrm{h}$ (d) $t = 65\,\mathrm{h}$ (e) $t = 6\,\mathrm{days}$

(f) Back, $t = 0\,\mathrm{h}$ (g) $t = 10\,\mathrm{days}$ (h) $t = 14\,\mathrm{days}$

Figure 12.4: *(a)-(e) Plastron on the top-side of the superhydrophobic Nelumbo leaf* ($H = 55\,cm$). *The plastron becomes less reflective over time. (f)-(g) Plastron on the back-side Nelumbo leaf under water* ($H = 25\,cm$). *The plastron is quite stable until decay of the plant tissue commences (g).*

As the flowing water was oversaturated with air, longer stability times were expected. However, the high flux of the water in the immersion column setup seemed to have a strong influence on the plastron stability. The effects of the water flow and the immersion depth are thus convoluted for samples in flowing water. As a result of this, further analysis of the flowing water experiments was not conducted.

12.2 Underwater plastron on other surfaces

12.2.1 *Nelumbo nucifera* leaves

Decay of the plastron stability on the *Nelumbo* leaves was observed over time in the immersion setup. Due to the natural surface bending of the leaves, mounting difficulty and the limited sample availability, quantitative analysis of the plastron evolution was difficult. Qualitative observations were made and compared to the stability analysis of the plastron on Teflon samples. Figure 12.4a-12.4e show the evolution of the air-film on the top side of a *Nelumbo* leaf at an immersion depth of $H = 55\,\mathrm{cm}$. Due to the directional reflectivity of the plastron and the high natural bending of the *Nelumbo* leaf, imaging of the plastron with an angularly fixed camera was difficult. Therefore, only a small surface area could be observed and analysed.

For the *Nelumbo* leaf, a qualitatively different plastron evolution was observed. The thick strongly reflective air-film shown in Figure 12.4a and 12.4f decayed within hours ($t_{\mathrm{Top}} = 1\,\mathrm{h}$), leaving a less reflective surface still coated with a thinner air-film as seen in Figure 12.4b and 12.4g. The residual reflection might well correspond to the thin secondary air-film discussed for low immersion depth on Teflon samples. It was stable for many days. For the leaf imaged from the top-side at an immersion depth of $H = 55\,\mathrm{cm}$, the secondary air-film was stable for 7 days. For the leaf imaged from the back-side immersed at $H = 25\,\mathrm{cm}$, the secondary air-film was stable for 14 days, when the leaf started decomposing.

The total stability time (taking into account the primary and secondary air-films) of the plastron on the Lotus leaf was found to be similar to the stability time established for Teflon surfaces under water (Section 12.1). However, for both buoyancy and friction reduction, we believe that the primary film stability is of particular importance due to its thickness (Section 12.3). This makes the Lotus leaf a less ideal superhydrophobic surface for underwater applications.

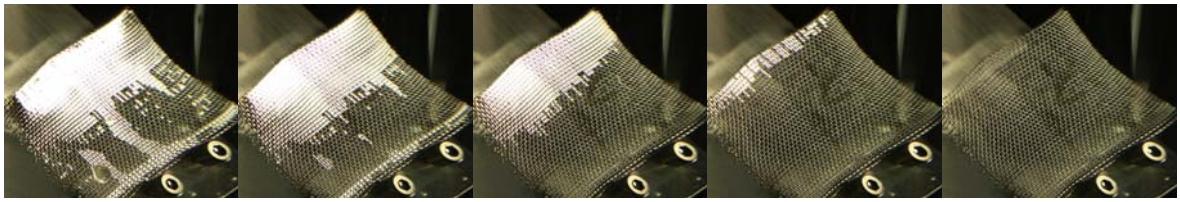

(a) $t = 0\,\mathrm{h}$ (b) $t = 10\,\mathrm{h}\ 20\,\mathrm{min}$ (c) $t = 12\,\mathrm{h}\ 10\,\mathrm{min}$ (d) $t = 13\,\mathrm{h}\ 40\,\mathrm{min}$ (e) $t = 14\,\mathrm{h}\ 00\,\mathrm{min}$

Figure 12.5: *Superhydrophobic grid under water ($H(4) = 110\,cm$).*

12.2.2 Superhydrophobic grid samples

Superhydrophobic boats and grids were produced according to the procedure described in Section 8.2.2. Two experiments were performed:

1. The boats were placed onto a water bath, loaded and their behaviour was observed over time.
2. The copper grid was observed in the immersion column setup.

The boats were seen to stay afloat for multiple days up to weeks. It was found that the boats expulsed water from within through a floating shield. Small water droplets that fell inside the boats dissolved through the plastron. The water passed through the plastron and left a dry inner surface and a floating boat. It seems that the energy of the impacting droplet was large enough to pass through the plastron to an energetically more favourable state outside the boat.

The boats on water floated for very long times (over 14 days). It was difficult to establish whether the boats eventually sank due to instabilities in the plastron or due to vibrations or movements of the water bath setup. Very long floating times for small boats at a maximum immersion depth of $H(a) = 1\,\mathrm{cm}$ are to be expected, when comparing the plastron life-time of the superhydrophobic grid to the Teflon samples at low immersion depths. Extrapolating from the fit of the Teflon plastron stability times in Figure 12.2 would predict floating times longer than 14 days.

The modified superhydrophobic grid was also mounted and observed in the immersion tank. It behaved very similarly to the Teflon samples. Due to difficulties in immersing

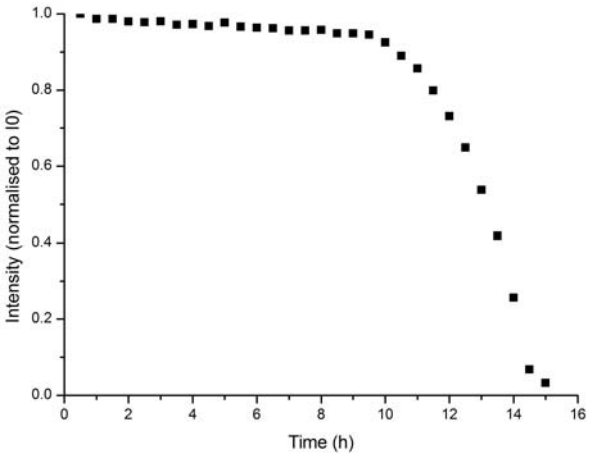

Figure 12.6: *Plastron decay on a submerged superhydrophobic grid normalised for original grid coverage.*

the sample, a significant part of the plastron was lost at immersion. The air-film on the surface was very stable, however. Its stability behaviour corresponded to that seen for the Teflon samples: A very stable plateau with little change in the reflectivity, followed by a quick dissolution of the air-film in the decay regime (Figure 12.6). No secondary air-film was observed

The time-scale of plastron stability for the modified superhydrophobic grid was similar to that observed for Teflon samples. A superhydrophobic copper grid immersed at $H(4) = 110\,\text{cm}$ retained its air-film for approximately 14 h. At the same immersion depth, the Teflon sample retained the air-film for approximately 12 h.

12.2.3 Cellulose and aerogel samples

The stability of the plastron covering cellulose gel and ambiphobic aerogel samples was recorded with the same methods as for all other underwater experiments (Section 9.2.2).

Plastron stability on ambiphobic gels

The life-time of the plastron surrounding the ambiphobic gel was tested twice. In the first test, the gel ripped off the sample holder (after 1 day immersion), as the glue did

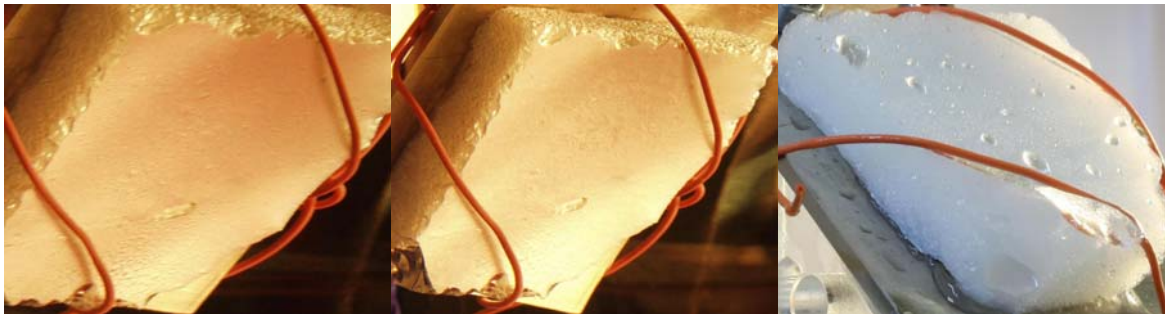

(a) Plastron (10 days in H_2O) (b) Plastron (21 days in H_2O) (c) Wet surface after removal

Figure 12.7: *Plastron on ambiphilic sample: The air-film is shiny and highly reflective. (a) air-film half-way through decay. (b) air-film before removal from immersion setup (c) wet ambiphobic surface after removal from immersion setup*

not support the high buoyancy of the gel. The second test was therefore conducted with a modified immersion tank setup: The sample was mounted facing 45° downward, not upward. The gel was immersed to a depth of $H(5) = 135\,\text{cm}$ below the water surface. The plastron was intact when measurements began.

On Teflon samples, this depth results in air-film stability times of $t < 2\,\text{days}$. The plastron on the ambiphobic gel was found to be significantly more stable. Only small changes were seen over a period of 21 days (Figure 12.7). The early immersion data was lost due to software issues; however, the plastron looked exactly the same throughout the measurement. After removal from the immersion setup, the sample was observed to have lost its superhydrophobicity (Figure 12.7c). The plastron had still been present when the sample was removed from the setup, making this a surprising observation.

This could be explained by incomplete plastron coverage of the surface during the secondary air-film stage, as the loss of superhydrophobicity was also seen on Teflon samples during late plastron decay stages. Teflon samples with very thin air-films during the last stages of the experiments were also often found to have experienced a significant loss of superhydrophobicity upon removal from the immersion setup.

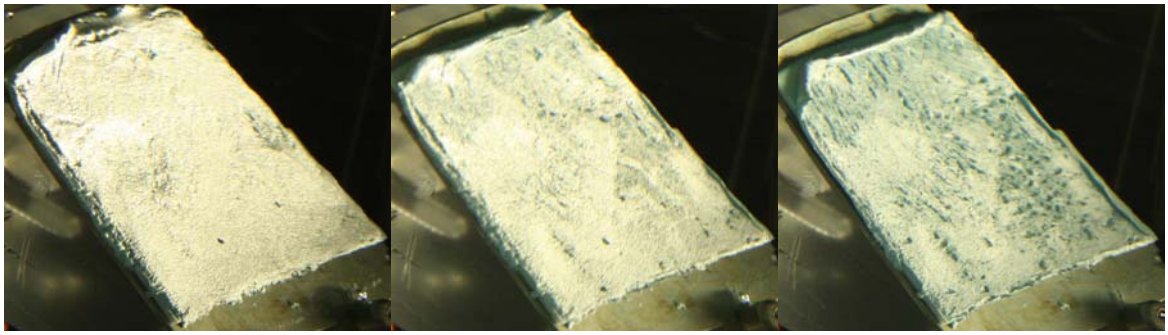

(a) Plastron (fresh) (b) Plastron (1 1/2 days) (c) Wet sample in water (5 days)

Figure 12.8: *Cassie-Baxter air-film on a Nelumbo leaf: (a) top side (b) back side. The silvery film shows that the leaf is still hydrophobic. Due to the leaf curvature, the silvery film is difficult to observe from one fixed angle*

Plastron stability on cellulose gels

The air-film stability observed on the cellulose gels (coloured or white) was similar to that reported for the Teflon samples. For white and for coloured cellulose gels, it was difficult to observe the plastron decay, which is why only an upper boundary on the decay time could be established. The unevenness of the sample and the inherent shimmer of the cellulose material made an exact analysis of the stability curve beyond the ability of this experimental setup.

Two samples were tested at $H(4) = 110\,\text{cm}$ immersion depth. The upper boundary life-times for the two samples were: $t \approx 2\,\text{days}$. The survival times were slightly longer than for Teflon samples, but significantly shorter than for the ambiphobic gel samples.

It was difficult to determine whether the film observed corresponded to the primary or secondary plastron, as the sample structure showed cracking after removal from the immersion setup. The observed loss of superhydrophobicity could therefore not be clearly attributed.

12.2.4 Plastron stability comparison

Here, we combine the results from all samples tested using the immersion setup. The maximum life-time of the plastron is recorded as a function of immersion depth.

The major difficulty in the comparison of the plastron stability on all these different samples was due to the nature of the plastron decay. As mentioned in Section 12.1 and explored in Section 12.3, two different stable air-film regimes existed on many samples.

Sample	H(1)	H(2)	H(3)	H(4)	H(5)
Teflon	384 ± 24	173 ± 6	39 ± 6	52 ± 6	7 ± 1
Nelumbo	-	-	1.0 ± 0.3	-	-
Grid	-	-	18 ± 2	14 ± 2	-
Cellulose gel	-	-	-	24 ± 12	-
Aerogel	-	-	-	-	500 (*)

Table 12.2: *Plastron stability times (hours) derived from 90% plastron decay time.* $H(1) \approx 25 - 30\,cm$, $H(2) \approx 50 - 55\,cm$, $H(3) \approx 80 - 85\,cm$, $H(4) \approx 105 - 110\,cm$, $H(5) \approx 130 - 135\,cm$. ** The star is explained further in the main text.*

On Teflon samples, these regimes were easily distinguished and only the first air-film regime was taken into account for the plastron stability, as the second air-film regime seemed to be associated with a loss of air-film thickness (and therefore buoyancy) and superhydrophobicity.

Table 12.2 shows the plastron stability times (90% decay) for all samples observed and measured in the immersion setup. For samples other than the Teflon surfaces, distinction between the primary and the secondary air-film was not always easy. For the superhydrophobic grid (which has only a macroscopic air-film pinning roughness and therefore only showed a primary air-film) and the *Nelumbo* leaves (which has a surface structure very similar to the Teflon samples), the distinction was clear and only the primary film life-time was taken into account. As noted in Table 12.2* a distinction between the primary and the secondary film for the aerogel was very difficult. The fact that the ambiphobic aerogel had lost its superhydrophobicity during immersion suggests that the observed plastron corresponded secondary air-film. This could explain the strong difference between the data recorded for the aerogel and the other samples.

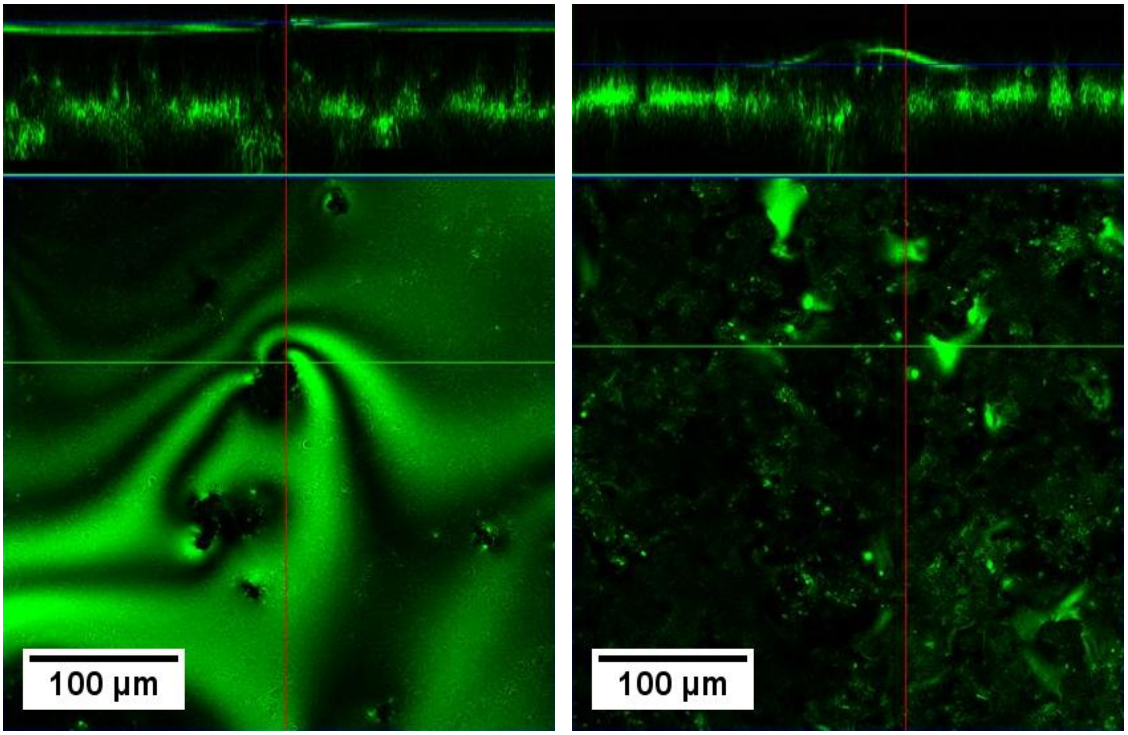

(a) Decay time about 15 min (b) Decay time about 30 min

Figure 12.9: *Confocal microscopy surface image and cross sectional slice: The surface slice is focused on the water-air interface. (a) primary air-film after 15 min (b) air bubbles after 30 min. The position of the cross sections are indicated by the postion of the lines. From top to bottow, water, air and teflon are shown.*

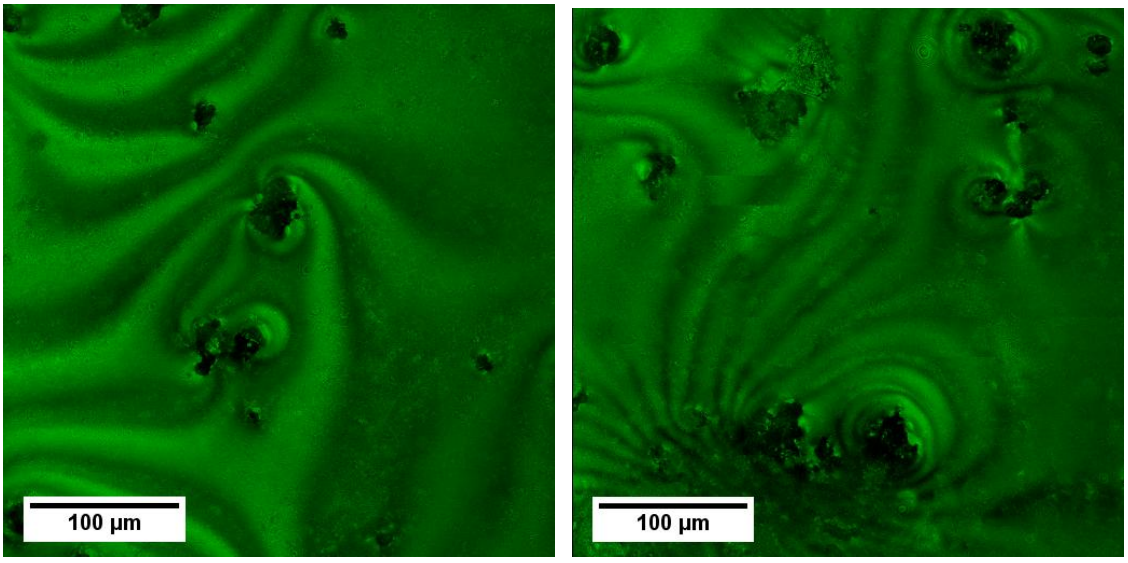

(a) Immediately after immersion (b) 1 h after immersion

Figure 12.10: *Changes in the air-film with time (a) Surface reconstruction immediately after immersion (b) Surface reconstruction 1 h after immersion*

12.3 Underwater confocal microscopy on Teflon

The underwater plastron decay on Teflon surfaces was observed using confocal microscopy. Initially, a thick air-film, with very few pinning points, spanned the super rough surface (Figure 12.9a). The air film was found to be nearly flat and no significant curvature could be measured. The second stage of the plastron decay is shown in Figure 12.9b. It is a scan of the same area, 15 min later. A sample was also scanned after multiple days of immersion (Figure 12.13).

Continuous air-film regime

A continuous air-film regime was observed for relatively freshly immersed samples. Figure 12.10 shows two scans taken of the same sample. For both scans we can clearly see the air-film in the surface reconstruction. The second scan (Figure 12.10b) was taken 1 h after the first scan (Figure 12.10a), which was taken within minutes of immersion of the sample into water. Both scans are taken within a few minutes of focusing the laser onto the area to be scanned.

While the air-film height seems to change over the course of 1 hr, the samples are qualitatively very similar. The second scan shows more pinning points. We can also observe imaging issues in the lower left corner. We believe this corresponds to a change in the air-film occurring during the imaging process.

Air bubble regime

The decay of the air-film happens quickly for the samples observed with confocal microscopy compared to samples in the immersion tank. Figure 12.11 shows air bubbles on the surface in the decay stage of the air-film. The air bubble size decreased rapidly during the measurement, and therefore laser exposure time.

The bubble seen in Figure 12.11 was the largest bubble observed with confocal microscopy. It most likely corresponds to the time just after break-up of the continuous

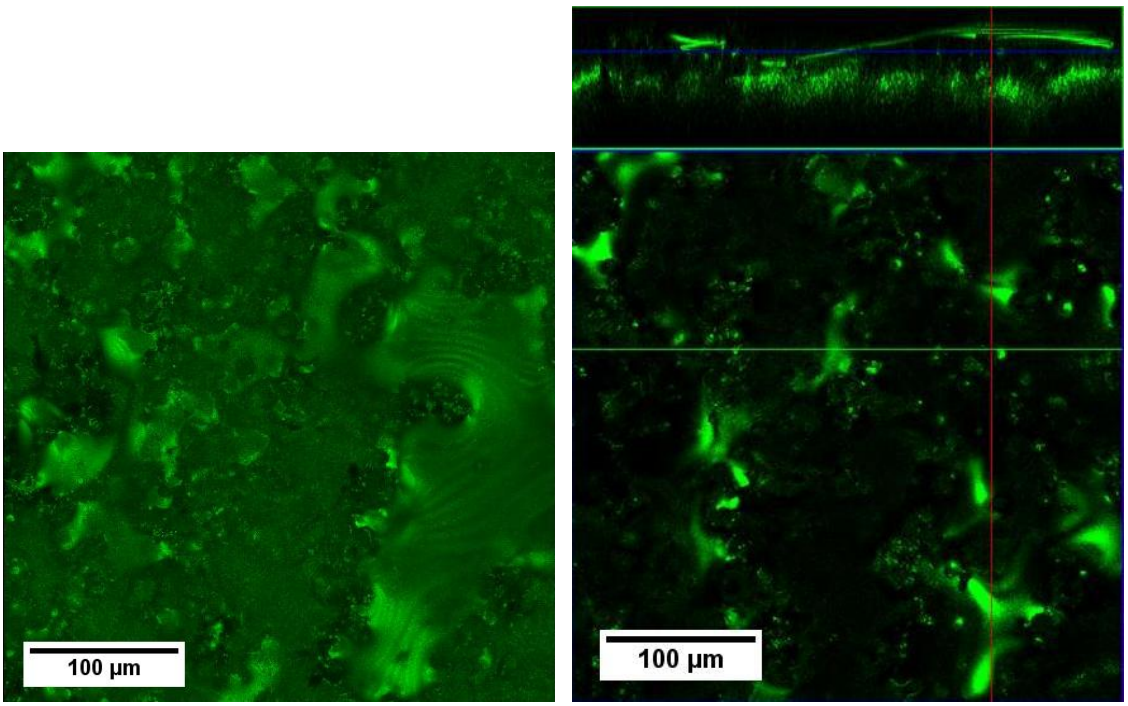

(a) Surface reconstruction (b) Surface slice and cross-section

Figure 12.11: *(a) Confocal microscopy surface reconstruction image of an air film after approximately 30 min. (b) Surface slice and cross-section through the same film.*

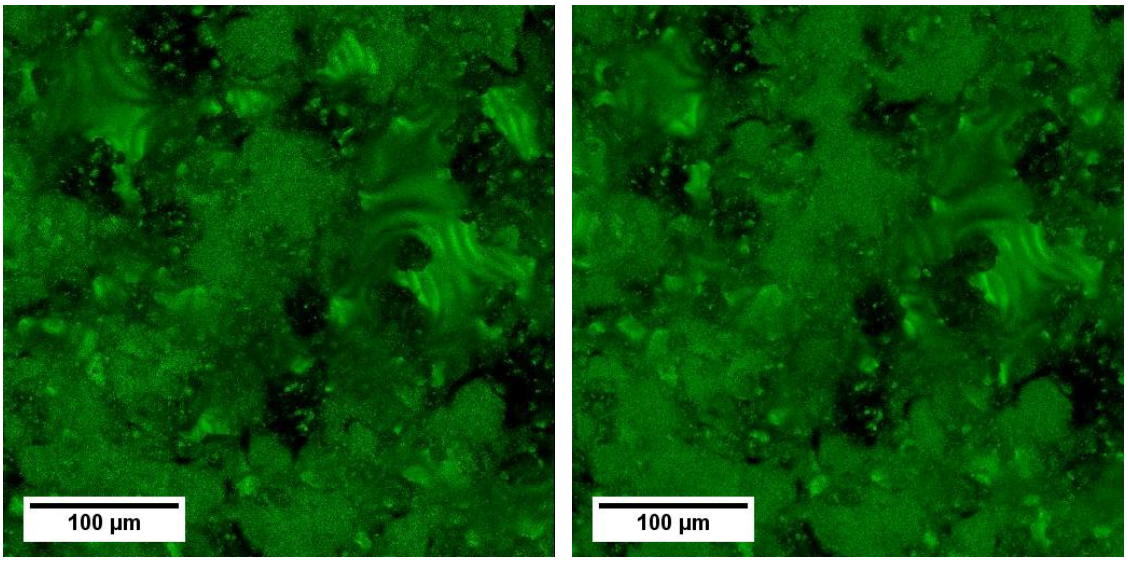

(a) Decay time about 45min (b) Decay time about 60min

Figure 12.12: *Confocal microscopy surface reconstruction images of (a) an air film after approximately 45 min. (b) the same air film after 60 min. Local changes can be seen even for an aged air-film.*

air-film.

From Figure 12.11, the angle of the air bubble to the surface is measured to be $\theta_{\text{bubble}} = 15 \pm 10°$, which is roughly on the order of magnitude of an expected $\theta_{\text{bubble}} = 180° - \theta_{\text{S}} \approx 20°$. The surface diameter of the dome-bubble is 100 µm $< d_{\text{bubble}} <$ 350 µm. The central height of the bubble is approximately $h_{\text{bubble}} = 20 \pm 10$ µm. The radius of curvature is therefore $R_{\text{curv}} \approx 155$ µm.

The contact angle for all other confocally imaged bubbles was in a similar range: $10° < \theta_{\text{bubble}} < 30°$. This corresponds very well to the expected angle, as the underwater air-bubble angle θ_{bubble} and the static contact angle θ_{S} should add up to 180°. $\theta_{\text{bubble}} = 180° - \theta_{\text{S}}$.

Figure 12.12 shows the changes observed in the air-bubbles on the surface between two confocal imaging scans. While differences are small, they can be attributed to further film or bubble break-down or retraction of the bubble to lower planes. No new bubble creation could be observed.

Secondary air-film

Another sample was measured with the confocal setup after 5 days of immersion. The plastron was was less brightly coloured than that of the freshly immersed sample; the decay of the plastron had already started. The surface picture of the air-film after 5 days is shown in Figure 12.13. The average air-film sample distance (air-film thickness) was now much smaller ($d_{\text{surf}} = 10 \pm 5$ µm). Distinction of the two surfaces by confocal microscopy became difficult. The only difference was the apparent reduced roughness for the air-covered areas. The film was pinned everywhere and had broken up into many small films / bubbles. This could have corresponded to a mixed state of the primary decay regime and the secondary air-film (Figure 12.17).

Due to the transparency of the air-film, it is possible to deconstruct the total image to achieve a better understanding of whether there is any air left on the sample or not. Since the sample looked optically still silvery (though less brightly coloured), it was

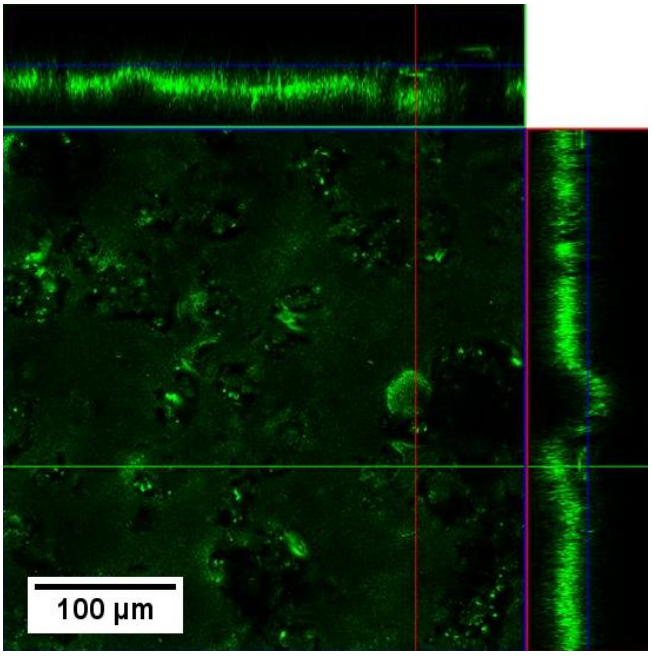

Figure 12.13: *Confocal microscopy image of the air film after 5 days immersion in water. It is unclear from the surface image and the cross section whether any air is still on the surface.*

assumed that air must still be present. In Figure 12.13, the presence of the air-film at the surface was difficult to observe.

Confocal microscopy allows us to reconstruct the lower underlying structure of the rough Teflon in Figure 12.14a and top surface of the sample including the air-film in Figure 12.14b. Using the deconstruction method, the air-film can be distinguished from the Teflon surface, even though the two overlap.

Cross-section comparison - quantitative

Looking closer at the cross-sections of the air films, we observe that the air film was pinned on the highest structures and was relatively thick ($d = 70 \pm 10$ µm). After 1 hr underwater, the air film has decreased in thickness ($d = 50 \pm 10$ µm).

Confocal microscopy images were used to determine rough values for the bubble size, height and radius of curvature. Generally, the air bubbles were relatively small. One of these images is shown in Figure 12.15c. This air bubble has a surface diameter

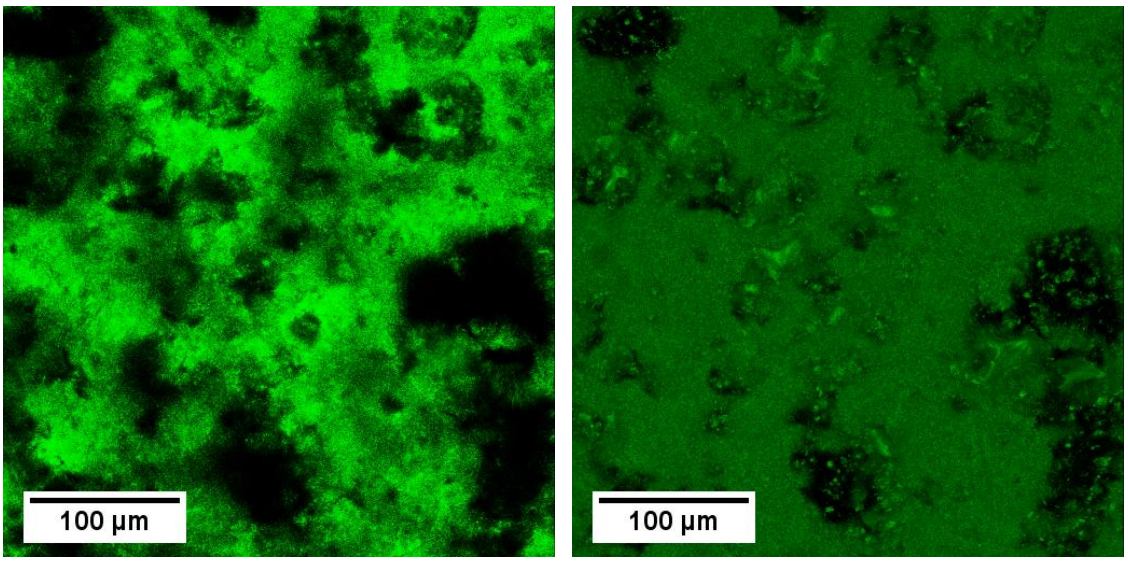

(a) Lower half reconstruction (b) Upper half reconstruction

Figure 12.14: *Reconstructions of the (a) lower and (b) upper half of the image. The flat air-film section can clearly be seen.*

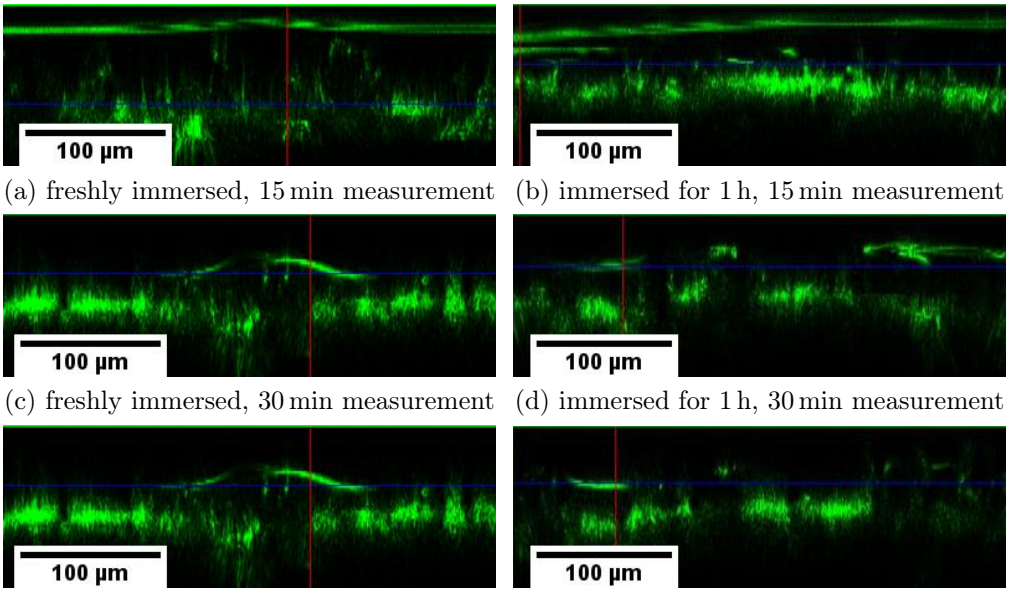

(a) freshly immersed, 15 min measurement (b) immersed for 1 h, 15 min measurement

(c) freshly immersed, 30 min measurement (d) immersed for 1 h, 30 min measurement

(e) freshly immersed, 45 min measurement (f) immersed for 1 h, 45 min measurement

Figure 12.15: *Confocal microscopy height section: Air-film evolution under confocal microscope. (a) The air-film after 10-15 min measurement, directly after immersion into water. The initial air-film is about* $d = 70 \pm 10$ *µm thick. (b) The air-film after 10-15 min of a sample that has been immersed for 1 hr into water prior to the measurement. The air-film is about* $d = 50 \pm 10$ *µm thick. (c, e) Evolution of the freshly immersed air-film. (d, f) Evolution of the pre-immersed air-film.*

$d_{\text{surf}} = 130 \pm 20$ µm, a maximum height of $h_{\max} = 15 \pm 5$ µm and an approximate surface contact angle of $\theta_{\text{bubble}} = 20 \pm 5°$.

12.4 Teflon surfaces: Changes in wetting behaviour

The characteristic contact angles on Teflon surfaces were measured using contact angle goniometry (Section 9.2.1). Measurements were performed on fresh Teflon samples, on Teflon samples after immersion in the water tank (Section 9.2.2) and on Teflon samples after cleaning trials.

As expected, the fresh surfaces were very hydrophobic. Contact angle measurements were difficult, as the drops did not stay in the measurement area.

Sample	Advancing CA	Static CA	Receding CA	Hysteresis
New (a)	168 ± 3	164 ± 2	162 ± 6	4
Old (b)	166 ± 3	157 ± 8	138 ± 33	28
Cleaned (c)	166 ± 6	165 ± 8	147 ± 17	19

Table 12.3: *Contact angles on Teflon surfaces (a) as produced (b) after immersion into the water tank (c) after cleaning with ethanol or isopropanol. The errors reported here are based on the measurement statistics (standard deviation). An additional inherent fitting error due to base-line identification causes an additional error of* $\text{Err}_{base} = 5$.

After immersion into the water tank for multiple days, some Teflon surfaces were observed to have lost their superhydrophobicity. In particular, the average receding contact angle decreased significantly as seen in Table 12.3. It was noted, that while the behaviour of some samples was unchanged after immersion, others experienced very strong changes in their wetting behaviour upon immersion. This explains the high standard deviation associated with the receding and static contact angle measurement for these samples.

Therefore, two groups of samples were identified: The first group experienced no or little change to their wetting behaviour; contact angles measured on these samples after immersion corresponded to contact angles measured on fresh samples. The second group experienced strong changes to their wettability after immersion in the water

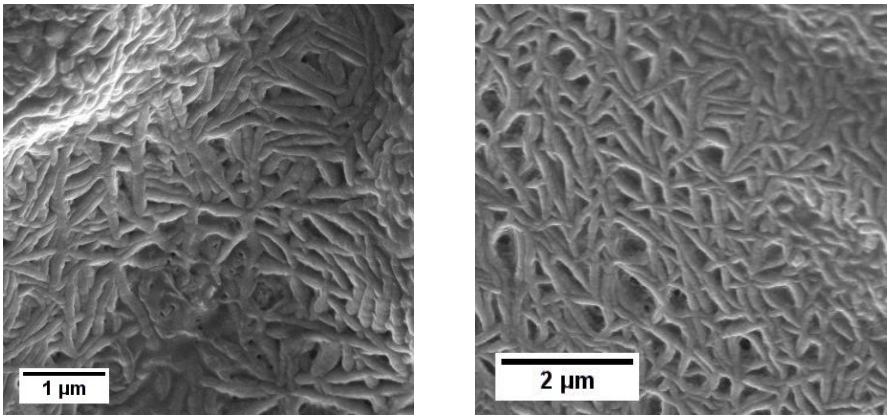

(a) Fresh Teflon surface (b) Teflon surface after immersion

Figure 12.16: *SEM image of (a) new and (b) old Teflon surfaces: No significant surface structure changes due to the immersion could be observed.*

column. The contact angles measured upon removal were significantly smaller: Some samples showed extremely high contact angle hysteresis after removal from the tank ($\Delta\theta_{\mathrm{J2,\ old}} = 125°$).

It was observed that the influence of immersion on sample quality was greater for samples that were immersed for long time periods. Samples that experienced only one or two days of water contact normally recovered their superhydrophobicity fully upon drying of the surface.

The superhydrophobicity of samples after removal from the immersion setup could be partially recovered by cleaning of the surface with different solutions: dish-washing liquid, ethanol and acetone followed by isopropanol. The samples were immersed into the solutions for 5-15 min. Differences between the washing solutions were statistically irrelevant. On average, the cleaning of contaminated samples seemed to improve the sample superhydrophobicity slightly (Table 12.3). In particular, the receding contact angle increased after washing.

The samples were also imaged with optical microscopy and SEM in order to find out whether the change in wetting behaviour could be correlated to visible contamination of the surface. No significant contamination on the surfaces was identified using either technique (Figure 12.16).

Further work on cleaning methods to improve the superhydrophobicity of samples after long immersion periods under water will be necessary. The origin of the loss of the superhydrophobicity through immersion needs also further study.

12.5 Plastron stability

Based on the experiments described in Section 12.1, 12.2 and 12.3, we provide a qualitative description of the decay of the air plastron on a superhydrophobic surface under water. The stability of the air-plastron is divided into three separate regimes: The primary plateau regime, the primary decay regime and the secondary film regime. In this section, we will present some theoretical arguments supporting this picture. The three regimes postulated in this section are schematically depicted in Figure 12.17.

The stability of the primary and the secondary air-film can be correlated with the roughness structure of the superhydrophobic sample. Differences in the plastron stability on different surfaces can be explained in terms of the characteristic length scales of the features.

Figure 12.17d shows the secondary air-film. This air-film was postulated due to the observed rest reflection intensity after the decay of the primary air-film. This secondary film could not be easily observed using confocal microscopy, as it exists within the structure that lies at the resolution limit of the confocal microscope. In Section 12.3, the existence of a very thin air-film within the structure was shown through splitting of the confocal images into lower and upper plane information. While the data presented in Sections 12.1-12.3 is sufficient to observe and describe the primary plastron stability with some detail, our understanding of the secondary film is still rudimentary. This is partially due to the hidden location of the film and the small scale nature of the film, making it inherently more difficult to observe and quantify.

The superhydrophobic Teflon surface and the Lotus leaf surface have hierarchical surface roughness ranging from micrometre sized pillars to nanometre scale needles (Figure 12.18). The Teflon surfaces are very similar to the dried Lotus leaf surfaces.

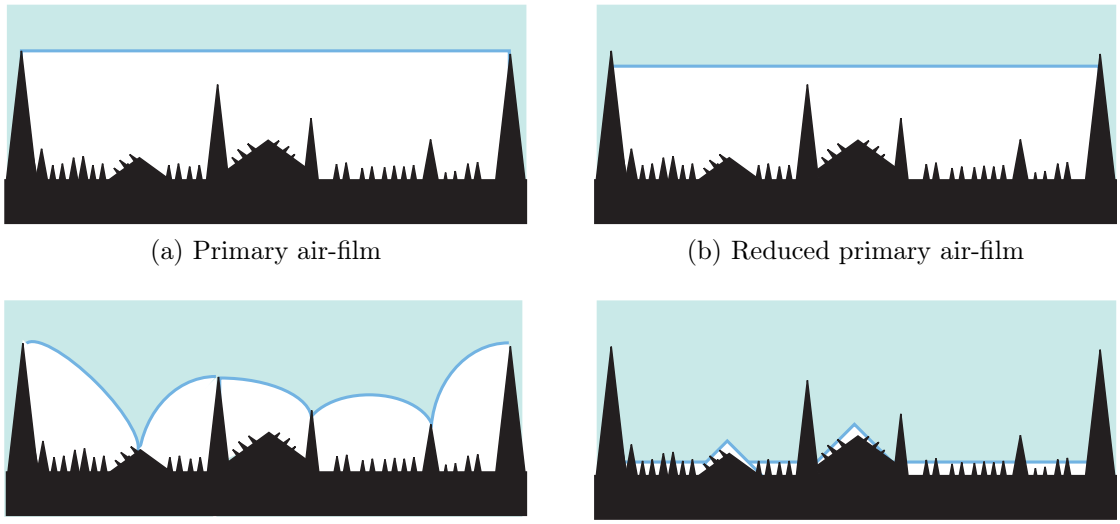

(a) Primary air-film

(b) Reduced primary air-film

(c) Primary air-film break-up through bubbles

(d) Secondary air-film

Figure 12.17: *Schematic of the postulated changes in the plastron with time (a) original meniscus shape $t_0 = 0$ (b) meniscus after some time t_1, when the primary film has broken up into large surface-attached bubbles (c) meniscus at t_2. Only the secondary film is still attached to the secondary scale roughness.*

Both exhibit two stable intensity regimes in the decay. The primary film exhibits a very bright uniform surface reflection. Later bubbles forming on the surface during the primary decay regime and the thin secondary air-film are significantly less bright. The reflectance is no longer uniform.

For the superhydrophobic grid, only a primary air-film was observed. This can be explained by the macroscopic pore size of the grid (Figure 12.6). The cellulose and the ambiphobic aerogel display only a very unstable primary air-film, if any. The secondary air-film for the aerogel was found to be very stable. This could be due to the porous nature of the gel and the associated very high nanometre scale roughness.

The stability of the primary air-film depends on the meniscus stability before pinning (Section 12.5.1) and the stability of individual air-bubbles on the surface once pinning has occured (Section 12.5.2). The secondary-film is probably a smaller scale version of the primary air-film.

The decay time t_{Tot} of the primary air-film is composed of the plateau decay time (Section 12.5.1) and the air-bubble regime life-time (Section life-time). Experiments

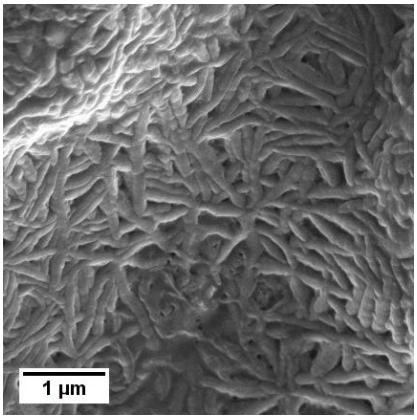

(a) Teflon surface (close up)

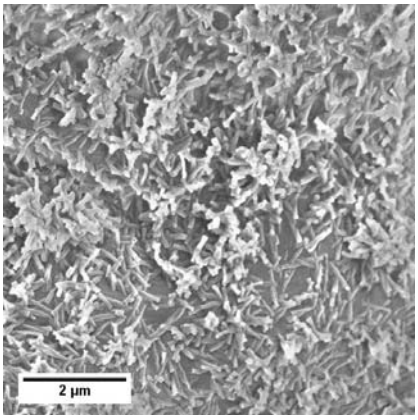

(b) Dried Lotus leaf (close up)

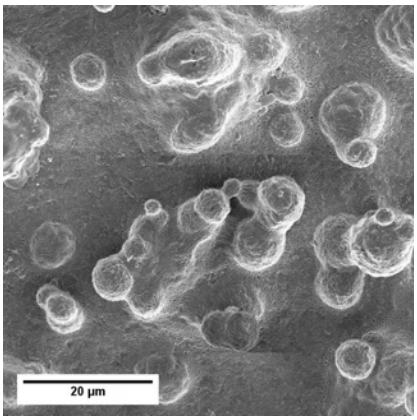

(c) Teflon surface

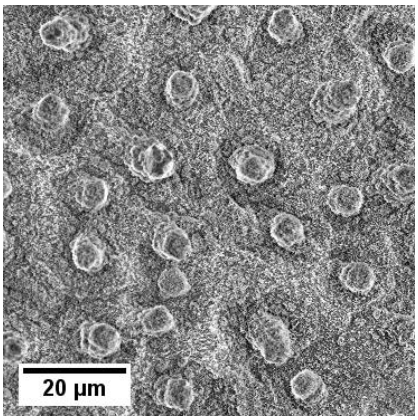

(d) Dried Lotus leaf

Figure 12.18: *SEM images of the Teflon surfaces and a dried Lotus leaf for comparison (a) Teflon structure on the nanometre length-scale (b) Dried Lotus leaf structure on the nanometre length-scale (c) Teflon structure on the micrometre length-scale (b) Dried Lotus leaf structure on the micrometre length-scale*

suggest that the plateau decay time is much larger than the air-bubble decay time, such that $t_{\text{Tot}} = t_{\text{stable}} + t_{\text{decay}} \approx t_{\text{stable}}$.

12.5.1 Meniscus stability

Upon immersion of a superhydrophobic Teflon surface, an air-film is trapped by the large scale surface features (Figure 12.17a). The original air-film is very thick ($d \approx$ 100 µm). Through diffusion of the air into the water, the air-film slowly reduces in thickness (Figure 12.17b). The observed change in the reflection of the plastron surface is very small. This can be explained by the fact that the reflection intensity is not

dependent on the thickness of the air-film, only on its curvature.

The air-film remains globally flat, as only the area very close to the pinning points is influenced by the boundary condition of the Young's contact angle. Slowly, more pinning points appear due to the reduction of the film thickness. Further, fluctuations of the interface can also cause pinning. The reflection intensity remains nearly constant, until the balance shifts toward a bent air-film surface rather than a flat air-film surface. At this point, the air-film begins breaking up into smaller bubbles (Figure 12.17c).

In the experiments described in Section 12.1, a strong non-linear depth dependence of the plateau stability on the immersion depth was shown. The diffusion behaviour is not significantly influenced by immersion depth. The pressure as a function of immersion depth (Section 7.5.3, Equation 7.40) only describes the diffusive part of the depth dependence:

$$p(h) = p_0 + p_{\mathrm{L}} + p_{\mathrm{hydro}} = p_0 + \frac{2\gamma}{a(t)} + \rho g h$$

This equation predicts a linear dependence on the immersion depth. Further, the dependence is much weaker than shown by the experiments in Section 12.1. The observed depth dependence of the plastron stability can therefore not be explained by purely diffusion-driven phenomena. The strongly non-linear depth dependence of the primary air-film stability could be caused by capillary fluctuation of the plastron, which we do, at present, not fully understand.

In the following section, we will focus on the decay mechanism of the plastron once the meniscus breaks and the film becomes an assembly of surface-attached bubbles.

12.5.2 Bubble life-time calculation

When the primary film breaks into large surface-attached air-bubbles (Figure 12.17c), the reflection of the air-film changes dramatically. The continuous size reduction of the air-bubbles reduces the reflection further. The experiment therefore shows a decay

in the signal. The reduction of the bubble size has also been seen in the confocal images of the air-film (Section 12.3). The primary air-film decay regime can therefore be understood better through a study of underwater air-bubble decay.

The life-time of a bubble on a superhydrophobic surface can be calculated from the equations derived by Ljunggren *et al.* (Section 7.5.2) by making some assumptions and some small modifications based on the experimental observations in this chapter.

These assumptions are:

- The air film is made of individual bubbles with the same size.
- The air disappears by diffusion only. Ripening and lift-off due to buoyancy, as well as dissolution due to convection is ignored.
- The film behaviour is dominated by nitrogen (N_2 diffusion constants are used for air diffusion)
- The contact angle of the bubbles on the surface is always the same and dominated by Young's equation, as concluded from confocal microscopy measurements

Assuming these conditions, we need to re-examine the calculations by Ljunggren *et al.* in order to adapt them with a few modifications to our experimental conditions. The necessary modifications include

- Distinction between the radius of curvature R_{curv} and the bubble surface area S
- The inclusion of the hydrostatic pressure p_{hydro} in the external pressure p_{E} ($p_{\mathrm{E}} = p_0 + p_{\mathrm{hydro}}$)

The life-time of the dome-shaped bubble (Figure 12.19b) can be calculated by introducing the necessary modifications, due to the change to the volume V of the dome-shaped bubble on the surface in comparison with a spherical bubble in liquid. The new volume is given by

$$V = \pi a(t) h^2(t) - \frac{1}{3}\pi h^3(t) \tag{12.2}$$

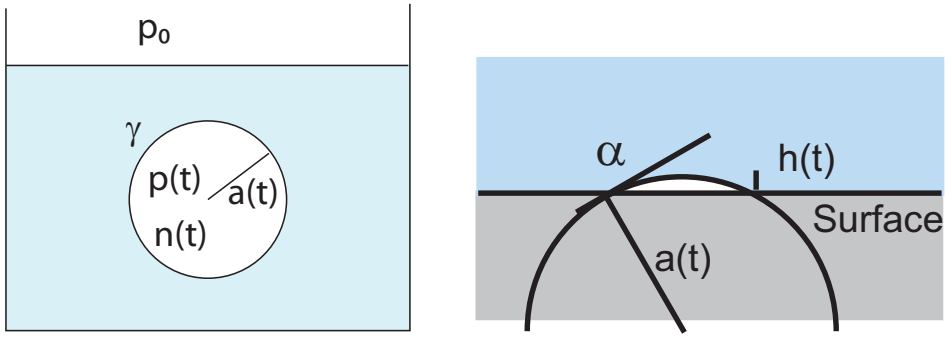

(a) Complete air bubble underwater (b) Dome-shaped air bubble underwater

Figure 12.19: *Stability calculation modification (a) Bubble as described by Ljunggren et al. [97] (b) Top part of 30° contact angle corresponds in volume to less than 2%.*

where $h(t)$ denotes the height of the dome-shaped bubble in the centre of the dome, and α denotes the contact angle for the bubble. For a hydrophobic surface underwater $\alpha = 180° - \theta_S$.

Since $h(t) = a(t)(1 - \cos(\alpha))$, we get

$$V = \frac{(\cos(\alpha) - 1)^2(\cos(\alpha) + 2)}{3}\pi a^3(t) = B_0 \pi a^3(t) \tag{12.3}$$

where

$$B_0 = \frac{(\cos(\alpha) - 1)^2(\cos(\alpha) + 2)}{3}$$

While the Laplace pressure (Eqn. 7.33) does not change for a dome-shaped bubble, the ideal gas law (Eqn. 7.34) used by Ljunggren must be modified as follows in order to include the changes in the volume:

$$B_0 a^3(t) p(t) = n(t) RT \tag{12.4}$$

Accordingly, the derivation follows as for Ljunggren. The only changes are the correction of the formula by the factor B_0. The decay time we derived for small dome-shaped bubbles on a surface is given by

$$t_{\text{small}} = \frac{B_0 K a^2(0)}{4RTD} \tag{12.5}$$

For large, dome shaped bubbles, the decay time is given by

$$t_{\text{big}} = \frac{B_0 K a^3(0) p_{\text{E}}}{8RTD\gamma} \tag{12.6}$$

As Ljunggren and Eriksson showed, large air bubbles can survive in water for a very long time. Due to the flat nature of the primary air-film before pinning, we cannot use the arguments derived here to estimate the associated life-time. However, due to the low curvature and the large volume, the equilibrium life-time of the flat primary air-film (Figure 12.17a) should be significantly longer than the life-times calculated for the individual air-bubbles (Figure 12.17c).

We can apply the equations for the dome-shaped bubbles to the decay-regime of the surface-attached air bubbles. Due to their small volume and large radius of curvature, these air-bubbles should have moderate life-times.

For a dome bubble with a contact angle of $\theta = 30°$ and a radius of curvature of $r_{\text{Laplace}} = 1\,\text{mm}$, the life-time is approximately $t_{\text{dome}} = 26\,\text{h}$, instead of $t_{\text{bubble}} = 2037\,\text{h}$, as calculated by Ljunggren *et al.* [97]. Since our bubbles show radius of curvatures in the range of $100\ \mu\text{m} < r_{\text{Laplace}} < 500\ \mu\text{m}$, this gives us a free bubble decay time of $2\,\text{h} < t_{\text{bubble}} < 250\,\text{h}$, and a decay time for a surface attached bubble of $1.6\,\text{min} < t_{\text{dome}} < 3\,\text{h}$.

The life-time calculated using Equation 12.6 is of the same order of magnitude as the experimentally measured bubble decay time of primary air-film (Figure 12.17c).

12.5.3 Secondary air-film

The secondary air-film observed after decay of the primary plastron on superhydrophobic surfaces, during the immersion experiments, is not yet well understood. It was also seen in confocal microscopy images. While in the untreated image (Figure 12.13 cross-

section), no air-film could be identified, the secondary air-film could be seen upon deconstruction of the image (Figure 12.14). The surface roughness and the air-film completely overlap in height, which made observation difficult and prevented analysis of the crosssectional data. Therefore, no contact angle could be established.

We postulate, that this secondary air-film corresponds to tiny air-bubbles trapped by the small scale structure of the surface (Figure 12.17d). The significance and behaviour of the secondary plastron could not be studied in detail.

Samples removed from the immersion setup during the secondary air-film regime, had often lost their superhydrophobicity. This could be due to the large amount of surface coming into contact with the liquid.

We believe that while the physics governing the stability of the secondary plastron are interesting, the secondary plastron is of no technological interest. In particular, the secondary plastron may not have the desired properties for underwater applications of superhydrophobic surfaces: The small amount of air of the secondary plastron should not contribute significantly to buoyancy. Further, the high amount of surface in contact with the liquid phase and the rough gas-solid-liquid interface found for the secondary plastron also should not have the drag reducing properties associated with the primary air plastron.

12.6 Underwater wetting: Discussion

We have observed and described the air plastron stability on different superhydrophobic surfaces qualitatively and on very rough Teflon surfaces quantitatively. The plastron decay was studied in an open system, to establish the behaviour of the plastron under conditions with a high relevance to real life technological applications. We have shown that for all superhydrophobic surfaces immersed under water for long periods of time, the air plastron decayed and the surface was wetted.

The phenomenon of the loss of superhydrophobicity due to immersion has been

mentioned by Herminghaus [90]. Our experimental study shows quantitative and qualitative results not previously reported in any experimental work on underwater superhydrophobicity. These results are in contrast to theoretical work on the subject. In theoretical work, including the work by Marmur on underwater superhydrophobicity [6], only closed systems are studied. The decay of the plastron was not predicted. The basic assumption of this theoretical work is the coexistance of three phases at an interphase. However, for nearly all real life applications of superhydrophobic materials under water, the system is open. In an open system, the plastron is solubilised in the surrounding water, which continuously outgases. This leads to the decay of the plastron observed in our experiments.

Through immersion experiments, we have established an inverse depth dependence for the plastron stability on superhydrophobic hierarchically structured Teflon surfaces. The plastron life-time exhibited a strongly non-linear depth dependence: At small immersion depths the plastron was found to be stable for weeks, while at much larger immersion depths the plastron life-time was reduced to hours. Movement of the water accelerated the dissolution of the plastron.

The plastron decay has further been observed using confocal microscopy. The combined data from long-term immersion experiments and confocal imaging has yielded a qualitative description of the changes occurring in the plastron over time on Teflon surfaces.

On hierarchically structured superhydrophobic surfaces (Teflon and Lotus leaf), the plastron decay can be described in terms of three regimes. These regimes are: A flat primary air-film, a bubble regime, which occurs upon break-up of the primary film and finally, a very thin secondary air-film.

The primary air-film is very thick (Regime 1). It is flat and highly reflective as it is pinned to the surface at very few points. The air-film reduces in thickness over time. The decay is strongly depth dependent. The shrinkage of the film leads to further pinning, until the film breaks into individual air-bubbles on the surface (Regime 2). Driven by diffusion, these bubbles then decay relatively quickly. The complete decay of

the large surface bubbles can leave a secondary air-film, which was observed as residual intensity before the complete wetting of the Teflon surface (Regime 3). The secondary air-film was attributed to trapping of air between small scale roughness features.

Through comparison with other superhydrophobic material surfaces and their roughness scaling, a correlation between the three regimes and the surface roughness was found: Samples with large scale roughness had a very stable highly reflective primary plastron, whereas samples with smaller scale roughness exhibited a more stable secondary plastron. For samples with only large features, no secondary plastron could be observed. Hierarchically structured surfaces exhibited all three regimes, irrespective of the exact surface structure or chemistry.

The work presented here severely limits the potential use of superhydrophobic surfaces in underwater applications. While an increase in buoyancy and a decrease in friction on such surfaces have been shown [7, 9], the limited life-time of the plastron is a significant technological challenge. Further, the strong immersion depth dependence shown experimentally in this study limits the use of such materials for many underwater applications. The reduction of the plastron life-time due to flowing water could also introduce technological difficulties.

13 Wetting conclusions

In Part II, we explored the wetting of water on different rough and structured surfaces. Particular emphasis has been paid on understanding the possibilities and limitations of the Cassie-Baxter air-pocket wetting state. This work was driven by the need for a better understanding of the non-equilibrium properties of these systems. Our work provides a systematic study of superhydrophobic surfaces under water in an open system and the study of surfaces exhibiting metastable Cassie-Baxter wetting states for water droplets.

In Chapter 10, we discussed metastable Cassie-Baxter wetting states on highly structured hydrophilic materials. The systematic study of these wetting states has provided insight into the optimal design parameters involved in this process. We showed that the fabrication of surfaces designed to exhibit metastable wetting states needs to obey the design criteria shown by Tuteja *et al.* [1], but that these are not sufficient for the successful design of a robust metastable wetting state.

We showed the dependance of the apparent contact angle on the spacing ratio D^*. This had been postulated by Tuteja *et al.*, but had not been shown experimentally. Our data showed a clear dependence of the apparent contact angle on the feature width and spacing. This allows for surfaces to be designed through careful consideration to exhibit high contact angles for metastable Cassie-Baxter wetting states. It must be remembered however, that the Young's contact angle nonetheless has a strong influence; structuring cannot replace the control of the surface chemistry.

We have shown four supplementary important criteria determining the robustness

of the metastable wetting states: Firstly, the surface of the protruding structure must not be laterally smooth and continuous so that a uninterrupted water contact line cannot form, as interconnected surface structures do not exhibit the desired wetting states. Therefore, microhoodoos are prefered to microtraps. Secondly, the fabrication of defect free surfaces is paramount. Defects in superhydrophobic surfaces can have very low break-through pressures and induce instantaneous Wenzel wetting. Thirdly, the overhang width of the microhoodoo structures influences the stability of metastable wetting states. Lastly, we have shown that the introduction of secondary overhangs can enhance or reduce the stability of the metastable state. The exact effect seems to depend on the shape and the spacing of these secondary features.

The surfaces with the highest pressure resistance recorded in our experiments were structured with secondary overhangs. Surfaces could therefore be designed to exhibit robust metastable Cassie-Baxter wetting states on hydrophilic surfaces through the careful fabrication of individual christmas tree structures with multiple overhangs and high $A^{*'}$ values. Further work to establish the dependence on the spacing, width and thickness of the secondary overhangs is necessary to allow for advanced surface structures with robust metastable superhydrophobicity. The use of this technology could allow for a new class of self-cleaning surfaces made from materials which are so far considered inaccessible for self-cleaning surface properties.

In Chapter 12, we discussed underwater wetting of superhydrophobic surfaces quantitatively and qualitatively under water in an open system. It had been shown experimentally [93] and theoretically [6] that superhydrophobic surfaces are surrounded by a plastron when submersed. This plastron decays over time. Here, we have presented the first systematic study of the plastron decay. The study was conducted on superhydrophobic Teflon surfaces with micrometre and nanometre scale roughness. The decay of the plastron on these surfaces was studied using a water immersion setup and underwater confocal imaging of the air-film. The results found for Teflon surfaces were compared to the qualitative study of the underwater wetting behaviour of other superhydrophobic materials.

On Teflon surfaces, the plastron life-time has been shown to depend strongly on immersion depth and water flow. The immersion depth dependence was highly non-linear and could not be explained by a purely diffusion driven process. A qualitative theory describing the three life-time stages of the plastron has been developed to describe the experimental results.

Upon immersion, the plastron forms a thick flat air-film pinned at a few points to the surface. Over time, this film reduces in thickness until further pinning introduces significant local curvature of the air-film; the plastron breaks into individual surface-attached air bubbles. Due to their small size, the air bubbles disappear quickly, leaving only a thin secondary air-film within the nanometre scale of the surface roughness.

Qualitative observation of the plastron decay on other samples showed that micrometre scale roughness was required to obtain a thick plastron. Nanometre scale roughness was required for the presence of a secondary air-film. Samples with micrometre and nanometre roughness exhibited first a primary and then a secondary plastron.

We believe that the presence of the secondary plastron is of only limited technological interest, as it does not significantly contribute to the attributes that are usually attributed to superhydrophobicity (low contact angle hysteresis, enhanced buoyancy). Due to the large amount of structured surface in direct contact with the water, the drag reduction effect should also be reduced. Further, Teflon samples which were in contact with water for an extended amount of time, exhibited a loss of superhydrophobicity. The small surface coverage of the secondary film allows for a large amount of surface to come in contact with the surrounding water. This could cause a general loss of the superhydrophobicity.

Superhydrophobic samples exhibiting micrometre scale roughness are therefore best for underwater applications. If possible, samples should exhibit hierarchical roughness in order to allow for multiple stable air-water interfaces which can support a thick plastron over a long period of time. Nonetheless, the plastron life-time is limited even on highly designed surfaces. Applications designed to exploit the plastron for technological purposes should therefore be constructed such that the plastron can be

regularly regenerated, either through drying of the surface or through a mechanism permitting replenishing of the air-film through pores in the surface itself.

In the absence of these (presently unestablished) plastron restoration mechanisms, our study shows that superhydrophobicity is limited to surfaces that are only intermittently wetted by water, ruling out their use for longtime immersion. In particular, the superhydrophobic effect cannot be used for drag reduction in pipes and coating of underwater surfaces of ships, or for the inside surface of liquid storage containers.

Bibliography

[1] Anish Tuteja, Wonjae Choi, Joseph M. Mabry, Gareth H. Mckinley, and Robert E. Cohen. Robust omniphobic surfaces. *Proceedings of the National Academy of Sciences*, 105(47):18200–18205, November 2008.

[2] Wilhelm T.S. Huck. Responsive polymers for nanoscale actuation. *Materials Today*, 11(7-8):24 – 32, 2008.

[3] W. Barthlott and C. Neinhuis. Purity of the sacred lotus, or escape from contamination in biological surfaces. *Planta*, 202:1–8, 1997.

[4] Anish Tuteja, Wonjae Choi, Minglin Ma, Joseph M. Mabry, Sarah A. Mazzella, Gregory C. Rutledge, Gareth H. McKinley, and Robert E. Cohen. Designing superoleophobic surfaces. *Science*, 318(5856):1618–1622, 2007.

[5] Abraham Marmur. From hygrophilic to superhygrophobic: Theoretical conditions for making high-contact-angle surfaces from low-contact-angle materials. *Langmuir*, 24(14):7573–7579, 2008.

[6] Abraham Marmur. Underwater superhydrophobicity: Theoretical feasibility. *Langmuir*, 22(4):1400–1402, 2006.

[7] Qinmin Pan and Min Wang. Miniature boats with striking loading capacity fabricated from superhydrophobic copper meshes. *Applied Materials & Interfaces*, 1:420–423, 2009.

[8] Jan Genzer and Kirill Efimenko. Recent developments in superhydrophobic surfaces and their relevance to marine fouling: a review. *Biofouling: The Journal of Bioadhesion and Biofilm Research*, 22(5):339–360, 2006.

[9] Ari Laiho. Drag reduction by superhydrophobic surfaces. in preparation, 2009.

[10] Michael Rubinstein and Ralph H. Colby. *Polymer Physics*. Oxford University Press, 2003.

[11] William J. Brittain and Sergiy Minko. A structural definition of polymer brushes. *Journal of polymer science A*, 45(16), 2007.

[12] S. Alexander. Adsorption of chain molecules with a polar head a scaling description. *J. Phys. France*, 38:983ff, 1977.

[13] P. G. de Gennes. Conformations of polymers attached to an interface. *Macromolecules*, 13(5):1069–1075, 1980.

[14] S. Milner, T. Witten, and M. Cates. Theory of the grafted polymer brush. *Macromolecules*, 21(8), 1998.

[15] Bharat Bhushan. *Handbook of micro/nanotribology*. CRC Press, 1999.

[16] Richard Jones. *Soft Condensed Matter*. Oxford University Press, 2002.

[17] Philip Pincus. Colloid stabilization with grafted polyelectrolytes. *Macromolecules*, 24(10):2912–2919, 1991.

[18] R. S. Ross and P. Pincus. The polyelectrolyte brush: poor solvent. *Macromolecules*, 25(8):2177–2183, 1992.

[19] O. V. Borisov, T. M. Birshtein, and E. B. Zhulina. Collapse of grafted polyelectrolyte layer. *Journal de Physique II*, 1(5):521–526, may 1991.

[20] O. V. Borisov, E. B. Zhulina, and T. M. Birshtein. Diagram of the states of a grafted polyelectrolyte layer. *Macromolecules*, 27(17):4795–4803, 1994.

[21] F. Csajka, R. Netz, C. Seidel, and J.-F. Joanny. Collapse of polyelectrolyte brushes: Scaling theory and simulations. *European Physical Journal E*, 4:505, 2001.

[22] Nobushiko Yui, Randall Mrsny, and Kinam Park. *Reflexive Polymers and Hydrogels - Understanding and designing fast responsive polymeric systems*. CRC Press, 2004.

[23] Feng Zhou and Wilhelm Huck. Three-stage switching of surface wetting using phosphate-bearing polymer brushes. *Chemical Communications*, 48:5999, 2005.

[24] Rupert Konradi and Jürgen Rühe. Interaction of poly (methacrylic acid) brushes with metal ions: Swelling properties. *Macromolecules*, 38:4345, 2005.

[25] Rupert Konradi. *Weak Polyacid Brushes: Synthesis, Swelling Behavior, Complex Formation and Micropatterning*. PhD thesis, Albert-Ludwigs-UniversitÍat Freiburg im Breisgau, 2005.

[26] Omar Azzaroni, Sergio Moya, Tamer Farhan, Andrew Brown, and Wilhelm Huck. Switching the properties of polyelectrolyte brushes via "hydrophobic collapse". *Macromolecules*, 38:10192, 2005.

[27] Tamer Farhan, Omar Azzaroni, and Wilhelm Huck. Afm study of cationically charged polymer brushes: switching between soft and hard matter. *Soft Matter*, 1:66, 2005.

[28] Svetlana Prokhorova, Alexey Kopyshev, Ayothi Ramakrishnan, Haining Zhang, and Jurgen Rühe. Polymer substrates as a medium for motion of nano objects. *Proceedings of the SPIE*, 5118:30, 2003.

[29] S. Prokhorova, A. Kopyshev, A. Ramakrishnan, H. Zhang, and J. Rühe. Can polymer brushes induce motion of nano-objects. *Nanotechnology*, 14:1098, 2003.

[30] Rigoberto Advincula, William Brittain, Kenneth Caster, and Jürgen Rühe. *Polymer Brushes*. Wiley-VCH Verlag GmbH & Co. KGaA, 2004.

[31] Sergiy Minko. *Responsive polymer materials: design and applications*. Wiley-Blackwell, 2006.

[32] Omar Azzaroni, Andrew Brown, and Wilhelm Huck. Ucst wetting transitions of polyzwitterionic brushes driven by self-association. *Angewandte Chemie (International Edition)*, 45:1770, 11 2006.

[33] Toyoichi Tanaka. Collapse of gels and the critical endpoint. *Phys. Rev. Lett.*, 40(12):820–823, Mar 1978.

[34] Toyoichi Tanaka, Izumi Nishio, Shao-Tang Sun, and Shizue Ueno-Nishio. Collapse of gels in an electric field. *Science*, 218(4571):467–469, 1982.

[35] Lilit Yeghiazarian, Hitesh Arora, Vasile Nistor, Carlo Montemagno, and Ulrich Wiesner. Teaching hydrogels how to move like an earthworm. *Soft Matter*, 3(8), 2007.

[36] Dirk Schmaljohann, Mirko Nitschke, Roland Schulze, Andreas Eing, Carsten Werner, and Klaus-Jochen Eichhorn. In situ study of the thermoresponsive behavior of micropatterned hydrogel films by imaging ellipsometry. *Langmuir*, 21:2317, 2005.

[37] Jinyu Huang, Brian Cusick, Joanna Pietrasik, Li Wang, Tomasz Kowalewski, Qiao Lin, and Krzysztof Matyjaszewski. Synthesis and in situ atomic force microscopy characterization of temperature-responsive hydrogels based on poly(2-(dimethylamino)ethyl methacrylate) prepared by atom transfer radical polymerization. *Langmuir*, 23(1):241–249, 2007.

[38] Feng Zhou, P. Maarten Biesheuvel, Eun-Young Choi, Wenmiao Shu, Rosa Poetes, Ullrich Steiner, and Wilhelm T. S. Huck. Polyelectrolyte brush amplified electroactuation of microcantilevers. *Nano Letters*, 8(2):725–730, 2008.

[39] Krzysztof Matyjaszewski and Jianhui Xia. Atom transfer radical polymerization. *Chemical Reviews*, 101(9):2921–2990, 2001.

[40] Steve Edmondson, Vicky Osborne, and Wilhelm Huck. Polymer brushes via surface-initiated polymerization. *Chemical Society Review*, 33:14, 2004.

[41] Jin-Shan Wang and Krzysztof Matyjaszewski. Controlled/"living" radical polymerization. atom transfer radical polymerization in the presence of transition-metal complexes. *Journal of the American Chemical Society*, 117(20):5614–5615, 1995.

[42] H. Yim and M. Kent. Temperature-dependent conformational change of pnipam grafted chains at high surface density in water. *Macromolecules*, 2004:1994, 2004.

[43] Ron Oren. PhD thesis, University of Cambridge, 2009.

[44] Evan Spruijt. Electrochemically responsive polymer surfaces. Master's thesis, Wageningen University, 2008.

[45] Harland Tompkins. *Handbook of Ellipsometry*. William Andrew Inc., 2005.

[46] www.wikipedia.com.

[47] Peter Thiesen. Nanofilm technologie gmbh. www.nanofilm.de, 2006.

[48] Harland Tompkins and William McGahan. *Spectroscopic Ellipsometry and Reflectometry - A User's Guide*. John Wiley & Sons, Inc, 1999.

[49] R. Azzam and N. Bashara. *Ellipsometry and Polarized Light*. North Holland Personal Library, 1987.

[50] Joseph Keddie. Structural analysis of organic interfacial layers by ellipsometry. *Colloid & Interface Science*, 6:102, 2001.

[51] Jörg Habicht, Markus Schmidt, Jürgen Rühe, and Diethelm Johannsmann. Swelling of thick polymer brushes investigated with ellipsometry. *Langmuir*, 15:2460, 1999.

[52] Markus Biesalski and Jürgen Rühe. Scaling laws for the swelling of neutral and charged polymer brushes in good solvents. *Macromolecules*, 35:499, 2002.

[53] Markus Biesalski, Jürgen Rühe, and Diethelm Johannsmann. Segment density profiles of polyelectrolyte brushes determined by fourier transform ellipsometry. *Journal of chemical physics*, 111:7029, 1999.

[54] Markus Biesalski, Diethelm Johannsmann, and Jürgen Rühe. Electrolyte-induced collapse of a polyelectrolyte brush. *Journal of chemical physics*, 120(18):8807, 2004.

[55] Markus Biesalski, Jürgen Rühe, and Diethelm Johannsmann. Tailoring the charge density of surface-attached polyelectrolytes. *Macromolecules*, 37:2196, 2004.

[56] Cold Spring Harbor Laboratory. http://www.luxpop.com/, 1998.

[57] D. Huber, R. Manginell, M. Samara, B Kim, and B. Bunker. Programmed adsorption and release of proteins in a microfluidic device. *Science*, 201:352, 2003.

[58] Feng Zhou, Zijian Zheng, Bo Yu, Weimin Liu, and Wilhelm T. S. Huck. Multicomponent polymer brushes. *Journal of the American Chemical Society*, 128(50):16253–16258, 2006.

[59] Jakob Heier, Jan Groenewold, and Ullrich Steiner. Pattern formation in thin polymer films by spatially modulated electric fields. *Soft Matter*, 2009.

[60] Glenn Fredrickson, Armand Ajdari, Ludwig Leibler, and Jean-Pierre Carton. Surface modes and deformation energy of a molten polymer brush. *Macromolecules*, 25:2882–2889, 1992.

[61] Vijay Shenoy and Ashutosh Sharma. Stability of a thin solid film with interactions. *ArXiv Condensed Matter e-prints*, cond-mat/0005324, May 2000.

[62] Erik Schaeffer, Thomas Thurn-Albrecht, Thomas P. Russell, and Ullrich Steiner. Electrically induced structure formation and pattern transfer. *Nature*, 403:874–877, 2000.

[63] Stephan Harkema. *Capillary instabilities in thin polymer films : mechanism of structure*. PhD thesis, Rijksuniversiteit Groningen, 2006.

[64] David R. Barbero and Ullrich Steiner. Nonequilibrium polymer rheology in spincast films. *Physical Review Letters*, 102(24), 2009.

[65] P. S. Laplace. *Mechanique Celeste*. Duprat, 1806.

[66] Thomas Young. An essay on the cohesion of fluids. *Phil. Trans. R. Soc. Lond.*, 95:65–87, 1805.

[67] Robert Wenzel. Resistance of solid surfaces to wetting by water. *Ind. Eng. Chem.*, 28:988–994, 1936.

[68] A. B. D. Cassie and S. Baxter. Wetting of porous surfaces. *Trans. Faraday Soc.*, 40:546–551, 1944.

[69] Pierre-Gilles de Gennes, Francoise Brochard-Wyart, and David Quere. *Capillarity and Wetting Phenomena: Drops, Bubbles, Pearls and Waves*. Springer, 2004.

[70] Abraham Marmur. Wetting on hydrophobic rough surfaces: To be heterogeneous or not to be. *Langmuir*, 19:8343–8348, 2003.

[71] Bo He, Junghoon Lee, and Neelesh Patankar. Contact angle hysteresis on rough hydrophobic surfaces. *Colloids and Surfaces A*, 248:101–104, 2004.

[72] C. Ishino, K. Okumura, and D. Quere. Wetting transitions on rough surfaces. *EPL (Europhysics Letters)*, 68(3):419–425, 2004.

[73] Jose Bico, Uwe Thiele, and David Quere. Wetting of textured surfaces. *Colloids and Surfaces A*, 206:41–46, 2002.

[74] Abraham Marmur and Eyal Bittoun. When wenzel and cassie are right: Reconciling local and global considerations. *Langmuir*, 25(3):1277–1281, 2009.

[75] Michael Nosonovsky and Bharat Bhushan. Stochastic model for metastable wetting of roughness-induced superhydrophobic surfaces. *Microsystems Technology*, 12:231–237, 2006.

[76] C. Ishino and K. Okumura. Wetting transitions on textured hydrophilic surfaces. *The European Physical Journal E*, 25:415–424, 2008.

[77] Mathilde Callies and David Quere. On water repellency. *Soft Matter*, 1:55–61, 2005.

[78] Mathilde Callies, Yong Chen, Frédéric Marty, Anne Pépin, and David Quéré. Microfabricated textured surfaces for super-hydrophobicity investigations. *Microelectronic Engineering*, 78-79:100 – 105, 2005. Proceedings of the 30th International Conference on Micro- and Nano-Engineering.

[79] Lichao Gao and Thomas McCarthy. Artificial lotus leaf prepared using a 1945 patent and a commercial textile. *Langmuir*, 22:5998–6000, 2006.

[80] Christian Dorrer and Juergen Ruehe. Drops on microstructured surfaces coated with hydrophilic polymers: Wenzel's model and beyond. *Langmuir*, 24:1959–1964, 2008.

[81] Paul Roach, Neil Shirtcliffe, and Michael Newton. Progress in superhydrophobic surface development. *Soft Matter*, 4:224–240, 2008.

[82] Weici Wu, Xiaolong Wang, Daoai Wang, Miau Chen, Feng Zhou, Weimin Liu, and Qunji Xue. Alumina nanowire forests via unconventional anodization and super-repellency plus low adhesion to diverse liquids. *Chemical Communications*, pages 1043–1045, 2009.

[83] C Dorrer and J Ruehe. Wetting of silicon nanograss: From superhydrophilic to superhydrophobic surfaces. *Advanced Materials*, 20(1), 2007.

[84] Ralf Blossey. Self-cleaning surfaces - virtual realities. *Nature Materials*, 2:301–306, 2003.

[85] Rulon E. Johnson and Robert Dettre. Contact angle hysteresis iii. study of an idealized heterogeneous surface. *The Journal of Physical Chemistry*, 68(7), 1964.

[86] R. Johnson and R. Dettre. *Contact angle, wettability and adhesion*, volume 43, chapter Contact angle hysteresis, page 112. Advances in chemistry series, 1964.

[87] Tom Krupenkin, J. Ashley Taylor, Evelyn Wang, Paul Kolodner, Marc Hodes, and Todd Salamon. Reversible wetting - dewetting transitions on electrically tunable superhydrophobic nanostructured surfaces. *Langmuir*, 23:9128–9133, 2007.

[88] David Quere. Wetting and roughness. *Annual Review of Materials Research*, 38, 2008.

[89] M. I. Newton N. J. Shirtcliffe, G. McHale. Learning from superhydrophobic plants: The use of hydrophilic areas on superhydrophobic surfaces for droplet control. *Langmuir*, ASAP, 2009.

[90] Stephan Herminghaus. Roughness-induced non-wetting. *Europhysics Letters*, 52(2):165–170, 2000.

[91] Yang-Tse Cheng and Daniel E. Rodak. Is the lotus leaf superhydrophobic? *Applied Physics Letters*, 86(14):144101, 2005.

[92] PJ Holloway and CE Jeffree. *Encyclopedia of Applied Plant Sciences*, chapter Epicuticular waxes, pages 1190–1204. Elsevier, 2005.

[93] Kerstin Koch and Wilhelm Barthlott. Superhydrophobic and superhydrophilic plant surfaces: an inspiration for biomimetic materials. *Phil. Trans. R. Soc. A*, 367:1487–1509, 2009.

[94] Michael Nosonovsky and Bharat Bhushan. Multiscale effects and capillary interactions in functional biomimetic surfaces for energy conversion and green engineering. *Phil. Trans. R. Soc. A*, 367(1893):1511–1539, 2009.

[95] Stanislav Gorb. *Functional Surfaces in Biology: Little Structures with Big Effects*, chapter Dry in the water: the superhydrophobic water fern. Springer, 2009.

[96] P. S. Epstein and M. S. Plesset. On the stability of gas bubbles in liquid-gas solutions. *Journal of Chemical Physics*, 18(11):1505–1509, 1950.

[97] Stig Ljunggren and Jan Christer Eriksson. The lifetime of a colloid-sized gas bubble in water and the cause of the hydrophobic attraction. *Colloids and Surfaces A*, 129:151–155, 1997.

[98] Jan Christer Eriksson and Stig Ljunggren. On the mechanically unstable free energy minimum of a gas bubble which is submerged in water and adheres to a hydrophobic wall. *Colloids and Surfaces A: Physicochemical and Engineering Aspects*, 159(1):159 – 163, 1999.

[99] Nosonovsky. *Multiscale Dissipative Mechanisms and Hierarchical Surfaces.* Springer, 2008.

[100] J. Lyklema, G. J. Fleer, and H. P. van Leeuwen. *Fundamentals of Interface and Colloid Science*, volume 11. Academic Press, 2000.

[101] Marc Madou. *Fundamentals of Microfabrication: The Science of Miniturization.* CRC, 2002.

[102] Pieter van der Wal and Ullrich Steiner. Super-hydrophobic surfaces made from teflon. *Soft Matter*, 3:426–429, 2007.

[103] Maik Scherer. Nanostructured materials via self-assembled templates. Master's thesis, Universitat Konstanz, 2009.

[104] Mamdouh Abdelsalam, Philip Bartlett, Timothy Kelf, and Jeremy Baumberg. Wetting of regularly structured gold surfaces. *Langmuir*, 21:1753–1757, 2005.

[105] Kathrin Holtzmann. Master's thesis, Universitat Beyreuth, 2009.

[106] D. Almawlawi, K. Bosnick, and M. Moskovits. Fabrication of nanometer-scale patterns by ion-milling with porous anodic alumina masks. *Advanced Materials*, 12(17):1252–1257, 2000.

[107] Oxford Instruments. Manual and webpage, 2008.

[108] R. Hild, C. David, H. U. Muller, B. Volkel, D. R. Kayser, and M. Grunze. Formation and characterization of self-assembled monolayers of octadecyltrimethoxysilane on chromium: Application in low-energy electron lithography. *Langmuir*, 14(2):342–346, 1998.

[109] Ilke Anac and Thomas McCarthy. Chemical modification of chromium oxide surfaces using organosilanes. *Journal of Colloid and Interface Science*, 331:139–142, 2009.

[110] Minghui Hu, Suguru Noda, Tatsuya Okubo, Yukio Yamaguchi, and Hiroshi Komiyama. Structure and morphology of self-assembled 3-mercaptopropyltrimethoxysilane layers on silicon oxide. *Applied Surface Science*, 181(3-4):307 – 316, 2001.

[111] Harms Hauke. Superhydrophobic surfaces. Practical Term - Report, 2007.

[112] Bouwe Pieter van der Wal. *Static and dynamic wetting of porous Teflonő surfaces*. PhD thesis, University of Groningen, 2006.

[113] www.surface-tension.de.

[114] Iain Larmour, Steven Bell, and Graham Saunders. Remarkably simple fabrication of superhydrophobic surfaces using electroless galvanic deposition. *Angewandte Chemie International Edition*, 119(10):1740–1742, 2007.

[115] Marjo Paakko, Jaana Vapaavuori, Riitta Silvennoinen, Harri Kosonen, Mikael Ankerfors, Tom Lindstrom, Lars Berglund, and Olli Ikkala. Long and entangled native cellulose i nanofibers allow flexible aerogels and hierarchically porous templates for functionalities. *Soft Matter*, 4:2492–2499, 2008.

[116] Hua Jin, Marjo Pääkkö, Hanna Pynnönen, Jouni Paltakari, Olli Ikkala, and Robin Ras. Superamphiphobic aerogels as bio-inspired cargo carriers on water and oil. to be published, 2009.

[117] Nicola Hüsing and Ulrich Schubert. Aerogels - airy materials: Chemistry, structure, and properties. *Angew. Chem. Int. Ed.*, 37:22–45, 1998.

[118] J. Goldstein, D.E. Newbury, C.E. Joy, D.C. and. Lyman, P. Echlin, E. Lifshin, L. Sawyer, and J. Michael. *Scanning Electron Microscopy and X-ray Microanalysis*. Springer, 2007.

[119] A.F. Stalder, G. Kulik, D. Sage, and L. and Barbieri. A snake-based approach to accurate determination of both contact points and contact angles. *Colloids And Surfaces A: Physicochemical And Engineering*, 286(1-3):92–103, 2006.

[120] James Pawley. *Handbook of Biological Confocal Microscopy*. Springer, 2006.

[121] Nosonovsky M. Multiscale roughness and stability of superhydrophobic biomimetic interfaces. *Langmuir*, 23(6):3157–3161, 2007.

[122] Heather Whitney, Veronica Bennett, Rosa Poetes, Lucy Sandbach, David Prince, Ullrich Steiner, Lars Chittka, and Beverley Glover. Petal epidermal cell shape influences flower wettability more strongly than temperature. to be published, 2009.

[123] Ken-ichi Noda, Beverley Glover, Paul Linstead, and Cathie Martin. Flower colour intensity depends on specialized cell shape controlled by a myb-related transcription factor. *Nature*, 369:661–664, 1994.